

Structural and mechanistic insights of amyloid protein and designed inhibitor interaction in presence or absence of membrane interface

Thesis Submitted for the Degree of
Doctor of Philosophy (Science)
of
Jadavpur University



By
RANIT PARIARY
Department of Chemical Sciences
Bose Institute
Kolkata-700091
India

बसु विज्ञान मंदिर
BOSE INSTITUTE



(विज्ञान एवं प्रौद्योगिकी विभाग, भारत सरकार के एक स्वायत्त संस्था)
(An Autonomous institute of Department of Science & Technology, Govt. of India)


रासायनिक विज्ञान विभाग / Department of Chemical Sciences
समन्वित शैक्षिक परिसर / Unified Academic Campus
ब्लॉक-ई एन, प्लॉट नं-८०, सेक्टर-V, सॉल्ट लेक सिटी, कोलकाता-700 091
Block-EN, Plot No.-80, Sector-V, Salt Lake City, Kolkata-700 091

संदर्भ सं. / Ref. No.

दिनांक / Date :

CERTIFICATE FROM THE SUPERVISOR

This is to certify that the thesis entitled "Structural and mechanistic insights of amyloid protein and designed inhibitor interaction in presence of or absence of membrane interface" submitted by Sri Ranit Pariary who got his name registered on 9th September 2019, for the award of Ph. D. (Science) degree of Jadavpur University, is absolutely based upon his own work under the supervision of Prof. Anirban Bhunia, Department of Chemical Sciences, Bose Institute Unified Campus, Kolkata - 700091 and that neither this thesis nor any part of it has been submitted for either any degree / diploma or any other academic award anywhere before.

 26/6/2024

(Signature of the Supervisor date with official seal)



डॉ. अनिर्बान भुनिया / Dr. Anirban Bhunia
प्रोफेसर / Professor

रासायनिक विज्ञान विभाग / Department of Chemical Sciences
बसु विज्ञान मंदिर / BOSE INSTITUTE
ई एन 80, सेक्टर V, बिधाननगर / EN 80, Sector V, Bidhannagar
कोलकाता / Kolkata-700 091 (भारत / India)

Dedication

To

My Dear

Maa and Baba,

with all love and respect

Acknowledgements

First and foremost, I would like to express my deepest gratitude to **Sri Ramakrishna, Sri Sarada Devi, Swami Vivekananda, and Swami Premanand ji** for their spiritual guidance which have empowered me to proceed successfully. I would like to take this moment to acknowledge everyone whose warm support has made it possible for me to write this thesis.

I would like to pay my deep and sincere gratitude to my Ph.D. Supervisor, **Prof. Anirban Bhunia**, Department of Chemical sciences, Bose Institute, Kolkata. I am grateful to him for giving me the opportunity to work in his laboratory and for providing the essential facilities to complete my research work. This work would not have been achievable without his guidance, support, and constant encouragement throughout my candidature. His vision, sincerity, and motivation, along with his vast knowledge and unwavering positivity, have always inspired and fascinated me.

I would like to thank **Prof. Uday Bandyopadhyay**, Director of the Bose Institute, Kolkata, for giving me the opportunity to work here. I am also grateful **Prof. Anup Kumar Mishra**, Chairman of Department of Chemical science, for his valuable suggestions and providing the necessary facilities.

I sincerely appreciate the collaborative help and valuable discussions during my time as a research fellow. I extend my heartfelt thanks to **Prof. Atin Kumar Mandal** and his scholars **Bajjayanti Ghosh** and **Gourav Shome** for his collaboration and support with *in vivo* experiment facilities. I am especially thankful to **Gourav Shome** who contributed a major part in my research work. I want to extend my gratitude to **Prof. Nakul Chandra Maiti** and his scholar **Dr. Sandip Dolui** from CSIR-IGCB for helping me in inhibition studies. I am grateful to **Dr. Ishu Saraogi** and his scholar **Dr. Anirban Das** from IISER Bhopal for helping in small molecule inhibitor studies. I would like to give my gratitude to all of my collaborators, **Prof. Dulal Senapati** from Saha Institute of Nuclear Physics, **Dr. Suman Iha** from NIT Rourkela, **Dr. Bhubaneswar Mandal** from IIT Guwahati, **Dr. Amaravadhi Harikishoree** from NTU, Singapore, **Dr. Vijayalekshmi Sarojini** from University of Auckland, New Zealand and **Dr. Zuzana Gazova** from Institute of Experimental Physics, Slovakia.

I would like to thank **UGC** for providing me with the research fellowship for five years. I am thankful to all the staff and members of the Central Instrument Facilities, Bose Institute, specifically, **Swaroop da, Tannoy da, Souvik da, Dipak da, Soumya da, Sheelee di, Narayan da, Kaberi di, Yadav da, Smiriti da, Barun da, Ranjan da, Mrinal da and Amarendra da**. Also, I would like to thank to **Dibakar Da** and all other staff of Bose Institute.

My PhD journey was interesting, enjoyable, and seamless, thanks to my lab mates, whose names deserve special mention. I would like to thank my senior **Dr. Bhisma Narayan Ratha** for his generous help and support to standardize insulin model system. I am thankful to my seniors **Dr. Swapna Bera** and **Dr. Humaira Ilyas** for their guidance and motivations in lab. I would also like to thank **Dr. Dipita Bhattacharyya** for her support and the valuable discussions for my work. A big thank you to my senior **Dr. S.K. Abdul Mohid** for his helpfulness and important suggestions in overcoming scientific challenges throughout my tenure. A special thanks to my senior and technical guru, **Shruti Mukherjee**, for always extending a helping hand whenever I faced issues with software or programming scripts. I am grateful to my lab mate **Dibakar Sarkar**. His friendship and support made the PhD journey more enjoyable. I am extremely fortunate to have my lab mate **Karishma**

Biswas, share my experiences. She provided not only academic support but also played a crucial role during my Ph.D. tenure by offering invaluable suggestions, helping with decisions, sharing delicious food, reviewing my writings, and guiding me every step of the way as an elder sister. I will be always thankful to her. I'd also like to thank to my lab mate **Dipanwita Roy** and project trainees **Nabarupa di**, **Tishita**, **Sourabh**, and **Koustav** for engaging in both scientific and non-scientific discussions beyond the lab.

I have always been eager to learn and feel fortunate to have been guided by excellent teachers who have, in various ways, consistently encouraged for higher studies in basic science. I am grateful to my science teachers, **Ranjit babu** and **Nirmal Babu** who sparked my interest in the subject. I want to express my gratitude to all my teachers in school. All my college teachers, specifically, **Dr. Arogya Varam Saha**, **Dr. Prasanta Ghosh**, and **Dr. Hrishikesh Chatterjee** were a great influenced for me to pursue research. I am thankful to **Prof. Kumar Biradha** and his scholars **Kartik da** and **Karabi di** for their support and guidance to complete my project in supramolecular chemistry during my Msc.

I want to extend special thanks to all my friends who have consistently supported me throughout this journey. A special thanks to my all sisters and brothers for their love, support and encouragement. I would like to acknowledge my relatives (**Mama**, **Mami**, **Masi**, **Ritu masi**, **Meso**, and **Pisima**) who have consistently shown enthusiasm and joy for my academic achievement. I convey my special thanks to **Tripti Masi** for preparing such delicious meals for me every day.

No one can achieve success without the blessings of parents. I am deeply grateful to Baba (**Patit Taran Pariary**), Maa (**Tanusri Pani Pariary**) and my sister (**Anuska Pariary**), for their unwavering support and faith in me. I owe a tremendous debt to my parents for the sacrifices they made for us throughout their lives. I feel incredibly fortunate to have their unconditional love and blessings in my life, which have always motivated me.

Ranit Pariary

June, 2024

List of Abbreviations

A β : amyloid β	LUV: Large Unilamellar Vesicles
AD: Alzheimer's disease	MS: Mass Spectrometry
AFM: Atomic Force Microscopy	m/z: Mass to charge ratio
BI: Bovine Insulin	NFT: Neurofibrillary tangles
CBBG: Coomassie brilliant blue G-250	nM: Nano meter
CD: Circular Dichroism	NMR: Nuclear Magnetic Resonance
CL: Cardiolipin	NOE: Nuclear Overhauser Effect
CSP: Chemical Shift Perturbation	NOESY: Nuclear Overhauser Effect Spectroscopy
DLS: Dynamic Light Scattering	PBS: Phosphate Buffer Saline
DMSO: Dimethyl Sulfoxide	PD: Parkinson's disease
DOPC: 1,2-Dioleoyl-sn-glycero-3 phosphocholine	PDB: Protein data bank
D ₂ O: Deuterium oxide	PI: Propidium Iodide
ESI-MS: Electrospray Ionisation Mass Spectrometry	ROS: Reactive oxygen species
FBS: Fetal bovine serum	RP-HPLC: Reverse Phase High Performance Liquid Chromatography
FDA: Food and Drug Administration	TBLE: Total brain lipid extract
GI: Glargine Insulin	TEM: Transmission Electron Microscopy
HFIP: Hexafluoro-2-propanol	TFA: Trifluoroacetic Acid
HI: Human Insulin	ThT: Thioflavin T
HMQC: Heteronuclear Multiple Quantum Coherence	TOCSY: Total Correlation Spectroscopy
HPLC: High Performance Liquid Chromatography	trNOESY: transferred Nuclear Overhauser Effect Spectroscopy
HSQC: Heteronuclear Single Quantum Coherence	SEM: Scanning Electron Microscopy
IDP: Intrinsically disordered protein	STD: Saturation Transfer Difference
ITC: Isothermal Titration Calorimetry	1D/2D: One/Two Dimensional
LDH: Lactate dehydrogenase	Å: Angstrom
LG: Lasunadya Ghrita	μ M/mM: Micro/ Millimolar

Abstract

Title: Structural and mechanistic insights of amyloid protein and designed inhibitor interaction in presence or absence of membrane interface

Index no.- 77/19/Life Sc./26

Amyloidogenic disorders are currently rising as a global health issue, prompting the requirement of extensive studies dedicated to the development of effective targeted therapeutics. Protein amyloidogenesis, involving proteins or peptides such as amyloid β , α -synuclein, and insulin, is crucial in the progression of several human diseases, including neurodegenerative disorders like Alzheimer's (AD) and Parkinson's (PD), and metabolic disorders like Type-2 Diabetes, respectively. The inherent tendency of these amyloidogenic proteins to interact with biological membranes introduce additional complexities to the system. Several literature reports have enhanced our understanding of the system, through the application of *in vitro*, *in vivo*, and *in silico* methods. However, achieving success with these methods has been challenging, partly because of the intricate nature of the aggregation process as well as due to the poor understanding of the mechanism and the targets of the inhibitors.

In this context, the goals of this study are outlined through five chapters. (1) The first chapter provides an overview of amyloid formation in association with membrane, alongside mentioning various therapeutic agents designed for treating or preventing the studied amyloid diseases. (2) In second chapter, inhibition of insulin aggregation was performed using two small molecules, namely Coomassie Brilliant Blue G-250 (CBBG) as well as PAD-S. It's worth mentioning that insulin has been shown to form amyloid deposits at the site of administration. So, inhibition of insulin amyloid not only preserves insulin's therapeutic efficacy but also reduces complications associated with insulin administration in patients. The present investigation established that CBBG and PAD-S, serve as a chemical chaperone that effectively prevents the fibrillation of insulin and disrupted matured fibrils into nontoxic fragments. (3) In the next chapter, PWWP motif, which is known to inhibit the amyloidogenesis, was used in designing a small peptide library and their effect was elucidated in inhibition of insulin. The *de novo* designed cyclic peptide KR7CC (KCPWWPCRR-NH₂), was non-toxic, stable in serum, and effectively inhibited insulin fibrillation in both membrane and non-membrane environments. Several biophysical spectroscopic studies successfully revealed the specific mechanism of inhibition at the atomistic level. (4) In Chapter 4, small peptide and peptidomimetics were designed and synthesized by altering the "RWSLMRPF" recognition motif to specifically target amyloid β peptides (A β) in AD. Peptide1 (P1) and Peptide2 (P2) were synthesized by substituting S and RWS residues, respectively, with β -breaker element (2-aminobenzoic acid) in the RF8 peptide sequence, resulting in novel, serum-stable, and non-toxic peptides with anti-AD activity. Further, P1, a potent inhibitor effectively prevented in late-stage AD by inhibiting A β 42 fibril formation and converting mature fibrils into nontoxic aggregates, followed by an off-pathway aggregation kinetics. (5) Chapter 5 focuses on repurposing Lasunadya Ghrita (LG), an ancient Indian medicine traditionally used to treat gut dysregulation and mental disorder, for AD. Different extracts of LG were analyzed for their potential to inhibit A β aggregation, revealing that the water extract exhibited greater efficacy in preventing A β peptide aggregation and disintegrating mature fibrils. Non-toxic to both neuronal cells and mouse models, LG (water extract) effectively rescues A β toxicity in neuronal SH-SY5Y cells by decreasing ROS generation, membrane leakage, cellular apoptosis, and calcium dyshomeostasis. This research provides a pathway for the development of future medications to combat amyloidosis, offering promising prospects for treating amyloid disorders.

Ranit Pariary
(Ranit Pariary) 26/06/2024

ABi 26/6/2024

(Sign of the Supervisor with Seal and Date)

✻ डॉ. अनिबान भुनिया / Dr. Anirban Bhunia
प्रोफेसर / Professor
रासायनिक विज्ञान विभाग / Department of Chemical Sciences
बसु विज्ञान मंदिर / BOSE INSTITUTE
ई एन 80, सेक्टर V, बिधाननगर / EN 80, Sector V, Bidhannagar
कोलकाता / Kolkata-700 091 (भारत / India)

Preface

The entitled thesis “**Structural and mechanistic insights of amyloid protein and designed inhibitor interaction in presence or absence of membrane interface**” intended to be submitted by the investigator, **Ranit Pariary**, under the supervision of **Prof. Anirban Bhunia**, in the Department of Chemical Sciences, Bose Institute, Unified Campus, Kolkata-700091, India, for the Ph.D. (Sc.) degree in the Jadavpur University, is summarized below.

CHAPTER 1

Chapter 1 is a review of the literature and covers a brief introduction of the amyloid proteins and therapeutic agents to combat amyloid disease in presence and absence of membrane interface.

Parts of this chapter has been adapted from the following publications:

Pariary, R., Bhattacharyya, D. and Bhunia, A., **2019**. Mitochondrial-membrane association of α -synuclein: Pros and cons in consequence of Parkinson's disease pathophysiology. *Gene Reports*, 16, p.100423.

CHAPTER 2

Chapter 2 describes the small molecules serve as an inhibitor as well as fibril disaggregator to prevent insulin amyloidogenesis. Firstly, our studies show Coomassie Brilliant Blue G-250 as a promising chemical chaperone that stabilizes the α -helical native insulin conformers, disrupting their aggregation. Furthermore, it also increases the insulin secretion. This multipolar effect coupled with its non-toxic nature could be useful for developing highly bioactive, targeted and biostable therapeutic insulin.

Here, we also report another novel amphiphilic molecule called PAD-S, which acts as a chemical chaperone and completely inhibits fibrillation of insulin and its biosimilars. PAD-S is non-toxic and protects cells from insulin amyloid induced cytotoxicity. Notably, PAD-S successfully disintegrated preformed insulin fibrils to non-toxic smaller fragments. Since the structural and mechanistic features of amyloids are common to several human pathologies, the understanding of the amyloid disaggregation activity of CBBG and PAD-S will inform the development of small molecule disaggregators for other amyloids.

This chapter has been adapted from the following publications:

(A) **Pariary, R.**, Dolui, S., Shome, G., Mohid, S.A., Saha, A., Ratha, B.N., Harikishore, A., Jana, K., Mandal, A.K., Bhunia, A. and Maiti, N.C., **2023**. Coomassie brilliant blue G-250 acts as a potential chemical chaperone to stabilize therapeutic insulin. *Chemical Communications*, 59(52), pp.8095-8098.

(B) Das, A., Gangarde, Y.M., **Pariary, R.**, Bhunia, A. and Saraogi, I., **2022**. An amphiphilic small molecule drives insulin aggregation inhibition and amyloid disintegration. *International Journal of Biological Macromolecules*, 218, pp.981-991.

CHAPTER 3

Chapter 3 describes that small peptides can effectively target amyloidogenesis serving as an efficient therapeutic alternative in the amyloidogenic disorder. The structural uniqueness of the PWWP motif in the de novo designed heptapeptide, KR7 (KPWWPRR-NH₂) was demonstrated to target insulin fiber elongation specifically. By working on Insulin, an important model system in amyloidogenic studies, we gained several mechanistic insights into the inhibitory actions at the protein-peptide interface. Here, we report a second-generation non-toxic and serum stable cyclic peptide, based primarily on the PWWP motif that resulted in complete inhibition of insulin fibrillation both in the presence and absence of the model membranes. Using both low- and high-resolution spectroscopic techniques, we could delineate the specific mechanism of inhibition, at atomistic resolution. Our studies put forward an effective therapeutic intervention that redirects the default aggregation kinetics towards off-pathway fibrillation. Based on the promising results, this novel cyclic peptide can be considered an excellent lead to design pharmaceutical molecules against amyloidogenesis.

This chapter has been adapted from the following publications:

Pariary, R., Ghosh, B., Bednarikova, Z., Varnava, K.G., Ratha, B.N., Raha, S., Bhattacharyya, D., Gazova, Z., Sarojini, V., Mandal, A.K. and Bhunia, A., **2020**. Targeted inhibition of amyloidogenesis using a non-toxic, serum stable strategically designed cyclic peptide with therapeutic implications. *Biochimica et Biophysica Acta (BBA)-Proteins and Proteomics*, 1868(5), p.140378.

CHAPTER 4

Amyloidosis of amyloid- β (A β) triggers a cascade of events leading to oxidative damage and neuronal death. Therefore, inhibiting A β amyloidosis or disrupting the matured fibrils is the primary target to combat progressive Alzheimer's disease (AD) pathogenesis. Here, we undertake optimization strategies to improve the anti-amyloid efficiency of our previously reported NF11 (NAVRWSLMRPF) peptide. Among the series of peptides tested, non-toxic and serum-stable peptide 1 or P1 containing an anthranilic acid residue shows immense potential in not only inhibiting the A β 42 amyloid formation but also disrupts the mature A β 42 fibrils into non-toxic small molecular weight soluble species. Our studies provide high-resolution characterization for the peptide's mechanism of action. With a binding affinity within micromolar range for both monomer and aggregated A β 42, this α/β hybrid peptide can efficiently modulate A β amyloidosis, while facilitating the clearance of toxic aggregates, and impart protection from apoptosis. Thus, our studies highlight that the incorporation of a β -amino acid not only imparts protection from proteolytic degradation and improved stability, but also function effectively as a β breaker, redirecting the aggregation kinetics towards off-pathway fibrillation.

This chapter has been adapted from the following publications:

Pariary, R., Shome, G., Kalita, S., Kalita, S., Roy, A., Harikishoree, A., Jana, K., Senapati, D., Mandal, B., Mandal, A.K. and Bhunia, A., **2024**. Peptide-Based Strategies: Combating Alzheimer's Amyloid Beta Aggregation through Ergonomic Design and Fibril Disruption. *Biochemistry*, (manuscript submitted).

CHAPTER 5

Amyloid proteins and peptides play a pivotal role in the etiology of various neurodegenerative diseases, including Alzheimer's disease (AD). Synthetically designed small molecules /peptides / peptidomimetics show promise toward inhibition of various kinds of amyloidosis. However, exploration of compounds isolated from natural extracts having such potential is lacking. In chapter 5, we have investigated the repurposing of a traditional Indian medicine Lasunadya Ghrita (LG) in AD. LG is traditionally used to treat gut dysregulation and mental illnesses. Various extracts of LG were obtained, characterized, and analyzed for inhibition of A β aggregation. Biophysical studies show that the water extract of LG (LG_{WE}) is more potent in inhibiting A β peptide aggregation and defibrillation of A β 40/A β 42 aggregates. NMR studies showed that LG_{WE} binds to the central hydrophobic area and C-terminal residues of A β 40/A β 42, thereby modulating the aggregation, and reducing cell membrane damage. Additionally, LG_{WE} rescues A β toxicity in neuronal SH-SY5Y cells evident from decreases in ROS generation, membrane leakage, cellular apoptosis, and calcium dyshomeostasis. Notably, LG_{WE} is non-toxic to neuronal cells and mouse models. Our study thus delves into the mechanistic insights of a repurposed drug LG_{WE} with the potential to ameliorate A β induced neuroinflammation.

This chapter has been adapted from the following publications:

Pariary, R., Shome, G., Dutta, T., Roy, A., Misra, A.K., Jana, K., Rastogi, S., Senapati, D., Mandal, A.K. and Bhunia, A., **2024**. Enhancing Amyloid Beta Inhibition and Disintegration by Natural Compounds: A Study utilizing Spectroscopy, Microscopy and Cell Biology. *Biophysical Chemistry*, (manuscript under review).

Contents

Structural and mechanistic insights of amyloid protein and designed inhibitor interaction in presence or absence of membrane interface.....	1
Chapter 1	1
1. A brief introduction of Amyloids and therapeutic development	1
1.1. Protein misfolding and amyloid fibril formation	1
1.2. Metabolic disorder: Insulin-derived amyloidosis	3
1.3. Neurodegenerative diseases	7
1.4. Role of lipid membrane in amyloid disease.....	13
1.5. Evaluating design inhibitor activity through biophysical techniques	17
1.6. Reference	18
Chapter 2	29
2. Small molecule act as a chemical chaperone to prevent insulin aggregation and disaggregate amyloids	29
2.1. Coomassie brilliant blue G-250 acts as a potential chemical chaperone to stabilize therapeutic insulin	29
2.1.1. Introduction.....	29
2.1.2. Experimental Methods	29
2.1.3. Results and discussion	40
2.1.4. Conclusion	52
2.1.5. Appendix 2.1	53
2.1.6. References	58
2.2. An amphiphilic small molecule drives insulin aggregation inhibition and amyloid disintegration	61
2.2.1. Introduction	61
2.2.2. Experimental Methods	62
2.2.3. Results and discussion	66
2.2.4. Conclusion	78
2.2.5. Appendix 2.2	79
2.2.6. References	81
Chapter 3	84
3. Targeted inhibition of amyloidogenesis using A non-toxic, serum stable strategically designed cyclic peptide with therapeutic implications.....	84
3.1. Introduction	84
3.2. Experimental Methods	86
3.3. Results and discussion	94
3.4. Conclusion	108

3.5. Appendix 3	109
3.6. References	112
 Chapter 4	 116
4. Peptide-based strategies: combating Alzheimer's amyloid beta aggregation through ergonomic design and fibril disruption	 116
4.1. Introduction	116
4.2. Experimental Methods	118
4.3. Results and discussion	126
4.4. Conclusion	143
4.5. Appendix 4	144
4.6. References	148
 Chapter 5	 154
5. Enhancing amyloid beta inhibition and disintegration by natural compounds: a study utilizing spectroscopy, microscopy and cell biology.....	154
5.1. Introduction	154
5.2. Experimental Methods	156
5.3. Results and discussion	164
5.4. Conclusion	180
5.5. Appendix 5	181
5.6. References	184
 Summary and future outlook	 190

Peer-reviewed publications.

Chapter 1

1. A brief introduction of Amyloid Diseases and therapeutic development

This chapter has been adapted partially from the following publication:

Pariary, R., Bhattacharyya, D. and Bhunia, A., 2019. Mitochondrial-membrane association of α -synuclein: Pros and cons in consequence of Parkinson's disease pathophysiology. *Gene Reports*, 16, p.100423.

1.1 Protein misfolding and amyloid fibril formation

Proteins, which serve diverse functions in all organisms, require precise folding to maintain their specific three-dimensional structure for optimal functioning. The primary structure of protein is defined as the unique arrangement of amino acids joined by peptide bonds into a polypeptide chain. The secondary structural components, α -helix and β -sheet are constructed by hydrogen bonds formed between the carbonyl oxygen and the amino hydrogen of the polypeptide backbone. These components are further organized to produce overall three-dimensional protein shape, from which the tertiary and quaternary structures emerge. The native states adopted by proteins define the most thermodynamically stable structure under physiological conditions. The inability of any specific peptide or protein to retain its native functional and conformational state may lead to manifestation of a wide range of diseases in humans ¹. One such case is amyloidosis, an abnormal accumulation of misfolded proteins in tissues that further impairs tissue and organ function. Amyloid fibrils are mostly found in the extracellular area, while intracellular inclusion is not uncommon ². This phenomenon has been linked to a variety of age-related pathological conditions, including neurodegenerative and metabolic disorders. Amyloid is associated to the transformation of some peptides or proteins from their soluble functional forms into insoluble states of higher order fibrillar aggregates ³. These non-branching fibrils are held together by intermolecular contacts between β -strands that align orthogonally to the fibril axis to produce cross- β conformations ⁴. However, EM and AFM studies have also shown the fibrils are composed of several parallel thin protofilaments, range in width from 2.4 to 6 nm ⁵.

The kinetics involved during amyloid fibrillation is a complex process in which the aggregation of misfolded proteins leads to insoluble toxic fibrils. A protein with a specific core sequence is frequently used to create a unique amyloid fibril. The structure is very repetitive, and the same interprotein interactions stabilize the strands over the fibril's length. Thioflavin T, a unique dye

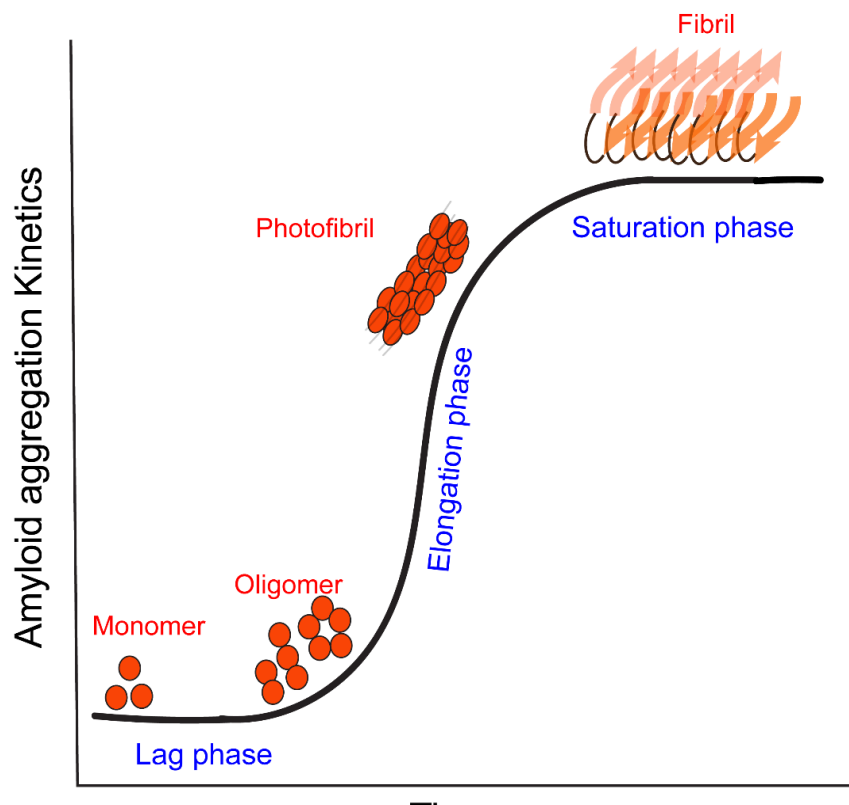


Figure 1.1. A characteristic sigmodal curve for amyloid fibril formation. The curve is generally segmented into three phases: the initial lag phase, the elongation or growth phase, and the final saturation plateau. A monomer transforms into an oligomer, then into a protofibril, and finally produces a fibril.

that excites at 440 nm and emits at 480 nm, may bind to the amyloid β -sheet region and create intense fluorescence ⁶. The first-order kinetics of fibril formation follows a nucleation-dependent self-assembly mechanism with sigmoidal growth kinetics (Figure 1.1) ⁷. To induce fibril formation, the native folded protein/peptide must be unfolded or misfolded that are prone to aggregation. The conventional fibril formation process begins with forming a nucleus during the lag phase in which newly formed monomers react with one another to produce oligomers (Figure 1.1). Following that, oligomers form protofibrils, and rapid fibril growth is observed during the elongation phase (Figure 1.1). Finally, in a saturation phase, most soluble proteins/peptides are

transformed into fibrils and the process reaches equilibrium (Figure 1.1). The main factors affecting amyloid aggregation kinetics are the initial concentration, temperature, pH, ionic strength, salt, mutation, preformed fibrils or seeded elements, and foreign molecules. Homogeneous nucleation occurs spontaneously, but heterogeneous nucleation is facilitated by preformed or fragmented fibrils seed and surfaces. The presence of seeds can bypass the primary nucleation process by allowing fibril growth to be fast, resulting in a reduced or abolished the lag phase in amyloid formation ⁸. This may trigger a rapid accumulation of amyloid aggregates, which are thought to be the fundamental cause of many neurodegenerative disorders.

1.2. Metabolic disorder: Insulin-derived amyloidosis

1.2.1. Overview

Insulin is a 51-residue long protein hormone secreted by the pancreatic β -cells that plays an important role in glucose metabolism, assisting in the maintenance of normal blood glucose levels. However, in diabetic patients, the body either produces inadequate insulin or is unable to use the insulin that is produced efficiently, resulting in impaired blood glucose levels. The last resort in the treatment of Diabetes included insulin infusion into patients. However, repeated Insulin injections can result in insulin-derived amyloidosis, a condition in which amyloid protein accumulates under the skin and develops the subcutaneous mass at the site of injection ⁹. These deposits commonly known as the "insulin ball" ¹⁰, pose challenges in diagnosing systemic amyloidosis in individuals with diabetes. Insulin fibrilization results in poor penetration of functional insulin, decreasing insulin potency, and triggering a negative immune response in diabetic patients ¹¹. Further, insulin amyloid aggregates can cause local tissue inflammation and complications at injection sites. Insulin forms amyloid intermediates throughout the manufacturing, purification, long-term storage and transportation processes. In some circumstances, such as while undergoing insulin treatment for diabetes, the injected insulin may experience structural changes and form amyloid fibrils.

In a kinetic model of insulin fibrillation, four types of species are usually generated; (a) hexamer which is comprised of six monomers or three dimers and stabilized by Zn^{2+} , (b) monomer, (c) cluster, (d) fibril ¹². The rate-determining step in the aggregation process is the association of insulin monomers to form a nucleus. During the kinetics of insulin fibrillation, there is a lag phase that is characterised by the transition of the insulin hexamer into partly unfolded monomers, which

then associate to form a nuclear structure. The reported kinetic mechanism comprises of three distinct stages: hexamer disintegration, nucleation process, and fibrillation stage ¹³.

1.2.2. The structure of Insulin

The monomer consists of a 21-residue A chain and a 30-residue B chain connected by one intra-chain and two inter-chain disulphide bonds. The A-chain consists of an N-terminal α -helix (residues A1–A8), followed by a noncanonical turn, a second helix (A12–A18), and a C-terminal segment (A19–A21) (Figures 1.2 A-B) ¹⁴. On the other hand, the B-chain exhibits an N-terminal segment (residues B1–B6), a type II β -turn (B7–B10), a central α -helix (B11–B19), a type I β -turn (B20–B23), and a C-terminal β -strand (B24–B28), which is extended by less well-ordered terminal residues B29 and B30 (Figures 1.2A-B) ¹⁴. The extended region (residues B1-B8) at the N-terminal of the B-chain in the T-state (tense) achieves α -helical structure in the R-state (relaxed) ¹⁵. Nuclear magnetic resonance (NMR) derived structures of insulin and monomeric insulin analogues show that these structural components are preserved in solution ¹⁶. Insulin exists at

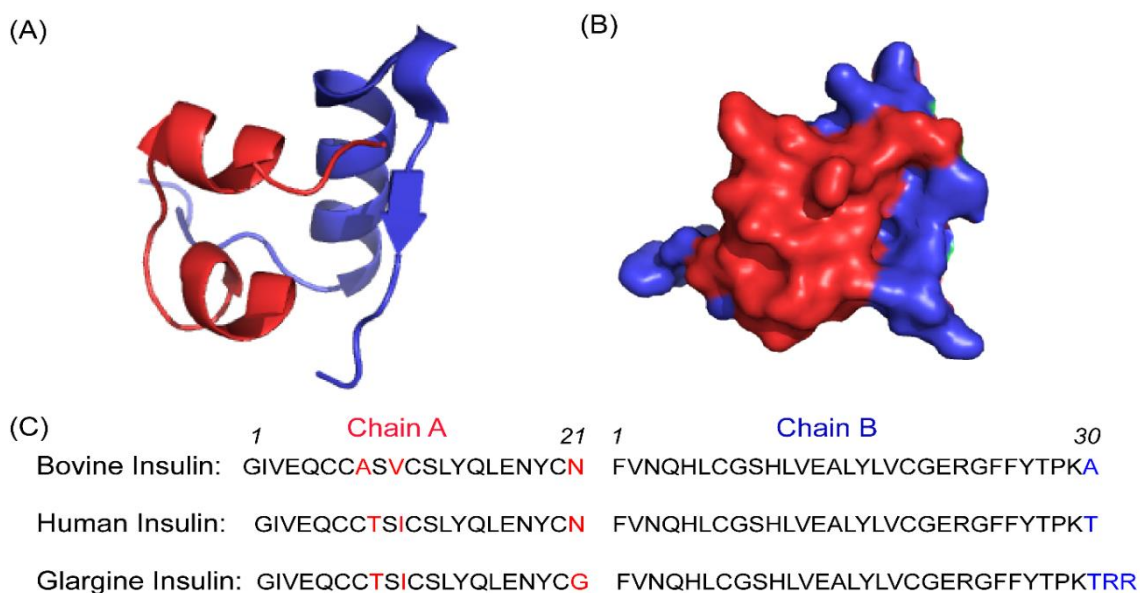


Figure 1.2. Structure and amino acid sequence of insulin. (A) The secondary structure of insulin (PDB :1GUJ; illustrated in PyMOL). The A-chain (red) consists of two α -helices. The B-chain (blue) shows an α -helix flanked by random coil regions. (B) Surface view of A chain (red) and B chain (blue) of insulin. (C) The primary amino acid sequence of bovine insulin, human insulin and glargine insulin.

extremely low amounts as a monomeric unit, or the biologically active form. However, at higher concentrations, it rapidly converts into dimers and assembles into hexamers in the presence of zinc ions in solution at neutral pH. The electrostatic repulsion between protonated histidine and Zn^{2+} ions at low pH facilitates the conversion of insulin hexamers into insulin dimers in the presence of Zn^{2+} . At pH 2.0 and room temperature, insulin forms dimers, as confirmed by solution-state NMR^{14, 16a, 17} and X-ray crystallography¹⁸. The native structures of three insulin variants bovine insulin (BI), human insulin (HI), and modified glargine insulin (GI) are addressed here (Figure 1.2C). It's noteworthy that specific residues, including ValB12, LeuB15, PheB24, and TyrB26, play a crucial role in the interaction of insulin with its receptor¹⁹. However, PheB1, ValB2, GluB13, GlnB4, AlaB14, LeuB17, ValB18, CysB19, and GlyB20 from the insulin B-chain, and LeuA13, TyrA14, and GluA17 from the insulin A-chain, impart its activity in initiating insulin nucleus assembly. As reported by Ivanova et al., the core structure of insulin fibrils predominantly consists of the B-chain residues LVEALYLV²⁰.

1.2.3. Prevention of Insulin Aggregation

Inhibition of the aggregation process may be mediated by improving the stability of monomers, dimers, and hexameric states. The earliest approach of preventing insulin aggregation was to facilitate insulin self-association by adding metal ions such as Zn^{2+} or Ca^{2+} that stabilized the hexameric state of insulin²¹. Currently, phenol, m-cresol, or both are included in significant concentrations, ranging from 29 to 32 mM or 2.7 to 3.2 mg/ml, as preservatives in commercial insulin formulations. Alternatively, there is a growing interest in targeting the inhibition of nucleating intermediates as an appealing therapeutic strategy in insulin and other amyloidogenic pathologies. In addition, stabilizing off-pathway intermediates may reduce the production of toxic oligomers. Several small molecules, peptides, and macrocyclic are used as targeted interventions (Table 1.1). However, the primary limitation of these inhibitors is that none have advanced to clinical trials. Another, challenges abound in making insulin orally bioavailable, though a fundamentally different approach is being pursued with some progress. These studies underscore the necessity of substituting current excipients with new inhibitors that offer improved biocompatibility.

Table 1.1. Several reported inhibitors and their mode of action to inhibit insulin amyloidogenesis.

INHIBITOR	CLASS OF COMPOUND	MODE OF ACTION	REF.
CURCUMIN	Polyaromatic	Interaction with B-chain to inhibit insulin aggregation	Rabiee et al., 2013 ²²
EGCG	Polyaromatic	Slowing down the denaturation and dissociation of insulin	Wang et al., 2012 ²³
BSPOTPE	tetraphenylene core and two sulfonate	Binding with partially folded conformation	Hong et al., 2012 ²⁴
ALIZARIN, PURPURIN	anthraquinone	Disintegrate mature insulin fibrils	Wang et al., 2021 ²⁵
MORIN HYDRATE	Flavonoid	maintaining the native α -helical structure of insulin	Patel et al., 2018 ²⁶
ROSMARINIC ACID	Polyphenol	Binding to a pocket on the surface of insulin dimer and prevent to thermal unfolding	Zheng et al., 2018 ^{17b}
GELATIN	Hydrogel	Stabilized the native structure of insulin	Jayamani et al., 2016 ²⁷
M1	oligopyridylamide	Disrupted fibril elongation	Das et al., 2020 ²⁸
ASCORBIC ACID	Monosaccharide	Disaggregates insulin fibrils	Hsu et al., 2018 ²⁹
METHYLENE BLUE	Dye	Inhibition of nucleus formation	Mukherjee et al., 2018 ³⁰
ORANGE G	Dye	Inhibition of amyloid fibril formation by binding to insulin monomer	Patel et al., 2022 ³¹
NK9 (NIVNVSLVK)	Peptide	Inhibiting insulin nucleation, reducing fibril formation	Banerjee et al., 2013 ³²
NL6 ((NFGAIL), NL6X (X C₇H₇NO₂))	Peptide	Stabilized insulin in its native form by interacting with aggregation prone region of insulin B-chain.	Ratha et al., 2019 ³³

KR7 (KPWWPRR)	Peptide	Targeted the fiber elongation step by binding with LVEALYL residues of insulin	Ratha et al., 2016 ³⁴
IS1 (VYYR)	Peptide	Inhibit heat and storage-induced fibrillation of insulin	Mukherjee et al., 2021 ³⁵
CB[7]	Cucurbituril	Disrupted intermolecular contact after partial unfolding of insulin	Lee et al., 2014 ³⁶
SCX4/6	Sulfonatocalixarene	Encapsulation of the native insulin within the supramolecular cavity.	Shinde et al., 2016 ³⁷
(SBE_{7B}-CD)	Sulfobutylether- β -cyclodextrin	Encapsulation of the insulin side chain within the supramolecular cavity and disintegrate mature fibrils.	Shinde et al., 2017 ³⁸

1.3. Neurodegenerative diseases

1.3.1. Overview

As global life expectancy rises, the emergence of age-related neurodegenerative disorders becomes a greater public health concern. A group of disorders characterized by the progressive degeneration of neurons is described by the broad term "neurodegenerative disease". It progressively impacts the structure and function of neurons in the brain. Alzheimer's disease (AD) and Parkinson's disease (PD) are two well-known neurodegenerative diseases that exhibit the same underlying pathogenesis. AD is a progressive neurodegenerative disorder, characterized by a gradual and irreversible loss of memory, cognitive function, and social skills. AD is a multifactorial disease linked to age, genetics, vascular diseases, infections, head injuries, and environmental factors (e.g., heavy metals)³⁹. As per literature survey, the condition affects 3% of those aged 65 to 74, 17% of people aged 75 to 84, and almost 50% of those aged 85 and higher⁴⁰. The neuropathology of Alzheimer's disease is characterized by several key features such as the accumulation of amyloid beta (A β) plaques, the development of neurofibrillary tangles (NFT), progressive neuronal loss, chronic inflammation and disruption of synaptic function. Amyloid precursor proteins (APP) are transmembrane glycoproteins with 695 to 770 amino acid residues that undergo proteolytic processing to form A β peptides. The peptides A β 40 and A β 42 are commonly associated with AD pathology, and they display predominance in the context of the disease. Over the past decade,

nucleation of amyloid β peptide ($A\beta$) aggregates on the surfaces of $A\beta$ fibrils has emerged as a significant pathway. Initiated by a slow nucleation phase, $A\beta$ monomers aggregate to form oligomeric nuclei. Subsequently, a rapid growth phase ensues, characterized by the addition of monomers, fibril formation, and their further growth. The aggregation of amyloidogenic proteins into soluble intermediate aggregates such as oligomers or proto fibrils and mature fibrils is associated with toxic effects on neuronal cells⁴¹. The proposition of an inverse correlation between the size of soluble aggregates and their toxicity potency implies that larger soluble aggregates may possess comparatively lower levels of toxic effects than their smaller counterparts^{41b}. $A\beta$ oligomers disrupt membranes, increase oxidative stress and induce dysfunction in cellular organelles, leading to toxicity. $A\beta$ -induced neurotoxicity activates apoptosis signal-regulating kinase 1 (ASK1) through its generation of reactive oxygen species (ROS)⁴². Further, PD is the most well-spread movement disorder and the second most common neurodegenerative disorder after AD⁴³. The disease is identified by motor disturbances such as resting tremor, rigidity, bradykinesia, and postural instability, prompted by the slow and progressive death of dopaminergic (DA) neurons from the substantia nigra⁴⁴. The SNCA locus from the fourth chromosome, encoding the α -synuclein protein is among the first loci recognized and identified to be associated with the autosomal dominant inherited form of PD. The disease

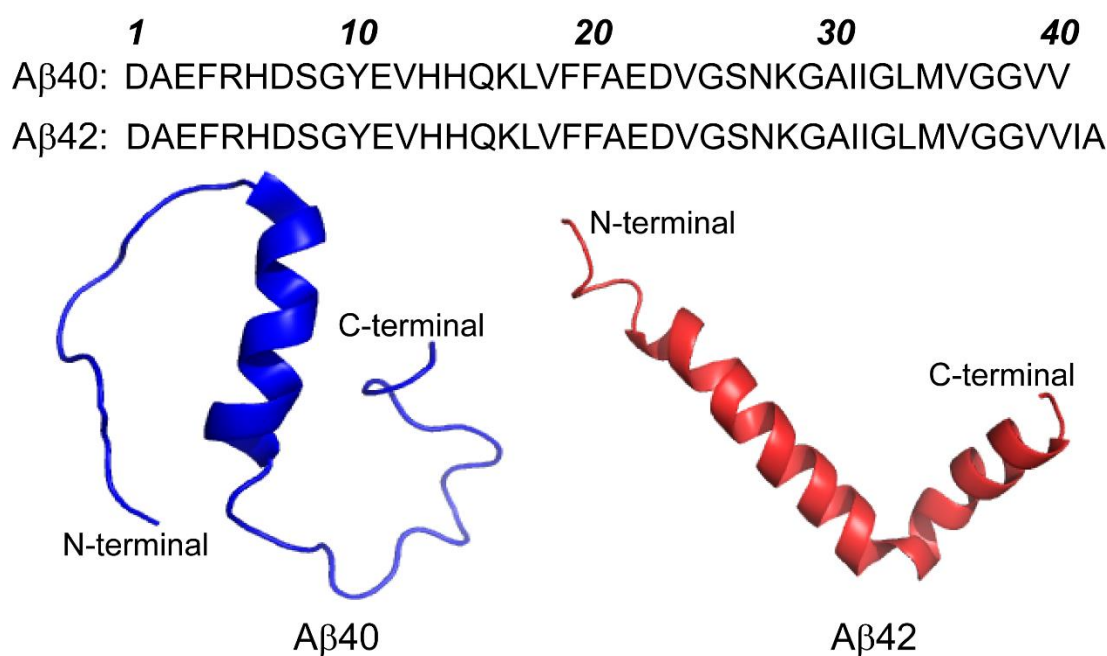


Figure 1.3. The primary amino acid sequence and cartoon model of $A\beta_{40}$ (PDB: 2LFM) and $A\beta_{42}$ (PDB: 1IYT).

pathophysiology is almost always marked by the presence of dense cellular inclusions mainly composed of the amyloidogenic protein aggregates in the form of Lewy bodies in the DA neurons (commonly referred to as Lewy neurites). The hallmarks of PD-affected neurons involve similar evidence of excessive oxidative stress, protein damage, deposition in MAMs, and most importantly, mitochondrial dysfunction ⁴⁵. The overexpression of α -synuclein complies with mitochondrial dysfunction promoting an impairment of complex-I activity, an increase in ROS production, and mitochondrial fragmentation.

1.3.2. The structure of A β and α -synuclein

In 1984, researchers first identified the primary amino acid sequence of A β from extracellular deposits and amyloid plaques ⁴⁶ (Figure 1.3). A β is generally considered to be intrinsically unstructured and, as a result, is challenging to crystallize using conventional methods. NMR spectroscopy, molecular dynamics (MD) techniques, and X-ray crystallography have been employed to determine the 3D solution structure of various fragments of the A β peptide. NMR simulations revealed distinct structural states between A β peptides A β 40 and A β 42 ⁴⁷. The A β 40 peptide has an α -helix shape from residues 15 to 36, with a kink or hinge at residues 25-27, while remaining unstructured between residues 1 and 14 ⁴⁸ (Figure 1.3). In contrast, The C-terminus of A β 42 is highly structured, with residues 31-34 and 38-41 forming a β -hairpin that reduces the region's flexibility (Figure 1.3). The structural difference between A β 42 and A β 40 may be a key factor influencing the increased tendency of A β 42 to form amyloid aggregates (Figure 1.3).

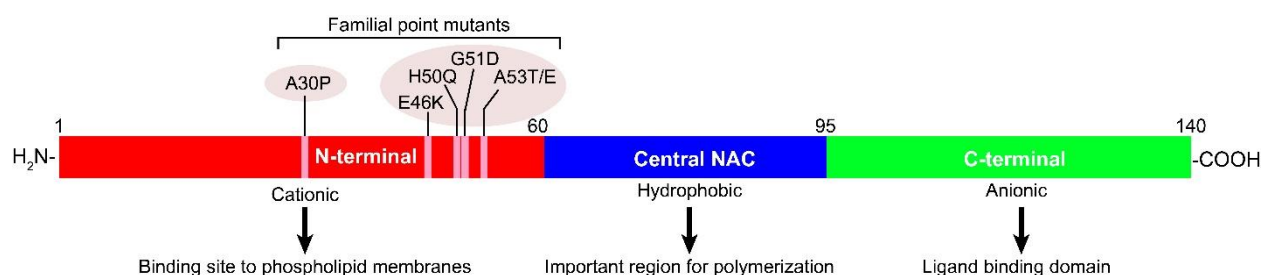


Figure 1.4. Schematic representation of the primary protein structure of α -synuclein. The diagram shows the three segments of the protein and their uniqueness that dictates, in part, the protein's biological functioning. The N-terminal region (red) composed of the repeating amphipathic motifs is rich in cationic residues that underlie the membrane-affinity of the molecule. Interestingly, all of the known familial mutant forms of the protein lie in this region, thus, alternatively suggesting upon the critical role played by this segment in the protein's physiological functions. Figure is adapted with copyright permission from© 2019 Elsevier Inc.

The 140 amino acid long α -synuclein protein, encoded by the SNCA gene is divided into three distinct domains: (i) a positively charged N-terminal region (amino acids 1–60); (ii) the central fibrillating core (amino acid 61–95) that has a high propensity to aggregate⁴⁹; and (iii) a highly acidic C-terminal domain (amino acid 96–140) rich in proline and negatively charged the protein's propensity in binding to phospholipid vesicles⁵¹. Interestingly, all these point mutations are reported in the N-terminal region of α -synuclein, suggesting the significance of this domain in the pathological dysfunction of α -synuclein⁵² (Figure 1.4). The fibrillating core region of the molecule is marked by the central stretch of hydrophobic residues that have previously been shown to be the Non-Amyloid- β Component (NAC) in patients with AD⁵³. The NAC region has a high propensity for adopting β -sheet secondary structure conformation and is essential for aggregation^{49, 54}. The C-terminal is inherently unstructured with five prolines, making it more flexible⁵⁵. Formerly known to be responsible for maintaining the protein's solubility, the C-terminal remains free when associated with the membrane surfaces⁵⁶. This allowed subsequent studies that showed a phosphorylation-prone sequence that further affects the protein's natural physiological functions in association with biologically significant membranes⁵⁷.

1.3.3. Inhibition of amyloid aggregation in neurodegenerative disease

In AD and PD, targeting the aggregation of the A β peptide and α -synuclein protein has emerged as a valid therapeutic strategy⁵⁸. Several potent inhibitors were developed to inhibit amyloid formation, with a primary focus on enhancing the activity of self-recognition segments (L¹⁷VFFA²¹) within the A β ⁵⁹. Alternatively, mutating the consecutive G29xxxG33xxxG37 motifs in the C-terminal domain with Leu or Ile significantly reduced A β 40 and A β 42 production⁶⁰. Similarly, α -synuclein repeat motifs (KTKEGV) was crucial for the amyloid aggregation process, and their disruption resulted in neurotoxicity resembling PD⁶¹. Recent years have seen extensive efforts directed towards developing small molecules designed to inhibit A β and α -synuclein aggregation. Crossing the blood-brain barrier remains a major challenge even in this case, restricting small molecule therapeutic development for central nervous system targets⁶². Numerous naturally occurring small molecules have been studied as inhibitors for A β and α -synuclein. Natural products, with their various compositions and multiple health advantages, provide a viable option for identifying amyloid inhibitors with therapeutic potential. Several plant extracts and phytochemicals, including curcumin, quercetin, epigallocatechin-3-gallate, luteolin,

morin, delphinidins, resveratrol, oleocanthal, and others like huperzine A, azaphilones and limonoids have been reported for their therapeutic potential in neurological disorder ⁶³. Scyllo-inositol, (–)-epigallocatechin-3-gallate (EGCG) and Homotaurine ((3-amino-1-propanesulfonic acid), the small molecule inhibitors, have shown efficacy in disintegrating amyloid fibrils ⁶⁴. Natural remedies, with drug-like qualities, can penetrate the biological membranes and disrupt protein-protein associations ^{63,65}. While exploring food-based drugs for AD and PD, it's essential to concurrently develop pharmacological preparations for effective treatment. Traditional systems like Ayurveda, Unani, Siddha, and Chinese Herbal Medicines commonly use food and natural sources as supplements for various conditions. Polyphenols of phytochemicals, such as flavonoids, curcuminoids, tannins, stilbenes, phenolic acids, anthocyanidins, lignans, chalcones, and related compounds, act as antioxidants, protecting against the development of neurodegenerative diseases ⁶⁶. Flavonoids with a catechol structure and multiple adjacent hydroxyl groups, such as quercetin, taxifolin, epicatechin, and fisetin, exhibit excellent inhibitory effects on amyloid aggregation ⁶⁷. Flavonoids without a catechol structure, including datiscetin, morin, and kaempferol, exhibit anti-aggregative activities against A β ⁶⁸. Resveratrol reduced AD-like amyloid neuropathology and improved A β -related spatial memory decline in Tg2576 mice ⁶⁹. Curcumin, a diarylheptanoid identified in turmeric (*Curcuma longa*) extracts, stimulates anti-inflammatory IL-4 cytokine production, inhibit the formation of large toxic A β oligomers and lowers A β concentrations in mice by inhibiting APP maturation ⁷⁰. The disruption of the β -sheet is preceded by a deformation of its structure, attributed to hydrophobic interactions with nearby curcumin ⁷¹. Curcumin analogues exhibit metal-chelating properties, serve as potent antioxidants within mitochondria and inhibiting the production of amyloid fibrils ^{70a,72}. Alkaloids inhibit the onset of neurotrophic factors (BDNF) and reducing apoptosis in nerve cells ⁷⁴. Over the past decade, there has been a significant focus on developing small peptides that prevent amyloid aggregation (Table 1.2). The main hurdle with therapeutic peptide inhibitors is their limited ability to cross membranes, susceptibility to proteolytic degradation, and tendency to self-aggregate. However, the performance of designed inhibitors aimed at preventing amyloidogenic protein aggregation has consistently fallen short of efficacy benchmarks in clinical trials.

Table 1.2. Reported peptide inhibitors and their mode of action for A β inhibition.

PEPTIDE INHIBITOR	SEQUENCE	MODE OF ACTION	REF.
KLVFF	KLVFF	Disrupting A β aggregation by binding to A β peptides	Tjernberg et al., 1996 ⁷⁵
LK7	Ac-LVFFARK-NH ₂	Inhibit A β aggregation in a dose-dependent manner	Xiong et al., 2015 ⁷⁶
NF11	NAVRWSLMRPF	Slowing down the denaturation and dissociation of insulin	Ghosh et al., 2017 ⁷⁷
H102	HKQLPFFEED	Inhibition and disaggregation of A β fibril	Lin et al., 2014 ^{59b}
IAB5P	LPFFD	Inhibits A β 40 fibril formation and facilitates amyloid plaque disaggregation	Soto et al., 1996 ⁷⁸
DIPEPTIDE	NH ₂ -D-Trp-Aib-OH	Targeting A β assembly into oligomers and disintegrated fibrils	Frydman-Marom et al., 2009 ⁷⁹
PEPTIDE D1	QSHYRHISPAQV	Inhibits A β aggregation and A β -induced cytotoxicity	Wiesehan et al., 2003 ⁸⁰
TFP5	FITCGGGKEAFWDRCL SVINLMSSKMLQINAY ARAARRAARR	Inhibiting the formation of toxic oligomers of A β	Shukla et al., 2017 ⁸¹
D3	RPRTRLHTHRNR	Inhibited A β aggregation and disaggregated pre-existing amyloid plaques	Van Groen et al., 2008 ⁸²
BSBHP 3	Ac-LXFFDNH ₂ (X=C ₇ H ₇ NO ₂)	Disrupts and re-dissolves preformed A β 40 amyloid fibrils	Paul et al., 2015 ⁸³
RI-OR2,	rGffvlkGr (small letters using for D-form amino acids)	Blocks the formation and toxicity of the A β oligomers	Taylor et al., 2010 ^{59a}

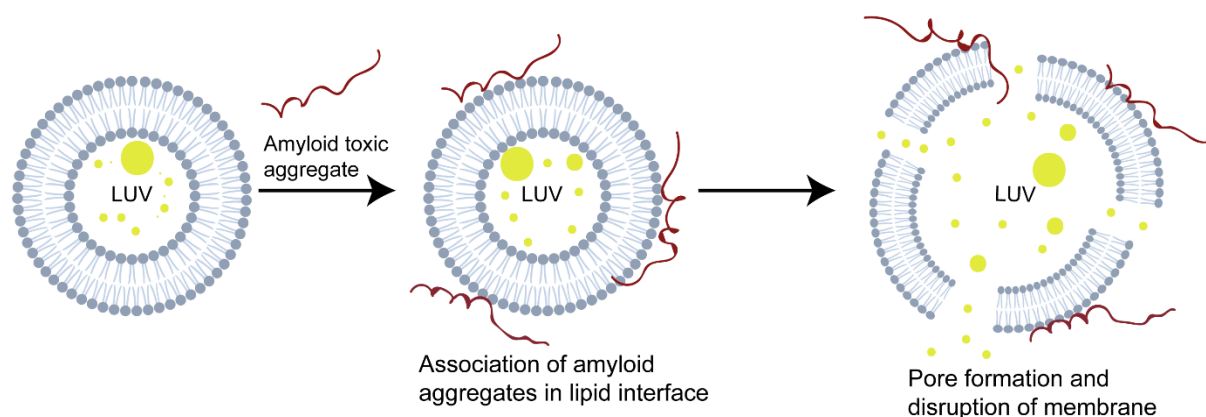


Figure 1.5. Amyloid aggregates insert themselves into the lipid bilayer of the large unilamellar vesicle (LUV), creating pores or destabilizing the membrane structure. A part of the figure was prepared with <https://biorender.com>.

1.4. Role of lipid membrane in amyloid disease

Cell membrane is a place where plethora of biological reaction takes place. Lipids are a predominant class of biological molecules highly prevalent in both subcutaneous fat and cell membranes. Bio membranes play an important role in affecting the overall aggregation kinetics of numerous amyloidogenic proteins at the lipid interface, adding complexity to the system. The protein harbors varying degrees of affinity for different membranes adopting alternate conformations that possibly underlies its homeostatic functioning at the lipid-peptide interface. Depending on the lipid composition, some studies have shown that the membrane induced amyloid protein conformations have the potential to disrupt the associated membranes ⁸⁴ (Figure 1.5). While, others have shown a vesicle turnover functioning of the protein ⁸⁵, some suggest a membrane-associated signalling role of the molecule ⁸⁶. All these studies indicated that the molecular interaction with the membranes initiates the adoption of higher order aggregates ⁸⁶⁻⁸⁷. These higher order conformations are susceptible to misfolding and unchecked aggregation, often related to disease etiology ⁸⁸. However, the interaction of insulin with membrane models is largely unknown. Insulin is stored at a very high concentration (~40 mM) within pancreatic β -cells, yet it does not form amyloids in these cells. In contrast, when therapeutic insulin is administered chronically, it can cause local amyloid formation at the injection sites. To address the problem, our group have previously reported two model membrane surfaces: 7:3 DOPC:DOPG LUVs, and 6:4 POPC:Cholesterol LUVs, mimicking the pancreatic β -cell membrane and eukaryotic cell membrane respectively ⁸⁹. Intermediates formed during insulin fibrillation interact with both

pancreatic β -cell membranes and cholesterol-containing mammalian cell membrane models. The fibrillation of insulin is accelerated by cholesterol-containing eukaryotic cell membranes, while a β -cell membrane model has minimal impact on the early stages of fibrillation kinetics. Further, studies show that the amphiphilic surfactant DHPC suppresses insulin fibrillation⁹⁰ by enabling insulin insertion in the lipid bilayer, thereby decreasing the molecular interaction for aggregation. But the presence of salt increases insulin aggregation, particularly when combined with DOPC in presence of DOPS or DOPE⁹¹. Thus, the kinetics of insulin aggregation were influenced differentially by the length of the saturated lipid chain and the composition of hydrophilic head groups, depending on the pH and salt conditions⁹¹. Further exploration and understanding of these interactions could contribute to insights into the molecular mechanisms underlying insulin fibrillation and its impact on cellular membranes.

In neurodegenerative diseases, brain membrane plays a critical role by regulating the aggregation and toxicity of pathogenic proteins, maintaining synaptic function, and supporting neuronal signaling. Alterations in membrane composition and fluidity can affect the formation of toxic protein aggregates, such as amyloid β plaques in AD and α -synuclein aggregates in PD. The understanding of these interactions is crucial for unravelling the molecular mechanisms that contribute to the pathology of the disease⁹². One of the extensively researched aspects of A β -membrane interactions involves A β insertion into membranes, resulting in the formation of pores and subsequent disruption of the membrane (Figure 1.5)⁹³. Over the years, the blood-brain barrier (BBB) is known to have a role in the pathogenesis of AD. The BBB serves as a protective shield, regulating the passage of A β between the bloodstream and the brain to maintain controlled levels. When the normal transport mechanisms of the BBB are disturbed, increased permeability occurs, enabling the accumulation of A β in the brain⁹⁴. The inability of the BBB to uphold the central nervous system (CNS) homeostasis, as a result of Cerebral Amyloid Angiopathy (CAA), might play a role in the neuropathic processes associated with AD⁹⁵. Early research on A β aggregation found that fibril formation is accelerated by endosomal and lysosomal membranes, while Golgi membranes inhibit fibril formation, promoting exclusive oligomer development⁹⁶. A β interactions with lipid surfaces have been studied using several models, including solid support, self-assembled monolayers, and membrane mimics^{92, 97}. In a particular study, it was found that the presence of anionic phospholipids accelerated the fibrillation of A β , while neutral, zwitterionic, and lipids

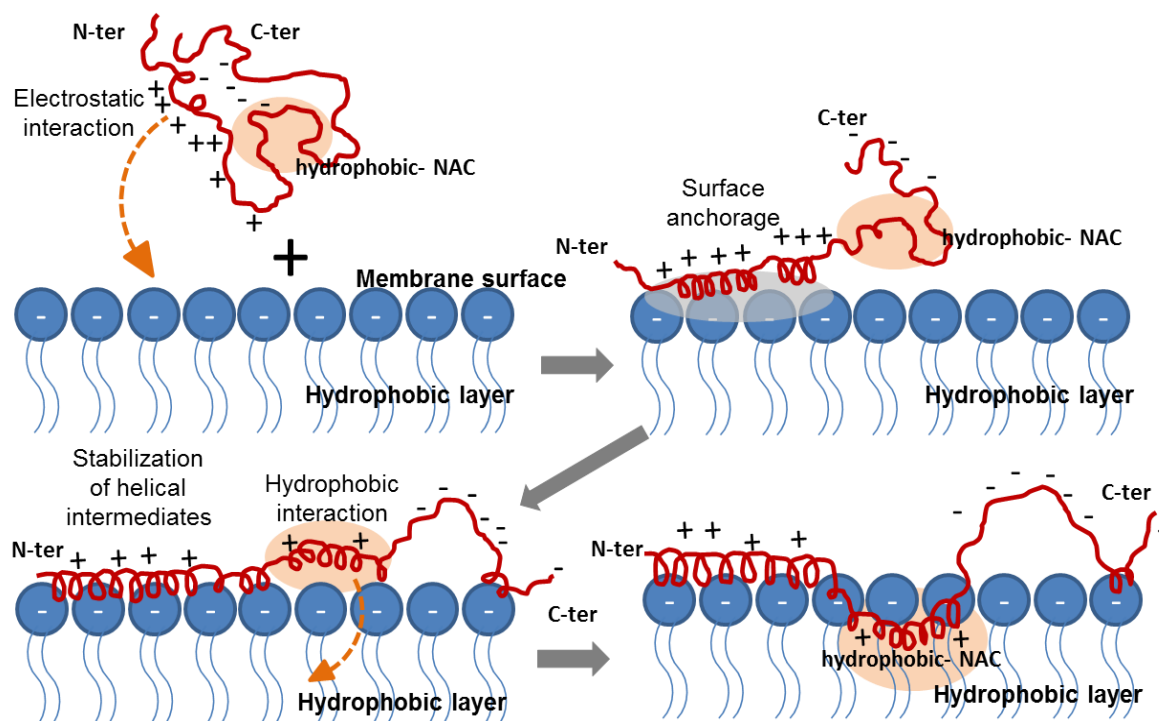


Figure 1.6. Membrane-associated segregation of the functions for each segment α -synuclein. Understanding the segment-specific uniqueness of the proteins residual composition enables us to understand the segregation of each upon membrane binding and association. This eventually is expected to lead to membrane-induced structural uptake of the otherwise intrinsically disordered protein. Several studies have shown that the cationic N-terminal mediates the initial anchorage of the protein to the membrane surface. This opens the fibrillating hydrophobic central core sequence, promoting the formation of higher-order structures upon attaining the hydrophobic protection of the acyl region of the membrane system. The C-terminal on the other hand remains more or less free. Figure is adapted with copyright permission from© 2019 Elsevier Inc.

without phosphate groups did not significantly affect the rates of A β fibrillation⁹⁸. A β exhibited aggregation in zwitterionic lipids such as DPPC and anionic lipids like DOPG. Conversely, A β demonstrated membrane insertion and disruption in the presence of cationic lipids like DOTAP and zwitterionic lipids such as DOPC⁹³. Numerous studies have emphasized the significance of both GM1 and cholesterol in influencing A β fibrillation on membranes⁹⁹. A β recognizes GM1-containing liposome clusters and influences their aggregation processes, which are controlled by cholesterol and ganglioside concentrations within the liposomes¹⁰⁰. Ganglioside clusters act as a unique platform at the hydrophobic/hydrophilic interface, allowing A β molecules to bind and aggregate on them¹⁰¹. In specific scenarios, such as when cholesterol levels are low and membrane fluidity is increased, A β tends to insert into the membrane partially. However, when cholesterol

levels are high, A β diffuses into a more rigid membrane, resulting in larger associations with the membrane ^{99b}. In fact, α -synuclein-membrane interactions have been shown to modulate both protein and membrane properties ¹⁰². The aggregation rate of α -synuclein in the presence of a particular membrane might depend on two factors: the chemical composition of lipids and the lipid-to-protein ratio ¹⁰³. This molecular association results in membrane remodelling, alterations

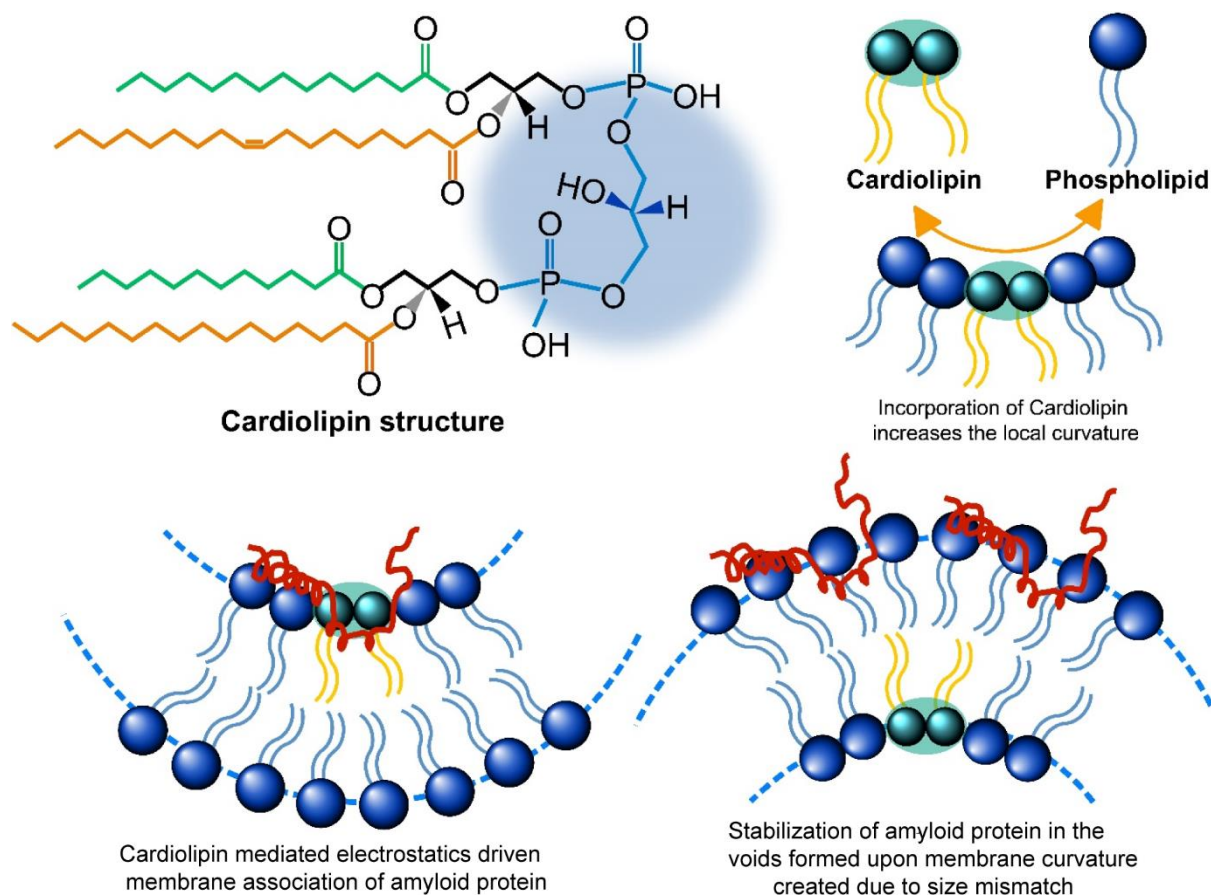


Figure 1.7. Effect of Cardiolipin (CL) on the mitochondrial membrane structure, promoting structural stabilization to membrane-bound amyloid protein. Figure is adapted with copyright permission from© 2019 Elsevier Inc.

in curvature, membrane thinning, and membrane expansion ¹⁰⁴. Several studies have shown that this N-terminal mediated anchorage of the protein to the membrane surface opens the fibrillating core region of the molecule, making it susceptible to fibrillation (Figure 1.6) ^{88b, 105}. Cationic N-terminal region of α -synuclein preferentially bind to the membrane composed majorly of negatively charged lipids by electrostatic interactions ^{88b, 106}. Membrane association provides hydrophobic protection mediated by the acyl chain regions of the lipid layers (Figure 1.6), hence

serving as a template for further protein-protein interaction associated with the higher ordered conformations^{103b, 107}. Studies have shown the favoured binding of α -synuclein to membranes that mainly contain lipid-packing defects and are marked by a high membrane curvature¹⁰⁸. α -synuclein has been suggested to be able to insert and accommodate more easily into lipid bilayers, inducing lateral expansion of the lipid layer, resulting in a reduction of the average bilayer thickness^{102b, 104d}. Among the specific membranous targets studied extensively for α -synuclein interaction, the mitochondrial membrane-associated functioning has often surfaced to be significant in initiating the early pathophysiological conditions¹⁰⁹. Mitochondria dysfunction has often been associated with multiple neurodegenerative diseases. Evidence from several *in vitro* and *in vivo* studies suggested the localization of mutated A β in AD, (DJ1), parkin, and α -synuclein in PD was in mitochondria and MAMs¹¹⁰. This suggests a crucial involvement of mitochondria and its associated membranes in the normal physiological functioning of the proteins. α -Synuclein appears to have a strong preferential binding affinity for mitochondrial or mitochondria-associated membranes (MAM)^{50a}. The mitochondrial membrane is majorly composed of phosphatidylethanolamine (PE), phosphatidylcholine (PC), cardiolipin (CL) and a small amount of cholesterol^{50a, 111}. The presence of CL in the mitochondrial membranes has been shown to play a crucial role in generating the negative charge of the mitochondrial membranes, underlying the molecular attraction of amyloid protein for mitochondria (Figure 1.7)¹¹². Comprehending the dynamics of membrane-mediated amyloid aggregation offers valuable insights for potential therapeutic strategies, aiming to target the initial stages of aggregation or prevent its interaction with membranes.

1.5. Evaluating design inhibitor activity through biophysical techniques

Extensive research has been dedicated to understanding the amyloidogenic role of proteins or peptides in disease, yet their normal physiological function remains elusive. Grasping the dynamics of these molecules is crucial for a comprehensive understanding of the system, particularly in linking protein or peptide disorder to function and misfolding. Designing inhibitors for amyloid aggregation is a multifaceted endeavor that requires a deep comprehension of the structural and functional characteristics of amyloidogenic proteins or peptides and the pathways through which they aggregate. To develop potent inhibitors, it is important to identify the primary aggregation-prone regions inside the amyloid protein or peptide sequence and determine where

inhibitors can bind on monomers, oligomers, or fibrils. Several biophysical experiments, ranging from low-resolution methods such as fluorescence and circular dichroism to high-resolution techniques like nuclear magnetic resonance (NMR) spectroscopy and molecular docking, have been conducted to elucidate the mechanistic interactions at the functional interface that inhibit amyloid peptide or protein aggregation. Additionally, microscopic visualization techniques, including scanning electron microscopy (SEM), atomic force microscopy (AFM), and transmission electron microscopy (TEM), offer valuable insights for thoroughly evaluating the effectiveness of inhibitors in combating amyloid aggregation. Identifying specific therapeutic targets that regulate amyloidogenesis while maintaining their functional connection with membranes is crucial. The aggregation kinetics of amyloid can be influenced by modifications to biological membranes. Vesicles, such as small unilamellar vesicles (SUVs), large unilamellar vesicles (LUVs), giant unilamellar vesicles (GUVs), and multilamellar vesicles (MLVs), are commonly used as biological membrane mimics due to their ease of preparation, handling, and manipulation. Various biophysical methods, including fluorescence dye leakage assays, phase contrast microscopic analysis, and confocal laser scanning microscopy (CLSM), have been employed to explore the interaction between amyloid proteins and membrane mimicking lipid vesicle models. These studies aim to shed light on the mechanisms that underlie amyloid aggregation and identify potential therapeutic strategies.

The main objectives of this thesis are:

- (1) To identify the structural and mechanistic insights of amyloid peptides and proteins, specifically focusing on Insulin and Amyloid β and to understand their aggregation processes, cytotoxic effects, and/ or interactions with membranes.
- (2) To investigate the inhibition of amyloidogenic protein or peptide aggregation using small molecules and designed peptides, providing valuable insights into molecular interactions that could aid in the therapeutic development targeting amyloid proteins.

1.6. References

1. Lindorff-Larsen, K.; Rogen, P.; Paci, E.; Vendruscolo, M.; Dobson, C. M., Protein folding and the organization of the protein topology universe. *Trends Biochem Sci* **2005**, 30 (1), 13-9.

2. Obici, L.; Perfetti, V.; Palladini, G.; Moratti, R.; Merlini, G., Clinical aspects of systemic amyloid diseases. *Biochim Biophys Acta* **2005**, *1753* (1), 11-22.
3. Chiti, F.; Dobson, C. M., Protein misfolding, functional amyloid, and human disease. *Annu Rev Biochem* **2006**, *75*, 333-66.
4. Chuang, E.; Hori, A. M.; Hesketh, C. D.; Shorter, J., Amyloid assembly and disassembly. *J Cell Sci* **2018**, *131* (8).
5. (a) Goldsbury, C.; Kistler, J.; Aebi, U.; Arvinde, T.; Cooper, G. J., Watching amyloid fibrils grow by time-lapse atomic force microscopy. *J Mol Biol* **1999**, *285* (1), 33-9; (b) Chamberlain, A. K.; MacPhee, C. E.; Zurdo, J.; Morozova-Roche, L. A.; Hill, H. A.; Dobson, C. M.; Davis, J. J., Ultrastructural organization of amyloid fibrils by atomic force microscopy. *Biophys J* **2000**, *79* (6), 3282-93; (c) Serpell, L. C.; Sunde, M.; Benson, M. D.; Tennent, G. A.; Pepys, M. B.; Fraser, P. E., The protofilament substructure of amyloid fibrils. *J Mol Biol* **2000**, *300* (5), 1033-9.
6. Biancalana, M.; Koide, S., Molecular mechanism of Thioflavin-T binding to amyloid fibrils. *Biochim Biophys Acta* **2010**, *1804* (7), 1405-12.
7. Chatani, E.; Yamamoto, N., Recent progress on understanding the mechanisms of amyloid nucleation. *Biophys Rev* **2018**, *10* (2), 527-534.
8. Linse, S., Monomer-dependent secondary nucleation in amyloid formation. *Biophys Rev* **2017**, *9* (4), 329-338.
9. Gupta, Y.; Singla, G.; Singla, R., Insulin-derived amyloidosis. *Indian J Endocrinol Metab* **2015**, *19* (1), 174-7.
10. Nagase, T.; Katsura, Y.; Iwaki, Y.; Nemoto, K.; Sekine, H.; Miwa, K.; Oh, I. T.; Kou, K.; Iwaya, K.; Noritake, M.; Matsuoka, T., The insulin ball. *Lancet* **2009**, *373* (9658), 184.
11. (a) Brange, J.; Andersen, L.; Laursen, E. D.; Meyn, G.; Rasmussen, E., Toward understanding insulin fibrillation. *J Pharm Sci* **1997**, *86* (5), 517-25; (b) Dodson, G.; Steiner, D., The role of assembly in insulin's biosynthesis. *Curr Opin Struct Biol* **1998**, *8* (2), 189-94; (c) Ahmad, A.; Millett, I. S.; Doniach, S.; Uversky, V. N.; Fink, A. L., Partially folded intermediates in insulin fibrillation. *Biochemistry* **2003**, *42* (39), 11404-16; (d) Mayer, J. P.; Zhang, F.; DiMarchi, R. D., Insulin structure and function. *Biopolymers* **2007**, *88* (5), 687-713.
12. (a) Serio, T. R.; Cashikar, A. G.; Kowal, A. S.; Sawicki, G. J.; Moslehi, J. J.; Serpell, L.; Arnsdorf, M. F.; Lindquist, S. L., Nucleated conformational conversion and the replication of conformational information by a prion determinant. *Science* **2000**, *289* (5483), 1317-21; (b) Pallitto, M. M.; Murphy, R. M., A mathematical model of the kinetics of beta-amyloid fibril growth from the denatured state. *Biophys J* **2001**, *81* (3), 1805-22.
13. Lee, C. C.; Nayak, A.; Sethuraman, A.; Belfort, G.; McRae, G. J., A three-stage kinetic model of amyloid fibrillation. *Biophys J* **2007**, *92* (10), 3448-58.
14. Hua, Q. X.; Weiss, M. A., Mechanism of insulin fibrillation: the structure of insulin under amyloidogenic conditions resembles a protein-folding intermediate. *J Biol Chem* **2004**, *279* (20), 21449-60.
15. Kosinova, L.; Veverka, V.; Novotna, P.; Collinsova, M.; Urbanova, M.; Moody, N. R.; Turkenburg, J. P.; Jiracek, J.; Brzozowski, A. M.; Zakova, L., Insight into the structural and

- biological relevance of the T/R transition of the N-terminus of the B-chain in human insulin. *Biochemistry* **2014**, *53* (21), 3392-402.
16. (a) Hua, Q. X.; Weiss, M. A., Comparative 2D NMR studies of human insulin and des-pentapeptide insulin: sequential resonance assignment and implications for protein dynamics and receptor recognition. *Biochemistry* **1991**, *30* (22), 5505-15; (b) Hua, Q. X.; Hu, S. Q.; Frank, B. H.; Jia, W.; Chu, Y. C.; Wang, S. H.; Burke, G. T.; Katsoyannis, P. G.; Weiss, M. A., Mapping the functional surface of insulin by design: structure and function of a novel A-chain analogue. *J Mol Biol* **1996**, *264* (2), 390-403; (c) Olsen, H. B.; Ludvigsen, S.; Kaarsholm, N. C., Solution structure of an engineered insulin monomer at neutral pH. *Biochemistry* **1996**, *35* (27), 8836-45.
 17. (a) Jorgensen, A. M.; Kristensen, S. M.; Led, J. J.; Balschmidt, P., Three-dimensional solution structure of an insulin dimer. A study of the B9(Asp) mutant of human insulin using nuclear magnetic resonance, distance geometry and restrained molecular dynamics. *J Mol Biol* **1992**, *227* (4), 1146-63; (b) Zheng, Q.; Lazo, N. D., Mechanistic Studies of the Inhibition of Insulin Fibril Formation by Rosmarinic Acid. *J Phys Chem B* **2018**, *122* (8), 2323-2331.
 18. Whittingham, J. L.; Scott, D. J.; Chance, K.; Wilson, A.; Finch, J.; Brange, J.; Guy Dodson, G., Insulin at pH 2: structural analysis of the conditions promoting insulin fibre formation. *J Mol Biol* **2002**, *318* (2), 479-90.
 19. Das, A.; Shah, M.; Saraogi, I., Molecular Aspects of Insulin Aggregation and Various Therapeutic Interventions. *ACS Bio Med Chem Au* **2022**, *2* (3), 205-221.
 20. Ivanova, M. I.; Sievers, S. A.; Sawaya, M. R.; Wall, J. S.; Eisenberg, D., Molecular basis for insulin fibril assembly. *Proc Natl Acad Sci U S A* **2009**, *106* (45), 18990-5.
 21. Hill, C. P.; Dauter, Z.; Dodson, E. J.; Dodson, G. G.; Dunn, M. F., X-ray structure of an unusual Ca²⁺ site and the roles of Zn²⁺ and Ca²⁺ in the assembly, stability, and storage of the insulin hexamer. *Biochemistry* **1991**, *30* (4), 917-24.
 22. Rabiee, A.; Ebrahim-Habibi, A.; Ghasemi, A.; Nemat-Gorgani, M., How curcumin affords effective protection against amyloid fibrillation in insulin. *Food Funct* **2013**, *4* (10), 1474-80.
 23. Wang, S.-H. D., X.-Y.; Sun, Y., Effect of (-)-Epigallocatechin- 3-Gallate on Human Insulin Fibrillation/Aggregation Kinetics. *Biochem. Eng. J.* **2012**, *63*, 38-49.
 24. Hong, Y.; Meng, L.; Chen, S.; Leung, C. W.; Da, L. T.; Faisal, M.; Silva, D. A.; Liu, J.; Lam, J. W.; Huang, X.; Tang, B. Z., Monitoring and inhibition of insulin fibrillation by a small organic fluorogen with aggregation-induced emission characteristics. *J Am Chem Soc* **2012**, *134* (3), 1680-9.
 25. Wang, W.; Zhang, J.; Qi, W.; Su, R.; He, Z.; Peng, X., Alizarin and Purpurin from *Rubia tinctorum* L. Suppress Insulin Fibrillation and Reduce the Amyloid-Induced Cytotoxicity. *ACS Chem Neurosci* **2021**, *12* (12), 2182-2193.
 26. Patel, P.; Parmar, K.; Das, M., Inhibition of insulin amyloid fibrillation by Morin hydrate. *Int J Biol Macromol* **2018**, *108*, 225-239.
 27. Jayamani, J., & Shanmugam, G., Gelatin as a potential inhibitor of insulin amyloid fibril formation. *ChemistrySelect*, **2016**, *1*(15), 4463-4471.

28. Das, A.; Gangarde, Y. M.; Tomar, V.; Shinde, O.; Upadhyay, T.; Alam, S.; Ghosh, S.; Chaudhary, V.; Saraogi, I., Small-Molecule Inhibitor Prevents Insulin Fibrillogenesis and Preserves Activity. *Mol Pharm* **2020**, *17* (6), 1827-1834.
29. Hsu, H. K.; Hsu, K. H.; Cheng, Y. M.; Suen, H. Y.; Peng, S. F., Development and In Vitro Evaluation of Linear PEI-Shelled Heparin/Berberine Nanoparticles in Human Osteosarcoma U-2 OS Cells. *Molecules* **2018**, *23* (12).
30. Mukherjee, M.; Jana, J.; Chatterjee, S., A Small Molecule Impedes Insulin Fibrillation: Another New Role of Phenothiazine Derivatives. *ChemistryOpen* **2018**, *7* (1), 68-79.
31. Patel, P. N.; Parmar, K.; Patel, S.; Das, M., Orange G is a potential inhibitor of human insulin amyloid fibrillation and can be used as a probe to study mechanism of amyloid fibrillation and its inhibition. *Int J Biol Macromol* **2022**, *220*, 613-626.
32. Banerjee, V.; Kar, R. K.; Datta, A.; Parthasarathi, K.; Chatterjee, S.; Das, K. P.; Bhunia, A., Use of a small peptide fragment as an inhibitor of insulin fibrillation process: a study by high and low resolution spectroscopy. *PLoS One* **2013**, *8* (8), e72318.
33. Ratha, B. N.; Kar, R. K.; Kalita, S.; Kalita, S.; Raha, S.; Singha, A.; Garai, K.; Mandal, B.; Bhunia, A., Sequence specificity of amylin-insulin interaction: a fragment-based insulin fibrillation inhibition study. *Biochim Biophys Acta Proteins Proteom* **2019**, *1867* (4), 405-415.
34. Ratha, B. N.; Ghosh, A.; Brender, J. R.; Gayen, N.; Ilyas, H.; Neeraja, C.; Das, K. P.; Mandal, A. K.; Bhunia, A., Inhibition of Insulin Amyloid Fibrillation by a Novel Amphipathic Heptapeptide: MECHANISTIC DETAILS STUDIED BY SPECTROSCOPY IN COMBINATION WITH MICROSCOPY. *J Biol Chem* **2016**, *291* (45), 23545-23556.
35. Mukherjee, M.; Das, D.; Sarkar, J.; Banerjee, N.; Jana, J.; Bhat, J.; Reddy, G. J.; Bharatam, J.; Chattopadhyay, S.; Chatterjee, S.; Chakrabarti, P., Prion-derived tetrapeptide stabilizes thermolabile insulin via conformational trapping. *iScience* **2021**, *24* (6), 102573.
36. Lee, H. H.; Choi, T. S.; Lee, S. J.; Lee, J. W.; Park, J.; Ko, Y. H.; Kim, W. J.; Kim, K.; Kim, H. I., Supramolecular inhibition of amyloid fibrillation by cucurbit[7]uril. *Angew Chem Int Ed Engl* **2014**, *53* (29), 7461-5.
37. Shinde, M. N.; Barooah, N.; Bhasikuttan, A. C.; Mohanty, J., Inhibition and disintegration of insulin amyloid fibrils: a facile supramolecular strategy with p-sulfonatocalixarenes. *Chem Commun (Camb)* **2016**, *52* (14), 2992-5.
38. Shinde, M. N.; Khurana, R.; Barooah, N.; Bhasikuttan, A. C.; Mohanty, J., Sulfobutylether- β -Cyclodextrin for Inhibition and Rupture of Amyloid Fibrils. *J. Phys. Chem. C* **2017**, *121* (36), 20057–20065.
39. Wang, H.; Yang, F.; Zhang, S.; Xin, R.; Sun, Y., Genetic and environmental factors in Alzheimer's and Parkinson's diseases and promising therapeutic intervention via fecal microbiota transplantation. *NPJ Parkinsons Dis* **2021**, *7* (1), 70.
40. (a) Fratiglioni, L.; Grut, M.; Forsell, Y.; Viitanen, M.; Grafstrom, M.; Holmen, K.; Ericsson, K.; Backman, L.; Ahlbom, A.; Winblad, B., Prevalence of Alzheimer's disease and other dementias in an elderly urban population: relationship with age, sex, and education. *Neurology* **1991**, *41* (12), 1886-92; (b) Qiu, C.; Kivipelto, M.; von Strauss, E., Epidemiology

- of Alzheimer's disease: occurrence, determinants, and strategies toward intervention. *Dialogues Clin Neurosci* **2009**, *11* (2), 111-28; (c) 2022 Alzheimer's disease facts and figures. *Alzheimers Dement* **2022**, *18* (4), 700-789.
41. (a) Walsh, D. M.; Selkoe, D. J., A beta oligomers - a decade of discovery. *J Neurochem* **2007**, *101* (5), 1172-84; (b) Sengupta, U.; Nilson, A. N.; Kaye, R., The Role of Amyloid-beta Oligomers in Toxicity, Propagation, and Immunotherapy. *EBioMedicine* **2016**, *6*, 42-49.
 42. Kadowaki, H.; Nishitoh, H.; Urano, F.; Sadamitsu, C.; Matsuzawa, A.; Takeda, K.; Masutani, H.; Yodoi, J.; Urano, Y.; Nagano, T.; Ichijo, H., Amyloid beta induces neuronal cell death through ROS-mediated ASK1 activation. *Cell Death Differ* **2005**, *12* (1), 19-24.
 43. Meissner, W. G.; Frasier, M.; Gasser, T.; Goetz, C. G.; Lozano, A.; Piccini, P.; Obeso, J. A.; Rascol, O.; Schapira, A.; Voon, V.; Weiner, D. M.; Tison, F.; Bezard, E., Priorities in Parkinson's disease research. *Nat Rev Drug Discov* **2011**, *10* (5), 377-93.
 44. (a) Wood-Kaczmar, A.; Gandhi, S.; Wood, N. W., Understanding the molecular causes of Parkinson's disease. *Trends Mol Med* **2006**, *12* (11), 521-8; (b) Gazewood, J. D.; Richards, D. R.; Clebak, K., Parkinson disease: an update. *Am Fam Physician* **2013**, *87* (4), 267-73; (c) Rao, S. S.; Hofmann, L. A.; Shakil, A., Parkinson's disease: diagnosis and treatment. *Am Fam Physician* **2006**, *74* (12), 2046-54; (d) Rezak, M., Current pharmacotherapeutic treatment options in Parkinson's disease. *Dis Mon* **2007**, *53* (4), 214-22.
 45. Reddy, P. H., Role of mitochondria in neurodegenerative diseases: mitochondria as a therapeutic target in Alzheimer's disease. *CNS Spectr* **2009**, *14* (8 Suppl 7), 8-13; discussion 16-8.
 46. Glenner, G. G.; Wong, C. W., Alzheimer's disease: initial report of the purification and characterization of a novel cerebrovascular amyloid protein. *Biochem Biophys Res Commun* **1984**, *120* (3), 885-90.
 47. Sgourakis, N. G.; Yan, Y.; McCallum, S. A.; Wang, C.; Garcia, A. E., The Alzheimer's peptides Abeta40 and 42 adopt distinct conformations in water: a combined MD / NMR study. *J Mol Biol* **2007**, *368* (5), 1448-57.
 48. Chen, G. F.; Xu, T. H.; Yan, Y.; Zhou, Y. R.; Jiang, Y.; Melcher, K.; Xu, H. E., Amyloid beta: structure, biology and structure-based therapeutic development. *Acta Pharmacol Sin* **2017**, *38* (9), 1205-1235.
 49. Giasson, B. I.; Murray, I. V.; Trojanowski, J. Q.; Lee, V. M., A hydrophobic stretch of 12 amino acid residues in the middle of alpha-synuclein is essential for filament assembly. *J Biol Chem* **2001**, *276* (4), 2380-6.
 50. (a) Guardia-Laguarta, C.; Area-Gomez, E.; Rub, C.; Liu, Y.; Magrane, J.; Becker, D.; Voos, W.; Schon, E. A.; Przedborski, S., alpha-Synuclein is localized to mitochondria-associated ER membranes. *J Neurosci* **2014**, *34* (1), 249-59; (b) Bayer, T. A.; Jakala, P.; Hartmann, T.; Havas, L.; McLean, C.; Culvenor, J. G.; Li, Q. X.; Masters, C. L.; Falkai, P.; Beyreuther, K., Alpha-synuclein accumulates in Lewy bodies in Parkinson's disease and dementia with Lewy bodies but not in Alzheimer's disease beta-amyloid plaque cores. *Neurosci Lett* **1999**, *266* (3), 213-6.
 51. (a) Vamvaca, K.; Lansbury, P. T., Jr.; Stefanis, L., N-terminal deletion does not affect alpha-synuclein membrane binding, self-association and toxicity in human neuroblastoma cells,

- unlike yeast. *J Neurochem* **2011**, *119* (2), 389-97; (b) Bodner, C. R.; Dobson, C. M.; Bax, A., Multiple tight phospholipid-binding modes of alpha-synuclein revealed by solution NMR spectroscopy. *J Mol Biol* **2009**, *390* (4), 775-90.
52. (a) Dehay, B.; Bourdenx, M.; Gorry, P.; Przedborski, S.; Vila, M.; Hunot, S.; Singleton, A.; Olanow, C. W.; Merchant, K. M.; Bezard, E.; Petsko, G. A.; Meissner, W. G., Targeting alpha-synuclein for treatment of Parkinson's disease: mechanistic and therapeutic considerations. *Lancet Neurol* **2015**, *14* (8), 855-866; (b) Bhattacharyya, D.; Kumar, R.; Mehra, S.; Ghosh, A.; Maji, S. K.; Bhunia, A., Multitude NMR studies of alpha-synuclein familial mutants: probing their differential aggregation propensities. *Chem Commun (Camb)* **2018**, *54* (29), 3605-3608.
 53. Bisaglia, M.; Trolino, A.; Bellanda, M.; Bergantino, E.; Bubacco, L.; Mammi, S., Structure and topology of the non-amyloid-beta component fragment of human alpha-synuclein bound to micelles: implications for the aggregation process. *Protein Sci* **2006**, *15* (6), 1408-16.
 54. Ueda, K.; Fukushima, H.; Masliah, E.; Xia, Y.; Iwai, A.; Yoshimoto, M.; Otero, D. A.; Kondo, J.; Ihara, Y.; Saitoh, T., Molecular cloning of cDNA encoding an unrecognized component of amyloid in Alzheimer disease. *Proc Natl Acad Sci U S A* **1993**, *90* (23), 11282-6.
 55. Ulmer, T. S.; Bax, A.; Cole, N. B.; Nussbaum, R. L., Structure and dynamics of micelle-bound human alpha-synuclein. *J Biol Chem* **2005**, *280* (10), 9595-603.
 56. (a) Levitan, K.; Chereau, D.; Cohen, S. I.; Knowles, T. P.; Dobson, C. M.; Fink, A. L.; Anderson, J. P.; Goldstein, J. M.; Millhauser, G. L., Conserved C-terminal charge exerts a profound influence on the aggregation rate of alpha-synuclein. *J Mol Biol* **2011**, *411* (2), 329-33; (b) Wang, C.; Zhao, C.; Li, D.; Tian, Z.; Lai, Y.; Diao, J.; Liu, C., Versatile Structures of alpha-Synuclein. *Front Mol Neurosci* **2016**, *9*, 48.
 57. (a) Sato, H.; Kato, T.; Arawaka, S., The role of Ser129 phosphorylation of alpha-synuclein in neurodegeneration of Parkinson's disease: a review of in vivo models. *Rev Neurosci* **2013**, *24* (2), 115-23; (b) Ma, M. R.; Hu, Z. W.; Zhao, Y. F.; Chen, Y. X.; Li, Y. M., Phosphorylation induces distinct alpha-synuclein strain formation. *Sci Rep* **2016**, *6*, 37130; (c) Nakamura, T.; Yamashita, H.; Takahashi, T.; Nakamura, S., Activated Fyn phosphorylates alpha-synuclein at tyrosine residue 125. *Biochem Biophys Res Commun* **2001**, *280* (4), 1085-92.
 58. Estrada, L. D.; Soto, C., Disrupting beta-amyloid aggregation for Alzheimer disease treatment. *Curr Top Med Chem* **2007**, *7* (1), 115-26.
 59. (a) Taylor, M.; Moore, S.; Mayes, J.; Parkin, E.; Beeg, M.; Canovi, M.; Gobbi, M.; Mann, D. M.; Allsop, D., Development of a proteolytically stable retro-inverso peptide inhibitor of beta-amyloid oligomerization as a potential novel treatment for Alzheimer's disease. *Biochemistry* **2010**, *49* (15), 3261-72; (b) Lin, L. X.; Bo, X. Y.; Tan, Y. Z.; Sun, F. X.; Song, M.; Zhao, J.; Ma, Z. H.; Li, M.; Zheng, K. J.; Xu, S. M., Feasibility of beta-sheet breaker peptide-H102 treatment for Alzheimer's disease based on beta-amyloid hypothesis. *PLoS One* **2014**, *9* (11), e112052; (c) Bett, C. K.; Serem, W. K.; Fontenot, K. R.; Hammer, R. P.; Garino, J. C., Effects of peptides derived from terminal modifications of the abeta central hydrophobic core on abeta fibrillization. *ACS Chem Neurosci* **2010**, *1* (10), 661-78; (d) Matharu, B.; El-Agnaf, O.; Razvi, A.; Austen, B. M., Development of retro-inverso peptides as anti-aggregation drugs for beta-amyloid in Alzheimer's disease. *Peptides* **2010**, *31* (10), 1866-72.

60. Kienlen-Campard, P.; Tasiaux, B.; Van Hees, J.; Li, M.; Huysseune, S.; Sato, T.; Fei, J. Z.; Aimoto, S.; Courtoy, P. J.; Smith, S. O.; Constantinescu, S. N.; Octave, J. N., Amyloidogenic processing but not amyloid precursor protein (APP) intracellular C-terminal domain production requires a precisely oriented APP dimer assembled by transmembrane GXXXG motifs. *J Biol Chem* **2008**, 283 (12), 7733-44.
61. Dettmer, U.; Newman, A. J.; von Saucken, V. E.; Bartels, T.; Selkoe, D., KTKEGV repeat motifs are key mediators of normal alpha-synuclein tetramerization: Their mutation causes excess monomers and neurotoxicity. *Proc Natl Acad Sci U S A* **2015**, 112 (31), 9596-601.
62. Gosselet, F.; Loiola, R. A.; Roig, A.; Rosell, A.; Culot, M., Central nervous system delivery of molecules across the blood-brain barrier. *Neurochem Int* **2021**, 144, 104952.
63. Bhat, B. A.; Almilaibary, A.; Mir, R. A.; Aljarallah, B. M.; Mir, W. R.; Ahmad, F.; Mir, M. A., Natural Therapeutics in Aid of Treating Alzheimer's Disease: A Green Gateway Toward Ending Quest for Treating Neurological Disorders. *Front Neurosci* **2022**, 16, 884345.
64. (a) McLaurin, J.; Franklin, T.; Chakrabartty, A.; Fraser, P. E., Phosphatidylinositol and inositol involvement in Alzheimer amyloid-beta fibril growth and arrest. *J Mol Biol* **1998**, 278 (1), 183-94; (b) Ehrnhoefer, D. E.; Bieschke, J.; Boeddrich, A.; Herbst, M.; Masino, L.; Lurz, R.; Engemann, S.; Pastore, A.; Wanker, E. E., EGCG redirects amyloidogenic polypeptides into unstructured, off-pathway oligomers. *Nat Struct Mol Biol* **2008**, 15 (6), 558-66; (c) Aisen, P. S.; Saumier, D.; Briand, R.; Laurin, J.; Gervais, F.; Tremblay, P.; Garceau, D., A Phase II study targeting amyloid-beta with 3APS in mild-to-moderate Alzheimer disease. *Neurology* **2006**, 67 (10), 1757-63.
65. Chen, Z.; Zhong, C., Oxidative stress in Alzheimer's disease. *Neurosci Bull* **2014**, 30 (2), 271-81.
66. Pandey, K. B.; Rizvi, S. I., Plant polyphenols as dietary antioxidants in human health and disease. *Oxid Med Cell Longev* **2009**, 2 (5), 270-8.
67. (a) Ansari, M. A.; Abdul, H. M.; Joshi, G.; Opii, W. O.; Butterfield, D. A., Protective effect of quercetin in primary neurons against Abeta(1-42): relevance to Alzheimer's disease. *J Nutr Biochem* **2009**, 20 (4), 269-75; (b) Bastianetto, S.; Yao, Z. X.; Papadopoulos, V.; Quirion, R., Neuroprotective effects of green and black teas and their catechin gallate esters against beta-amyloid-induced toxicity. *Eur J Neurosci* **2006**, 23 (1), 55-64; (c) Porat, Y.; Abramowitz, A.; Gazit, E., Inhibition of amyloid fibril formation by polyphenols: structural similarity and aromatic interactions as a common inhibition mechanism. *Chem Biol Drug Des* **2006**, 67 (1), 27-37; (d) Sato, M.; Murakami, K.; Uno, M.; Nakagawa, Y.; Katayama, S.; Akagi, K.; Masuda, Y.; Takegoshi, K.; Irie, K., Site-specific inhibitory mechanism for amyloid beta42 aggregation by catechol-type flavonoids targeting the Lys residues. *J Biol Chem* **2013**, 288 (32), 23212-24.
68. Hanaki, M.; Murakami, K.; Akagi, K.; Irie, K., Structural insights into mechanisms for inhibiting amyloid beta42 aggregation by non-catechol-type flavonoids. *Bioorg Med Chem* **2016**, 24 (2), 304-13.
69. Ma, T.; Tan, M. S.; Yu, J. T.; Tan, L., Resveratrol as a therapeutic agent for Alzheimer's disease. *Biomed Res Int* **2014**, 2014, 350516.

70. (a) Chainoglou, E.; Hadjipavlou-Litina, D., Curcumin in Health and Diseases: Alzheimer's Disease and Curcumin Analogues, Derivatives, and Hybrids. *Int J Mol Sci* **2020**, *21* (6); (b) Zhang, C.; Browne, A.; Child, D.; Tanzi, R. E., Curcumin decreases amyloid-beta peptide levels by attenuating the maturation of amyloid-beta precursor protein. *J Biol Chem* **2010**, *285* (37), 28472-80.
71. Zhao, L. N.; Chiu, S. W.; Benoit, J.; Chew, L. Y.; Mu, Y., The effect of curcumin on the stability of Abeta dimers. *J Phys Chem B* **2012**, *116* (25), 7428-35.
72. Prasad, S.; DuBourdieu, D.; Srivastava, A.; Kumar, P.; Lall, R., Metal-Curcumin Complexes in Therapeutics: An Approach to Enhance Pharmacological Effects of Curcumin. *Int J Mol Sci* **2021**, *22* (13).
73. Liu, Q. F.; Jeon, Y.; Sung, Y. W.; Lee, J. H.; Jeong, H.; Kim, Y. M.; Yun, H. S.; Chin, Y. W.; Jeon, S.; Cho, K. S.; Koo, B. S., Nardostachys jatamansi Ethanol Extract Ameliorates Abeta42 Cytotoxicity. *Biol Pharm Bull* **2018**, *41* (4), 470-477.
74. (a) Xiao, Q.; Wang, C.; Li, J.; Hou, Q.; Li, J.; Ma, J.; Wang, W.; Wang, Z., Ginkgolide B protects hippocampal neurons from apoptosis induced by beta-amyloid 25-35 partly via up-regulation of brain-derived neurotrophic factor. *Eur J Pharmacol* **2010**, *647* (1-3), 48-54; (b) Yoo, K. Y.; Park, S. Y., Terpenoids as potential anti-Alzheimer's disease therapeutics. *Molecules* **2012**, *17* (3), 3524-38.
75. Tjernberg, L. O.; Naslund, J.; Lindqvist, F.; Johansson, J.; Karlstrom, A. R.; Thyberg, J.; Terenius, L.; Nordstedt, C., Arrest of beta-amyloid fibril formation by a pentapeptide ligand. *J Biol Chem* **1996**, *271* (15), 8545-8.
76. Xiong, N.; Dong, X. Y.; Zheng, J.; Liu, F. F.; Sun, Y., Design of LVFFARK and LVFFARK-functionalized nanoparticles for inhibiting amyloid beta-protein fibrillation and cytotoxicity. *ACS Appl Mater Interfaces* **2015**, *7* (10), 5650-62.
77. Ghosh, A.; Pradhan, N.; Bera, S.; Datta, A.; Krishnamoorthy, J.; Jana, N. R.; Bhunia, A., Inhibition and Degradation of Amyloid Beta (Abeta40) Fibrillation by Designed Small Peptide: A Combined Spectroscopy, Microscopy, and Cell Toxicity Study. *ACS Chem Neurosci* **2017**, *8* (4), 718-722.
78. Soto, C.; Kindy, M. S.; Baumann, M.; Frangione, B., Inhibition of Alzheimer's amyloidosis by peptides that prevent beta-sheet conformation. *Biochem Biophys Res Commun* **1996**, *226* (3), 672-80.
79. Frydman-Marom, A.; Rechter, M.; Shefler, I.; Bram, Y.; Shalev, D. E.; Gazit, E., Cognitive-performance recovery of Alzheimer's disease model mice by modulation of early soluble amyloid assemblies. *Angew Chem Int Ed Engl* **2009**, *48* (11), 1981-6.
80. Wiesehan, K.; Buder, K.; Linke, R. P.; Patt, S.; Stoldt, M.; Unger, E.; Schmitt, B.; Bucci, E.; Willbold, D., Selection of D-amino-acid peptides that bind to Alzheimer's disease amyloid peptide abeta1-42 by mirror image phage display. *Chembiochem* **2003**, *4* (8), 748-53.
81. Shukla, V.; Seo, J.; Binukumar, B. K.; Amin, N. D.; Reddy, P.; Grant, P.; Kuntz, S.; Kesavapany, S.; Steiner, J.; Mishra, S. K.; Tsai, L. H.; Pant, H. C., TFP5, a Peptide Inhibitor of Aberrant and Hyperactive Cdk5/p25, Attenuates Pathological Phenotypes and Restores Synaptic Function in CK-p25Tg Mice. *J Alzheimers Dis* **2017**, *56* (1), 335-349.

82. van Groen, T.; Wiesehan, K.; Funke, S. A.; Kadish, I.; Nagel-Steger, L.; Willbold, D., Reduction of Alzheimer's disease amyloid plaque load in transgenic mice by D3, A D-enantiomeric peptide identified by mirror image phage display. *ChemMedChem* **2008**, *3* (12), 1848-52.
83. Paul, A.; Nadimpally, K. C.; Mondal, T.; Thalluri, K.; Mandal, B., Inhibition of Alzheimer's amyloid-beta peptide aggregation and its disruption by a conformationally restricted alpha/beta hybrid peptide. *Chem Commun (Camb)* **2015**, *51* (12), 2245-8.
84. Winner, B.; Jappelli, R.; Maji, S. K.; Desplats, P. A.; Boyer, L.; Aigner, S.; Hetzer, C.; Loher, T.; Vilar, M.; Campioni, S.; Tzitzilonis, C.; Soragni, A.; Jessberger, S.; Mira, H.; Consiglio, A.; Pham, E.; Masliah, E.; Gage, F. H.; Riek, R., In vivo demonstration that alpha-synuclein oligomers are toxic. *Proc Natl Acad Sci U S A* **2011**, *108* (10), 4194-9.
85. Fusco, G.; De Simone, A.; Arosio, P.; Vendruscolo, M.; Veglia, G.; Dobson, C. M., Structural Ensembles of Membrane-bound alpha-Synuclein Reveal the Molecular Determinants of Synaptic Vesicle Affinity. *Sci Rep* **2016**, *6*, 27125.
86. Lee, H. J.; Choi, C.; Lee, S. J., Membrane-bound alpha-synuclein has a high aggregation propensity and the ability to seed the aggregation of the cytosolic form. *J Biol Chem* **2002**, *277* (1), 671-8.
87. Hu, R.; Diao, J.; Li, J.; Tang, Z.; Li, X.; Leitz, J.; Long, J.; Liu, J.; Yu, D.; Zhao, Q., Intrinsic and membrane-facilitated alpha-synuclein oligomerization revealed by label-free detection through solid-state nanopores. *Sci Rep* **2016**, *6*, 20776.
88. (a) Dikiy, I.; Eliezer, D., Folding and misfolding of alpha-synuclein on membranes. *Biochim Biophys Acta* **2012**, *1818* (4), 1013-8; (b) Bhattacharyya, D.; Mohite, G. M.; Krishnamoorthy, J.; Gayen, N.; Mehra, S.; Navalkar, A.; Kotler, S. A.; Ratha, B. N.; Ghosh, A.; Kumar, R.; Garai, K.; Mandal, A. K.; Maji, S. K.; Bhunia, A., Lipopolysaccharide from Gut Microbiota Modulates alpha-Synuclein Aggregation and Alters Its Biological Function. *ACS Chem Neurosci* **2019**, *10* (5), 2229-2236.
89. Ratha, B. N.; Kim, M.; Sahoo, B.; Garai, K.; Lee, D.; Bhunia, A., Insulin-eukaryotic model membrane interaction: Mechanistic insight of insulin fibrillation and membrane disruption. *Biochim Biophys Acta Biomembr* **2018**, *1860* (9), 1917-1926.
90. Wang, S. S.; Liu, K. N.; Han, T. C., Amyloid fibrillation and cytotoxicity of insulin are inhibited by the amphiphilic surfactants. *Biochim Biophys Acta* **2010**, *1802* (6), 519-30.
91. Grudzielanek, S.; Smirnovas, V.; Winter, R., The effects of various membrane physical-chemical properties on the aggregation kinetics of insulin. *Chem Phys Lipids* **2007**, *149* (1-2), 28-39.
92. Niu, Z.; Zhang, Z.; Zhao, W.; Yang, J., Interactions between amyloid beta peptide and lipid membranes. *Biochim Biophys Acta Biomembr* **2018**, *1860* (9), 1663-1669.
93. Rangachari, V.; Dean, D. N.; Rana, P.; Vaidya, A.; Ghosh, P., Cause and consequence of Abeta - Lipid interactions in Alzheimer disease pathogenesis. *Biochim Biophys Acta Biomembr* **2018**, *1860* (9), 1652-1662.
94. Montagne, A.; Zhao, Z.; Zlokovic, B. V., Alzheimer's disease: A matter of blood-brain barrier dysfunction? *J Exp Med* **2017**, *214* (11), 3151-3169.

95. (a) Biffi, A.; Greenberg, S. M., Cerebral amyloid angiopathy: a systematic review. *J Clin Neurol* **2011**, 7 (1), 1-9; (b) Gireud-Goss, M.; Mack, A. F.; McCullough, L. D.; Urayama, A., Cerebral Amyloid Angiopathy and Blood-Brain Barrier Dysfunction. *Neuroscientist* **2021**, 27 (6), 668-684.
96. Waschuk, S. A.; Elton, E. A.; Darabie, A. A.; Fraser, P. E.; McLaurin, J. A., Cellular membrane composition defines A beta-lipid interactions. *J Biol Chem* **2001**, 276 (36), 33561-8.
97. (a) Williams, T. L.; Serpell, L. C., Membrane and surface interactions of Alzheimer's Abeta peptide--insights into the mechanism of cytotoxicity. *FEBS J* **2011**, 278 (20), 3905-17; (b) Wang, Q.; Zhao, J.; Yu, X.; Zhao, C.; Li, L.; Zheng, J., Alzheimer Abeta(1-42) monomer adsorbed on the self-assembled monolayers. *Langmuir* **2010**, 26 (15), 12722-32.
98. Chauhan, A.; Ray, I.; Chauhan, V. P., Interaction of amyloid beta-protein with anionic phospholipids: possible involvement of Lys28 and C-terminus aliphatic amino acids. *Neurochem Res* **2000**, 25 (3), 423-9.
99. (a) Ariga, T.; McDonald, M. P.; Yu, R. K., Role of ganglioside metabolism in the pathogenesis of Alzheimer's disease--a review. *J Lipid Res* **2008**, 49 (6), 1157-75; (b) Rudajev, V.; Novotny, J., Cholesterol as a key player in amyloid beta-mediated toxicity in Alzheimer's disease. *Front Mol Neurosci* **2022**, 15, 937056.
100. (a) Wakabayashi, M.; Okada, T.; Kozutsumi, Y.; Matsuzaki, K., GM1 ganglioside-mediated accumulation of amyloid beta-protein on cell membranes. *Biochem Biophys Res Commun* **2005**, 328 (4), 1019-23; (b) Kakio, A.; Nishimoto, S.; Yanagisawa, K.; Kozutsumi, Y.; Matsuzaki, K., Interactions of amyloid beta-protein with various gangliosides in raft-like membranes: importance of GM1 ganglioside-bound form as an endogenous seed for Alzheimer amyloid. *Biochemistry* **2002**, 41 (23), 7385-90.
101. Yagi-Utsumi, M.; Kato, K., Structural and dynamic views of GM1 ganglioside. *Glycoconj J* **2015**, 32 (3-4), 105-12.
102. (a) Pineda, A.; Burre, J., Modulating membrane binding of alpha-synuclein as a therapeutic strategy. *Proc Natl Acad Sci U S A* **2017**, 114 (6), 1223-1225; (b) Shi, Z.; Sachs, J. N.; Rhoades, E.; Baumgart, T., Biophysics of alpha-synuclein induced membrane remodelling. *Phys Chem Chem Phys* **2015**, 17 (24), 15561-8.
103. (a) Galvagnion, C.; Brown, J. W.; Ouberaï, M. M.; Flagmeier, P.; Vendruscolo, M.; Buell, A. K.; Sparr, E.; Dobson, C. M., Chemical properties of lipids strongly affect the kinetics of the membrane-induced aggregation of alpha-synuclein. *Proc Natl Acad Sci U S A* **2016**, 113 (26), 7065-70; (b) Zhu, M.; Li, J.; Fink, A. L., The association of alpha-synuclein with membranes affects bilayer structure, stability, and fibril formation. *J Biol Chem* **2003**, 278 (41), 40186-97.
104. (a) Westphal, C. H.; Chandra, S. S., Monomeric synucleins generate membrane curvature. *J Biol Chem* **2013**, 288 (3), 1829-40; (b) Pandey, A. P.; Haque, F.; Rochet, J. C.; Hovis, J. S., alpha-Synuclein-induced tubule formation in lipid bilayers. *J Phys Chem B* **2011**, 115 (19), 5886-93; (c) Jiang, Z.; de Messieres, M.; Lee, J. C., Membrane remodeling by alpha-synuclein and effects on amyloid formation. *J Am Chem Soc* **2013**, 135 (43), 15970-3; (d) Ouberaï, M. M.; Wang, J.; Swann, M. J.; Galvagnion, C.; Williams, T.; Dobson, C. M.; Welland, M. E.,

- alpha-Synuclein senses lipid packing defects and induces lateral expansion of lipids leading to membrane remodeling. *J Biol Chem* **2013**, 288 (29), 20883-20895.
105. (a) Vamvaca, K.; Volles, M. J.; Lansbury, P. T., Jr., The first N-terminal amino acids of alpha-synuclein are essential for alpha-helical structure formation in vitro and membrane binding in yeast. *J Mol Biol* **2009**, 389 (2), 413-24; (b) Davidson, W. S.; Jonas, A.; Clayton, D. F.; George, J. M., Stabilization of alpha-synuclein secondary structure upon binding to synthetic membranes. *J Biol Chem* **1998**, 273 (16), 9443-9.
106. (a) Pirc, K.; Ulrih, N. P., alpha-Synuclein interactions with phospholipid model membranes: Key roles for electrostatic interactions and lipid-bilayer structure. *Biochim Biophys Acta* **2015**, 1848 (10 Pt A), 2002-12; (b) Stockl, M.; Fischer, P.; Wanker, E.; Herrmann, A., Alpha-synuclein selectively binds to anionic phospholipids embedded in liquid-disordered domains. *J Mol Biol* **2008**, 375 (5), 1394-404.
107. Gaspar, R.; Pallbo, J.; Weininger, U.; Linse, S.; Sparr, E., Ganglioside lipids accelerate alpha-synuclein amyloid formation. *Biochim Biophys Acta Proteins Proteom* **2018**, 1866 (10), 1062-72.
108. Garten, M.; Prevost, C.; Cadart, C.; Gautier, R.; Bousset, L.; Melki, R.; Bassereau, P.; Vanni, S., Methyl-branched lipids promote the membrane adsorption of alpha-synuclein by enhancing shallow lipid-packing defects. *Phys Chem Chem Phys* **2015**, 17 (24), 15589-97.
109. Exner, N.; Lutz, A. K.; Haass, C.; Winklhofer, K. F., Mitochondrial dysfunction in Parkinson's disease: molecular mechanisms and pathophysiological consequences. *EMBO J* **2012**, 31 (14), 3038-62.
110. Filosto, M.; Scarpelli, M.; Cotelli, M. S.; Vielmi, V.; Todeschini, A.; Gregorelli, V.; Tonin, P.; Tomelleri, G.; Padovani, A., The role of mitochondria in neurodegenerative diseases. *J Neurol* **2011**, 258 (10), 1763-74.
111. (a) Zigoneanu, I. G.; Yang, Y. J.; Krois, A. S.; Haque, E.; Pielak, G. J., Interaction of alpha-synuclein with vesicles that mimic mitochondrial membranes. *Biochim Biophys Acta* **2012**, 1818 (3), 512-9; (b) Colbeau, A.; Nachbaur, J.; Vignais, P. M., Enzymic characterization and lipid composition of rat liver subcellular membranes. *Biochim Biophys Acta* **1971**, 249 (2), 462-92.
112. Dudek, J., Role of Cardiolipin in Mitochondrial Signaling Pathways. *Front Cell Dev Biol* **2017**, 5, 90.

Chapter 2

2. Small molecule act as a Chemical Chaperone to Prevent Insulin Aggregation and Disaggregate Amyloids

2.1. Coomassie brilliant blue G-250 acts as a potential chemical chaperone to stabilize therapeutic insulin

This chapter has been adapted from the following publication:

Pariary, R., Dolui, S., Shome, G., Mohid, S.A., Saha, A., Ratha, B.N., Harikishore, A., Jana, K., Mandal, A.K., Bhunia, A. and Maiti, N.C., 2023. Coomassie brilliant blue G-250 acts as a potential chemical chaperone to stabilize therapeutic insulin. *Chemical Communications*, 59(52), pp.8095-8098.

2.1.1 Introduction

Insulin amyloidoma marked by extracellular fibrils at the injection site is a medical condition complicating insulin therapy ¹. The instability of monomeric insulin and its fibrillation also interfere with its manufacture, long-term storage, and pharmaceutical use ². Overcoming this problem through inclusion of a chemical chaperone such as small molecule, peptide or macrocycle may abrogate fibrilization in insulin formulations ³. Recent reports have established promising effect of Coomassie Brilliant Blue G-250 (CBBG) and its analogues in preventing amyloid fibrilization ⁴. In the current investigation, we have examined the interaction of the CBBG dye with human insulin (HI) and its stabilizing effect on the helical folds of HI protein.

2.1.2. Experimental Methods

2.1.2.1. Materials and sample preparation

Human HI (HI, 91077C), Thioflavin T (ThT), Coomassie brilliant blue G-250 (CBBG), NaCl and HCl were purchased from Sigma-Aldrich. Milli-Q water was used in the preparation of a buffer and stock solution of ThT dye. HI solution was prepared in 25 mM HCl containing 100 mM NaCl (pH ~1.6) to form a stock solution and then centrifuged at 15000 rpm for 10 min and passed through a 0.22 μ m pore size filter to remove any insoluble aggregates. The stock concentration of

the protein solution was determined through JASCO-600 UV-vis spectrophotometer, using the extinction coefficient value of the protein studied was as follow $6200 \text{ M}^{-1} \text{ cm}^{-1}$ at 276 nm ^{3b}. For inducing amyloid fibrillation, freshly prepared HI ($320 \text{ }\mu\text{M}$ and $100 \text{ }\mu\text{M}$) solution in absence and presence of CBBG was incubated for several hours at $60 \text{ }^{\circ}\text{C}$ without agitation.

2.1.2.2. Thioflavin T (ThT) fluorescence assay

ThT fluorescence was recorded to investigate the kinetics associated with the fibril formation of human insulin in different solution conditions. ThT is a small dye molecule that becomes highly emissive upon binding to the cradle of the β -sheet present in amyloid fibrils and produces a typical fluorescence emission spectrum with a peak maximum at $\sim 482 \text{ nm}$ in an aqueous solution ⁵. The growth curve (kinetics) was made by measuring the fluorescence intensity of ThT in the presence of a quantitative amount of HI samples ($100, 320 \text{ }\mu\text{M}$) taken at different time points of incubation of the HI solution in the presence and the absence of CBBG. The samples were incubated at $60 \text{ }^{\circ}\text{C}$ in 25 mM HCl containing 100 mM NaCl ($\text{pH } 1.6$) or sodium phosphate buffer ($\text{pH } 7.2$), in the presence and absence of CBBG to confirm whether the interaction of CBBG indeed inhibits the HI self-assembly and fibrilization process. $4 \text{ }\mu\text{l}$ of incubated HI solution (either in the absence or presence with CBBG) was pipette out, added to $500 \text{ }\mu\text{l}$ solution of ThT ($\sim 22 \text{ }\mu\text{M}$) and mixed carefully for the acquisition of fluorescence emission spectra using a Cary Eclipse fluorescence spectrophotometer. The optical path length of the fluorescence cuvette was 10 cm . The fluorescence emission wavelength range was $450\text{-}600 \text{ nm}$ (excitation 440 nm , emission peak maximum $\sim 482 \text{ nm}$). ThT fluorescence peak intensity at 482 nm was plotted against time, analysed and fitted to the sigmoidal curve using equation 1 ⁶.

$$Y = y_i + m_i x + \frac{y_f + m_f x}{1 + e^{-\left[\frac{(x - x_0)}{\tau}\right]}} \dots \dots \dots (1)$$

Where Y is the ThT fluorescence intensity at a particular time (x), x is the incubation time, and x_0 is the time to reach 50 % of maximal fluorescence; other parameters are determined by the fitting. The lag time is defined by $x_0 - 2\tau$. The apparent rate constant ($1/\tau$), m_i and m_f are two constants (linear coefficients).

2.1.2.3. ^1H proton NMR

All NMR spectra were recorded on Bruker AVANCE III 700 MHz, equipped with RT probe and at 25 °C. All NMR data acquisition and processing were done by using Topspin v4.0.6 software (Bruker). The 1D NMR time kinetics of HI (100 μM) was performed in presence or absence of equimolar CBBG at 60 °C in 25 mM HCl buffer with 100 mM NaCl and 10% D_2O at pH ~1.6. Normalized peak intensity (I/I_0) was calculated by taking the total peak intensity of HI from aromatic and amide region with time in presence or absence of CBBG and normalized by the HI peak intensity at initial (I_0). The data was fitted using sigmoidal curve equation 1. To rule out the effect of ThT on HI fibril kinetics, we added equimolar ThT in HI and HI:CBBG (1:1 molar ratio) sample and incubated at 60 °C. The interaction of CBBG dye with HI (100 μM) in 25 mM HCl buffer with 100 mM NaCl and 10% D_2O at pH ~1.6 was determined through a series of one-dimensional (1D) ^1H proton NMR spectra of HI in presence of 0, 0.1, 0.25, 0.5, 0.75 and 1 molar excess of CBBG dye (from a stock of 3 mM CBBG). The NMR signal intensity data were fitted by using equation 2:

$$Y = Y_0 + A \left(\frac{X}{K_d + X} \right) \dots\dots\dots(2)$$

Here, Y is normalized signal intensity value, Y_0 is initial signal intensity value, A is the fraction of fast exchange protons under our condition, X is the concentration of added CBBG dye (μM), and K_d is the apparent intensity decay rate constant or fast exchange rate constant between free and bound CBBG.

Parallely, we also recorded 1D ^1H NMR of 500 μM CBBG with the treatment of 10 μM and 25 μM HI fibrils in 25 mM HCl containing 100 mM NaCl and 10% D_2O (pH ~1.6) at 25 °C.

HI (1 mM) was dissolved in 10 mM sodium phosphate buffer (pH 2.0) containing 10 mM NaCl and 10% D_2O , with or without the addition of CBBG at 1:1 molar ratio for kinetics experiment using NMR. One-dimensional ^1H NMR and two-dimensional homonuclear ^1H - ^1H NOESY NMR spectra (400 ms mixing time) were taken before and/or after incubation of samples at 60 °C for 24 h.

At the same time, zinc-free HI was prepared by the addition of EDTA followed by extensive dialysis and lyophilization. The lyophilized sample was then dissolved in 20% acetic acid- d_4 and

10% D₂O (pH 1.9) where the insulin exists as monomer ⁷. NOESY spectra of 350 µM HI were performed in the presence or absence of equimolar dye with a mixing time 200 ms at 25 °C. 512 increments in t₁ and 2048 data points in t₂ dimension along with excitation sculpting pulse sequence were used for water suppression for all NOESY spectra. All NOESY spectra of HI were also recorded at 25 °C with 64 scans and a spectral width of 12 ppm for both the dimension.

Normalized peak intensity (I/I₀) was measured by taken the intensity ratios of [HI]:[CBBG] (I) and HI control (I₀). The running average of I/I₀ was determined by calculating the average I/I₀ of CαH intensity for three sequential residues. CSP of residues was determined using equation no 3.

$$CSP = \sqrt{\Delta\delta_{\omega_1}^2 + \Delta\delta_{\omega_2}^2} \dots\dots\dots(3)$$

Here Δδ_{ω1} and Δδ_{ω2} represents ¹H chemical shift difference in ppm unit between HI alone and HI in presence of CBBG in ω₁ and ω₂ direction, respectively in 2D NOESY NMR.

2.1.2.4. Atomic Force Microscopy (AFM)

Morphologies of the insulin aggregates produced in the absence and presence CBBG were performed using Pico plus 5500 ILM AFM system (Agilent Technologies). Incubation and sample conditions were similar to sample prepared for ITC and ThT fluorescence assay measurement described earlier. Micro-fabricated silicon cantilevers (resonance frequency of 300 kHz and spring constant range of 21-98 N/m) was used derive the morphological features of the aggregates formed from the incubated samples. The aliquot taken at a defined time of incubation was diluted with water and drop-casting was made on freshly cleaved muscovite mica substrate. The solvent was removed by evaporation at room temperature in the open air. The images were captured with a scan speed of 0.5 lines/sec and processed using Pico view version 1.1 software (Agilent Technologies).

2.1.2.5. Cell viability assay

Rat pancreatic β-cells (RIN-5f) were acquired from National Centre for Cell Science (NCCS, India) and cultured in complete RPMI-1640 media (Gibco) supplemented with 10% FBS, penicillin-streptomycin (1 unit/ml), gentamycin (50 µg/ml), and amphotericin B (2.5 µg/ml) in a 5% CO₂ incubator at 37 °C. Experiments were conducted out at 70-80% cell confluency. Cell

viability was measured using 3-(4,5-dimethylthiazol-2-yl)-2,5-diphenyltetrazolium bromide (MTT), which depicts the mitochondrial activity of the living cells⁸. By using mitochondrial enzymes, live cells may convert MTT into purple formazan crystals, and the amount of formazan formed corresponds with cell viability. 1×10^4 cells/well were seeded in 96-well plate for 24 h. The media was exchanged with complete RPMI-1640 containing 50 μ M aggregated containing HI fibrils and coincubated HI:CBBG (at 1:1 molar ratio) complex and incubated for 24 h. In a separate set of experiments CBBG were treated in concentrations of 10 μ M, 20 μ M, 40 μ M, 80 μ M and 100 μ M and incubated for 24 h. In both set of experiments; 24 h incubation was allowed. After that at a final concentration of 0.5 mg/ml, MTT solution was applied to the wells, which were then placed in an incubator with 5% CO₂ humidity at 37 °C for 3.5 h. To dissolve the formazan precipitate 100 μ l of dimethyl-sulfoxide (DMSO) was added in each well. At 570 nm, the absorbance was measured with a microplate reader. Results were compared and expressed as a percentage of control non-treated cell.

We prepared two set of samples for MTT experiment to measure the toxicity of disintegrated fibril. In first set of samples, we incubated the matured HI fibril (100 μ m) in presence or absence of one- and two-fold molar excess of CBBG at 37 °C and 200 rpm for 3 h. The other set of samples were heated at 60 °C with no agitation. The cells were treated, with 50 μ M sample and followed the above MTT method.

2.1.2.6. Scanning Electron Microscopy (SEM)

RIN5f cells were processed similar as cell viability assay procedure. 50 μ M HI fibrils and/ or HI:CBBG (1:1) aggregated samples were added in RIN5f cells and incubated for 24 h. The cells were then prepared for SEM. Glutaraldehyde and formaldehyde were used as a primary fixative to stabilize the ultrastructure. Osmium Tetra oxide was used for secondary fixation. The samples were dehydrated using ethanol gradient. The drying process is then supplemented with HMDS and liquid CO₂. A sticky carbon disc was used to attach the specimen on the metal stub. Finally, conductive material was used for sputter coating and proceed for SEM.

2.1.2.7. Native PAGE

The HI aggregated solutions (100 μ M, without or with CBBG) were centrifuged at 5000 rpm for 5 min. The supernatant was studied by 15% native PAGE in tris-glycine running buffer (pH 8.8) for 1.5 h at 100 V, 80 A. Coomassie brilliant blue stain was used to detect the protein. The gels were imaged using ImageLab software in Bio-Rad ChemiDoc system. Using the ImageLab software, bands were quantified.

2.1.2.8. Mass spectrometry

1 μ l HI sample in absence or presence of equimolar CBBG was spotted onto MALDI plate and dried it. The mass spectrometry was recorded using a MALDI-TOF spectrometer (Autoflex sppe by Bruker Daltonics GmbH) in the positive ion reflector mode. MS data were processed by the use of Data Flex Analysis and Biotools 3.6 software.

2.1.2.9. Isothermal Titration Calorimetry (ITC)

ITC measurements were carried out at 25 $^{\circ}$ C on a VP-ITC titration microcalorimeter (Micro Cal Inc., Northampton, MA). HI and CBBG samples were thoroughly degassed on a thermovac before the use in titration. For the correction of heat of dilution, the sample cell was loaded with buffer (pH \sim 1.6) and the reference cell was also filled with the same buffer solution. The solution in the cell was stirred at 90 rpm by the syringe filled with 0.4 mM HI in an identical buffer solution. Injections of 4 μ l of the buffer in the syringe were started after baseline stability reached. 28 sequential such injections were made into the ITC cell containing buffer solution. The titration of the CBBG solution (0.01 mM) in the cell was followed by 28 sequential 4 μ l injections of 0.4 mM HI into the ITC cell containing 1.8 ml of CBBG solution. The protein and CBBG solution were made in identical buffer conditions (25 mM HCl containing 100 mM NaCl (pH \sim 1.6)). The raw calorimetric data profile (heat released) of interaction between CBBG and HI at 25 $^{\circ}$ C were collected automatically and subsequently fitted to a one-site binding model by the Microcal LLC Origin 7.0 software. After subtracting the heat of dilution, a non-linear least-squares algorithm was used to fit an equilibrium binding equation to the data points (heat flow per injection against the concentration ratio of HI and CBBG). This best fit provides the apparent binding stoichiometry (n), the change in enthalpy (ΔH), and the dissociation constant (K_d). The change in free energy

(ΔG) and change in entropy (ΔS) for the binding reaction were analyzed by the important equations of thermodynamics.

$$\Delta G = -RT \ln K \dots\dots\dots (4)$$

$$\Delta S = (\Delta H - \Delta G) / T \dots\dots\dots (5)$$

2.1.2.10. Circular dichroism (CD) measurements

Far-UV circular dichroism (CD) spectra were recorded at 25 °C on a Jasco J-815 spectro polarimeter (Easton, MD). For CD analysis, freshly prepared HI (320 μ M and 100 μ M) solution in the absence and presence of CBBG was incubated for several hours at 60 °C without agitation. HI solutions were prepared in 25 mM HCl containing 100 mM NaCl (pH ~1.6). The spectra were measured using diluted aliquots (final concentration was ~ 15 μ M of HI) at a different time point of incubation. 300 μ l of the incubated protein solution was taken in 0.1 cm path length cuvette and scanned between 200–250 nm with a scanning speed 50 nm/min, resolution of 0.2 nm. For each sample, the representative spectrum was average of at least three individual scans. We used BeStSel webserver for the deconvolution in default mode for extracting the secondary structure content from CD spectra.

2.1.2.11. Methods for *in vivo* animal-based experiments

a. Animals

Male C57BL/6J mice (6-8 weeks old, healthy) weighing 20-30 g were obtained from the Centre for Translational Animal Research (CTAR), Bose Institute, Kolkata, India. All animals were maintained according to the guiding principle of the Institutional Animal Ethics Committee (IAEC) using the CPCSEA approved protocol wide IAEC approval No # IAEC/BI/011/2021 dt. 28/09.2021. Before conducting the experiment, all animals were acclimatized for at least two weeks along with constant 12 h light/dark cycle with water and food ad libitum. All experiments complied with the National Research Council's Guide for the Care and Use of laboratory Animals (NIH Publication No.8023, revised 1978, U.S.A). All experiments also complied with ARRIVE guidelines (Animal Research: Reporting of *in vivo* Experiments; <https://arriveguidelines.org/arrive-guidelines>).

b. Design of Experiments

24 Male C57BL/6J Mice were randomly divided in Four (4) groups: Control, CBBG (1 mg), CBBG (5 mg), CBBG (10 mg). Each group contained Six (6) animals and administration was performed intraperitoneally with the following Schedule:

Control – Only PBS as vehicle.

CBBG (1 mg): 1 mg /kg body wt. of CBBG dissolved in PBS

CBBG (5 mg): 5 mg /kg body wt. of CBBG dissolved in PBS

CBBG (10 mg): 10 mg /kg body wt. of CBBG dissolved in PBS

Mice were Injected Once per week for Four weeks i.e., a month of time and were sacrificed one week after completion of the last treatment. On the day of sacrifice blood was collected in previously marked vials for biochemical and hematological examinations. The liver, spleen and kidney were isolated very carefully for histopathological examination and evaluated for cytoarchitectural alterations after additional processing.

c. Preparation of CBBG and Administration of CBBG Intraperitoneally

The body weights of animals and calculated doses of CBBG to be injected were recorded for each animal before their treatment. 70% ethanol was applied to the abdominal cavity of the animal. A 26-gauge DISPOVAN needle of 1 ml capacity was inserted inside the peritoneal cavity. The needle along with the syringe were kept at a very suitable angle in respect to the body. The respective dosage of CBBG (1 mg/kg, 5 mg/kg and 10 mg/kg) and PBS for control group was injected inside the peritoneum cavity slowly. The needle was removed with utmost care and gentle compression was applied over the region. Animals were returned to their cages. After completion of treatment for 4 weeks body weights of animals were recorded.

d. Examination of blood for biochemical and hematological parameters with respect to CBBG toxicity

The various biochemical parameters including serum glutamic oxaloacetic transaminase, serum urea, serum glutamic pyruvic transaminase, and creatinine were analyzed for subchronic toxicity of CBBG by taking commercially available diagnostic test kits (ARKRAY Healthcare Pvt. Ltd.). Using standard kits by following the manufacturer's manual, blood parameters (red blood cells, white blood cells, hemoglobin, eosinophil, neutrophil, basophil, monocyte, and lymphocyte) were estimated.

e. Histopathological examinations for sub-chronic toxicity studies

The Liver, Kidney, Spleen were isolated after sacrificing the animals and individual weights were recorded for each organ. The preserved liver, kidney, and spleen tissues were histopathologically examined. CBBG treated mice and control mice were sacrificed by decapitation following 4-weeks of treatment regimen. The Liver, Kidney, Spleen were collected and fixed onto 10% neutral buffered formalin for approximately 48 h. The organs were then further immersed in paraffin wax. Tissue sections were carefully cut with a microtome with a thickness of 5 μm . Prepared Slides were stained with Hematoxylin and eosin (H &E staining), Gomori Trichrome and Periodic Acid-Schiff for histological examinations. Stained Slides were observed using the light microscope (NIKON T2, India) for histopathological alternation (if any), and pictures were taken at 10x and 40x magnification.

2.1.2.12. Western Blot Analysis

The expression of the proteins pAKT, AKT1, and β -Actin was measured by Western blot analysis. The cells were serum starved for 12 h in DMEM media without serum. Afterwards, the cells were treated with only media, native insulin, untreated aggregated HI and CBBG treated HI at 100 nM concentration. About 5×10^6 cells were washed with cold PBS twice following 30-40 mins treatment, the cells were homogenized with ice-cold RIPA buffer containing 50 mM Tris-HCl (pH 7.5), 150 mM NaCl, 1 mM EDTA, 0.1% SDS, and 1 mM phenylmethylsulfonyl fluoride (PMSF) along with protease inhibitor cocktail. (Roche) Cell lysates were cleared at $12,000 \times g$ for 20 min at 4 °C. Protein were quantified using the Bicinchoninic acid (BCA) protein estimation kit

(ThermoFisher). Electrophoresis were carried out on 10% (W/V) SDS- Polyacrylamide gel (MiniPROTEAN® tetra cell with mini-trans Blot®, Bio-Rad, USA) which was then subsequently transferred onto a nitrocellulose membrane (Pall corporation) ⁹. Next, incubation of the membrane was done with fresh blocking buffer containing 5% nonfat-dried milk for 1 h at room temperature and then probed with primary antibodies Phospho-AKT1-S473 Rabbit pAb (Abclonal:AP0140), Anti β -Actin Rabbit pAb (BioBharati:BB-AB0024), AKT1 Monoclonal Antibody (Elabscience:E-AB-22210) overnight. The following day, membranes were washed three times with TBST solution followed by incubation with HRP conjugated goat anti-mouse, (Jackson Biolab 115-03-003), goat antirabbit secondary antibody (Jackson Biolab 111-035-003) for 2 h at room temperature. After that the membranes were washed three times in the TBST buffer. Immunoreactive bands were seen using the ECL substrate solution. Image Lab analysis was used to quantify the protein bands, which were normalised against the corresponding β -actin band.

2.1.2.13. Serum stability assay

A method described by Jenssen and Aspmo that was slightly modified was used to measure serum stability ¹⁰. It was warmed to 37 °C for 15 min before being added to 1 ml of RPMI 1640 supplemented with 25% (v/v) foetal bovine serum. To precipitate serum proteases CBBG was added at a final concentration of 100 μ g/ml, and at the appropriate time periods, the reaction mixture (100 μ l) was removed and mixed with 96% ethanol (400 μ l). To pellet down the precipitated serum protein, the hazy reaction mixture was centrifuged at 18,000 g for 2 min after being cooled at 4 °C for 15 min. Reverse-phase HPLC (SHIMADZU, Japan) was used to evaluate the reaction supernatant using a 250 x 4.6-mm C18 column. Gradient elution from 0.1% TFA in 100% acetonitrile to 0.1% TFA in water was carried out at a flow rate of 1 ml/min for 30 min. The area under the peak at 610 nm was calculated using SPINCHROME CFR software.

2.1.2.14. Protein solubility estimation by Bicinchoninic acid assay (BCA)

HI sample (100 μ M) was incubated at 60 °C for 24 h in absence or presence of CBBG at molar ratio 1:1 [HI]/ [CBBG] in 25 mM HCl containing 100 mM NaCl (pH ~1.6). The aggregated HI samples were centrifuged at 5000 rpm for 5 min and the supernatant was collected. Protein solubility was measured using Pierce (Thermo Scientific #2328) BCA reagent A and BCA reagent B in ratio of [50:1]. The reagents were mixed in given proportion according to manufacturer's

protocol. 1µl protein from each of sample of HI fibril, HI monomer and coincubated HI+CBBG were mixed with BCA reagents. The mixture was incubated at 37 °C in dark conditions and O.D was taken using a microplate reader at 562 nm. The soluble protein content was estimated from the standard curve values.

2.1.2.15. Insulin secretion assay

RIN-5f cells were seeded in 12-well plate at 1×10^5 cells per well. Treatment was carried out the following day after the cells became adherent. CBBG were added to the cell at different concentrations (0.5, 1, 2.5, 5 and 10 µM) along with buffer and control. Quercetin (20 µM) was added as positive control ¹¹. 24 h after treatment, cells were stimulated by exchanging media either with normal glucose RPMI-1640 [11 mM] or high glucose RPMI-1640 [22 mM]. After 24 h, aliquots from the wells were collected and determined the amount of secreted insulin in the cell media by Enzyme Linked Immunosorbent Assay (insulin ELISA kit, Ab100578, Abcam, Cambridge, UK) following the manufacturer's protocol. The amount of insulin secretion in the cell medium of treated cells was compared with the secreted insulin level of control cells ¹².

2.1.2.16. Molecular docking

a. *Protein Preparation*: Hexameric assembly of Insulin A and B subunits with pdb 2OM1 was utilized ¹³. The protein assembly was checked for any missing atoms in residues and overlapping hydrogen atoms were adjusted H-bond optimization and energy minimized using OPLSe force field in maestro - Schrödinger suite of Program ¹⁴.

b. *Ligand preparation*: Using prepare ligand modules, the 2D coordinates of Coomassie blue (CBBG) were converted into 3D and energy minimized using smart minimizer for 2000 steps via minimize ligands tools in Discovery studio ¹⁵.

c. *Docking*: Glide docking tool from Schrödinger suite of programs was utilized to dock the CBBG ¹⁴. The NMR CSP data highlighted residues were used to define the grid point using default settings. Next, Standard precision docking protocol was used to dock the CBBG with default parameters was used to rank the poses.

not alter much with CBBG doses (Table S2.1.1). We found no significant cytoarchitectural changes in the kidneys, liver, and spleen after administering 1 mg kg⁻¹ or 5 mg kg⁻¹ of CBBG (Figure 2.1.1C); however, a CBBG dosage of 10 mg kg⁻¹ showed minor changes in histopathological studies (Appendix 2.1, Figure S2.1.2). Interestingly, CBBG displayed high stability in fetal bovine serum (Figure 2.1.1D). These observations prompted us to consider its plausibility as a stabilizing agent for native HI.

2.1.3.2. CBBG inhibits amyloid aggregation of HI

HI rapidly produces amyloid fibrils *in vitro* under specific conditions such as low pH and high temperature³. HI fibrilization studies at pH 1.6 and 60 °C using ThT based fluorescence assay followed a typical sigmoidal curve for fibril formation with a lag time of $\sim 1.8 \pm 0.8$ h (Figure 2.1.2A, Table 2.1.1). The corresponding profile obtained from a 1D NMR study of HI showed a sigmoidal decay of the signal intensities with time. This corroborated the gradual formation of higher molecular weight species such as the protofibrils or fibrils in the aggregation pathway of HI (Figure 2.1.2A). In contrast, co- incubation of HI with CBBG at a 1:1 molar ratio in similar conditions resulted in no increase in ThT intensity while NMR showed a slight decrease in signal intensity, indicating the disruption of primary nucleation events (Figure 2.1.2A). In the presence of CBBG, an enhanced lag phase followed by the delayed appearance of fibrils in ThT and slow disappearance of the sharp peaks (corresponding to the monomeric sample) in NMR suggested the formation of nonfibrillar aggregates. ThT measurements also exhibited that CBBG inhibited fibre formation in a dose- dependent manner (Figure 2.1.2B, Table 2.1.1). Identical NMR curves of

Table 2.1.1. Lag time and growth rate constants from ThT experiments for Insulin amyloid fibril formation in the presence and absence of CBBG.

condition	reaction	lag phase	apparent rate (k _{app})
HI 100 µM, pH ~1.6	HI	1.8 h	0.83 h ⁻¹
HI 320 µM, pH ~1.6	HI	1.6 h	0.95 h ⁻¹
+CBBG 7.5 µM	HI/CBBG	3.06 h	0.42 h ⁻¹
+CBBG 15 µM	HI/CBBG	3.32 h	0.42 h ⁻¹
+CBBG 30 µM	HI/CBBG	3.68 h	0.32 h ⁻¹
HI 100 µM, pH ~7.2	HI	1.6 day	0.88 day ⁻¹

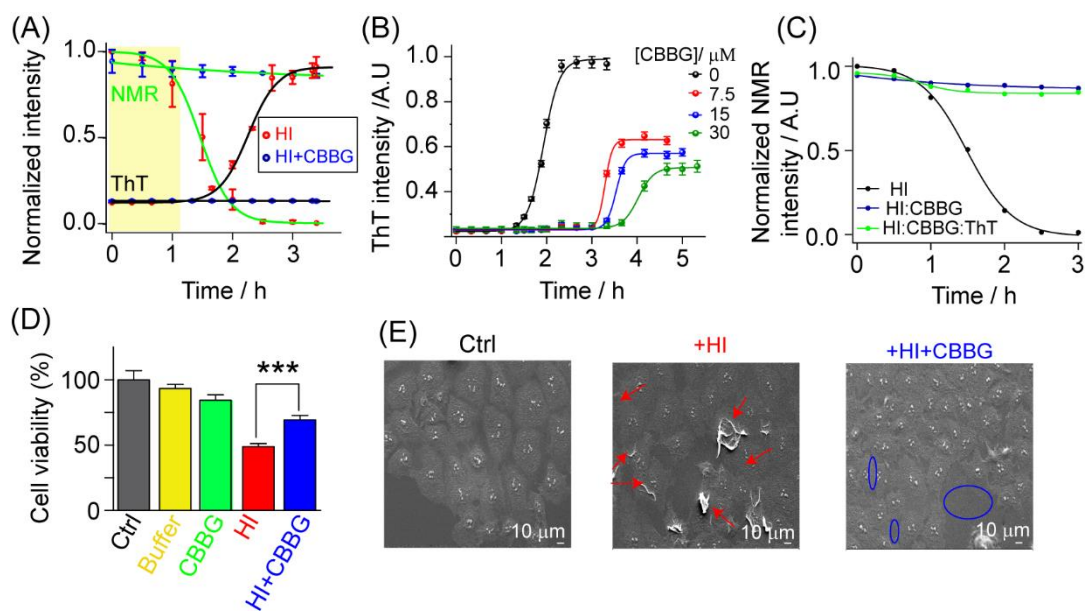


Figure 2.1.2. Inhibition of HI fibril by equimolar CBBG. (A) Overlay of ThT fluorescence (black line) and ¹H NMR kinetic traces (green line) of HI alone (red ball) and HI:CBBG (blue ball) at 60 °C in 25 mM HCl, 0.1 M NaCl, pH ~1.6. The error bar represents mean \pm SD of three independent experiments. (B) ThT fluorescence intensity against time for HI incubated at higher concentration (320 μ M) in the absence and presence of a different amount of CBBG (7.5, 15 and 30 μ M). (C) Time course HI aggregation by ¹H NMR and competition for HI binding between equimolar ThT and CBBG. Solid line represents by sigmoidal fits to normalized NMR signal intensity with time. (D) MTT assay showing cell viability of RIN5f cells with treatment of CBBG, HI fibril and co-incubated HI:CBBG sample (50 μ M). Values are represented as mean \pm SEM, n=6. ***indicates $p < 0.001$, significance was analysed using Mann-Whitney two tailed t-test. (E) SEM image of RIN5f cell with addition of HI fibril and co-incubated HI:CBBG (1:1).

CBBG-treated HI in the presence or absence of equimolar ThT revealed no effect of ThT on CBBG-induced HI aggregation kinetics (Figure 2.1.2C). We further confirmed the attenuation effect of CBBG on HI fibrilization at a physiological pH of ~7.2 (Appendix 2.1, Figure S2.1.3).

CBBG mediated HI assemblies were revealed to be functionally distinct from HI fibrils as monitored using the MTT cytotoxic assay (Figure 2.1.2D) and scanning electron microscopy (SEM) (Figure 2.1.2E) of Rat Insulinoma Pancreatic β -cells (RIN5f). SEM revealed that the HI fibril treatment resulted in cell membrane disruption, which decreased the cell viability to 50% (Figure 2.1.2D-E). Interestingly, the presence of nontoxic CBBG significantly improved the cell viability and prevented the toxic fibril-induced membrane disruption (Figure 2.1.2D-E).

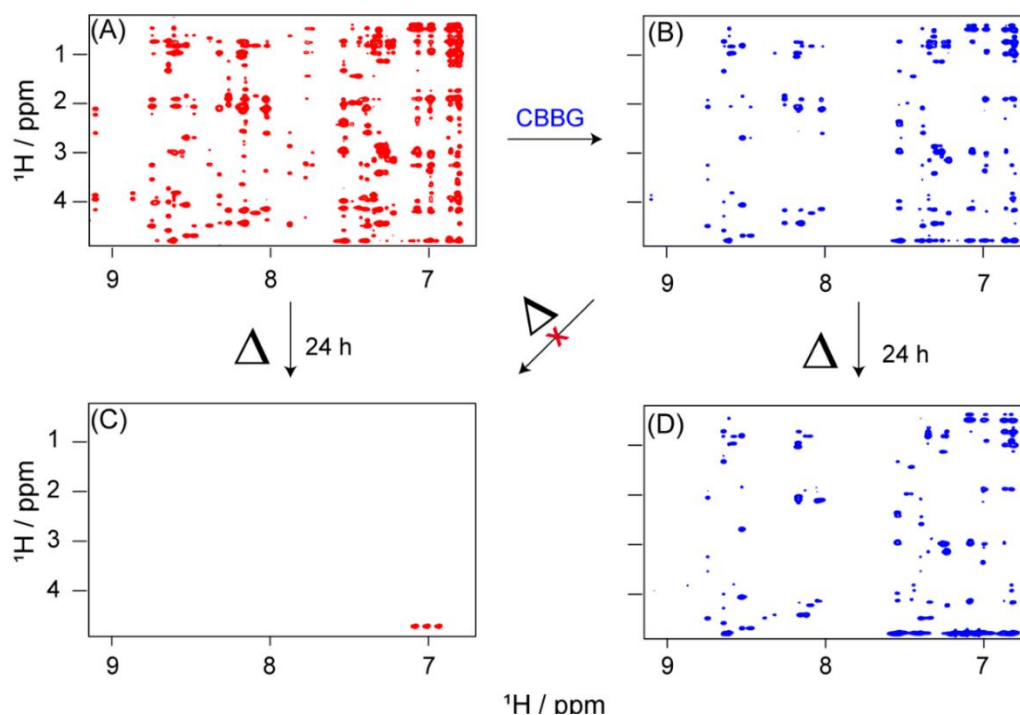


Figure 2.1.3. HI amyloid fibrillation by equimolar CBBG using NMR. Two-dimensional NOESY NMR spectra: (A) HI alone and (B) in the presence of CBBG at 1:1 molar ratio ([HI]/[CBBG] just before incubation; (C) HI solution after heating at 60 °C for 24 h shows no cross peak and (D) HI co-incubated with equimolar CBBG at 60 °C for 24 h. The experiment was performed in 10 mM sodium phosphate, 10 mM NaCl (pH=2.0) and 10% D₂O using Bruker Avance III 700 MHz at 25 °C.

To assess the influence of CBBG on inhibition process, two dimensional (2D) ^1H – ^1H nuclear Overhauser effect spectroscopy (NOESY) experiments were performed with HI in absence (Figure 2.1.3A) and/or presence of equimolar CBBG (Figure 2.1.3B) after and before incubation at 60 °C. Figure 2.1.3 shows a large number of NOE peaks of HI originating from the cross relaxation between two protons within 5 Å of each other¹⁷. After 24 h of incubation of the HI alone, all the NOE cross-peaks were completely broadened (Figure 2.1.3C), suggesting the formation of a larger assembly, which was beyond detection on the NMR time scale due to rapid spin–spin (T_2) relaxation¹⁸. In contrast, almost similar NOESY spectra of HI was obtained before (Figure 2.1.3B) and after incubation (Figure 2.1.3D) with CBBG. These data are also in good agreement with the results of 1D ^1H NMR experiments (Appendix 2.1, Figure S2.1.4). Collectively, the data confirmed that CBBG arrested the formation of large-size aggregates, affecting the overall aggregation kinetics.

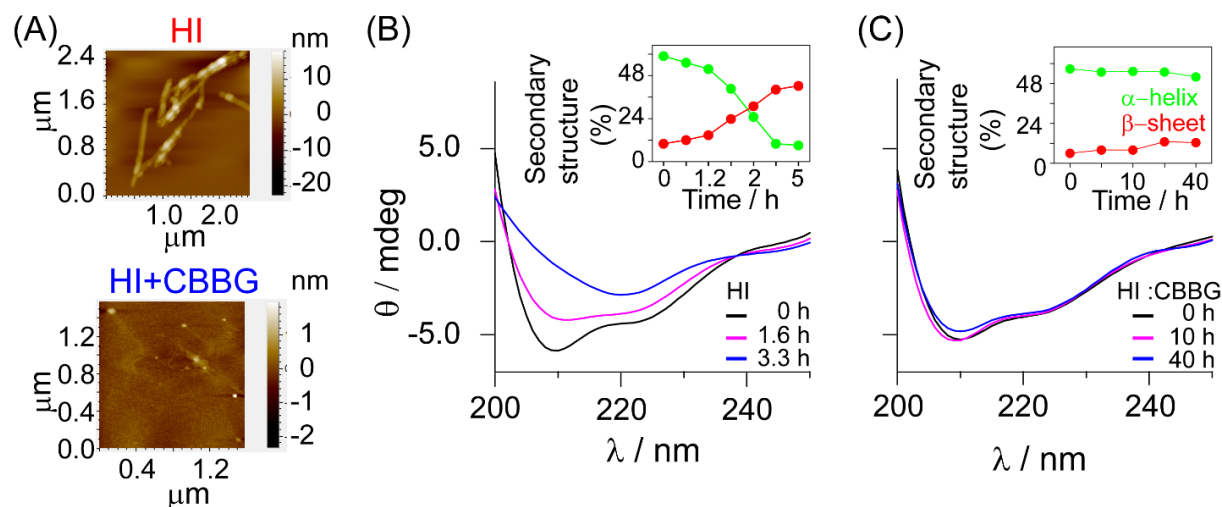


Figure 2.1.4. Binding interaction of HI and CBBG stabilized morphologically distinct lower molecular weight species. (A) AFM images at 3.3 h of HI fibril in absence and presence of equimolar CBBG. (B) CD spectra of HI (100 μ M) aggregation at different time of incubation. (T = 60 $^{\circ}$ C, 25 mM HCl, 100 mM NaCl, pH \sim 1.6); HI (black trace, 0 h, Pink trace, 1.6 h, blue trace, 3.3 h). (C) CD spectra of HI in the presence of CBBG at 1:1 molar ratio of [HI]/[CBBG] of selected time points: black trace (0 h), pink trace (10 h) and blue trace (40 h). The changes in the secondary structural component (%) against incubation time: α -helix (green) and β -sheet (red).

2.1.3.3. CBBG alters morphology and preserves native structure of HI

Time-lapse AFM imaging of HI also revealed the formation of small oligomers around 1 h (Appendix 2.1, Figure S2.1.5A) followed by protofibrillar aggregates within 1.6 h (Appendix 2.1, Figure S2.1.5B) leading to thread-like long, compact, and dense fibrils with \sim 10 nm diameters after 3.3 h (Figure 2.1.4A). However, no trace of fibrillar aggregates was detected in AFM for HI co-incubated with CBBG, confirming the inhibitory efficacy of CBBG (Figure 2.1.4A). Circular dichroism (CD) spectrum of HI provided information on the time-dependent structural transitions from the α -helical structure to β -sheet fibrils at 60 $^{\circ}$ C (Figure 2.1.4B). In contrast, HI remained in the α -helical conformation even after incubation for 40 h in the presence of equimolar CBBG at 60 $^{\circ}$ C (Figure 2.1.4B). Additionally, CBBG preserves the α -helical conformation of HI for a longer period. Taken together, these results suggested that CBBG acts as a chemical chaperone to stabilize the native conformation of HI.

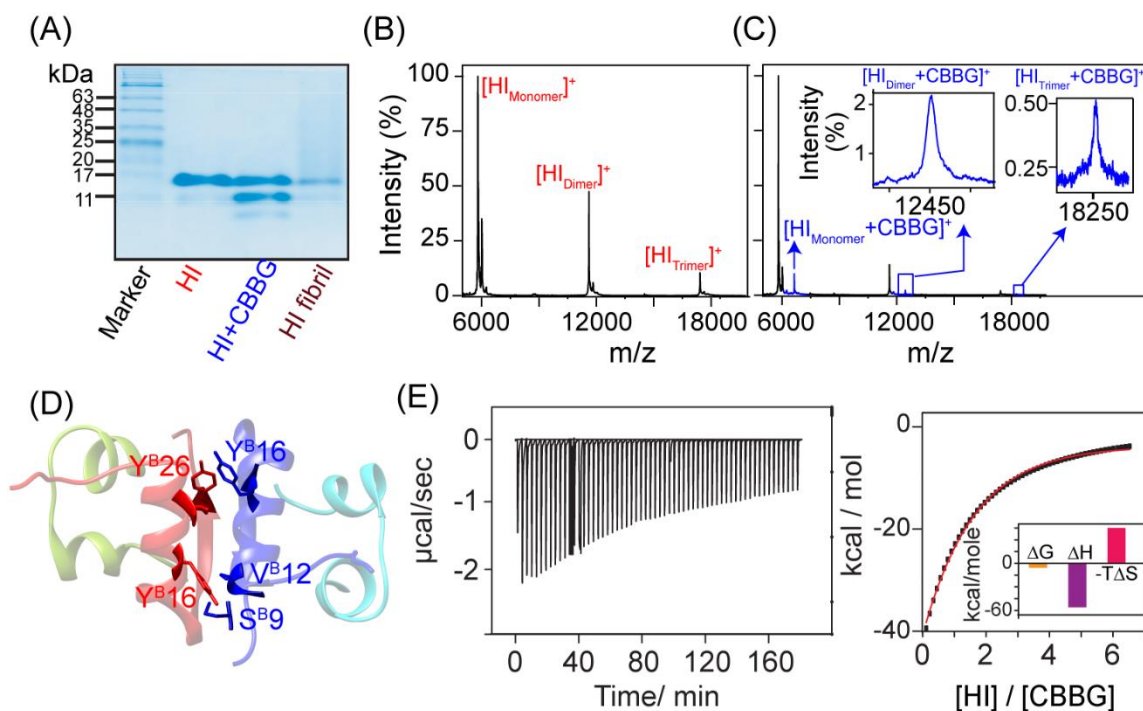


Figure 2.1.5. Binding interaction of HI and CBBG stabilized morphologically distinct lower molecular weight species. (A) 15 % Native PAGE gel for conformational distribution of native HI, CBBG-treated HI and fibril. MALDI mass spectra of (B) HI alone and (C) CBBG treated HI. Black line denotes HI peak and blue line denote CBBG bound HI peak. (D) Intermonomer residual interaction in HI dimer (PDB: 1GUJ). (E) ITC thermogram profile for HI binding to CBBG. The black line indicates the fitted curve assuming a one-site binding model with one type of site.

2.1.3.4. HI-CBBG interaction stabilizes distinct lower molecular weight Species

It should be noted that at pH ~2, hexameric HI formed predominantly dimers¹⁹ with few trimers and monomers, due to charge repulsion between Zn^{2+} and protonated $\text{H}^{\text{B}10}$, as confirmed by 15% native PAGE (Figure 2.1.5A), mass spectroscopy (Figure 2.1.5B) and NMR spectroscopy (Appendix 2.1, Figure S2.1.6). In the native PAGE, the extra bands in case of CBBG-treated HI (Figure 2.1.5A, lane 3) may be attributed to the stabilization of other oligomeric states of HI or breaking down of trimeric native HI, compared to the HI alone (Figure 2.1.5A, lane 2). Since large aggregates could not enter the gel matrix, HI fibrils did not produce any bands (Figure 2.1.5A, lane 4). Mass spectrometric data analysis confirmed the binding of CBBG is only with the monomeric, dimeric, and trimeric states of HI (Figure 2.1.5C). Comparing the dimeric structure of HI alone,

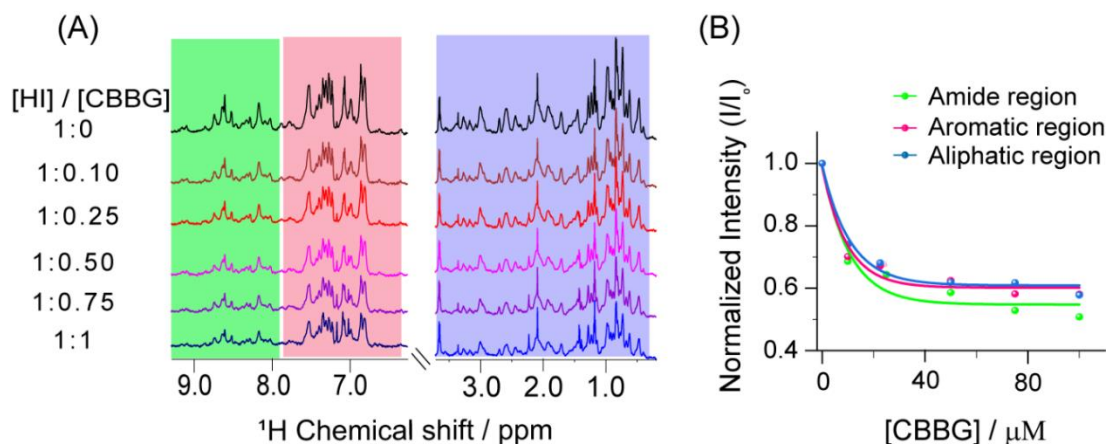


Figure 2.1.6. (A) ¹H NMR spectra of 100 μM HI in 25 mM HCl buffer with 100 mM NaCl (pH ~1.6, black curve) and the presence of a different concentration of CBBG at 25 °C. The concentration of CBBG were varied from 10 μM to 100 μM. Highlighted green for amide, red for aromatic and blue for aliphatic region of HI. (B) The NMR proton peak intensity decay of aliphatic (blue) aromatic (red) and amide (green) region of HI upon titration with CBBG. The solid lines represent at a particular CBBG concentration, the ¹H NMR signal intensity of insulin for corresponding region.

Table 2.1.2. Binding constants and thermodynamics of binding between CBBG and insulin as obtained from ITC and NMR experiments.

Complex	n	Method	K _d (μM)	ΔG (kcal/mol)	ΔH (kcal/mol)	-TΔS (kcal/mol)
HI-CBBG	2	ITC	12.5	-11.1	-57.2	46.1
		NMR	7.50 ± 1.5 (aliphatic region)			
			5.26 ± 1.6 (aromatic region)			
			7.54 ± 2.5 (amide region)			

before and after incubation with CBBG, confirmed the stabilization of the HI dimer by the presence of a number of intermolecular NOEs between the two monomers of the dimer (Figure 2.1.5D and Appendix 2.1, Figures S2.1.6B-C)²⁰. Isothermal titration calorimetry (ITC) supported that CBBG formed a 1:2 complex with HI (Table 2.1.2). Binding of CBBG with HI was exothermic i.e., an enthalpy driven process (Figure 2.1.5E and Table 2.1.2). The negative values of ΔH and ΔS suggested that the binding of HI to CBBG may be dominated by hydrogen bonding and van der

Waals interactions²¹. Additionally, titrating HI with CBBG resulted in a region-specific line broadening in ^1H NMR due to conformational exchange(s) between free and bound proteins (Figure 2.1.6). The intensity decay rate constants (K_d) of amide, aromatic, and aliphatic regions (upon CBBG binding) were in close agreement with the ITC-determined dissociation constant (K_d) values (12.5 mM) (Table 2.1.2), suggesting a moderate binding affinity between HI and CBBG.

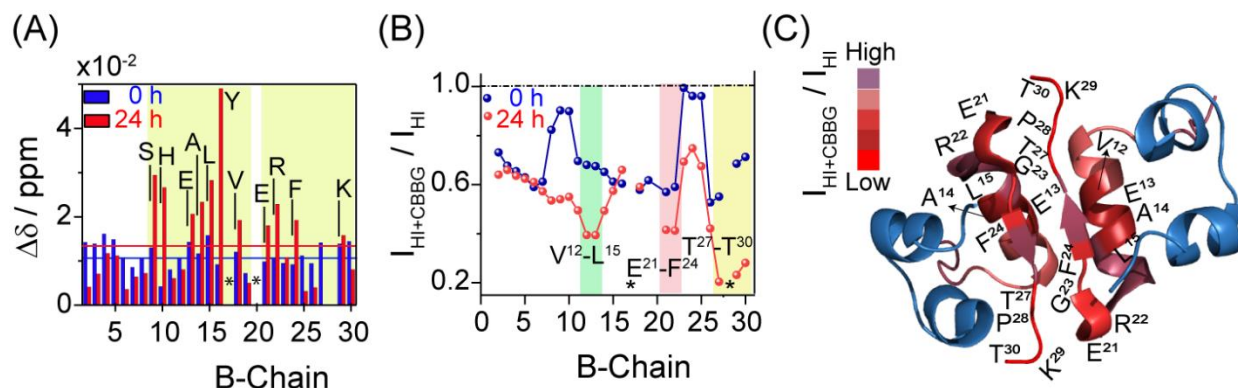


Figure 2.1.7. Mapping of CBBG binding site in HI dimer. (A) The CSP at B-chain of HI dimer C_α protons in presence of equimolar CBBG, before (blue) and after (red) heating of HI: CBBG complex at 60 °C for 24 h, respectively. Horizontal red and blue line represents average of all CSP values. (B) The running average of normalized NMR signal intensity of α protons in B-chain of HI dimer for three consecutive residues in presence of equimolar CBBG. (C) The region of A-chain (blue) and B-chain (red) in HI dimer atomic model that shows difference in intensity in presence of CBBG by using red color gradient. $I_{\text{HI+CBBG}}/I_{\text{HI}}$ denotes the normalized NMR peak intensity. 2D-NOESY NMR spectra were recorded on Bruker Avance III 700 MHz, equipped with RT-probe at 25 °C. Color background indicates interacting residues. Asterisks (*) indicate overlapping and/or unidentified residues.

2.1.3.5. Identification interaction site of CBBG in HI

To gain the residue-specific interaction of the HI dimer with CBBG, chemical shift perturbation (CSP) and broadening effects for HI were measured from 2D NOESY NMR at pH 2. Owing to several signal overlap, assignment of the A-chain without ambiguity was difficult. However, B-chain assignment was straightforward. We observed that the most perturbed residues in the B chain were V^{B2} , Q^{B4} , H^{B5} , S^{B9} and H^{B10} from the N-terminal; V^{B12} , E^{B13} , A^{B14} , L^{B15} and V^{B18} from the central helix region and K^{B29} and T^{B30} from the disordered C-terminal domain (Figure 2.1.7A and Appendix 2.1, Figure S2.1.7). Besides, a drop in peak intensity was observed for H^{B5} to G^{B8} , A^{B14} to C^{B19} , E^{B21} to F^{B24} , and Y^{B26} to T^{B27} sequential residues (Figures 2.1.7B-C). The results indicated

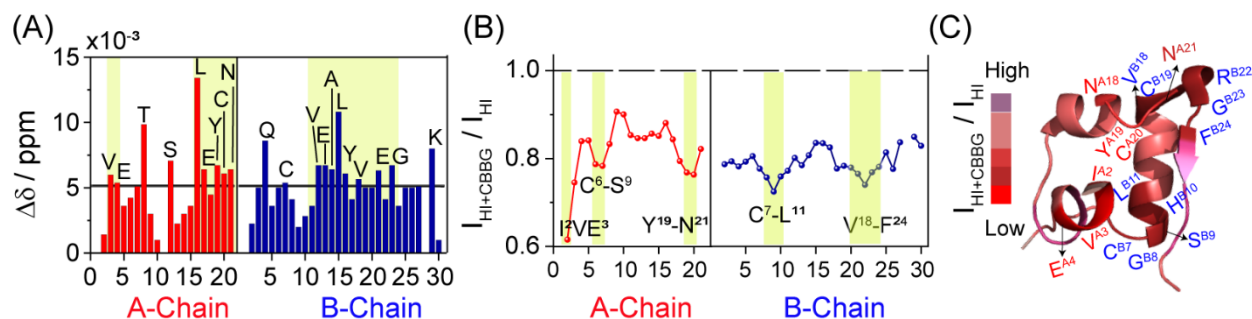


Figure 2.1.8. Mapping of CBBG binding site in HI monomer. (A) The CSP of all residues and (B) running average of NMR peak intensity of three consecutive residues from A-chain (red) and B-chain (blue) of HI in presence of equimolar CBBG. Yellow background indicates interacting residues. (C) atomic model of normalized peak intensity difference (red gradient) of HI monomer C_αH for A-chain and B-chain residues in presence of CBBG at a molar ratio of 1:1. The NMR spectra were recorded on Bruker Avance III 700 MHz, equipped with RT-probe at 25 °C.

that HI undergoes a local (residue level) conformational change upon binding to CBBG. In aggregation-prone circumstances (pH ~2 and 60 °C), the residue-specific interactions of HI with CBBG were more prominent. Interestingly, as shown in Figure 2.1.7A and Figure S2.1.7 (Appendix 2.1), enhanced CSP was observed for the S^{B9}, H^{B10}, E^{B13}, A^{B14}, L^{B15}, Y^{B16}, and V^{B18} residues from the central α-helix as well as for the E^{B21}, R^{B22}, F^{B24}, and K^{B29} residues from C-terminal segments, suggesting that the non-covalent interactions between CBBG and hydrophobic residues of the central region provided stability to the HI-CBBG complex. Furthermore, V^{B12}EAL^{B15}, E^{B21}RGF^{B24} and T^{B27}PKT^{B30} residues showed remarkable sequence-specific line broadening (Figures 2.1.7B-C). These NMR findings showed that the mobility of the aggregation prone central and C-terminus segments was completely restricted in the CBBG bound dimeric conformation, which might prevent further oligomerization.

In addition, we also recorded the NOESY NMR spectra of the HI monomer in the presence and absence of CBBG at a 1:1 molar ratio in 20% acetic acid-d₄ (pH 1.9)²². N terminal I^{A2}VE^{A3} and C^{A6}CTS^{A9} segments along with the C-terminal Y^{A19}CN^{A21} segment showed CSPs and sequence specific line broadening in the A-chain (Figures 2.1.8A-C). NOESY NMR spectra revealed moderate CSPs in central region V^{B12}EALYLV^{B18} and C-terminal residues, including E^{B21}, G^{B23} and K^{B29} (Figure 2.1.8A and Appendix 2.1, Figure S2.1.8A) and sequential broadening was found for N and C-terminal β-turns of the B chain (Figures 2.1.8B-C). Thus, 1D (Appendix 2.1, Figure S2.1.8B) and 2D NMR suggested a possible mechanism for arresting the nucleation step wherein

the C-terminal segment of the helical B chain moves away from the C-terminal helix of the A chain ²³. 1D NMR analysis showed that in the presence of equimolar CBBG, the NMR signal intensity of HI reduced to 0.71 unit (71%) and 0.88 unit (88%) for the dimer and monomer, respectively (Appendix 2.1, Figures S2.1.4B and S2.1.8B). This imparted a more favourable interaction occurring between the HI dimer and CBBG.

Exploiting this vital information from chemical shift perturbed residues as ambiguous interaction site points, we next evaluated the molecular interaction of CBBG on insulin using molecular docking. Our results suggested that the CBBG was docked onto the cavity formed between the A and B chains of insulin in one tetramer with a glide score of -6.7 kcal/mol. Chemically, CBBG bears a N,N-disubstituted tri-anilinyl-methane scaffold and with a IUPAC chemical name as 3-(((4-(((4-ethoxyphenyl)amino)phenyl)(4-(ethyl(3-sulfobenzyl)amino)-2-ethylphenyl)methyl)-3-methylphenyl)(ethyl)amino)methyl)benzenesulfonate]. Among the three phenyl rings of CBBG, two of the phenyl rings are oriented towards the B subunit, while the 3rd phenyl ring orients toward the A subunit. Among the three aniline fragments on triphenyl rings of CBBG, one fragment - N-ethoxy-phen-4-yl-aniline is sandwiched between two B subunits and one A subunit (Figure 2.1.9A). The N-ethoxy moieties in this fragment was engaged in hydrophobic interaction with L^{B11} / C^{B7} residues from one of the B subunits (3.9 Å / 3.0 Å) and L^{B6} residues (3.6 Å) from another B subunit (Figure 2.1.9). Phenyl ring is juxtaposed with face to edge π - π interaction between H^{B5} (3.1 Å) one B subunit and hydrophobic interaction with A^{B14} (3.4 Å) from another B subunit. The phenyl ring (to which - N-ethoxy-phen-4-yl-aniline substitution) is positioned in the vicinity of H^{B5} (3.1 Å), C^{B7} (3.0 Å), L^{B17} (4.1 Å), and L^{A13} (3.9 Å) at the interface of two B subunits at the tetrameric interface. The N-ethyl-N-(phenyl-3-sulfonic acid)-2-methyl-aniline fragment on one of the triphenyl rings was anchored to two B subunits. On one side, the SO₃ acid atoms on N-(phenyl-3-sulfonic acid moiety of this fragment was in H-bonding interaction with F^{B1} amino terminus (2.1 Å), while on the other side, the phenyl ring mediates cation interaction with K^{B29} residue (2.7 Å) from another B subunit. The-2-methyl-benzene ring was sandwiched in the vicinity between I^{A10} (3.4 Å) and E^{B21}-G^{B20} residues (3.3 -3.5 Å) from two B subunits. Lastly, the fragment-N-ethyl-N-(phenyl-3-sulfonic acid)-2-methyl-aniline was involved in hydrophobic interactions with two B subunit. The SO₃ acid atoms on N-(phenyl-3-sulfonic acid moiety of this fragment was engaged in H-bonded interaction with main chain atoms of I^{A10} residue (1.9 Å), while N-ethyl atoms on this fragment was in van der waal contacts with S^{A12} residue on A subunit. In molecular

docking studies, among the three-phenyl rings of CBBG, two of the phenyl rings are oriented towards the B subunits, while the 3rd phenyl ring is oriented toward the A subunits with predominantly hydrophobic interactions with L^{B11}, A^{B14}, L^{B17}, G^{B20}, P^{B28}, and K^{B29} residues of the B chain (Figures 2.1.9A and C). Polar contacts were mediated by sulphonic acid groups of CBBG

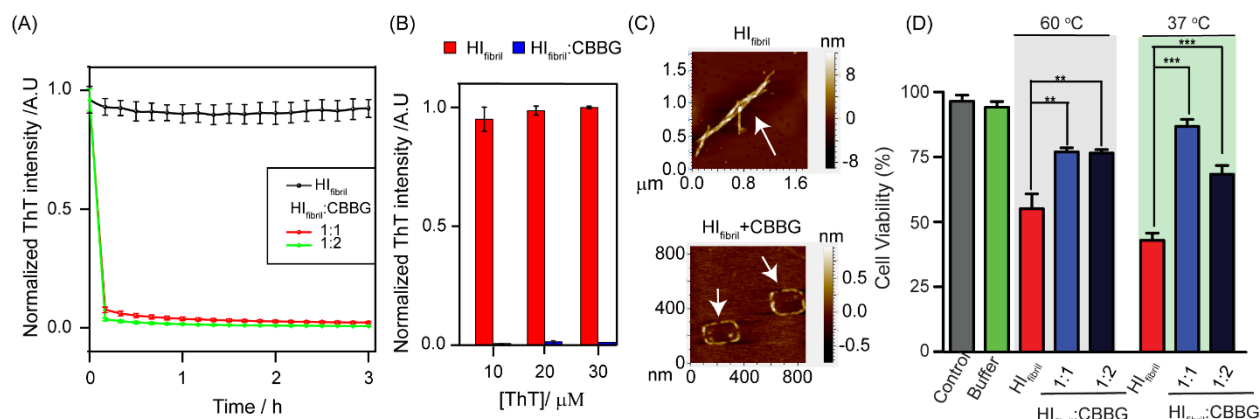


Figure 2.1.10. Disaggregation of HI fibril with treatment of CBBG. (A) Disassembly of preformed fibrils by using the one and two molar equivalent CBBG at 37 °C in HCl buffer with 100 mM NaCl (pH-1.6). (B) Final ThT intensity of HI fibril and disaggregation of fibrils upon addition of CBBG at 1:2 molar ratio in presence of different concentration of ThT (10, 20 and 30 μM). The standard deviation was represented by the error bar for three different experiments. (C) Disintegration of HI fibrils with addition of equimolar CBBG using AFM microscopy. (D) Relative cell viability measurements of RIN5F cell after addition of HI mature fibril (red) alone and co incubated in presence of CBBG at 1:1 (blue) and 1:2 (indigo) [HI fibril]/ [CBBG] molar ratio. The matured HI fibril with or without treatment of CBBG incubated for 3 h at 60 °C (no shaking) and 37 °C (with 200 rpm shaking) respectively in 25 mM HCl and 100 mM NaCl buffer (pH 1.6).

with the F^{B1} residue of the B chain and I^{A10} of the A chain (Figure 2.1.9). The molecular docking results are partly in agreement with NMR data.

2.1.3.6. CBBG disintegrates mature HI fibrils to non-toxic species

Next, disaggregation of preformed fibrils, a more accurate characteristic for a chemical chaperone²⁴, was monitored using ThT fluorescence and AFM after adding one- and two- fold molar excesses of CBBG to mature fibrils. The gradual loss in ThT intensity over time indicated disintegration of HI fibrils (Figure 2.1.10A). With a higher excess of ThT, a similar intensity trend was detected, indicating that ThT was not competing with CBBG for fibril binding (Figure 2.1.10B). AFM revealed the difference in the HI fibre morphology before and after the addition of CBBG (Figure

2.1.10C). Intriguingly, coincubation of HI fibrils with CBBG at 60 °C and 37 °C increased the cell viability in the MTT assay and converted the toxic mature fibrils into nontoxic disaggregate species (Figure 2.1.10D) ²⁵. We also noticed a dose dependent line-broadening in the ¹H NMR spectrum of CBBG in the presence of HI fibrils (Figure 2.1.11), suggesting that a molecular interaction between CBBG and HI fibrils is responsible for the CBBG induced disaggregation process.

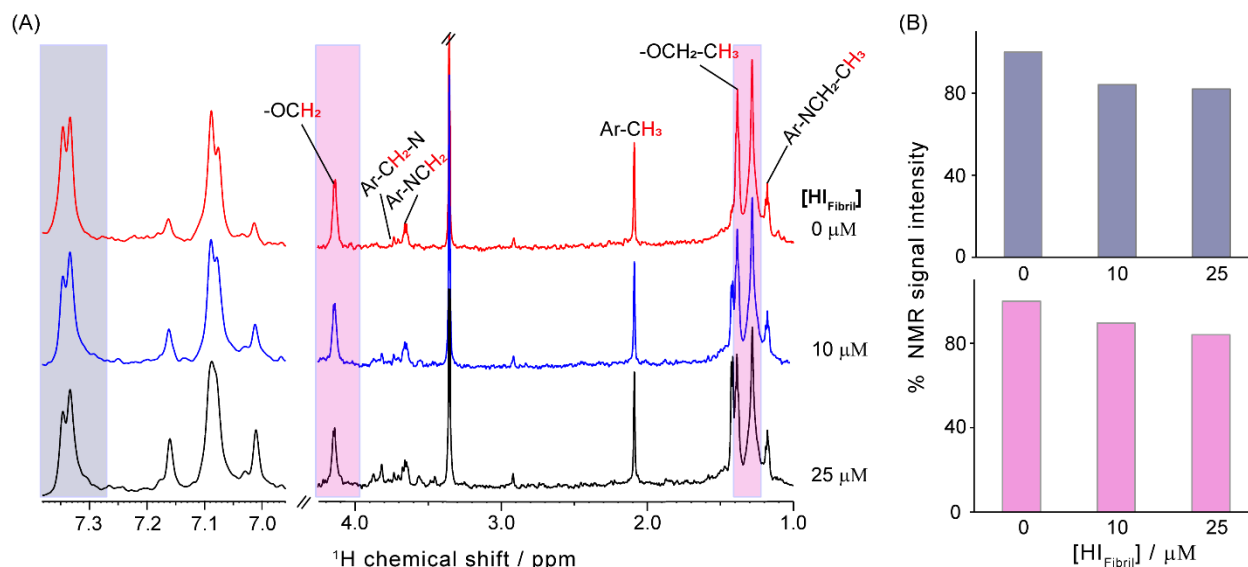


Figure 2.1.11. NMR signal intensities of the free and bound CBBG peaks upon titration with insulin fibril. (A) Selected section of 1D ¹H NMR spectra of CBBG (0.5 mM) acquired using Bruker Avance III 700 MHz at 25 °C showing the line width broadening with treatment of HI fibril. % of ¹H NMR signal intensity was calculated from the highlighted blue (B) and purple (C) color regions as a function of HI fibril concentration (0, 10 and 25 μM). CBBG dissolved in 25 mM HCl, 100 mM NaCl buffer with 10% D₂O at pH~1.6 at 25 °C.

2.1.3.7. CBBG treated HI is biologically active

Matured fibril deposition lowers the solubility of active HI in solution, as confirmed using the bicinchoninic acid assay (BCA), while co-incubating the HI and CBBG mixture at a 1:1 molar ratio effectively maintained soluble protein concentrations similar to native HI (Figure 2.1.12A). The interaction of HI with its cell surface receptor activates a signalling cascade resulting in enhanced Akt phosphorylation without changing the Akt1 levels, which is crucial for glucose absorption from plasma. CBBG-treated HI had phospho-Akt levels equivalent to native bioactive HI, but untreated or aggregated HI cells had baseline pAkt levels (Figure 2.1.12B). Therefore CBBG-treated HI was bioactive and activated signalling HI receptor.

2.1.3.8. CBBG increases the insulin secretion

Furthermore, it was observed that CBBG markedly increased HI secretion upon stimulation with high glucose (Figure 2.1.12C) in RIN5f cells. However, the mechanism is still unknown and needs further investigation.

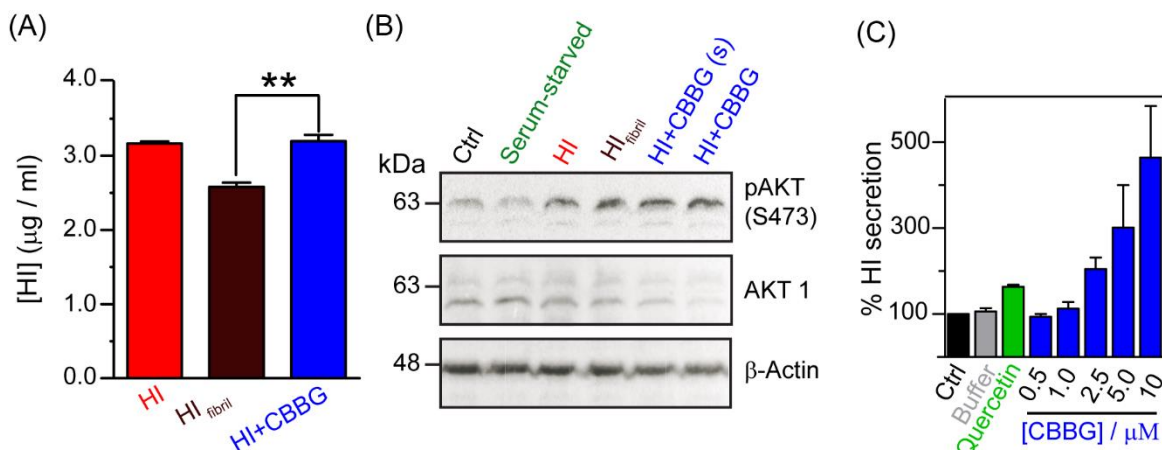
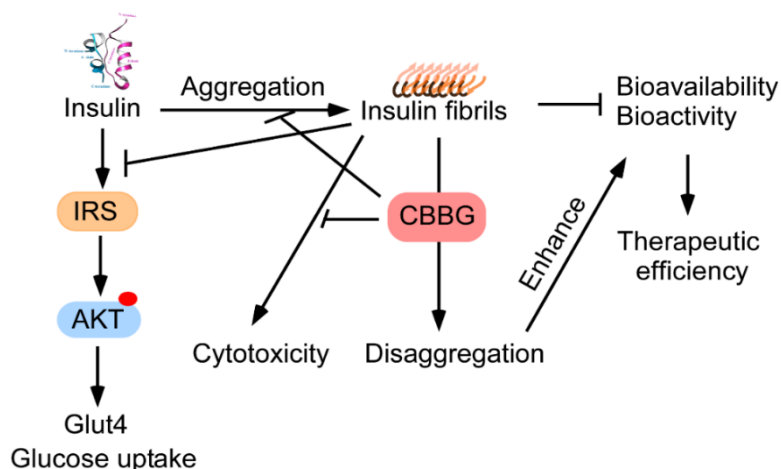


Figure 2.1.12. CBBG induced cellular changes. (A) BCA assay for measuring the soluble protein concentration in HI native, fibril and equimolar HI-CBBG complex. (B) Western blotting of HI and CBBG-treated HI to measure the phosphorylation of Akt (Ser 473). (C) The effect of CBBG on high glucose (22 mM) stimulated HI release (%) in RIN5f cells. Quercetin was used as a positive control. The values are represented as mean \pm SEM, $n=3$.

2.1.4. Conclusion

Our studies demonstrate the rationale behind the usage of small molecules such as CBBG in the production, storage, and delivery of pharmaceutical formulations of human insulin in its most active form. The enthalpy driven binding of CBBG to HI with micromolar affinity allows stabilization of its α -helical form, preventing further unfolding of the protein that serves as the nucleation step in HI fibrillation. The residue-specific interactions provide a clear understanding of the stepwise mechanism of interaction. Insulin fibril inhibition as well as disintegration by CBBG can help us in designing better analogues that can increase the shelf life of formulations (Scheme 2.1.1). Our findings contribute to a prospective treatment of type 2 diabetes in which CBBG improves the effectiveness and bioavailability of therapeutic insulin in its active state as well as plays a crucial role in stimulating insulin secretion from pancreatic β -cells.



Scheme 2.1.1. Schematic representation of role of CBBG in this study.

2.1.5. Appendix 2.1

Table S2.1.1. Biochemical Chart. Effect of CBBG on haematological and biochemical parameters in mice (n= 6 in each group). Packed Cell Volume (PCV); serum glutamic oxaloacetic transaminase (SGOT); serum glutamic pyruvic transaminase (SGPT), white blood cells (WBC).

HAEMATOLOGICAL PARAMETERS	Control Mice	CBBG (1 mg) Mice	CBBG (5 mg) Mice	CBBG (10 mg) Mice	Normal Range
HAEMOGLOBIN %	11.3±2	10.5±1.5	9.6±2.5	12±3	6.1-19.73
Red Blood Cell Count/Lac (10 ⁶)	4.1±0.5	3.9±0.6	3.8±0.3	4.5±0.5	3.57-11.7
PCV %	36±4	34.5±5	32.7±2	33.9±3.5	
PLATELETS COUNT/Lac (10 ⁶)	3.5±1	2.4±0.7	1.8±1.2	2.6±1.5	0.59-6.75
W.B.C Total Count/ Cu mm	9100±700	6000±500	5500±1500	7100±1000	5500-12500
Neutrophils %	33±5	30±3	32±2	28±3	3-27
Lymphocytes%	50±10	40±5	38±3	60±15	12-41
Monocytes %	02±1	01±2	03±1	02±1	00-04
Eosinophils %	01±2	01±1	01±1	02±1	00-01
Basophil %	00±0	00±0	00±0	00±0	00-01
ESR mm/1 st hr	20±3	18±2	26±3	30±5	
BIOCHEMICAL PARAMETERS					
Serum SGOT (AST) IU/L	70±2.5	62±3.7	75±5.9	55±3.2	
Serum SGPT (ALT) IU/L	90±2.1	110±3.5	80±3.8	120±2.9	
Serum Creatinine mg/dl	0.86±0.10	0.86±0.05	0.79±0.15	0.92±0.03	
Blood Urea mg/dl	20±5	39±7	52±4	32±10	

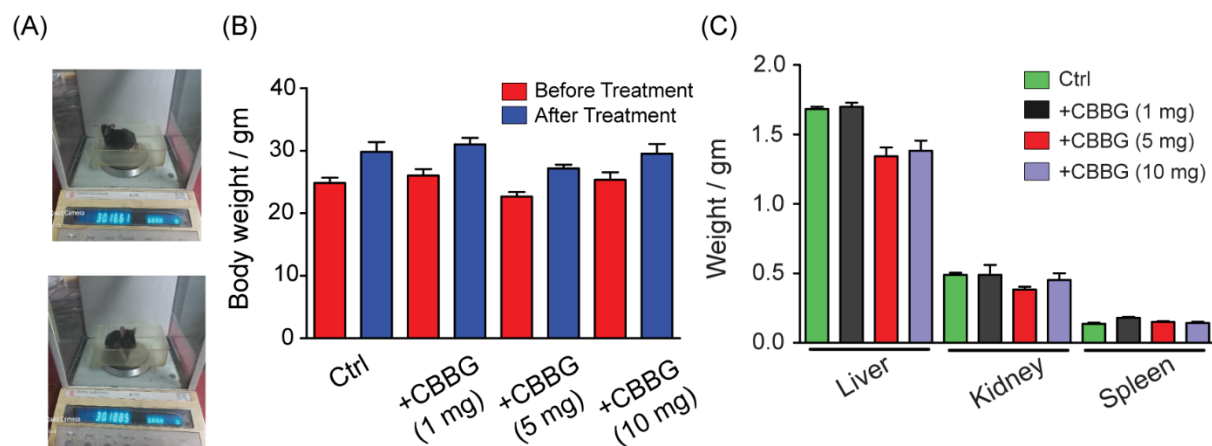


Figure S2.1.1. (A) The images of mouse (C57BL/6J) taken after treatment with CBBG. (B) Mice Body Weight Before and After Treatment with CBBG. (C) Mice Organ weight of Liver, Kidney, and Spleen for control and CBBG treated group after sacrifice.

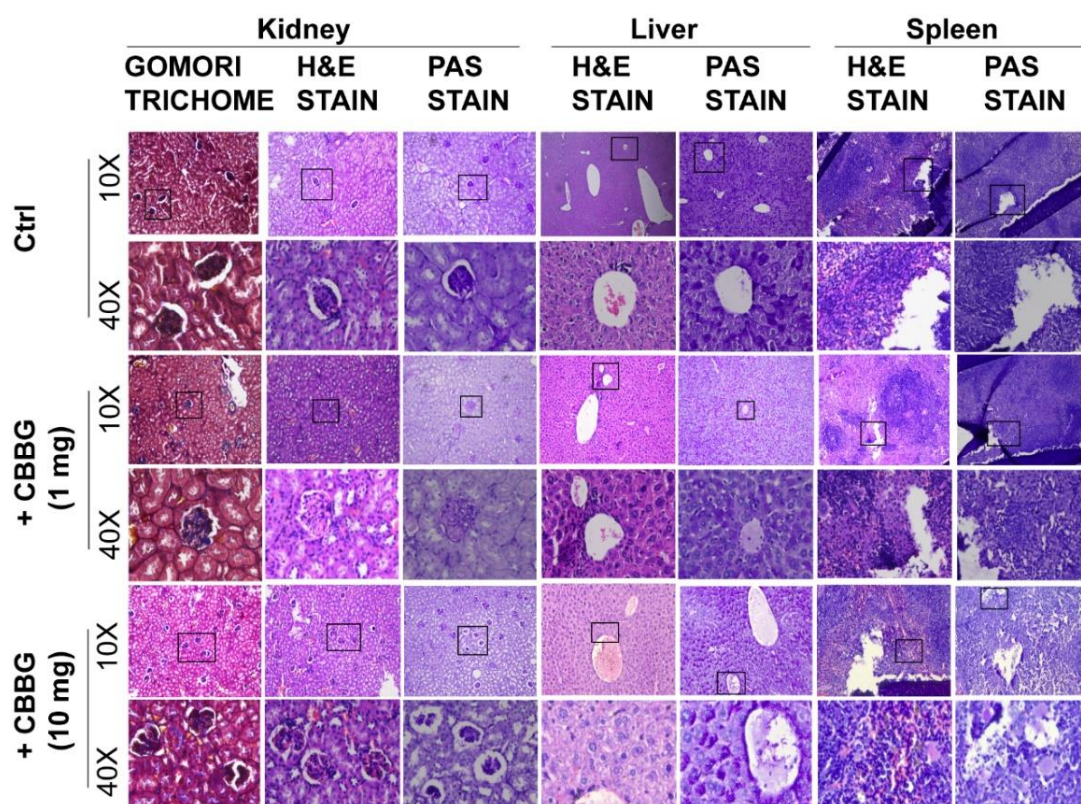


Figure S2.1.2. Histopathological examination of kidney, liver and spleen of the mice for sub chronic toxicity with treatment of 1 mg and 10 mg CBBG for per kg body weight of mice. The images S3 control (ctrl) have purposefully been maintained the same as in Figure 2.1.1A control, referring to the same composition. Haematoxylin and eosin (H and E staining), Gomori Trichrome and Periodic Acid-Schiff staining slides were shown under 10x and 40x magnification.

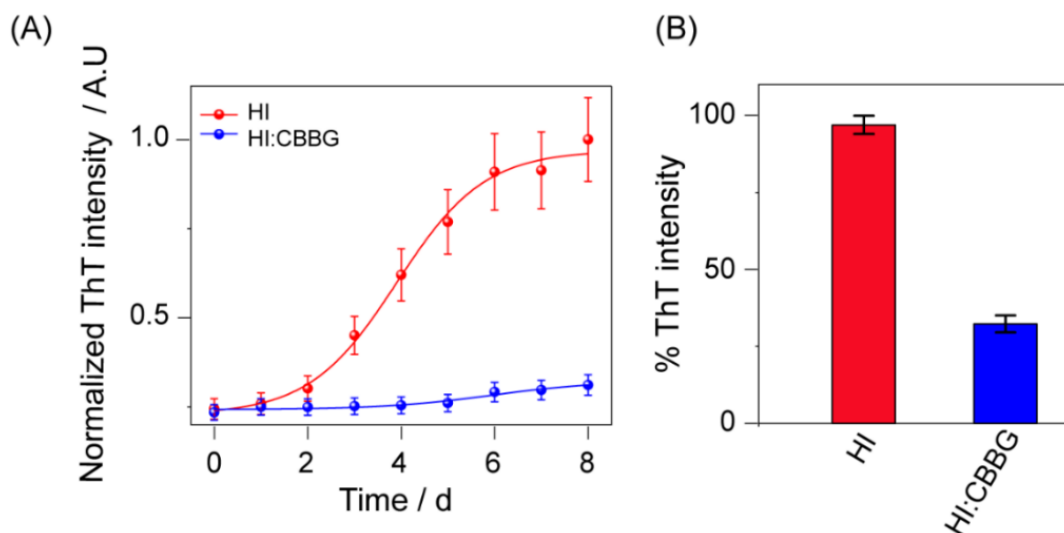


Figure S2.1.3. At pH 7.2, ThT fluorescence of HI aggregation and its inhibition by equimolar CBBG. (A) HI in absence (red trace) and presence (blue trace) of CBBG at HI:CBBG ratio of 1:1. HI (100 μ M) incubated at 60 oC, phosphate buffer, 0.1 M NaCl, pH 7.2, for 8 days. (B) Percentage of final ThT fluorescence intensity of HI incubated in the absence and presence of CBBG after 8 days.

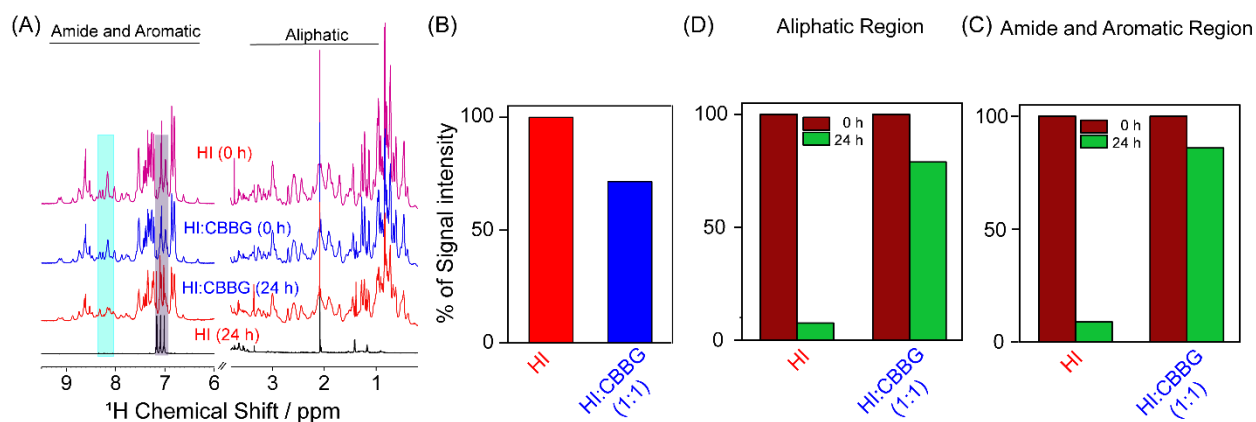


Figure S2.1.4. The aggregation kinetics of HI were acquired by one dimensional ^1H NMR. (A) Time-lapse ^1H NMR spectra of 1 mM HI and/or HI treated with equimolar CBBG in 10 mM sodium phosphate buffer (pH 2.0) with 10 mM NaCl. (B) Normalised signal intensity of HI upon addition of CBBG at 1:1 molar ratio. The percentage of ^1H NMR signal intensity of amide and aromatic region (C) and aliphatic region (D) of HI and/or HI+CBBG (1:1 molar ratio) for 0 and 24 h incubation at 60 $^{\circ}\text{C}$, calculated from the integrated total peak intensities of corresponding regions. Appearance and disappearance of new peaks after heating are highlighted. All the spectra were recorded on Bruker Avance III 700 MHz and at 25 $^{\circ}\text{C}$.

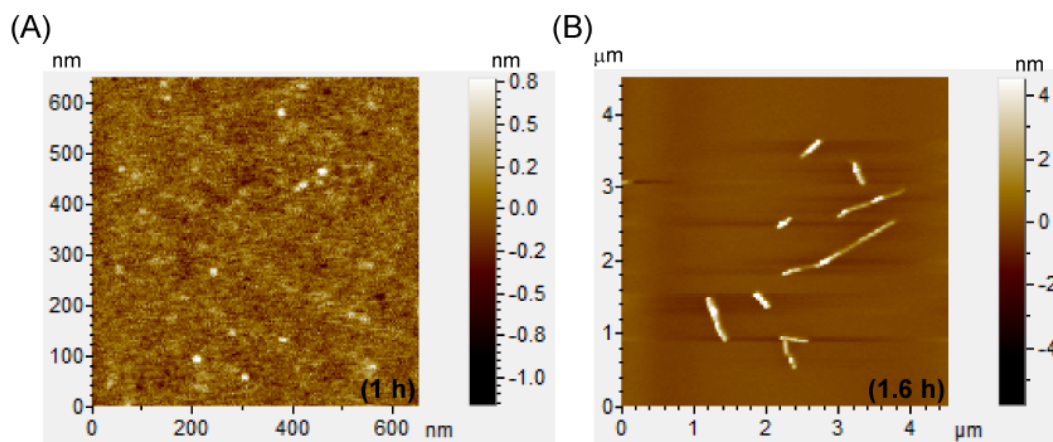


Figure S2.1.5. The aggregation kinetics of HI were acquired by one dimensional ^1H NMR. (A) Time-lapse ^1H NMR spectra of 1 mM HI and/or HI treated with equimolar CBBG in 10 mM sodium phosphate.

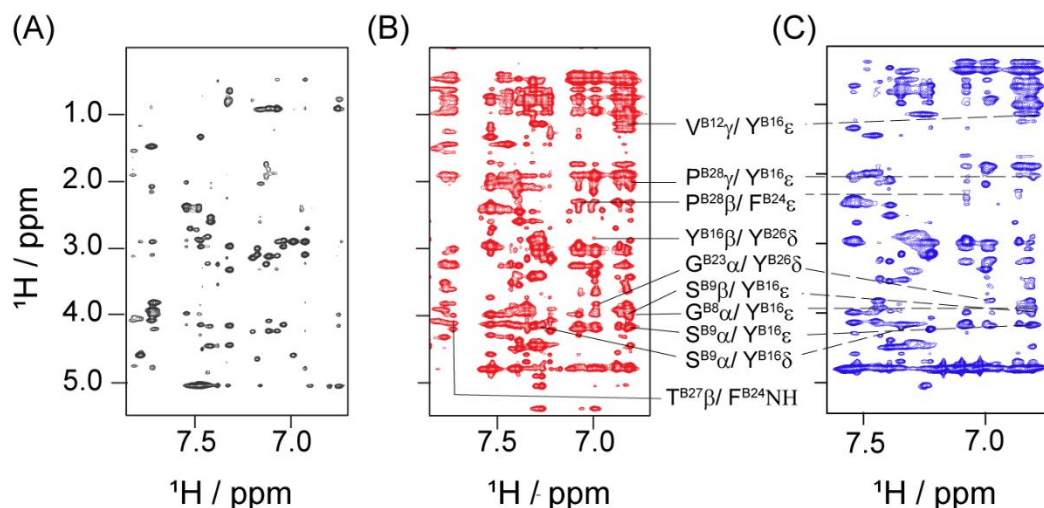


Figure S2.1.6. Structural difference between monomer and dimer HI using two-dimensional (2D) NMR. (A) 2D ^1H - ^1H NOESY spectra of HI monomer (black) in 20% acetic acid- d_4 containing 10% D_2O (pH 1.9). (B) NOESY spectra of HI dimer (red) in 10 mM sodium phosphate buffer, 10 mM NaCl containing 10% D_2O at pH 2.0. (C) NOESY NMR spectra of HI in presence of CBBG (blue) at 1:1 molar ratio after heating at 60 $^\circ\text{C}$ for 24 h. Intermonomer NOEs were detected and assigned for HI dimer. The spectra were recorded at 25 $^\circ\text{C}$ on 700 MHz Bruker NMR spectrometer.

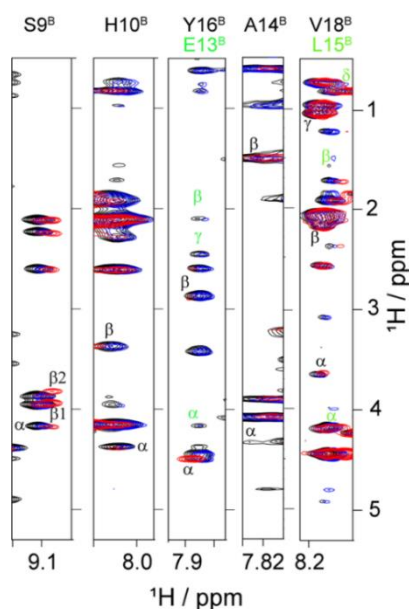


Figure S2.1.7. Strip plot from 2D NOESY spectra exhibiting the chemical shift perturbation and peak intensity broadening of insulin dimer from the B-chain domain in absence (black) or presence of CBBG at 1:1 molar ratio before (blue) and / or after (red) incubation at 60 °C. NOESY NMR spectrum were recorded at 25 °C in 10 mM sodium phosphate buffer (pH 2.0) containing 10 mM NaCl and 10% D₂O using a Bruker Avance III 700 MHz NMR spectrometer with a RT probe NMR.

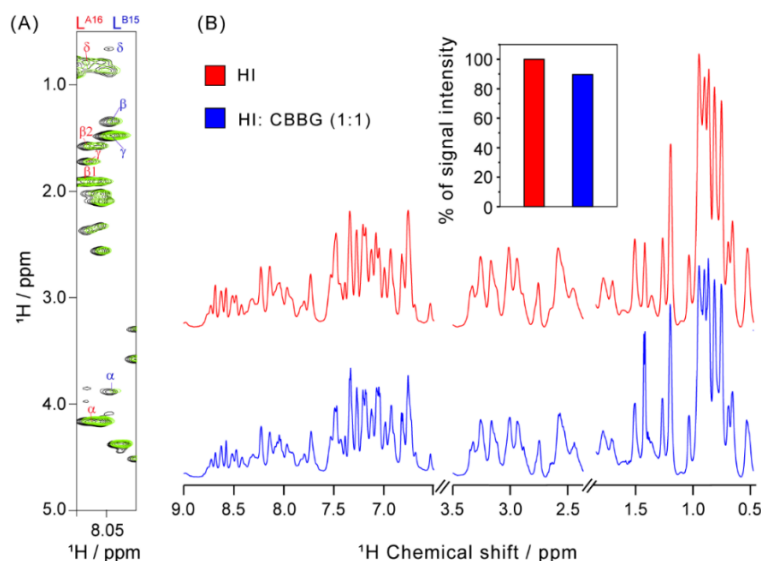


Figure S2.1.8. (A) Two dimensional NOESY Strip plot for Leu^{A15} (blue) and Leu^{B16} (red) residues from HI monomer displaying CSP and broadening in HI alone (black) and presence of 1:1 (green) molar ratio of [HI]/ [CBBG]. (B) One dimensional ¹H NMR spectra of HI monomer before (blue) and after (red) addition of equimolar CBBG in 20% acetic acid-d₄ and 10% D₂O at pH 1.9 (at 25 °C using Bruker Avance III 700 MHz NMR). ¹H NMR signal intensity (%) of selected region in HI reduces to 88% from 100% upon addition of CBBG at 1:1 molar ratio, is shown in inset.

2.1.6. References

1. (a) Grunes, D.; Rapkiewicz, A.; Simsir, A., Amyloidoma secondary to insulin injection: Cytologic diagnosis and pitfalls. *Cytojournal* **2015**, *12*, 15; (b) Samlaska, C.; Reber, S.; Murry, T., Insulin-derived amyloidosis: The insulin ball, amyloidoma. *JAAD Case Rep* **2020**, *6* (4), 351-353; (c) Ratha, B. N.; Kim, M.; Sahoo, B.; Garai, K.; Lee, D.; Bhunia, A., Insulin-eukaryotic model membrane interaction: Mechanistic insight of insulin fibrillation and membrane disruption. *Biochim Biophys Acta Biomembr* **2018**, *1860* (9), 1917-1926.
2. (a) D'Souza, A.; Theis, J. D.; Vrana, J. A.; Dogan, A., Pharmaceutical amyloidosis associated with subcutaneous insulin and enfuvirtide administration. *Amyloid* **2014**, *21* (2), 71-5; (b) Dolui, S.; Roy, A.; Pal, U.; Saha, A.; Maiti, N. C., Structural Insight of Amyloidogenic Intermediates of Human Insulin. *ACS Omega* **2018**, *3* (2), 2452-2462.
3. (a) Das, A.; Gangarde, Y. M.; Pariary, R.; Bhunia, A.; Saraogi, I., An amphiphilic small molecule drives insulin aggregation inhibition and amyloid disintegration. *Int J Biol Macromol* **2022**, *218*, 981-991; (b) Ratha, B. N.; Ghosh, A.; Brender, J. R.; Gayen, N.; Ilyas, H.; Neeraja, C.; Das, K. P.; Mandal, A. K.; Bhunia, A., Inhibition of Insulin Amyloid Fibrillation by a Novel Amphipathic Heptapeptide: MECHANISTIC DETAILS STUDIED BY SPECTROSCOPY IN COMBINATION WITH MICROSCOPY. *J Biol Chem* **2016**, *291* (45), 23545-23556; (c) Pariary, R.; Ghosh, B.; Bednarikova, Z.; Varnava, K. G.; Ratha, B. N.; Raha, S.; Bhattacharyya, D.; Gazova, Z.; Sarojini, V.; Mandal, A. K.; Bhunia, A., Targeted inhibition of amyloidogenesis using a non-toxic, serum stable strategically designed cyclic peptide with therapeutic implications. *Biochim Biophys Acta Proteins Proteom* **2020**, *1868* (5), 140378; (d) Shinde, M. N.; Barooah, N.; Bhasikuttan, A. C.; Mohanty, J., Inhibition and disintegration of insulin amyloid fibrils: a facile supramolecular strategy with p-sulfonatocalixarenes. *Chem Commun (Camb)* **2016**, *52* (14), 2992-5; (e) Sen, S.; Ali, R.; Onkar, A.; Ganesh, S.; Verma, S., Strategies for Interference of Insulin Fibrillogenesis: Challenges and Advances. *Chembiochem* **2022**, *23* (11), e202100678.
4. (a) Ahsan, N.; Siddique, I. A.; Gupta, S.; Surolia, A., A routinely used protein staining dye acts as an inhibitor of wild type and mutant alpha-synuclein aggregation and modulator of neurotoxicity. *Eur J Med Chem* **2018**, *143*, 1174-1184; (b) Iwamaru, Y.; Takenouchi, T.; Murayama, Y.; Okada, H.; Imamura, M.; Shimizu, Y.; Hashimoto, M.; Mohri, S.; Yokoyama, T.; Kitani, H., Anti-prion activity of Brilliant Blue G. *PLoS One* **2012**, *7* (5), e37896; (c) Jana, M. K.; Cappai, R.; Ciccotosto, G. D., Oligomeric Amyloid-beta Toxicity Can Be Inhibited by Blocking Its Cellular Binding in Cortical Neuronal Cultures with Addition of the Triphenylmethane Dye Brilliant Blue G. *ACS Chem Neurosci* **2016**, *7* (8), 1141-7.
5. Biancalana, M.; Koide, S., Molecular mechanism of Thioflavin-T binding to amyloid fibrils. *Biochim Biophys Acta* **2010**, *1804* (7), 1405-12.
6. Nielsen, L.; Khurana, R.; Coats, A.; Frokjaer, S.; Brange, J.; Vyas, S.; Uversky, V. N.; Fink, A. L., Effect of environmental factors on the kinetics of insulin fibril formation: elucidation of the molecular mechanism. *Biochemistry* **2001**, *40* (20), 6036-46.
7. (a) Uversky, V. N.; Garriques, L. N.; Millett, I. S.; Frokjaer, S.; Brange, J.; Doniach, S.; Fink, A. L., Prediction of the association state of insulin using spectral parameters. *J Pharm Sci* **2003**, *92* (4), 847-58; (b) Ratha, B. N.; Kar, R. K.; Bednarikova, Z.; Gazova, Z.; Kotler, S. A.; Raha, S.; De, S.; Maiti, N. C.; Bhunia, A., Molecular Details of a Salt Bridge and Its Role in

- Insulin Fibrillation by NMR and Raman Spectroscopic Analysis. *J Phys Chem B* **2020**, *124* (7), 1125-1136.
8. Sarkar, D.; Maity, N. C.; Shome, G.; Varnava, K. G.; Sarojini, V.; Vivekanandan, S.; Sahoo, N.; Kumar, S.; Mandal, A. K.; Biswas, R.; Bhunia, A., Mechanistic insight into functionally different human islet polypeptide (hIAPP) amyloid: the intrinsic role of the C-terminal structural motifs. *Phys Chem Chem Phys* **2022**, *24* (36), 22250-22262.
 9. Ghosh, B.; Karmakar, S.; Prasad, M.; Mandal, A. K., Praja1 ubiquitin ligase facilitates degradation of polyglutamine proteins and suppresses polyglutamine-mediated toxicity. *Mol Biol Cell* **2021**, *32* (17), 1579-1593.
 10. Jenssen, H.; Aspino, S. I., Serum stability of peptides. *Methods Mol Biol* **2008**, *494*, 177-86.
 11. Alshatwi, A. A.; Subash-Babu, P., Aloe-Emodin Protects RIN-5F (Pancreatic beta-cell) Cell from Glucotoxicity via Regulation of Pro-Inflammatory Cytokine and Downregulation of Bax and Caspase 3. *Biomol Ther (Seoul)* **2016**, *24* (1), 49-56.
 12. Khazaei, M.; Pazhouhi, M., Protective effect of hydroalcoholic extracts of *Trifolium pratense* L. on pancreatic beta cell line (RIN-5F) against cytotoxicity of streptozotocin. *Res Pharm Sci* **2018**, *13* (4), 324-331.
 13. Norrman, M.; Schluckebier, G., Crystallographic characterization of two novel crystal forms of human insulin induced by chaotropic agents and a shift in pH. *BMC Struct Biol* **2007**, *7*, 83.
 14. Schrödinger.
 15. BIOVIA D.S. *Discovery Studio* 2020.
 16. Azuma, K.; Noda, Y.; Hirasawa, K.; Ueta, T., BRILLIANT BLUE G-ASSISTED INTERNAL LIMITING MEMBRANE PEELING FOR MACULAR HOLE: A Systematic Review of Literature and Meta-Analysis. *Retina* **2016**, *36* (5), 851-8.
 17. Ivancic, V. A.; Ekanayake, O.; Lazo, N. D., Binding Modes of Thioflavin T on the Surface of Amyloid Fibrils Studied by NMR. *Chemphyschem* **2016**, *17* (16), 2461-4.
 18. Becker, W.; Bhattiprolu, K. C.; Gubensak, N.; Zangger, K., Investigating Protein-Ligand Interactions by Solution Nuclear Magnetic Resonance Spectroscopy. *Chemphyschem* **2018**, *19* (8), 895-906.
 19. (a) Whittingham, J. L.; Scott, D. J.; Chance, K.; Wilson, A.; Finch, J.; Brange, J.; Guy Dodson, G., Insulin at pH 2: structural analysis of the conditions promoting insulin fibre formation. *J Mol Biol* **2002**, *318* (2), 479-90; (b) Attri, A. K.; Fernandez, C.; Minton, A. P., pH-dependent self-association of zinc-free insulin characterized by concentration-gradient static light scattering. *Biophys Chem* **2010**, *148* (1-3), 28-33.
 20. Jorgensen, A. M.; Kristensen, S. M.; Led, J. J.; Balschmidt, P., Three-dimensional solution structure of an insulin dimer. A study of the B9(Asp) mutant of human insulin using nuclear magnetic resonance, distance geometry and restrained molecular dynamics. *J Mol Biol* **1992**, *227* (4), 1146-63.
 21. Du, X.; Li, Y.; Xia, Y. L.; Ai, S. M.; Liang, J.; Sang, P.; Ji, X. L.; Liu, S. Q., Insights into Protein-Ligand Interactions: Mechanisms, Models, and Methods. *Int J Mol Sci* **2016**, *17* (2).

-
22. (a) Hua, Q. X.; Weiss, M. A., Comparative 2D NMR studies of human insulin and des-pentapeptide insulin: sequential resonance assignment and implications for protein dynamics and receptor recognition. *Biochemistry* **1991**, *30* (22), 5505-15; (b) Zheng, Q.; Lazo, N. D., Mechanistic Studies of the Inhibition of Insulin Fibril Formation by Rosmarinic Acid. *J Phys Chem B* **2018**, *122* (8), 2323-2331.
23. Ratha, B. N.; Kar, R. K.; Brender, J. R.; Pariary, R.; Sahoo, B.; Kalita, S.; Bhunia, A., High-resolution structure of a partially folded i nsulin aggregation intermediate. *Proteins* **2020**, *88* (12), 1648-1659.
24. (a) Almeida, Z. L.; Brito, R. M. M., Amyloid Disassembly: What Can We Learn from Chaperones? *Biomedicines* **2022**, *10* (12); (b) Pithadia, A. S.; Bhunia, A.; Sribalan, R.; Padmini, V.; Fierke, C. A.; Ramamoorthy, A., Influence of a curcumin derivative on hIAPP aggregation in the absence and presence of lipid membranes. *Chem Commun (Camb)* **2016**, *52* (5), 942-5.
25. Grudzielanek, S.; Velkova, A.; Shukla, A.; Smirnovas, V.; Tatarek-Nossol, M.; Rehage, H.; Kapurniotu, A.; Winter, R., Cytotoxicity of insulin within its self-assembly and amyloidogenic pathways. *J Mol Biol* **2007**, *370* (2), 372-84.

2.2. An amphiphilic small molecule drives insulin aggregation inhibition and amyloid disintegration

This chapter has been adapted from the following publication:

Das, A¹., Gangarde, Y.M¹., **Pariary, R.**, Bhunia, A. and Saraogi, I., 2022. An amphiphilic small molecule drives insulin aggregation inhibition and amyloid disintegration. *International Journal of Biological Macromolecules*, 218, pp.981-991.

2.2.1 Introduction

Effective strategies for addressing protein aggregation are a significant unmet need in human health. Specifically, the aggregation of proteins into structured β -sheets known as amyloids has been implicated in numerous human diseases ¹. These aggregates represent a low-energy state in the folding funnel and are exceptionally stable ². Despite the presence of various quality control mechanisms *in vivo* to manage these aggregates, they often require substantial amounts of ATP ³, disaggregating amyloids using small molecules is a challenge and has hindered the use of therapeutic proteins like insulin.

The inhibition of insulin aggregation has been explored using small organic molecules, including polyphenolic compounds ⁴, supramolecules ⁵, and peptide-based inhibitors ⁶. Nevertheless, these methods have drawbacks, including non-specificity, incomplete inhibition even at high concentrations relative to insulin, susceptibility to proteolytic degradation, and limited understanding of their mechanisms of action. Saraogi et al. previously identified pyridyl amide derivatives that significantly reduced insulin fibrillation by over 80% ⁷. Among these derivatives, one compound (M1) demonstrated efficacy in maintaining insulin in its biologically active form ⁷. Here, we report a molecule called PAD-S (Figure 2.2.1A), derived from M1, functionalized with a terminal sulfonate group. This modification was inspired by the presence of sulfonate functionalities on some known inhibitors of insulin aggregation ^{4b, 5b, 8}. We found that PAD-S successfully inhibited aggregation of insulin and its biosimilars at equimolar ratio, and preserved the native structure and function of insulin thus acting as a chemical chaperone. It also successfully disintegrated preformed insulin fibrils to non-toxic forms, a property that is relatively rare for small molecules. Since amyloids originating from various proteins exhibit common structural and

mechanistic characteristics, PAD-S presents a valuable framework for developing ATP-independent small molecule disaggregates for other amyloidogenic proteins.

2.2.2. Experimental Methods

2.2.2.1. Materials

The reagents and solvents for chemical synthesis were purchased from commercial chemical suppliers. Recombinant human insulin was from MP Biomedicals, Cat. no. 0219390080). The following insulins were used in this study: Glargine (CAS Number 160337-95-1), Sigma Aldrich Cat. No. Y0001542); Lispro (CAS Number 133107-64-9), Sigma Aldrich Cat. No. Y0000348). Human recombinant insulin used for NMR experiments, was purchased from Sigma Aldrich (Cat No. 91077C-100MG) while Glargine insulin was purchased as 3ml BASALOG Refill from Biocon Biologics India limited (Bangalore, India). Acetic acid-d₄ was obtained from Cambridge Isotope Laboratories (DLM-12-10x0.5).

2.2.2.2. Insulin fibrillation

A stock of recombinant human insulin was prepared in 25 mM HCl containing 0.1 M NaCl (pH ~ 1.6). The stock was diluted to 0.087 mg/ml (15 μ M), and incubated at 60 °C in a thermo-mixer with agitation at 300-400 rpm to promote fibrillation.

2.2.2.3. Thioflavin T (ThT) assay

ThT stock solution (20 μ M) was prepared in milliQ water. 25 μ l of the aggregating insulin solution (15 μ M), (either alone or treated with given concentration of PAD-S) was pipetted out at specified time intervals, and added to 175 μ l of ThT solution. ThT fluorescence was measured using BioTek Cytation 1 Plate Reader. The excitation wavelength of ThT was 440 nm, and the emission was measured at 485 nm. ThT assay was done in IISER Bhopal, MP, India.

Seeded fibrillation was carried out using fibrils obtained by the aggregation of insulin solutions (15 μ M, pH 1.6, 60 °C). 3% seeds (v/v) were added to native insulin, either in the absence or presence of PAD-S before the onset of fibrillation. ThT measurements were performed as described above.

PAD-S (15 μ M) was added at different time points (0, 2, 4, 7 h) to aggregating insulin solutions. The ThT measurements were performed as described above.

2.2.2.4. Circular dichroism (CD) spectroscopy

CD spectra were recorded for untreated insulin (3.75 μ M) [human recombinant and insulin variants] and those incubated with varying concentrations of PAD-S using a Jasco J-815 CD Spectrophotometer (JASCO, Japan) at room temperature. The following parameters were used: 1 nm bandwidth with 100 nm/min scanning rate and data pitch of 0.5 nm. Three accumulations were taken for each sample, and an average of at least 4 independent readings were plotted using KaleidaGraph software (Synergy, USA). The secondary structure analysis was done using Bestsel software⁹. This experiment was performed at IISER Bhopal, MP, India.

2.2.2.5. Native PAGE

The aggregated insulin solutions (30 μ M, in the absence or presence of PAD-S) were centrifuged at 5000 rpm for 5 min. The supernatant was analysed by 15% native PAGE in tris-glycine running buffer (pH 8.8) at 100V, 80 A for 1.5 h. The protein was visualized using Coomassie brilliant blue stain. The gels were imaged using GeneSys software in GBOX (Syngene). Bands were quantified using Gene Tools software. This experiment was performed at IISER Bhopal, MP, India.

2.2.2.6. Titration of PAD-S with insulin

Human recombinant insulin (5 μ M) was titrated with increasing concentration of PAD-S (0-100 μ M). The samples were allowed to equilibrate for 30 min before each reading. Tyrosine (Excitation: 275 nm) fluorescence emission was measured between 290-350 nm. Tyrosine fluorescence at 303 nm was plotted for each concentration of PAD-S. The K_d was determined using the equation:

$$F = F_{\max} \frac{K_d + [\text{Ins}] + [\text{PAD} - \text{S}] - \sqrt{(K_d + [\text{Ins}] + [\text{PAD} - \text{S}])^2 - 4[\text{Ins}][\text{PAD} - \text{S}]}}{2[\text{Ins}]}$$

F_{\max} is the maximum fluorescence intensity at saturating PAD-S concentration, and K_d is the equilibrium dissociation constant of the Ins-PAD-S complex. This experiment was performed at IISER Bhopal, MP, India.

2.2.2.7. Protein-ligand docking

Molecular docking was performed to identify potential binding site(s) of PAD-S on insulin using Autodock 4.0. The 3-D structure of PAD-S was prepared using ChemDraw, and energy minimization was performed using Chem3D software. The native structure of insulin from RCSB Protein Data Bank (PDB: 1GUJ) comprised of insulin dimer consisting of two monomers (Chains A/B and identical C/D) was used for docking. Either A/B or C/D was removed to generate the insulin monomer for docking. The number of grid points along X-, Y- and Z- axes were fixed as 85, 85, and 85 respectively, with grid spacing 0.375 Å for the monomer and 119, 97, 126 with grid spacing of 0.375 Å for the insulin dimer. Blind docking was performed to identify the ligand binding site. Both protein and the ligand were prepared by applying Gasteiger charges. All other parameters were set to default. The results were analysed and figures were prepared using Discovery Studio Visualizer Software, Version 4.0 (2012). This experiment was done in IISER Bhopal, MP, India.

2.2.2.8. Nuclear magnetic resonance spectroscopy

All the NMR experiments were recorded in a Bruker AVANCE III 700 MHz, equipped with RT probe at 298K. 500 µM PAD-S was used in presence of 5 µM insulin fibril as 100:1 molar ratio for one-dimensional saturation transfer difference (STD) NMR experiment. The STD control spectrum of PAD-S was performed in the absence of insulin fibril. PAD-S in 20% acetic acid-d₄ was lyophilized and suspended in 100% D₂O. Selectively, saturated protein resonance for total 2s duration time was achieved by a train of 40 selective Gaussian shaped pulse for 49 ms each with an interval period of 1 ms. To irradiate the protein, on-resonance and off-resonance were set at -0.5 ppm and 40 ppm, respectively. The STD NMR was obtained by the subtraction off resonance spectrum from on resonance spectrum using phase cycling method. The reference and STD spectra were recorded for 512 and 1024 scans, respectively, with 16 dummy scans and a spectral width of 12 ppm. Zinc free insulin was prepared with the addition of EDTA followed by overnight dialysis and lyophilization^{6b, 10}. 2 mg/ml insulin was dissolved in 20% acetic acid-d₄, 70% water, and 10% D₂O at pH 1.9 for one dimensional (1D) and two-dimensional (2D) NMR experiments. 2D ¹H, ¹H NOESY NMR spectra of insulin were obtained in the absence and presence PAD-S at 1:1 and 1:5 molar ratio, respectively using mixing time of 200 ms for 64 scans at 298 K. 512 and 2048 data points respectively in t₁ and t₂ dimension along with excitation sculpting pulse sequence for water

suppression were used for NOESY spectra. Topspin v4.0.6 software (Bruker Biospin GmbH, Switzerland) was used for data acquisition and processing. Relative signal intensity (I/I_0) was calculated by taking the intensity ratios of insulin and PAD-S complex (I) and insulin alone (I_0). The running average of I/I_0 was calculated by taking the average I/I_0 of three consecutive residues.

A stock solution of insulin in DCl (pH 1.6, prepared by adding required amount of HCl in D_2O) containing 100 mM NaCl was diluted to 500 μ M (500 μ l) with DCl. Another solution of 500 μ M insulin with 500 μ M PAD-S (1:1) was prepared in DCl containing 100 mM NaCl from their respective stocks. These solutions were added to separate NMR tubes and their proton resonances were recorded at the initial time of aggregation. The same NMR tubes were kept in an incubator for the next 24 h at 60 °C with slight agitation and their proton resonances were recorded on Bruker Avance III 700 MHz NMR spectrometer at 25 °C.

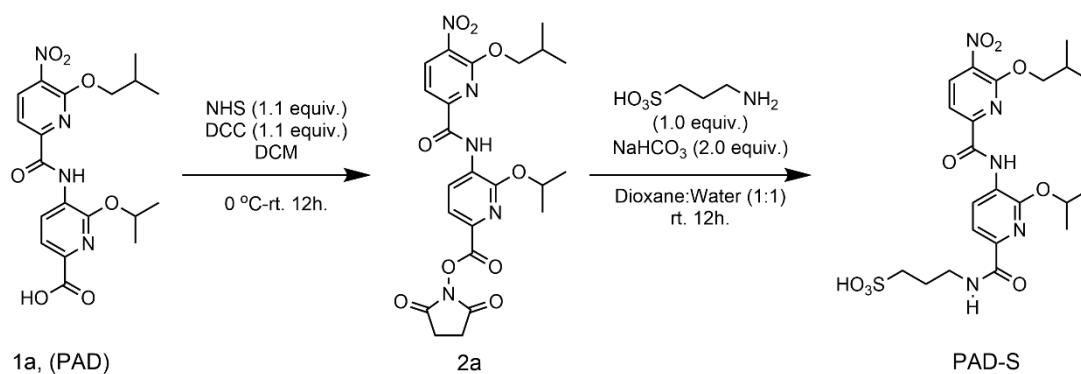
2.2.2.9. Transmission electron microscopy (TEM)

10 μ l of 1% (w/v) phosphotungstic acid solution was added to 10 μ l of insulin solution (15 μ M, alone or after incubation with PAD-S) for negative staining for 30 min at room temperature. The sample (10 μ l) was plated on Formavar protected carbon coated 400 mesh Cu grids (Ted Pella Inc.) and allowed to adsorb for 5 minutes. The excess sample was removed using a tissue paper, and the grid was dried in a vacuum desiccator. TEM analysis was performed on the dried samples using FEI Talos 200S system equipped with a 200kV Field Emission Gun (FEG). This experiment was performed at IISER Bhopal, MP, India.

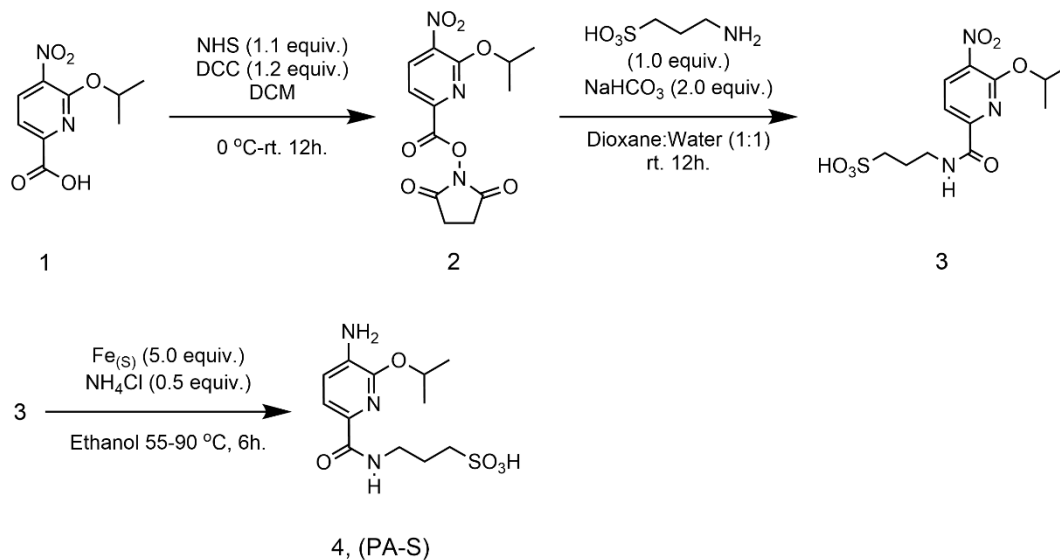
2.2.2.10. Cell viability assay

HEK-293T cells were grown in DMEM media having 10% fetal bovine serum (FBS), using a humidified atmosphere (5% CO_2) at 37 °C. 5000 cells were seeded in 96-well plates per well and incubated for 24 h. The media was removed and the cells were treated with 100 μ L of the serum media containing 5 μ M aggregated insulin solution containing a mixture of oligomers and fibrils (either alone or PAD-S treated) and incubated for 24 h. The cell viability was measured using an MTT assay (Sigma-Aldrich). 100 μ L of 5mg/ml MTT solution diluted in media, was added to each well and incubated for 4 h. The media was removed and 150 μ L of DMSO was added into each

well to dissolve the formazan crystals. The absorption was measured at 570 nm using BioTek Cytation 1 Plate Reader (USA). MTT assay was performed at IISER Bhopal, MP, India.



Scheme 2.2.1: Synthesis of sulfonated pyridylamide dimer



Scheme 2.2.2: Synthesis of sulfonated pyridyl monomer.

2.2.3. Results and discussion

2.2.3.1. Synthesis and structure-activity relationship (SAR) studies of PAD-S

The synthesis of PAD-S started with esterification of an acid (1a) with N-hydroxy succinimide (NHS) in the presence of dicyclohexyl carbodiimide (DCC) to give an activated ester (2a). Molecule 2a was coupled with 3-amino propane sulfonic acid (3-APS) to give the desired pyridyl amide with sulfonate modification (PAD-S) (Scheme 2.2.1 and Figure 2.2.1A). The bottom half

of PAD-S (PA-S) was synthesized as a control by reduction of a nitroamide containing a sulfonate functionality (3) (Scheme 2.2.2) ¹¹.

ThT fluorescence was used to monitor the degree of insulin fibrillation in the presence of PAD-S ¹². We incubated native insulin solution (15 μ M, pH 1.6 HCl, 0.1 M NaCl) in the presence of PAD-S and allowed it to aggregate at 60 °C. Insulin treated with a fivefold molar excess of PAD-S did not show any enhancement in ThT fluorescence (Figure 2.2.1B). In contrast, significant enhancement of ThT fluorescence was observed for insulin alone due to the formation of amyloid fibrils. These data indicate that PAD-S likely inhibits insulin fibrillation. To rationalize which molecular features of PAD-S were essential for the inhibitory activity, we tested fragments of PAD-S for insulin aggregation inhibition (Figure 2.2.1A). The fragment PAD, lacking the pendant sulfonate, or 3-APS containing only the sulfonate functionality did not have any effect on insulin aggregation (Figure 2.2.1B). A small (~30%) decrease in ThT fluorescence intensity was observed with the fragment PA-S containing only the lower half of PAD-S. The results of this analysis indicate that the presence of all the key molecular features and their proper spatial organization is required for optimal activity.

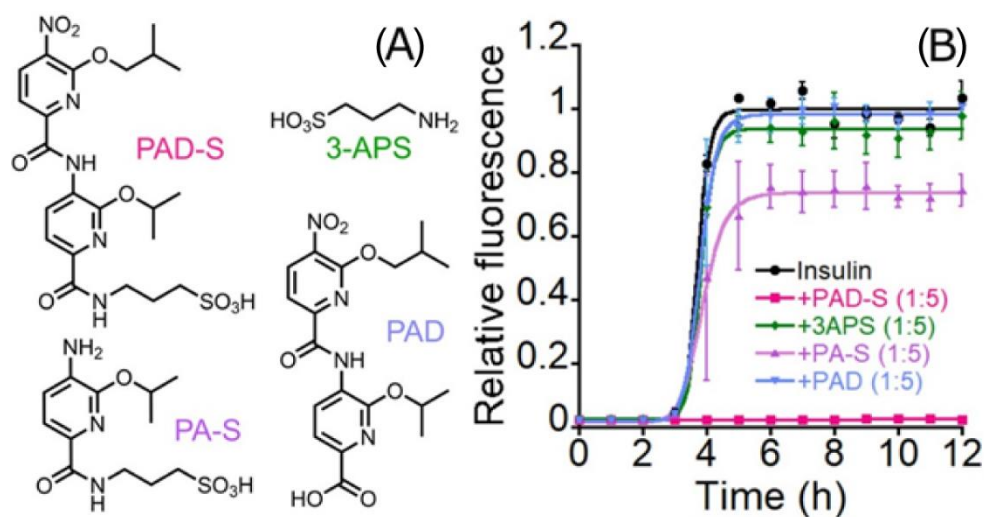


Figure 2.2.1. (A) Chemical structures of PAD-S and its fragments. (B) Insulin aggregation inhibition with PAD-S and its fragments (insulin: molecule = 1:5) monitored using ThT fluorescence. The insulin concentration was 15 μ M, and kinetics were carried out in pH 1.6 at 60 °C. Error bars indicate standard deviations from three independent experiments. The figure was adapted with copyright permission from © 2022 Elsevier B.V.

2.2.3.2. PAD-S inhibits insulin aggregation dose dependently

To assess the concentration dependent effect of PAD-S on insulin aggregation, we treated insulin with different concentrations of PAD-S, and the aggregation kinetics were monitored over time using ThT. PAD-S showed dose dependent inhibition of insulin fibrillation with complete inhibition beyond equimolar concentration (Figure 2.2.2A). The complete inhibition of aggregation indicated that PAD-S likely disrupted primary nucleation events during insulin fibrillation.

2.2.3.3. PAD-S preserves the native structure of insulin

Insulin contains four Insulin is a predominantly α -helical protein which upon fibrillation transforms into β -sheets that have been well characterized by circular dichroism (CD) ¹³. To evaluate the effect of PAD-S on insulin aggregation, the insulin-PAD-S complex was monitored by CD before and after 12 h of incubation at 60 °C. The minima at 208 and 222 nm in the CD spectrum of insulin before aggregation indicate that insulin predominantly exists in an α -helical form (Figure 2.2.2B, green). The appearance of a minimum at 218 nm after 12 h of aggregation (Figure 2.2.2B, black) signifies β -sheet character of insulin due to fibril formation. Insulin treated with equimolar PAD-S largely retained its helical signature (Figure 2.2.2B, yellow). However, a lower concentration of PAD-S (0.5 equivalents with respect to insulin) was unable to do so (Figure 2.2.2B, purple) in agreement with the ThT data.

We determined the amount of soluble insulin present after PAD-S treatment using a Bradford assay. PAD-S could successfully maintain the protein in its soluble form, comparable to native non-aggregated insulin (Figure 2.2.2C). In contrast, the insulin sample did not contain any soluble protein in the absence of PAD-S. Native polyacrylamide gel electrophoresis (PAGE) on a 15 % gel revealed that PAD-S treated insulin had a mobility similar to native insulin (Figure 2.2.2D) although PAD-S seems to have changed the conformational distribution of insulin. The extra bands in case of PAD-S treated insulin (lane 3) may be attributed to the stabilization of other oligomeric states of insulin, compared to the native form in which predominantly a single band was observed (lane 1). In contrast, aggregation of insulin in the absence of PAD-S did not show any distinct bands, as the large protein aggregates likely could not enter the gel matrix. These results were

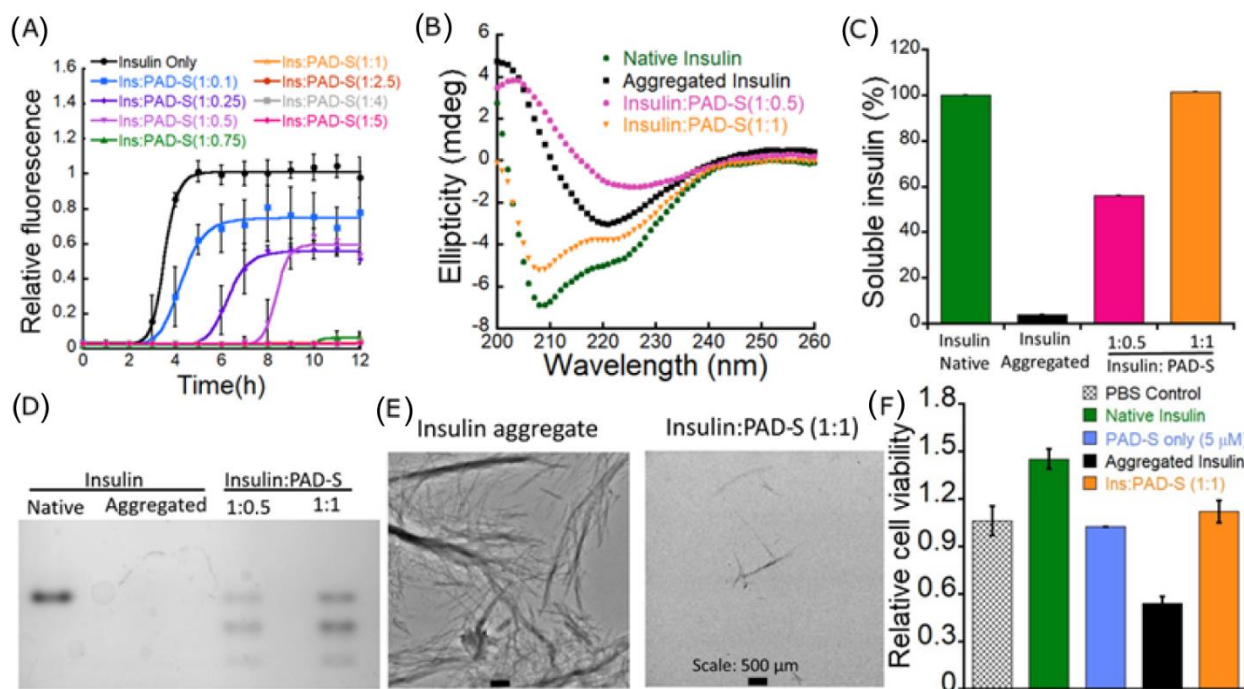


Figure 2.2.2. (A) Time dependent change in ThT fluorescence during insulin aggregation (15 μ M, pH 1.6, 60 $^{\circ}$ C) at different concentrations of PAD-S. (a)-Ins: PAD-S (1:0), (b)-Ins: PAD-S (1:0.1), (c)-Ins: PAD-S (1:0.25), (d)-Ins: PAD-S (1:0.5), (e)-Ins: PAD-S (1:0.75), (f)-Ins: PAD-S (1:1), (g)-Ins: PAD-S (1:2.5), (h)-Ins: PAD-S (1:4), (i)-Ins: PAD-S (1:5). (B) CD spectra of insulin (3.75 μ M, with or without PAD-S) after 12 h of incubation. (C) Bradford assay showing soluble insulin content after 12 h of incubation in the absence and presence of PAD-S. In B and C, native insulin (green) is shown as a control. All data are average of three independent experiments. (D) 15 % Native PAGE gel showing inhibition of insulin aggregation by PAD-S ([Ins] = 60 μ M). (E) TEM images of insulin (with or without equimolar concentration of PAD-S) at the end of fibrillation. Both data are representative of three independent experiments. (F) MTT assay showing cell viability of HEK293T cells in the presence of native insulin (5 μ M), insulin aggregates (5 μ M), PAD-S only (5 μ M), and insulin aggregated in the presence of PADS. The error bars indicate standard deviations from two independent experiments. The figure was adapted with copyright permission form © 2022 Elsevier B.V.

supported by transmission electron microscopy (TEM) images¹⁴, which showed no fibril formation in the case of insulin treated with equimolar PAD-S (Figure 2.2.2E).

To further analyze the effect of PAD-S on insulin aggregation we performed one-dimensional solution-state ^1H NMR analysis (Appendix 2.2, Figure S2.2.1). ^1H NMR spectra of insulin alone or in the presence of equimolar of PAD-S (500 μ M, pH 1.6 HCl) was recorded before aggregation (t=0 h), which showed sharp and well-resolved NMR signals in the spectrum (Figure S2.2.1A-B).

After 24 h of incubation at 60 °C, the proton NMR spectrum of insulin without PAD-S did not show any signal (Figure S2.2.1C), due to the formation of large insoluble aggregates (Figure S2.2.1E). In contrast, insulin treated with PAD-S retained most of the ^1H NMR signals (Figure S2.2.1D), and the solution remained clear even after 24 h incubation at 60 °C (Figure S2.2.1E), signifying inhibition of insulin fibrillation by PAD-S. Our results suggest that PAD-S not only inhibits insulin fibrillation, but also preserves the protein in its native form thus acting as a chemical chaperone.

2.2.3.4. PAD-S protects HEK293T cells from insulin amyloid induced toxicity

Since amyloid fibrils are known to be cytotoxic ¹⁵, we checked whether treatment of insulin with PAD-S could prevent fibril induced cytotoxicity. Cell viability was measured using MTT, which is converted to formazan in live cells and can be quantified by measuring its absorbance at 570 nm. Human embryonic kidney cells (HEK 293T) were treated with native insulin, insulin aggregates or insulin incubated in the presence of PAD-S (5 μM each) (Figure 2.2.2F). PAD-S treated insulin did not show any significant toxicity, compared to cells treated with insulin aggregates in which the cell viability was reduced to ~50%. This suggests that insulin treated with PAD-S is non-toxic to the cells mainly due to the absence of toxic aggregates. PAD-S (5 μM) was not toxic to the cells under the same conditions (Figure 2.2.2F).

2.2.3.5. PAD-S binds to insulin at key hydrophobic regions

Insulin contains four tyrosine residues viz. A14, A19, B16, B26 which are known to change fluorescence on small molecule binding ¹⁶. We used the change in tyrosine fluorescence as a readout to probe the direct binding of PAD-S with insulin. A fixed concentration of insulin (5 μM) was titrated with increasing concentrations of PAD-S. The fluorescence of Tyr decreased with increasing concentration of PAD-S, indicating interaction between insulin and the small molecule (Figure 2.2.3A). The K_d was calculated to be $14 \pm 3 \mu\text{M}$ between insulin and PAD-S.

Next, molecular docking studies were carried out using Auto-dock 4.0 to identify potential binding site of PAD-S to monomeric and dimeric insulin (PDB: 1GUJ) ¹⁷. The results showed stronger binding of PAD-S with the insulin dimer compared to the insulin monomer. The binding energies for the monomer and dimer were -4.0 and -5.9 kcal/mol, respectively. PAD-S interacted with the

insulin monomer (Figure 2.2.3B and Appendix 2.2, Figure S2.2.2) at the 'FFY' region, along with ThrB27, LysB29 residues in the insulin B chain. In the insulin dimer, PAD-S interacted with the hydrophobic sidechains of insulin and with the B-chain C- terminal residues (Appendix 2.2, Figures S2.2.2B-C), namely ThrB27, ProB28, LysB29, which are known to assist in the self-association and oligomerization of the protein ¹⁸.

2.2.3.6. NMR studies identify the interacting site of insulin to PAD-S

To gain further structural insights into insulin-PAD-S interaction, we have recorded two-dimensional ¹H, ¹H Nuclear Overhauser Effect spectroscopy (NOESY) NMR of insulin in presence of PAD-S in 20 % acetic acid-d₄ at pH 1.9. It is well known that insulin remains predominantly in the monomeric form in 20% acetic acid ^{6b, 10, 19}. Addition of equimolar PAD-S induced a significant chemical shift perturbation (CSP) of insulin due to fast chemical exchange between free and bound PAD-S-insulin complex in the intermediate kinetic regime of the NMR timescale. The residues including ValA3, ThrA8, SerA12, LeuA13, LeuA16, GluA17 residues in A-chain were perturbed over the threshold CSP values in the presence of equimolar PAD-S (Figure 2.2.3C and Appendix 2.2, Figure S2.2.3A) while the degree of resonance perturbations from B-chain was largest for AsnB3, GlnB4, HisB5, LeuB17, GluB21, PheB25, TyrB26 and LysB29 (Figure 2.2.3D and Appendix 2.2, Figure S2.2.3A). In addition, moderate CSP was seen at residues SerB9, LeuB11, AlaB14 and LeuB15 (Figure 2.2.3D and Appendix 2.2, Figure S2.2.3A). A further increase in PAD-S concentration (insulin: PAD-S=1:5) result-ed in higher CSP values with almost similar pattern (Figures 2.2.3C-D), indicating that increase of PAD-S concentration in-duces structural rearrangements in insulin. Nearly 13% and 15% NMR signal intensity of insulin monomer was reduced for A-chain and B-chain, respectively, with treatment of equimolar PAD-S (Appendix 2.2, Figure S2.2.3B). However, as shown in Figure 2.2.3E, a significant loss of signal intensity in A-chain for a stretch of ValA3-GluA4-GlnA5 and ThrA8-SerA9-IleA10 suggested a potential binding site for PAD-S on A chain helix region.

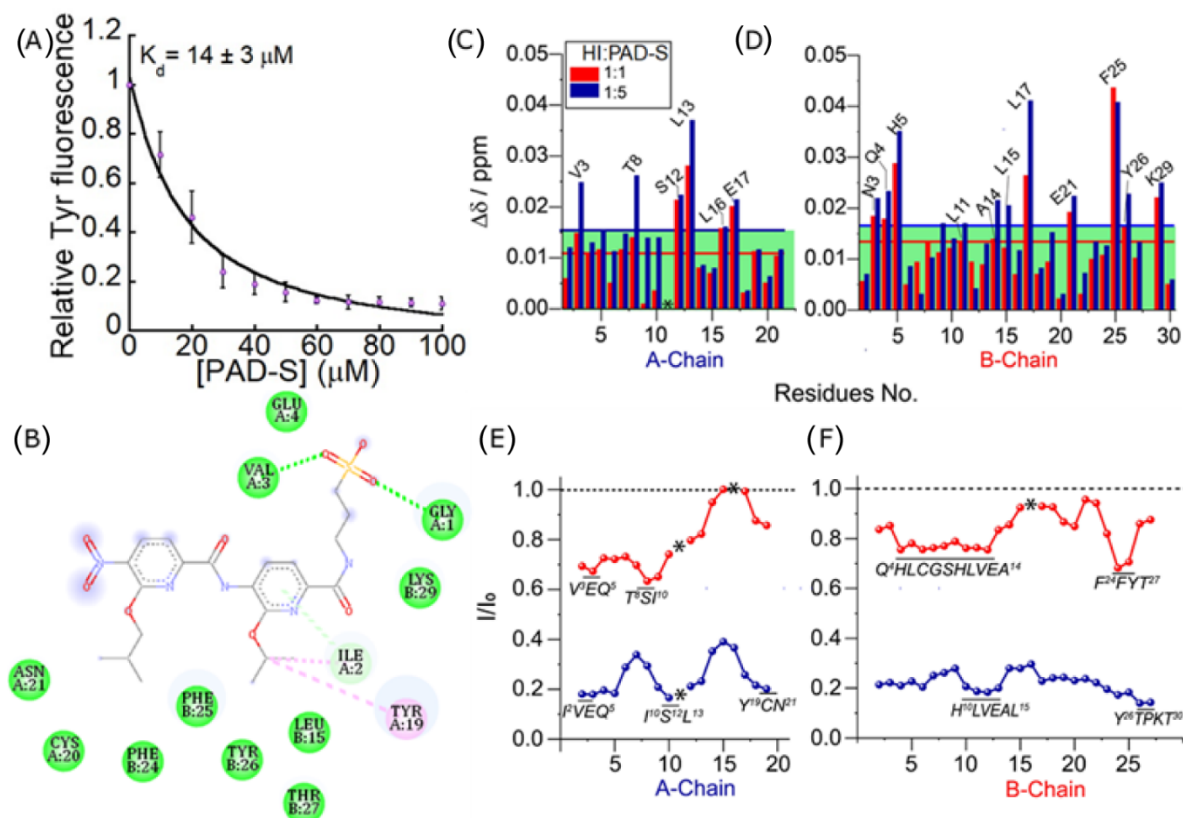


Figure 2.2.3. (A) Relative change in tyrosine fluorescence (λ_{ex} : 275 nm, λ_{em} : 303 nm) of insulin (5 μM) upon titration with PAD-S (0–100 μM). The error bars indicate standard deviations from two independent experiments. (B) Interacting residues upon binding of PAD-S to the insulin monomer (PDB: 1GUJ). Auto Dock 4.0 was used for docking. The pink colour denotes hydrophobic interactions while the green colour denotes Van der Waals interaction between PAD-S and insulin. H-bonding is shown with a dotted green line. Structural insights into the PAD-S complex with insulin were characterized by 2D NOESY NMR. Bar plot of the difference in chemical shift perturbation (CSP) for (C) insulin-A chain (D) insulin-B chain at 1:1 (red) and 1:5 (blue) molar ratio of [Insulin]/[PAD-S]. The red and blue horizontal solid lines with green shaded regions represent the average value of CSP in bar plots. Running average peak intensity (I/I_0) of $\text{C}\alpha$ protons of insulin for three consecutive residues in (E) A-chain (F) B-chain in the presence of PAD-S at a molar ratio of 1:1 (red) and 1:5 (blue), respectively. Overlapping or undetected residues with similar chemical shifts are marked with an asterisk (*). All data were recorded at 298 K in 20 % acetic acid- d_4 on a Bruker Avance III 700 MHz NMR spectrometer equipped with a room temperature probe. The figure was adapted with copyright permission form © 2022 Elsevier B.V.

Moreover, major broadening was observed in the stretch of insulin B-chain such as GlnB4-HisB5-LeuB6-CysB7-GlyB8-SerB9-HisB10 from N-terminal, LeuB11-ValB12-GluB13-AlaB14 from central hydrophobic region and PheB24-PheB25-TyrB26-ThrB27 from the C-terminal, revealing specific involvement of hydrophobic segments in the course of binding (Figure 2.2.3F and Appendix 2.2, Figure S2.2.3A). These results were also in good agreement with molecular docking studies (Figure 2.2.3B). Although, we could not consider the α -protons signal intensity of LeuA16 and TyrB16 due to severe signal overlap in presence of equimolar PAD-S, we detected the γ -proton signal intensity decay of LeuA16 with increasing PAD-S concentration (Appendix 2.2, Figure S2.2.3C). As insulin interacts with PAD-S in a dose-dependent manner, titrating insulin with a fivefold molar excess of PAD-S resulted in a loss of 78% signal intensity for insulin including chain-A and B, indicating intermediate chemical exchange regime present between the bound and unbound state (Appendix 2.2, Figure S2.2.3B). In the presence of 1:5 molar ratio of insulin:PAD-S, relatively broad segments were obtained for A-chain extending from IleA2 to GlnA5; IleA10 to LeuA13 and TyrA19 to AsnA21 (Figure 2.2.3E and Appendix 2.2, Figure S2.2.3A). Interestingly, the aggregation prone segment of the central hydrophobic region (HisB10 to LeuB15) and C-terminal region (TyrB26 to ThrB30) from B-chain showed greater attenuation in signal intensity (Figure 2.2.3F and Appendix 2.2, Figure S2.2.3A). These observations further suggested that the backbone mobility of PheB24, PheB25, TyrB26, ValB12, ValA3, and TyrA19 residues which are mainly responsible for creating a hydrophobic core in the centre of insulin during the course of aggregation, were totally restricted in PAD-S bound conformation²⁰. These observations corroborate the CSP and broadening profiles, explaining direct molecular association of PAD-S with these aggregation prone segments, resulting in modulation of amyloid aggregation propensity. Overall, molecular docking and NMR results suggest that residue-specific electrostatic and hydrophobic interactions are likely to be involved in insulin-PAD-S complex formation.

2.2.3.7. PAD-S inhibits aggregation of insulin biosimilars

Several insulin biosimilars are currently under use for treatment of diabetes²¹. For example, Glargine is a slow acting insulin analog that consists of a glycine residue at the C-terminal A-chain replacing asparagine (N21G of A chain) and two extra arginine residues (R31,R32 of B chain) at the B-chain C-terminal threonine. Insulin Lispro, a fast-acting insulin variant²² is made by reversal of amino acids at position 28 and 29 of the insulin B chain²³. It is a double mutant P28K, K29P

that has been developed to reduce dimerization, which results in its fast-acting property ²⁴. We asked whether PAD-S could effectively inhibit the aggregation of insulin biosimilars as it binds to

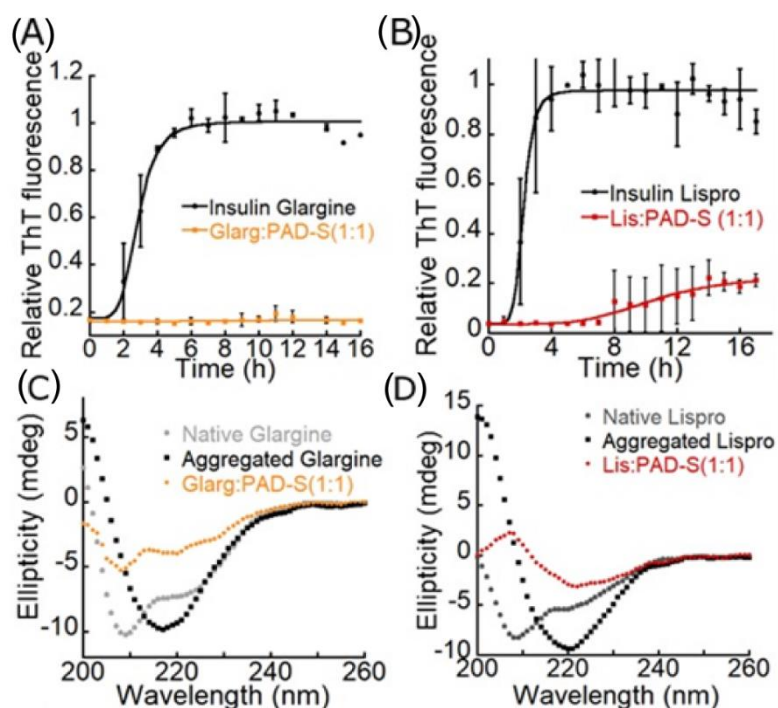


Figure 2.2.4. Fibrillation kinetics of insulin biosimilars measured using ThT fluorescence (A) insulin glargine, (B) insulin lispro in absence and presence of equimolar PAD-S (15 μ M, pH 1.6, 60 $^{\circ}$ C). CD Spectra of insulin glargine (C), insulin lispro (D) in the absence and presence of equimolar PAD-S (3.75 μ M) at the end of fibrillation. Data are average of three independent experiments. The figure was adapted with copyright permission from \copyright 2022 Elsevier B.V.

the L11VEAYL17 region which is intact in these variants. At equimolar concentration, PAD-S completely inhibited aggregation of glargine, while aggregation of lispro was inhibited by ~80% (Figures 2.2.4A-B). The weaker effect of PAD-S on lispro suggests that the interaction of PAD-S with Pro and Lys of insulin B chain is important to inhibit insulin aggregation, consistent with molecular docking and NMR studies (Figure 2.2.3B). These data were corroborated by CD spectroscopy, which showed stabilization of the α -helical structure of glargine, while some intermediate structures were observed in the case of insulin lispro (Figures 2.2.4C-D).

Two dimensional NOESY NMR further confirmed the residue-specific interaction of glargine with PAD-S. Addition of equimolar of PAD-S to glargine resulted in significant CSP and line broadening for both A and B-chains (Figure 2.2.5A, B and Appendix 2.2, Figure S2.2.4) of insulin.

In particular, A-chain residues ValA3, CysA7, IleA10, SerA12, LeuA13, LeuA16, GluA17, CysA20 and GlyA21 showed higher CSPs (Figure 2.2.5A and Appendix 2.2, Figure S2.2.4). On the other hand, B-chain showed significant sequence specific CSPs at central hydrophobic residues including LeuB11, AlaB14, LeuB15, TyrB16, LeuB17 and C-terminal residues such as PheB25, TyrB26, ThrB27, while distant perturbations were observed in N-terminal residues AsnB3, HisB5, CysB7, SerB9 (Figure 2.2.5B and Appendix 2.2, Figure S2.2.4). These results suggest that the

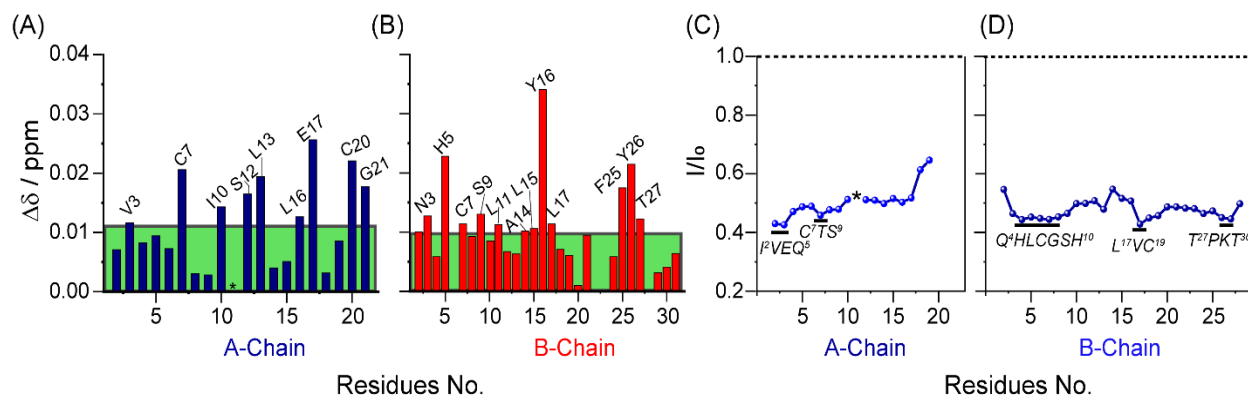


Figure 2.2.5. NMR data showing interaction of insulin glargine with PAD-S. Bar plot showing CSP of glargine insulin in presence of equimolar PAD-S for (A) A-chain (blue) and (B) B-chain (red) residues. The green colour background indicates the average of CSP values for individual chain. Running average of relative change in α -H peak intensity of glargine insulin upon addition of equimolar PAD-S for (C) A-chain and (D) B-chain residues. Undetected residues are marked with an asterisk (*). The NMR experiments were performed at 25 °C on a Bruker Avance III 700 MHz NMR spectrometer equipped with a RT probe in 20% acetic acid- d_4 (pH 1.9). The figure was adapted with copyright permission form © 2022 Elsevier B.V.

regional chemical environment changes around these residues upon addition of PAD-S. Interestingly, we also observed a line broadening effect on A-chain segments, namely IleA2-ValA3-GluA4-GlnA5 and CysA7-ThrA8-SerA9 (Figure 2.2.5C). Additionally, a sequential region-specific line broadening was seen for GlnB4-HisB5-LeuB6-CysB7-GlyB8-SerB9-HisB10-LeuB11, LeuB17-ValB18-CysB19 and TyrB26-ThrB27-ProB28-LysB29-ThrB30 from B-chain segments (Figure 2.2.5D). Taken together, these results suggest that the conformational changes due to intermolecular interaction with PAD-S alter glargine insulin fibrillation.

2.2.3.8. *PAD-S prevents elongation of insulin fibrils.*

To further probe the mechanism of inhibition of PAD-S, we monitored seeded aggregation kinetics using ThT. 3% preformed insulin fibrils were added as a template during insulin fibrillation to bypass the primary nucleation processes. The samples were treated with PAD-S at 1:1 and 1:5 molar ratios and the aggregation kinetics were monitored (Figure 2.2.6A). A concentration dependent decrease in the final ThT fluorescence intensity along with an extended lag phase of insulin aggregation indicated that PAD-S prevents elongation of insulin fibrillation. Thus, PAD-S prevents both primary nucleation (Figure 2.2.2A) and elongation likely by binding to native insulin.

To further validate the mode of inhibitory action of PAD-S, PAD-S was introduced at different time points (2, 4 and 7 h) after initiation of insulin aggregation. PAD-S showed strong inhibition of insulin aggregation when it was introduced 2 h after aggregation began (Figure 2.2.6B). Similarly, introduction of PAD-S at 4 h, which is at the start of log phase, arrested insulin aggregation significantly. This is consistent with strong inhibition of nucleation and elongation as discussed above. Surprisingly, introducing PAD-S after 7 h of incubation resulted in reduction of the ThT fluorescence intensity to ~60% of the maximum value. This is a striking result suggesting that PAD-S might disintegrate mature fibrils (Figure 2.2.6B).

2.2.3.9. *PAD-S disintegrates mature insulin fibrils to non-toxic species*

The previous finding led us to probe whether PAD-S could indeed disintegrate mature insulin fibrils. We added different concentrations of PAD-S to mature insulin fibrils (15 μ M) and monitored ThT fluorescence over time. Indeed, PAD-S disintegrated mature insulin fibrils in a time and dose dependent manner (Figure 2.2.6C) with maximum disintegration of insulin fibrils at 15-fold excess of PAD-S (Figure 2.2.6D). To ensure that the observed result was not due to displacement of ThT from the fibrils by PAD-S, we used three different concentrations of ThT (10, 20, 25 μ M) while keeping insulin fibril and PAD-S concentration fixed. If ThT and PAD-S were indeed competing for insulin fibrils, the ThT fluorescence emission would be different in each case. However, the ThT values were similar at all concentrations (Appendix 2.2, Figure

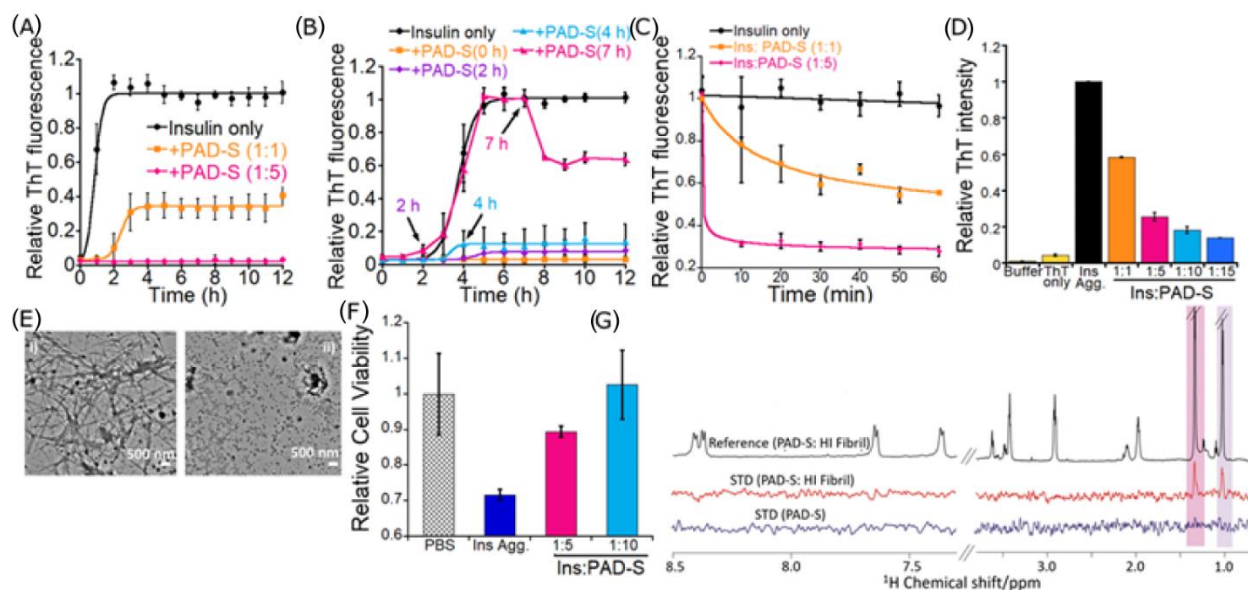


Figure 2.2.6. (A) Seeded (3% v/v) aggregation kinetics of insulin (15 μ M, pH 1.6, 60 $^{\circ}$ C) at specified insulin: PAD-S ratio. The error bars indicate standard deviations from three independent experiments. (B) Fibrillation kinetics of insulin with delayed addition of equimolar PAD-S (2, 4 and 7 h). The error bars indicate standard deviations from three independent experiments. (C) Time dependent kinetics showing disintegration of mature insulin fibrils by PAD-S at insulin: PAD-S concentration of 1:1 and 1:5 (15 μ M, pH 1.6, 60 $^{\circ}$ C). Data is average of two independent experiments. (D) Final ThT fluorescence intensity after disintegration of mature insulin fibrils (15 μ M, pH 1.6, 60 $^{\circ}$ C) by different concentrations of PAD-S after 1 h of agitation. Data is average of three independent experiments. (E) TEM imaging showing (i) mature insulin fibrils, (ii) Fibrils after treatment with PAD-S (1:1). (F) Relative cell viability of HEK293T cells after treatment with insulin aggregates (5 μ M), or mature insulin fibrils disintegrated in the presence of different concentrations of PAD-S. (G) One dimensional STD NMR of PAD-S in the presence of insulin fibrils at 700 MHz. Black color indicates reference 1 H spectrum of PAD-S (500 μ M) with insulin fibrils (5 μ M). Red and blue colors represent STD spectra of PAD-S in the presence and absence of insulin fibrils. The shaded peaks represent the methyl protons (iso-propyl and iso-butyl groups) of PAD-S. Figure was adapted with copyright permission from © 2022 Elsevier B.V.

S2.2.5A), supporting our conclusion that PAD-S actually disintegrated the fibrils, and the decrease in ThT fluorescence in Figures 2.2.6C, D was not an artifact of PAD-S outcompeting ThT for binding mature fibrils. This observation was confirmed by TEM imaging, where PAD-S treated insulin fibril (1:1) sample showed much fewer fibrils and small non-fibrillar aggregates (Figure 2.2.6E(ii)) compared to untreated mature fibrils (Figure 2.2.6E(i)). CD spectra further revealed that PAD-S was indeed able to disintegrate β -sheet rich mature insulin fibrils (black) and restore

partial α -helical character (orange) (Appendix 2.2, Figure S2.2.5B). Although PAD-S successfully disintegrated insulin fibrils (Figures 2.2.6C-D), it was important to determine if the species formed as a result were cytotoxic since aggregation intermediates often show enhanced toxicity²⁵. Hence, we checked the cytotoxicity of the disintegrated fibrils in an MTT assay. The insulin samples obtained after disintegration with PAD-S were less toxic to HEK 293T cells than mature fibrils, and cell viability was completely restored at 10-fold molar excess of PAD-S (Figure 2.2.6F). This indicates that PAD-S successfully converted the mature amyloid fibrils to alternative non-cytotoxic structures.

To identify and characterize the binding epitope of PAD-S to insulin fibrils, one dimensional saturation transfer difference (STD) NMR was performed. In this technique, the effective magnetization is transferred via spin-diffusion from large protein (insulin fibril) to small ligand (PAD-S) protons which are in close proximity to the protein²⁶. Initially, no STD signal was obtained from PAD-S alone (without insulin fibrils) at the applied on-resonance frequency of -0.5 ppm (blue line, Figure 2.2.6G). In contrast, on treatment of PAD-S with preformed insulin fibril at 100:1 molar ratio, strong STD signals were observed in the aliphatic region of PAD-S (red line, Figure 2.2.6G). The PAD-S protons that made close contact with insulin fibrils in the bound form were CH₃ protons of iso-propyl and iso-butyl groups (Figure 2.2.6G). This suggests that PAD-S interacts with the insulin fibrils through its hydrophobic side chains, leading to their disintegration.

2.2.4. Conclusion

In summary, we report the rational design of a small molecule called PAD-S, which acts as a chemical chaperone, and completely prevents aggregation of insulin and biosimilars. The sulfonate group attached to PAD-S makes it highly soluble in aqueous media, thereby facilitating its use in insulin formulations. PAD-S is non-toxic, and protects cells from insulin amyloid induced cytotoxicity. Molecular docking and mechanistic investigations lead to the conclusion that PAD-S binds to native insulin at the amyloid prone B11-B17 (L¹¹VEALYL¹⁷) residues. Furthermore, PAD-S is one of the very few synthetic molecules that can disintegrate mature insulin fibrils to non-toxic smaller fragments. PAD-S is thus a valuable lead for regulating insulin fibrillation in commercial formulations.

2.2.5. Appendix 2.2

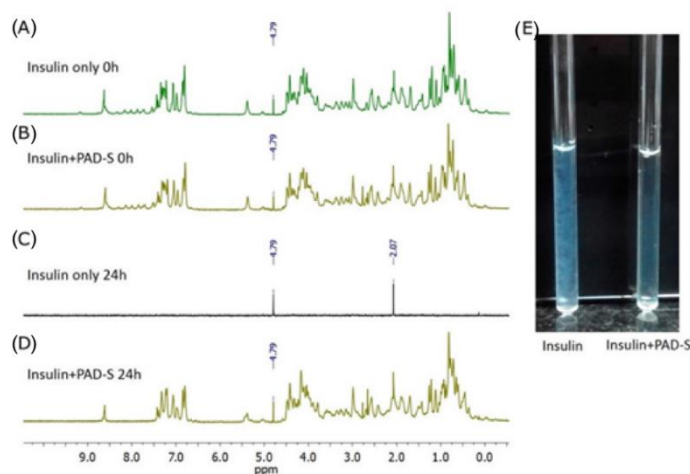


Figure S2.2.1. ^1H NMR spectra to monitor insulin aggregation. (A) ^1H NMR of insulin only (500 μM) before aggregation. (B) ^1H NMR of insulin with PAD-S (500 μM each) before aggregation ($t=0$ h). (C) ^1H NMR of insulin only (500 μM) after 24 h at 60 $^{\circ}\text{C}$. (D) ^1H NMR of insulin with PAD-S (500 μM each) after 24 h of aggregation at 60 $^{\circ}\text{C}$. The residual solvent peak in D_2O was assigned at 4.79 ppm. (The peak at 2.07 ppm is due to an unidentified impurity). The NMR spectra were recorded at 700 MHz in aqueous solution (pH 1.6 DCl) containing 100 mM NaCl. (E) Images of NMR tubes showing insulin only (left), and in the presence of PAD-S (1:1) incubated at 60 $^{\circ}\text{C}$ for 24 h.

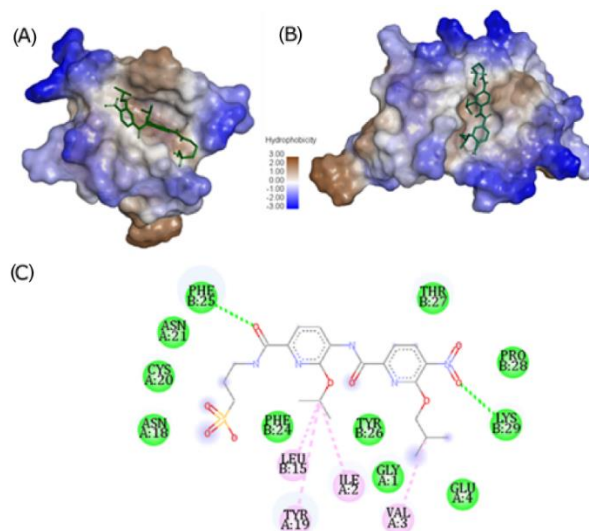


Figure S2.2.2. Molecular docking showing interaction between PAD-S and insulin. (A) PAD-S docked onto insulin monomer (PDB: 1GUJ), prepared by removing one monomer from the dimer. (B) PAD-S docked onto insulin dimer (PDB: 1GUJ). Auto Dock 4.0 was used for docking. (C) 2D Diagram depicting the interacting sites of insulin dimer with PAD-S. The pink color represents hydrophobic interactions and the green color represents Van der Waals interactions. Green dotted lines indicate H-bond interactions of PAD-S with LysB29 and PheB25.

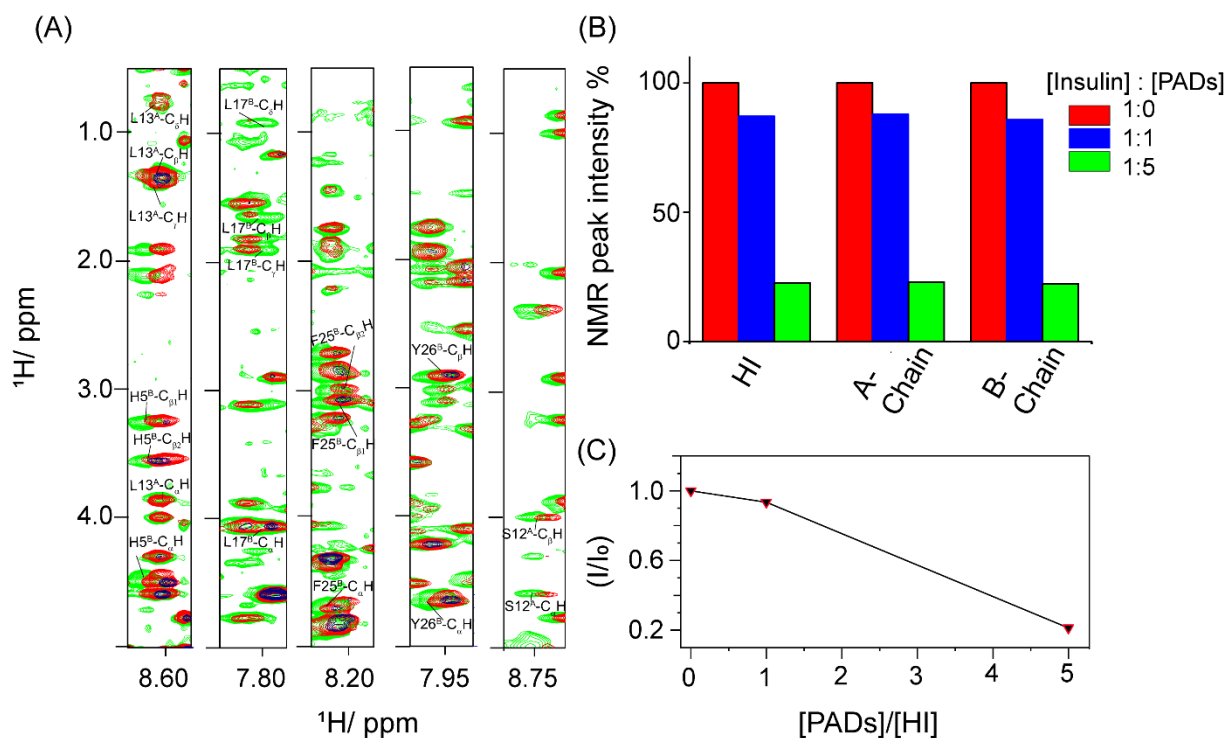


Figure S2.2.3. (A) Strip plot of important residues from insulin displaying chemical shift perturbation (CSP) and broadening in the absence (green) and presence of 1:1 (red) and/or 1:5 (blue) molar ratio of [Insulin]/[PAD-S]. (B) % ^1H NMR signal intensity from 2D NOESY spectrum of human insulin chain-A and chain-B upon addition of PAD-S at 1:1 (blue) and 1:5 (green) molar ratio. (C) Normalized signal intensity of γ -proton of LeuA16 from A-chain of insulin with increasing concentration of PAD-S.

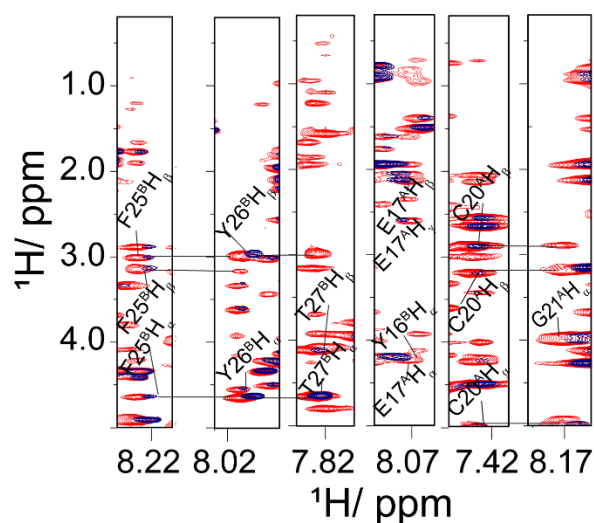


Figure S2.2.4. Strip plot of significant residues showing chemical shift perturbation as well as broadening for glargine insulin in the presence (blue) and absence (red) of equimolar PAD-S. The NOESY NMR spectra were recorded with Bruker Avance III 700MHz NMR spectrometer equipped with a RT probe at 298 K.

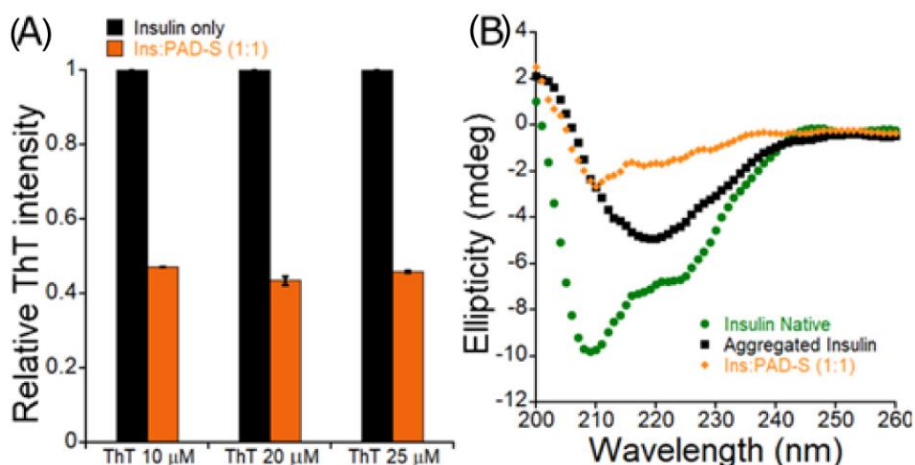


Figure S2.2.5. (A) PAD-S mediated mature insulin fibril (15 μM) disintegration at varying concentration of ThT. (B) CD spectra of native insulin (green), mature insulin fibrils (black), and fibrils after disintegration by PAD-S (orange). Insulin concentration during CD measurement was 3.75 μM and Ins: PAD-S=1:1. A higher concentration of PAD-S could not be used for this experiment due to interference from PAD-S.

2.2.6 References

1. (a) Eisenberg, D.; Jucker, M., The amyloid state of proteins in human diseases. *Cell* **2012**, *148* (6), 1188-203; (b) Rambaran, R. N.; Serpell, L. C., Amyloid fibrils: abnormal protein assembly. *Prion* **2008**, *2* (3), 112-7.
2. Adamcik, J.; Mezzenga, R., Amyloid Polymorphism in the Protein Folding and Aggregation Energy Landscape. *Angew Chem Int Ed Engl* **2018**, *57* (28), 8370-8382.
3. Nillegoda, N. B.; Wentink, A. S.; Bukau, B., Protein Disaggregation in Multicellular Organisms. *Trends Biochem Sci* **2018**, *43* (4), 285-300.
4. (a) Gong, H.; He, Z.; Peng, A.; Zhang, X.; Cheng, B.; Sun, Y.; Zheng, L.; Huang, K., Effects of several quinones on insulin aggregation. *Sci Rep* **2014**, *4*, 5648; (b) Das, A.; Shah, M.; Saraogi, I., Molecular Aspects of Insulin Aggregation and Various Therapeutic Interventions. *ACS Bio Med Chem Au* **2022**, *2* (3), 205-221; (c) Vilasi, S.; Iannuzzi, C.; Portaccio, M.; Irace, G.; Sirangelo, I., Effect of trehalose on W7FW14F apomyoglobin and insulin fibrillization: new insight into inhibition activity. *Biochemistry* **2008**, *47* (6), 1789-96; (d) Wang, J. B.; Wang, Y. M.; Zeng, C. M., Quercetin inhibits amyloid fibrillation of bovine insulin and destabilizes preformed fibrils. *Biochem Biophys Res Commun* **2011**, *415* (4), 675-9; (e) Zheng, Q.; Lazo, N. D., Mechanistic Studies of the Inhibition of Insulin Fibril Formation by Rosmarinic Acid. *J Phys Chem B* **2018**, *122* (8), 2323-2331.
5. (a) Lee, H. H.; Choi, T. S.; Lee, S. J.; Lee, J. W.; Park, J.; Ko, Y. H.; Kim, W. J.; Kim, K.; Kim, H. I., Supramolecular inhibition of amyloid fibrillation by cucurbit[7]uril. *Angew Chem Int Ed Engl* **2014**, *53* (29), 7461-5; (b) Shinde, M. N.; Barooah, N.; Bhasikuttan, A. C.; Mohanty, J., Inhibition and disintegration of insulin amyloid fibrils: a facile supramolecular strategy with p-sulfonatocalixarenes. *Chem Commun (Camb)* **2016**, *52* (14), 2992-5.

6. (a) Banerjee, V.; Kar, R. K.; Datta, A.; Parthasarathi, K.; Chatterjee, S.; Das, K. P.; Bhunia, A., Use of a small peptide fragment as an inhibitor of insulin fibrillation process: a study by high and low resolution spectroscopy. *PLoS One* **2013**, 8 (8), e72318; (b) Ratha, B. N.; Ghosh, A.; Brender, J. R.; Gayen, N.; Ilyas, H.; Neeraja, C.; Das, K. P.; Mandal, A. K.; Bhunia, A., Inhibition of Insulin Amyloid Fibrillation by a Novel Amphipathic Heptapeptide: MECHANISTIC DETAILS STUDIED BY SPECTROSCOPY IN COMBINATION WITH MICROSCOPY. *J Biol Chem* **2016**, 291 (45), 23545-23556; (c) Ratha, B. N.; Kar, R. K.; Kalita, S.; Kalita, S.; Raha, S.; Singha, A.; Garai, K.; Mandal, B.; Bhunia, A., Sequence specificity of amylin-insulin interaction: a fragment-based insulin fibrillation inhibition study. *Biochim Biophys Acta Proteins Proteom* **2019**, 1867 (4), 405-415; (d) Siddiqi, M. K.; Alam, P.; Iqbal, T.; Majid, N.; Malik, S.; Nusrat, S.; Alam, A.; Ajmal, M. R.; Uversky, V. N.; Khan, R. H., Elucidating the Inhibitory Potential of Designed Peptides Against Amyloid Fibrillation and Amyloid Associated Cytotoxicity. *Front Chem* **2018**, 6, 311.
7. Das, A.; Gangarde, Y. M.; Tomar, V.; Shinde, O.; Upadhyay, T.; Alam, S.; Ghosh, S.; Chaudhary, V.; Saraogi, I., Small-Molecule Inhibitor Prevents Insulin Fibrillogenesis and Preserves Activity. *Mol Pharm* **2020**, 17 (6), 1827-1834.
8. Mishra, N. K.; Joshi, K. B.; Verma, S., Inhibition of human and bovine insulin fibril formation by designed peptide conjugates. *Mol Pharm* **2013**, 10 (10), 3903-12.
9. (a) Micsonai, A.; Wien, F.; Kernya, L.; Lee, Y. H.; Goto, Y.; Refregiers, M.; Kardos, J., Accurate secondary structure prediction and fold recognition for circular dichroism spectroscopy. *Proc Natl Acad Sci U S A* **2015**, 112 (24), E3095-103; (b) Micsonai, A.; Wien, F.; Bulyaki, E.; Kun, J.; Moussong, E.; Lee, Y. H.; Goto, Y.; Refregiers, M.; Kardos, J., BeStSel: a web server for accurate protein secondary structure prediction and fold recognition from the circular dichroism spectra. *Nucleic Acids Res* **2018**, 46 (W1), W315-W322.
10. Hua, Q. X.; Weiss, M. A., Comparative 2D NMR studies of human insulin and des-pentapeptide insulin: sequential resonance assignment and implications for protein dynamics and receptor recognition. *Biochemistry* **1991**, 30 (22), 5505-15.
11. (a) Klostermeyer, H.; Humbel, R. E., The chemistry and biochemistry of insulin. *Angew Chem Int Ed Engl* **1966**, 5 (9), 807-22; (b) Giger, K.; Vanam, R. P.; Seyrek, E.; Dubin, P. L., Suppression of insulin aggregation by heparin. *Biomacromolecules* **2008**, 9 (9), 2338-44; (c) Yap, J. L. H., K.; Fletcher, S., Ortho-Selectivity in the Nucleophilic Aromatic Substitution (SNAr) Reactions of 3-Substituted, 2,6-Dichloropyridines with Alkali Metal Alkoxides. *Tetrahedron Lett* **2011**, 52 (32), 4172-4176.
12. Groenning, M.; Norrman, M.; Flink, J. M.; van de Weert, M.; Bukrinsky, J. T.; Schluckebier, G.; Frokjaer, S., Binding mode of Thioflavin T in insulin amyloid fibrils. *J Struct Biol* **2007**, 159 (3), 483-97.
13. Greenfield, N. J., Using circular dichroism spectra to estimate protein secondary structure. *Nat Protoc* **2006**, 1 (6), 2876-90.
14. Gras, S. L.; Waddington, L. J.; Goldie, K. N., Transmission electron microscopy of amyloid fibrils. *Methods Mol Biol* **2011**, 752, 197-214.
15. (a) Baglioni, S.; Casamenti, F.; Bucciantini, M.; Lheshi, L. M.; Taddei, N.; Chiti, F.; Dobson, C. M.; Stefani, M., Prefibrillar amyloid aggregates could be generic toxins in higher organisms. *J Neurosci* **2006**, 26 (31), 8160-7; (b) Yoshihara, H.; Saito, J.; Tanabe, A.; Amada, T.; Asakura,

- T.; Kitagawa, K.; Asada, S., Characterization of Novel Insulin Fibrils That Show Strong Cytotoxicity Under Physiological pH. *J Pharm Sci* **2016**, *105* (4), 1419-26; (c) Stefani, M., Biochemical and biophysical features of both oligomer/fibril and cell membrane in amyloid cytotoxicity. *FEBS J* **2010**, *277* (22), 4602-13.
16. Yanti, S. W.; Z.-W.; Agrawal, D. C.; Chien, W.-J, Interaction between Phloretin and Insulin: A Spectroscopic Study. *J. Anal. Sci. Technol* **2021**, *12*(1), 34.
 17. (a) Forli, S.; Huey, R.; Pique, M. E.; Sanner, M. F.; Goodsell, D. S.; Olson, A. J., Computational protein-ligand docking and virtual drug screening with the AutoDock suite. *Nat Protoc* **2016**, *11* (5), 905-19; (b) Cosconati, S.; Forli, S.; Perryman, A. L.; Harris, R.; Goodsell, D. S.; Olson, A. J., Virtual Screening with AutoDock: Theory and Practice. *Expert Opin Drug Discov* **2010**, *5* (6), 597-607.
 18. Brange, J.; Andersen, L.; Laursen, E. D.; Meyn, G.; Rasmussen, E., Toward understanding insulin fibrillation. *J Pharm Sci* **1997**, *86* (5), 517-25.
 19. Pariary, R.; Ghosh, B.; Bednarikova, Z.; Varnava, K. G.; Ratha, B. N.; Raha, S.; Bhattacharyya, D.; Gazova, Z.; Sarojini, V.; Mandal, A. K.; Bhunia, A., Targeted inhibition of amyloidogenesis using a non-toxic, serum stable strategically designed cyclic peptide with therapeutic implications. *Biochim Biophys Acta Proteins Proteom* **2020**, *1868* (5), 140378.
 20. Ratha, B. N.; Kar, R. K.; Brender, J. R.; Pariary, R.; Sahoo, B.; Kalita, S.; Bhunia, A., High-resolution structure of a partially folded insulin aggregation intermediate. *Proteins* **2020**, *88* (12), 1648-1659.
 21. (a) Adams, G. G.; Meal, A.; Morgan, P. S.; Alzahrani, Q. E.; Zobel, H.; Lithgo, R.; Kok, M. S.; Besong, D. T. M.; Jiواني, S. I.; Ballance, S.; Harding, S. E.; Chayen, N.; Gillis, R. B., Characterisation of insulin analogues therapeutically available to patients. *PLoS One* **2018**, *13* (3), e0195010; (b) Surin, A. K.; Grishin, S. Y.; Galzitskaya, O. V., Determination of amyloid core regions of insulin analogues fibrils. *Prion* **2020**, *14* (1), 149-162.
 22. Gualandi-Signorini, A. M.; Giorgi, G., Insulin formulations--a review. *Eur Rev Med Pharmacol Sci* **2001**, *5* (3), 73-83.
 23. Woods, R. J.; Alarcon, J.; McVey, E.; Pettis, R. J., Intrinsic fibrillation of fast-acting insulin analogs. *J Diabetes Sci Technol* **2012**, *6* (2), 265-76.
 24. Mukherjee, M.; Das, D.; Sarkar, J.; Banerjee, N.; Jana, J.; Bhat, J.; Reddy, G. J.; Bharatam, J.; Chattopadhyay, S.; Chatterjee, S.; Chakrabarti, P., Prion-derived tetrapeptide stabilizes thermolabile insulin via conformational trapping. *iScience* **2021**, *24* (6), 102573.
 25. Park, J. W.; Lee, I. H.; Hahn, J. S.; Kim, J.; Chung, K. C.; Paik, S. R., Disintegration of amyloid fibrils of alpha-synuclein by dequalinium. *Biochim Biophys Acta* **2008**, *1780* (10), 1156-61.
 26. Bhunia, A.; Bhattacharjya, S.; Chatterjee, S., Applications of saturation transfer difference NMR in biological systems. *Drug Discov Today* **2012**, *17* (9-10), 505-13.

Chapter 3

3. Targeted Inhibition of Amyloidogenesis Using A Non-Toxic, Serum Stable Strategically Designed Cyclic Peptide with Therapeutic Implications

This chapter has been adapted from the following publication:

Pariary, R., Ghosh, B., Bednarikova, Z., Varnava, K.G., Ratha, B.N., Raha, S., Bhattacharyya, D., Gazova, Z., Sarojini, V., Mandal, A.K. and Bhunia, A., 2020. Targeted inhibition of amyloidogenesis using a non-toxic, serum stable strategically designed cyclic peptide with therapeutic implications. *Biochimica et Biophysica Acta (BBA)-Proteins and Proteomics*, 1868(5), p.140378.

3.1. Introduction

Protein amyloidogenesis plays a crucial role in the pathophysiology of several human diseases, including neurodegenerative disorders such as Alzheimer's and Parkinson's as well as metabolic disorders like Diabetes ¹. The association of amyloidogenesis with the devastating pathological implications has led to an increase in developing inhibitors against this aggregation. Scientific advancements using in vitro, in vivo, and in silico strategies have added to our gradual understanding of the system ². However, success in implementing such approaches has been limited, in part due to the complexity of the aggregation process and also in part because of the fact that the mechanisms and targets of the inhibitors are poorly defined.

Over the years, several amyloidogenic model proteins have been identified, such as insulin, amyloid β , α -synuclein, etc. underlying some of the most devastating disorders (including Type-II Diabetes, Alzheimer's and Parkinson's Disease). The ease of availability of insulin over other amyloidogenic proteins has attracted several research groups to use it as a model protein for understanding amyloidogenesis ³. Insulin, apart from being an excellent amyloid model, is widely known for its significant pharmaceutical importance. However, owing to its innate aggregation propensity, insulin forms amyloid intermediates during its commercial production, formulation, transportation, and storage ⁴. Furthermore, insulin has been shown to form amyloid deposits at the site of administration ⁵, mostly due to a membrane-induced amyloidogenic attribute. Such deposits

have often been referred to as “insulin ball,^{5a, 5e}” which not only complicates the diagnosis of systemic amyloidosis in diabetes but also reduces insulin bioavailability and hence raises treatment costs^{5a, 5c}. In fact, biomembranes have been found to play a crucial role in modulating the overall aggregation propensity of several known amyloidogenic proteins at the lipid interface, thus adding further complexities to the system⁶. Though the adoption of next-generation needle free drug delivery can be a solution to this problem, it requires liposome-based drug delivery formulations⁷.

Alternatively, the inhibition of the nucleating intermediates has been gaining interest as a particularly attractive therapeutic target in insulin and other amyloidogenic pathogenesis. Several researchers have been focusing on the development of biocompatible alternatives that would specifically inhibit the target species modulating systemic amyloidogenesis. However, their mechanism of action and the underlying side effects has remained elusive owing to the limited knowledge of the amyloidogenic intermediates. In this context, small peptides and peptidomimetics are much valued aggregation inhibitors. Specifically, small peptides are effective in delaying fibrillation either by preventing the unfolding of native protein conformations or by interacting with the partially folded intermediates through covalent or non-covalent interactions⁸. In our previous study, we have reported a small peptide, KR7 (KPWWPRR-NH₂), designed from an antimicrobial peptide, indolicidin, to be particularly potential in targeting insulin fibrillation *in vitro*⁹. In this present study, we have modified the original peptide systematically to enhance its therapeutic potential. We have introduced Cys residues either before or after the “PWWP motif” resulting in two linear peptides, KCR7 (KCPWWPRR-NH₂) and KR7C (KPWWPCRR-NH₂) along with a cyclic peptide KR7CC (KCPWWPCRR-NH₂) with a disulfide bond between the two Cys residues (Scheme 3.1 and Appendix 3, Figures S3.1A-B, Table S3.1). Our studies including various low-resolution spectroscopic tools in conjunction with high-resolution microscopy enabled us to gain mechanistic insights into the functional interface of inhibiting bovine insulin (BI) aggregation. Furthermore, high-resolution nuclear magnetic resonance (NMR) spectroscopy was employed to characterize the epitope of inhibitory action at atomic resolution.

Peptide	Sequence
KR7	: KPWWPRR-NH ₂
KCR7	: KCPWWPRR-NH ₂
KR7C	: KPWWPCRR-NH ₂
KR7CC	: KCPWWPCRR-NH ₂

Scheme 3.1. The sequence of KR7-series peptides: KR7, KCR7, KR7C and KR7CC.

In accordance with the previous reports on cyclic peptides ¹⁰, KR7CC displayed superior activity in inhibiting the self-assembly of aggregation-prone sequences possibly due to its rigid conformation. In comparison to linear peptides, rigid cyclic peptides are known to help in reducing the randomness, thereby diminishing the entropy of the peptides upon binding with the targets ^{10b}. The structural rigidity imparts a specific orientation, which facilitates enhanced binding towards target molecules. It has also been reported that cyclic peptides have better penetrating capability into the cell membranes ^{10c}. Our results show that KR7CC not only has higher activity in comparison to other peptides against insulin fibrillation but also prevents the fibril formation and assists in arresting the non-toxic intermediates. Biophysical studies indicated a KR7CC-mediated reduction in the membrane-disruptive activity of insulin amyloids. The present study confirmed KR7CC to be a serum stable, non-toxic therapeutic alternative that effectively checks the insulin-imparted cytotoxicity in vitro as well as in pancreatic islet cells.

3.2. Experimental Methods

3.2.1. Chemicals

Bovine insulin (BI) from bovine pancreas was purchased from Sigma Aldrich Co. (St. Louis, USA). The KR7, KCR7, KR7C, KR7CC peptides were obtained from GL Biochem (Sanghai, China). HPLC and mass spectral (electrospray ionization-MS) analysis were confirmed that KR7-series peptides were >95% pure. 1,2-Dioleoyl-sn-glycero-3-phosphocholine (DOPC) and Cholesterol were bought from Avanti Polar Lipids Inc. (AL, USA). The highest analytical grade solvents and reagents were used directly without further purification.

3.2.2. *Synthesis of KR7CC Peptide*

The peptides were also manually synthesized on Tentagel resin on 0.2 mmol scales and purified following the SPPS protocol ¹¹ in university of Auckland, New Zealand. Excess of each Fmoc-amino acid (four-fold) and 3.9 equivalents of HCTU as coupling reagent was used along with DIPEA as the base. The Fmoc deprotection mixture was a solution of 20% piperidine in DMF. The disulphide bridge formation was performed on resin in the presence of iodine. For this reason Cys(Acm)Fmoc was used during the synthesis of the linear peptide. Once the elongation of the sequence was finished deprotection of the Acm group, and concomitant formation of the disulphide bridge were done in the presence of 10 equivalents of iodine in DMF: H₂O (4:1) for 1 h following standard procedures ¹². The resin was washed several times with DMF, isopropanol and 1% ascorbic acid prior to cleavage from the resin using TFA–TIS–H₂O–EDDT: 94:1:2.5:2.5 v/v. The cleavage mixture was evaporated under nitrogen, and then cold diethyl ether was added to precipitate the crude peptide. This was subjected to centrifugation, following which the resultant pellet was dissolved in a mixture of water and acetonitrile before lyophilization to recover the crude peptide.

3.2.3. *HPLC and Mass Spectrometry*

RP-HPLC was performed on a Thermo Scientific Dionex VWD 3x00 system using a Phenomenex Luna 5 µm C18 100 Å (250 mm × 10 mm) column which was used to purify the KR7CC peptide using 0.1% TFA in water as solvent A and 0.1% TFA and 0.09% water in 99% acetonitrile as solvent B at a flow rate of 10 ml per minute. The peptide was eluted using a linear gradient of 20–60% of solvent B over 25–30 min with UV detection at 214 nm. The purity was confirmed to be 98.5% as determined by analytical RP-HPLC performed using a Phenomenex Luna 5 µm C18 100 Å (250 mm × 4.6 mm) column using the same solvent system as above, at a flow rate of 1 ml per minute (Appendix 3, Figure S3.1A, Table S3.1). Identity of the peptide was established using ESI-MS recorded on a Bruker micrOTOFQ mass spectrometer (Appendix 3, Figure S3.1B and Table S3.1).

3.2.4. *Preparation of the Large unilamellar vesicles (LUVs)*

DOPC/Cholesterol (6:4) lipids were dissolved in a chloroform solution, followed by evaporation of all solvents under a stream of nitrogen (N₂) gas flow and lyophilized the lipid film overnight.

The required quantity of 10 mM sodium phosphate buffer (pH 7.4), 100 mM NaCl was added to re-hydrated lipid film and vortexed for few minutes at 4 °C until lipids were completely dissolved. This lipids solution underwent by 3 freeze-thaw cycles to make homogeneous MLV (Multi lamellar vesicle). LUVs were prepared by micro-extrusion of MLV through a 100 nm filter membrane 21 times above the transition temperature of the corresponding lipid mixtures ¹³. 6-Carboxyfluorescein (6-CF) entrapped LUVs were prepared at 2 mg/ml in a similar manner, however rehydrated with a 6-carboxyfluorescein solution. The size of LUVs was measured by dynamic light scattering (DLS) before and after incubation at 335 K to confirm their thermal stability using Zetasizer Nano S (Malvern Instruments).

3.2.5. *Insulin Fibrillation Kinetics by ThT Assay.*

Thioflavin T (ThT) dye has been used for amyloid aggregation kinetics to probe the presence of cross- β -sheet structures in amyloids ¹⁴. For this experiment, insulin was dissolved in 50 mM citrate phosphate buffer at pH 2.6 in the presence of 100 mM NaCl ^{3b,9}. The concentration of insulin with an extinction coefficient of 0.91 mg/ml for 1 OD at 276 nm in the Nanodrop instrument (Thermo Fisher Scientific) ¹⁵. The molar extinction coefficient of $36,000\text{M}^{-1}\text{cm}^{-1}$ was used to determine the concentration of thioflavin T (ThT) solution at UV absorbance at 412 nm by dissolving in Milli-Q water. KR7-series peptides were dissolved in same 50 mM citrate phosphate buffer at a concentration of 350 μM . For ThT assay, 2 mg/ml Insulin stock was prepared in the presence and absence of equimolar KR7-series peptides and incubated at 335 K in a water bath. Insulin and peptide were mixed in 1:1 molar ratio in the stock solution. Aliquots of the samples were taken from it at regular time intervals (30 min). Aliquots were diluted by adding 10 mM sodium phosphate buffer (pH 7.4) along with 100mM NaCl in presence of 10 μM ThT solution. ThT fluorescence assay was measured by using a quartz cuvette with path length of 0.1 cm in the spectrofluorometer (JASCO, FX-8500 and HITACHI F-7000 FL) where the excitation was set at 440 nm and an emission maximum was measured around 482 nm to monitor the kinetics of insulin fibrillation. The fluorescence intensity data at 482 nm at respective time points were plotted against time and the curve was fitted by Boltzmann equation (a nonlinear sigmoidal function), i.e. given by Equation (1)

$$Y = A_2 + \left[\frac{A_2 - A_1}{1 + e^{(t - t_{1/2})/\tau}} \right] \dots\dots\dots(1)$$

Here, A_1 is the initial fluorescence, A_2 is the maximum fluorescence, $t_{1/2}$ stands for the time where the fluorescence has reached to half of the maximum value, and $1/\tau$ is the apparent rate constant of fibril growth and lag time approximated to $t_{1/2}-2\tau$.

3.2.6. Seeding experiments using ThT Assay

Mature insulin fibrils and KR7CC-induced insulin fibrillar species were used to seed insulin aggregation kinetics. 5% of either fibrillar seeds were added at 0 min and the resultant aggregation kinetics of insulin was recorded using ThT fluorescence emission as described previously..

3.2.7. ThT kinetics in the presence of membrane

Insulin was dissolved in aqueous HCl solution (pH 1.9) at a 2 mg/ml final concentration ^{13a}. Four different set of experiments were prepared to investigate the insulin-membrane mediated aggregation kinetics. The first set of experiment was done with 2 mg/ml insulin solution incubated at 335 K in a water bath. In second set of experiment, LUVs were added at a molar ratio of 1:7 to that of insulin (pH was adjusted to 1.9) and incubated at 335 K. In third and fourth set of experiments, equimolar KR7 and/or KR7CC peptides were treated with insulin (2 mg/ ml) in the presence of LUVs (LUVs/ insulin =1:7) and the total solution was incubated at 335 K. The aliquots of respective time points were taken into in 10 mM phosphate buffer (pH 7.4) with 100 mM NaCl, and fluorescence intensity was measured as described above.

3.2.8. Dye Leakage Fluorescence Assay

The fractional release of dye entrapped inside vesicles used to determine peptide-induced membrane permeability. 6:4 DOPC/Cholesterol vesicles were prepared with 6- carboxyfluorescein as describe above LUVs preparation. After extrusion, dye-filled vesicles were separated on a Centricon column as per the protocol supplied by the manufacturer to remove the free 6-CF, which was not entrapped in the vesicles. 100 μ M dye vesicles were used for every dye leakage experiments ^{13a}. The excitation wave-length was set at 495 nm and the emission spectra at around 521 nm. Insulin aggregates (20 μ M) in the presence or absence of KR7CC (1:1) were added to observe the membrane permeability. LUVs were treated with 0.1% Triton-X to disrupt the vesicles for the maximum fluorescence measurement. The amount of dye leakage was calculated by equation-2.

$$\text{The amount of dye leakage} = \left(\frac{F - F_0}{F_T - F_0} \right) \times 100 \dots\dots\dots(2)$$

Where, F is the measured fluorescence intensity of LUVs after addition of insulin sample with or without equimolar KR7CC, F_0 is the fluorescence intensity of only LUVs and F_T is the maximum fluorescence intensity detected after treatment with Triton X100.

3.2.9. Circular dichroism (CD) spectroscopy

Circular dichroism (CD) spectra were applied to characterize conformational changes of insulin in presence and absence of KR7CC peptide at 1:1 molar ratio using a JASCO J-815 spectropolarimeter. 10 mM sodium phosphate buffer (pH 7.4) with 100mM NaF solution was added to dilute the aliquots of 2 mg/ml insulin stock solution at different incubation times. All spectra were recorded between 200 nm to 260 nm at 298K using 0.2 cm path length quartz cuvette with a scanning speed of 100 nm/min. Each CD spectrum was obtained by an accumulation of three subsequent scans. A control spectrum of only the KR7CC was also recorded to eliminate the contribution of KR7CC in the CD spectrum.

3.2.10. Raman spectroscopy

2 mg/ml insulin was incubated at 335 K in 20% acetic acid buffer (pH 1.9) with and without KR7CC (1:1) peptide. 20% acetic acid buffer was used to avoid the interference of citrate phosphate buffer in the Raman's spectra. 30 μ l of insulin at 0 h (non-fibrils) and 72 h (matured-fibrils) of incubation were placed on fresh and clean aluminium foil mounted on a glass slide and air-dried¹⁶. The spectra were collected in backscattering geometry using a LabRam HR -Jobin Yvon (Horiba, Kyoto, Japan) spectrometer equipped with a Peltier-cooled CCD. A 785 nm diode LASER was focused on the sample for excitation using a 50x objective¹⁷.

3.2.11. Fluorescence Anisotropy

Tryptophan fluorescence of 8 μ M KR7CC was measured in 50 mM citrate phosphate buffer with 100 mM NaCl medium (pH 2.6) using a Hitachi F-7000 FL spectrometer with the addition of insulin from 1 μ M to 25 μ M at room temperature. After each titration with insulin, the maximum emission was recorded upon excitation at 295 nm. The fluorescence anisotropy values (A) were calculated as:

$$A = \frac{(I_{VV} - G \times I_{VH})}{(I_{VV} + 2 \times G \times I_{VH})} \dots \dots \dots (3)$$

Here, I_{VV} and I_{VH} are the vertically and horizontally polarized components corresponding to the tryptophan fluorescence-emission intensities obtained with the excitation by vertically polarized light at 295 nm. G is the sensitivity factor for the instrument. The anisotropy values were plotted against insulin concentrations for a particular time point and fitted using the one site binding model equation for the calculation of apparent dissociation constant (K_D) of the peptide-protein interaction assuming a 1:1 binding stoichiometry or equivalent and independent binding sites.

$$y = y_0 + B_{max} \left(\frac{x}{K_D + x} \right) \dots \dots \dots (4)$$

Here, y is the measured anisotropy value, y_0 is the anisotropy value for KR7CC alone, x is the concentration of added insulin (μM), B_{max} is the maximum value of anisotropy during the binding process, and K_D is the dissociation constant of insulin-KR7CC complex.

The K_D value was used to calculate the Gibbs free energy (ΔG) of the corresponding time points using the equation (5).

$$\Delta G = RT \ln[K_D] \dots \dots \dots (5)$$

3.2.12. Confocal Study

The ThT samples were used to prepare confocal slides, in parallel. 10 μl aliquots of insulin and insulin+KR7CC samples collected at different incubation time points were placed onto clean glass slides and dried inside a laminar air-flow at room temperature in the absence of light. DPX was used as the mounting media. ThT fluorescence was observed in a Leica TCS SP8 confocal microscope using the 405 nm bandpass filter.

3.2.13. Atomic Force Microscopy (AFM)

AFM sample preparation was done using 350 μM of the fibrillar sample for each variant in 50 mM citrate phosphate buffer in the presence of 100 mM NaCl (pH 2.56) with and without KR7-series (1:1) peptide. The samples were cast on a mica surface and adsorbed for 5 min. Thereafter, the mica surface was washed with ultra-pure water and dried under N_2 gas. The structure of untreated BI fibrils and those treated with equivalent concentration (1:1) of KR7CC peptide was studied using Veeco diInnova microscope in tapping mode and the SNL - 10 tip (Bruker, USA). The image resolution was 1024 x 1024 pixels with a scan rate of 0.5 kHz.

3.2.14. NMR experiment

NMR spectra were recorded at 298 K or 335 K using either the Bruker AVANCE III 500 MHz (equipped with SMART probe) or the 700 MHz (equipped with QCI Cryoprobe) spectrometer. The NMR data so obtained were processed using the Topspin v4.0.6 software (Bruker).

For one dimensional ^1H NMR spectra, insulin samples in absence and presence of equimolar KR7CC (1:1) were dissolved in 50 mM citrate-phosphate buffer (pH 2.6) with 100 mM NaCl, 10% D_2O at 335 K temperature and recorded on Bruker Avance III 500 MHz NMR spectrometer. Here, high temperature (335 K) was maintained for NMR experiments to follow the aggregation dynamics. The intensities of the aromatic and amide region peaks were calculated at different time points. In case of insulin, the first stage and last stage of data were fitted with exponential (dotted line) and Boltzmann sigmoidal equation (solid line) respectively whereas, in the presence of KR7CC, both the stages were fitted using the exponential equation. To confirm the KR7CC-insulin interaction by utilizing one dimensional ^1H NMR spectra, 50 μM KR7CC was titrated against 5 μM and 25 μM insulin.

All saturation transfer difference (STD) experiments were performed at 298 K using standard STD pulse sequences with the WATERGATE 3-9-19 water suppression¹⁸. 1 mM KR7CC peptide was dissolved in water at pH 2.6 (pH was adjusted by HCl) and lyophilized overnight. Finally, the lyophilized sample was resuspended in an equal volume of D_2O and 5 μl insulin fibril was added. 1D STD experiment was carried out using a train of 40 selective Gaussian-shaped pulses (49 ms each) in an interval of 1 ms to saturate protein resonance for a total of 2 s saturation time. The protein was irradiated at -1 ppm (on-resonance) and at 40 ppm (off-resonance). Subtraction of the two spectra (on resonance-off resonance) by utilizing the phase cycling method yields signals appearing due to saturation transfer from protein to ligand. The total number of scans for one-dimensional reference and STD NMR spectra were carried out with 4096 and 8192, respectively, with 16 dummy scans and typically 12 ppm sweep width. The sample containing only KR7CC peptide was subjected to act as the control for one-dimensional STD NMR.

Zinc-free bovine pancreatic insulin sample for TOCSY and NOESY experiments were prepared by the addition of EDTA followed by extensive overnight dialysis at 4 °C followed by lyophilization to prevent the stable hexamer conformational uptake by insulin. As insulin remained in the monomeric form in the acetic acid buffer, all the samples were prepared at a concentration of 350 μM in 20% acetic acid- d_4 , 70% H_2O and 10% D_2O at pH 1.9. Mixing times of 60 ms for

two dimensional TOCSY and 200 ms for NOESY were used respectively with a spectral width of 12 ppm at 298 K in presence and absence of KR7CC peptide using the 700 MHz NMR spectrometer. All two-dimensional TOCSY and NOESY experiments with 64 scans were recorded in phase-sensitive mode (TPPI) with 512 increments in t_1 and 2048 data points in t_2 along with selective excitation of the water resonance (WATERGATE).

Two-dimensional (2D) trNOESY (transfer-NOESY) experiments of 1 mM KR7CC with the insulin fibril at a molar ratio of 1:20 (insulin:KR7CC) were carried out at 25°C in 20% acetic acid- d_4 , 70% water, and 10% D_2O (pH 1.9) buffer using Bruker Avance III 500 MHz NMR spectrometer. 200 ms mixing time was recorded with 512 increments in t_1 and 2048 data points in t_2 along with 12 ppm spectral width in both dimensions. After 16 dummy scans, 120 scans were recorded per t_1 increment. After zero-filling in t_1 , TOCSY and trNOESY spectra were processed using 4K (t_2) \times 1K (t_1) data matrices.

3.2.15. Cell culture and cell viability assay

Rin5F (Rat pancreatic islet B cells) cells were cultured in Roswell Park Memorial Institute (RPMI) medium supplemented with 10 % fetal bovine serum (FBS), 150 μ g/ml penicillin/streptomycin, 50 μ g/ml gentamycin, and 2.5 μ g/ml amphotericin B at 37 °C in 5% CO_2 . Cells were counted using a hemocytometer. 5×10^3 cells were seeded per well in a 96 well plate. After 24 h of seeding, the cells were treated with 50 μ M insulin in the presence and/or absence of equimolar KR7CC peptide as described previously ^{3b}. Insulin samples were prepared by incubating 2 mg/ml insulin in HCl, 100 mM NaCl buffer (pH 2.0) at 335 K with and/ or without equimolar KR7CC. Sample aliquots were collected at regular time intervals (keeping the ThT experiments in mind). Percentage cell viability was determined using 3-(4,5-dimethylthiazol-2-yl)-2,5-diphenyltetrazolium bromide (MTT) ⁹. A microplate reader (MultiscanGo, Thermo Scientific) was used to read the plates at 570 nm. Independent experimental data were obtained in triplicates and the Standard Deviations were calculated and represented as double-sided error bars. The significance was calculated by Mann-Whitney test One-tailed.

3.2.16. Serum Stability Assay

Jenssen and Aspomo method (with slight modifications) was used to perform the serum stability assay ¹⁹. After adding 100 mg/ml final concentration of KR7CC in 1 ml of RPMI media 1640 supplemented with 25% (v/v) fetal bovine serum, the solution was incubated at 37 °C for 15 min.

100 ml of the reaction mixture was collected at respective time points and mixed with 400 ml of 96% ethanol for precipitation of serum proteases. The precipitated solution was cooled at 4 °C for 15 min and was centrifuged at 17,000×g for 2 min to pellet down the precipitated serum protein. The collected supernatants were then analyzed using LC-20AT reverse-phase HPLC system (SHIMADZU, Japan) on a 250×10 mm (pore size 100 Å, particle size 5 µm) Phenomenix C18 column with the gradient elution from 0.1% TFA in 100% acetonitrile to 0.1% TFA in water at room temperature along with 3 ml/min flow rate. The amount of existing non-degradable peptide was integrated at 220 nm. The area under the peak was calculated using SPINCHROME CFR software. The percent of serum stable peptide after each time point was calculated using equation no. 6.

$$\% \text{ remaining} = (\text{peak area of intensity at the respective time} / \text{intensity of free peptide}) \times 100 \dots \dots \dots (6)$$

3.3. Results and Discussion

3.3.1. The KR7-series of peptides modulate amyloid aggregation kinetics *in vitro*, resulting in effective inhibition

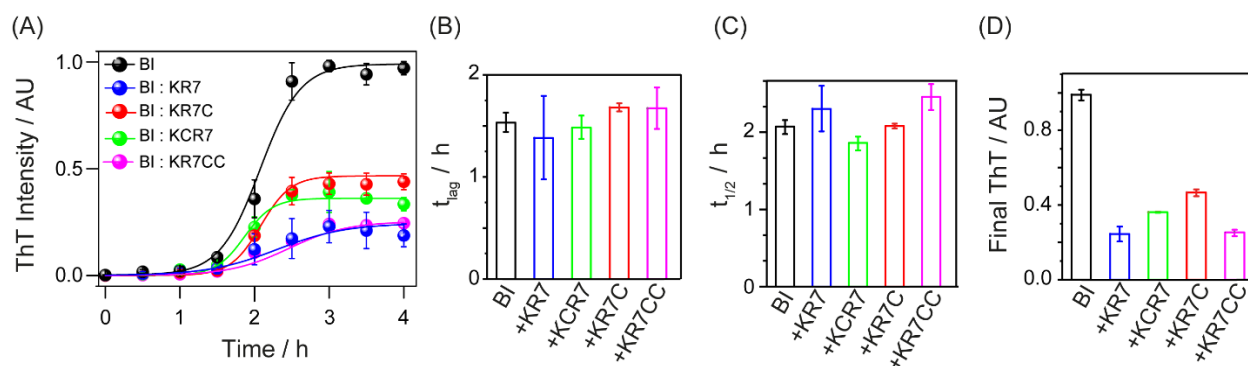


Figure 3.1. The designed peptides modulate aggregation kinetics *in vitro*. (A) ThT aggregation kinetics of 2 mg/ml bovine insulin in 50 mM citrate phosphate buffer with 100 mM NaCl (pH 2.6) at 335 K; control sample- insulin alone depicted in black and sample treated with 1 mole equivalent KR7 (blue), KR7C (red), KCR7 (green) and KR7CC (pink). (B) Bar plots of observed t_{lag} , (C) $t_{1/2}$ and (D) the final fibril mass indirectly indicated by ThT fluorescence emission intensity. Error bars represent standard deviation for three independent experiments.

The kinetics of amyloid fibril formation follows a nucleation dependent pathway, initiating from non-native monomers to meta-stable oligomeric species followed by protofibril formation and

finally, the mature fibrils ^{3e}. An in-depth understanding of the amyloidogenic pathways and toxic intermediate nucleating steps enables effective screening of inhibitors for a targeted therapeutic approach against amyloidogenesis. For this purpose, the external fluorogenic indicator, Thioflavin T (ThT) was used to monitor the fibrillation kinetics of insulin in the presence and absence of the designed peptides. ThT is a specific dye and gives intense fluorescence upon binding to the hydrophobic grooves of β -sheet fibrils ^{3f}. Further analyses of the intensity profiles as a function of time allows quantitative characterization of the aggregation kinetics in *in vitro* (Table 3.1, Figure 3.1). As shown previously for the parent peptide, treatment with our second-generation KCR7, KR7C, and KR7CC resulted in a significant reduction of the ThT fluorescence intensity in comparison to insulin alone. This clearly illustrated a quantitative decrease in fibril formation in presence of the inhibitors (Figures 3.1A-D). The linear peptides, KR7C, and KCR7 peptides reduced the total amount of fibril formation by 50% and 60%, respectively without significant modulation of the lag phase (t_{lag}) and the duration to reach the half maximal ($t_{1/2}$) ThT fluorescence

Table 3.1. Parameters obtained from ThT fluorescence kinetic assay.

Sample	Lag time (t_{lag}) /min	Half time ($t_{1/2}$) /min
Insulin	91.94 \pm 5.84	124.39 \pm 5.07
Insulin: KR7 (1:1)	82.88 \pm 24.76	138.19 \pm 17.96
Insulin: KCR7 (1:1)	89.01 \pm 7.02	111.85 \pm 4.82
Insulin: KR7C (1:1)	100.88 \pm 2.47	125.02 \pm 1.77
Insulin: KR7CC (1:1)	100.35 \pm 12.34	147.48 \pm 10.00

intensity (Table 3.1; Figures 3.1B-D). Interestingly, the cyclic KR7CC, showed up to ~77% reduction (comparable to the parent, KR7), in the fibrillary species at saturation with $t_{1/2}$ varying from 124.4 \pm 5.0 min for insulin alone to ~147.5 \pm 10.0 min for KR7CC (Table 3.1, Figures 3.1B-D). Hence, clearly depicting the enhanced activity of the cyclic peptide over the other peptides in the series. Thus, KR7CC served as the lead inhibitory peptide candidate against insulin aggregation. Therefore, the remaining part of this study focused majorly on the inhibitory effects of KR7CC.

Since some previous studies with ThT had reported several drawbacks and limitations of the probe ⁴, parallely, we adopted high-resolution NMR to observe the insulin-fibrillation inhibition

by KR7CC under similar conditions. With increasing the incubation time, the insulin solution resulted in a significant line broadening in the one-dimensional proton NMR spectra of the protein (Figures 3.2A). It is noteworthy to mention that the line broadening effect in the ^1H NMR spectra can be correlated to the formation of higher molecular weight species such as the protofibrillar forms or the fibrils^{5a, 20}. Strikingly, the decay of the aromatic and amide protons of insulin from the one-dimensional ^1H NMR spectra was almost similar to the ThT assay (highlighted region in Figures 3.2). Collectively, two distinct phase profiles were obtained that implied (i) a non-amyloid intermediate formation to be the nucleation step, (ii) followed by the fiber elongation step. Interestingly, the addition of KR7CC did not alter the nucleation phase ($t_i = 33.5 \pm 11.0$ min for

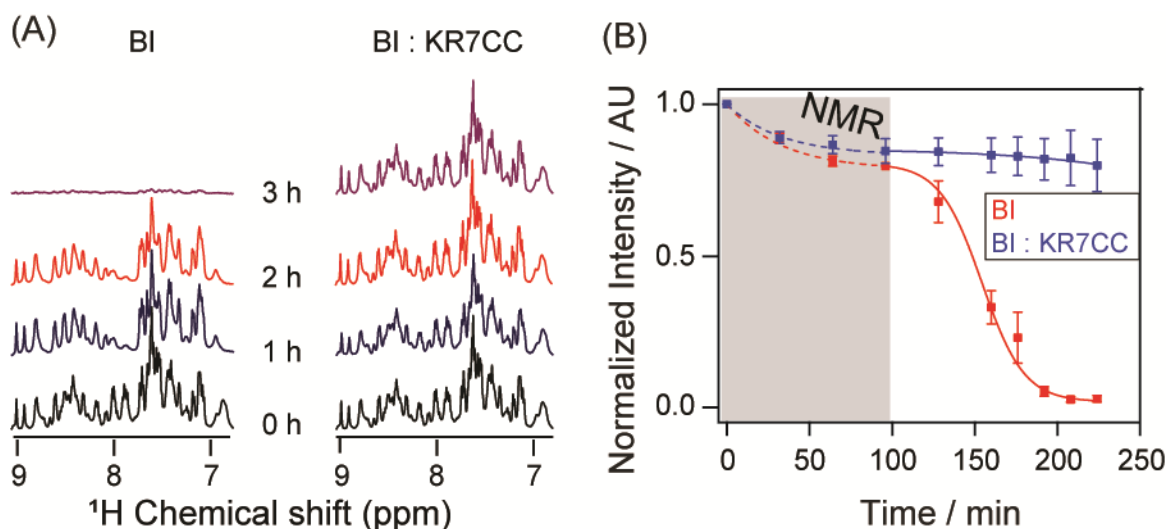


Figure 3.2. (A) One-dimensional ^1H NMR of insulin showing the aromatic and amide regions of insulin in the absence (left) and presence (right) of KR7CC at 1:1 molar ratio. NMR experiments were performed using 2 mg/ml insulin at 335 K in 50 mM citrate phosphate buffer with 100 mM NaCl at pH 2.6. (B) The NMR signal intensity with time was plotted for time dependent aggregation kinetics.

insulin and $t_{i+KR7CC} = 32.5 \pm 10.0$ min for insulin treated with KR7CC), suggesting a slow transformation of globular insulin units into larger oligomers (Figure 3.2B). Immediately after this, a rapid exponential decay was obtained, signifying the conversion of the oligomers to protofibrils and mature fibrils. This, however, went undetected in NMR owing to a slower tumbling rate, longer correlation time and rapid T_2 relaxation (Figure 3.2B). Taken together, KR7CC considerably inhibits the fiber elongation (elongation time for insulin $t_{In} = 12.8 \pm 2.2$ min and with KR7CC, $t_{In+KR7CC} = 65.1 \pm 26.0$ min) phase, modulating the intermediate species and hence insulin

aggregation *in vitro*. Interestingly, the unchanged nucleation phase and a delay in the fiber elongation phase suggested an interaction with the oligomeric intermediates, causing hindrance in the formation of the protofibrils or the matured fibrillary forms.

3.3.2. KR7CC arrests and stabilizes the aggregating intermediates in off-pathway aggregation kinetics

Amyloid aggregation is closely associated with global conformational changes in the protein's secondary structure. This inherent feature of amyloids can be exploited to gain structural in-sights into the intermediates. Insulin is mainly α -helical in the native conformation, which undergoes a conformational transition to β -sheet during fibril formation²¹. To attain a clear discernment of the

Table 3.2. Raman spectra analysis.

	Amide I band Width (cm ⁻¹)	Time (h)	α -helix			Organized β -sheet			Loose β -Strand, PPII and others			Undefined		
			Peak (cm ⁻¹)	Width (cm ⁻¹)	*Area %	Peak (cm ⁻¹)	Width (cm ⁻¹)	*Area %	Peak (cm ⁻¹)	Width (cm ⁻¹)	*Area %	Peak (cm ⁻¹)	Width (cm ⁻¹)	*Area %
BI	46.2	0	1657	20	50	1673	19.8	13	1684	24.5	25	1644	24.5	12
	31	72	1659	19.6	26	1671	22.8	62	1683	20.6	6	1647	20.7	6
BI:KR7CC (1:1)	46.4	0	1661	24	52	1674	19.6	14	1684	24.5	24	1644	21	10
	40	72	1663	24.1	47	1673	19.5	27	1685	24.6	15	1644	23	11

effect of KR7CC on the conformational conversion of insulin upon aggregation, far-UV CD spectroscopy was performed, which is a very useful method to observe the secondary structural changes typically associated with amyloidogenesis. Aliquots were drawn at regular intervals from fibrillating insulin mixture and studied for any global change in the secondary structure of the protein. Though there is a conformational transition from α -helical state to β -sheet conformation for insulin alone (Figure 3.3A), in presence of KR7CC it retained the α -helical conformation till 3 h of incubation, indicating an excellent agreement with the observed inhibition process (Figure 3.3B). The quantification of structural change from CD spectra can introduce errors because of the

scattering from large aggregates; hence Raman spectroscopy was performed, which works on the principles of scattering. Of note, 20% acetic acid buffer (pH 1.9) was used for Raman spectroscopy

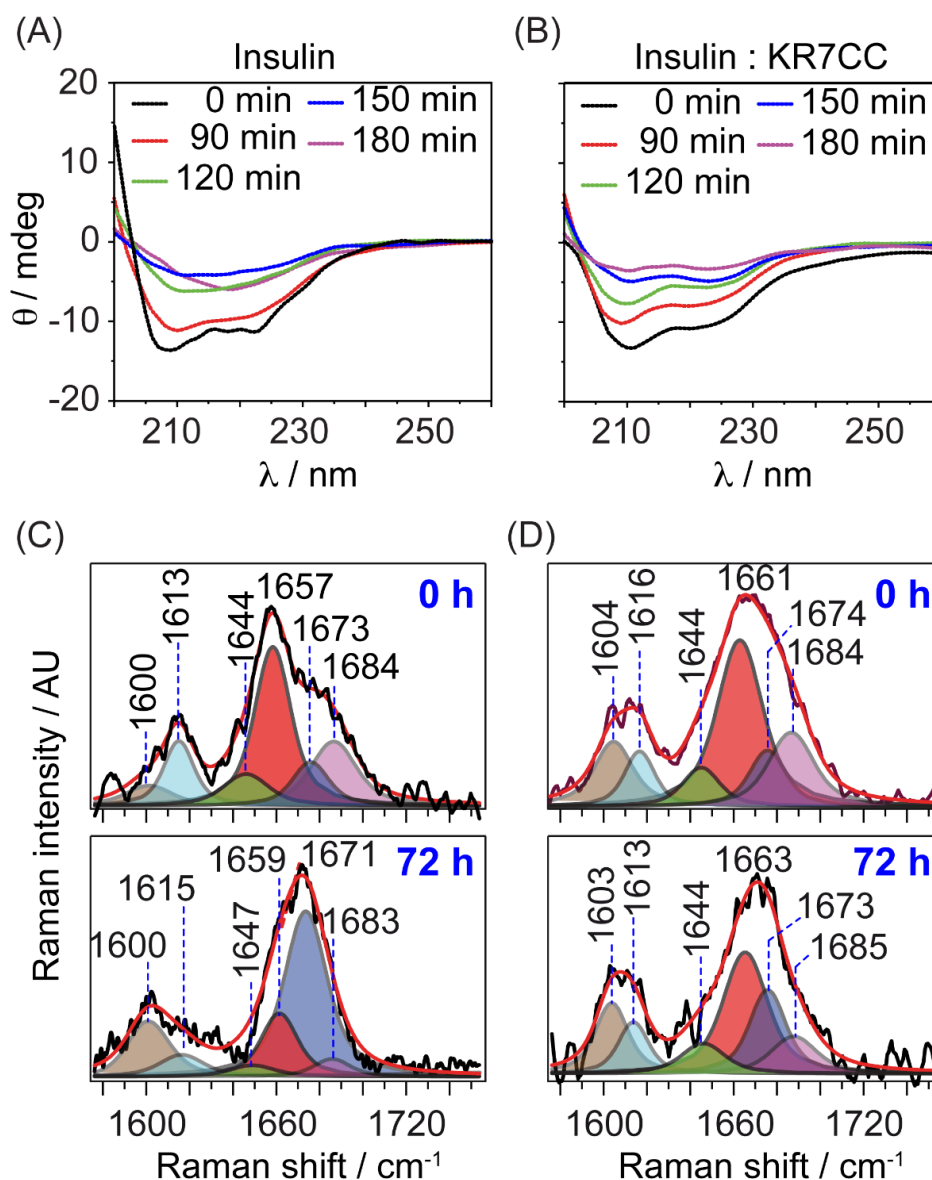


Figure 3.3. Inhibitory mechanism of KR7CC induces conformational changes in the insulin aggregation-intermediates. The conformational change in secondary structure observed by far UV CD spectra for (A) insulin alone and (B) in the presence of an equimolar concentration of KR7CC. (C-D) Raman spectra of insulin monomer (at 0 h) and fibril (at 72 h) represented in the frequency range of 1575–1750 cm^{-1} . Insulin was incubated in 20% acetic acid (pH 1.9) at 335 K in the absence (C) and presence of KR7CC (D).

to avoid the interference of citrate phosphate buffer in the Raman spectra. As previously reported, citrate phosphate buffer was slower the aggregation kinetics of insulin *in vitro*^{17, 22}. The spectral deconvolution of amide I region of Raman spectra can accurately predict the composite structural elements. The observed signature amide I region ($1575\text{--}1750\text{ cm}^{-1}$) for insulin is shown in Figures 3.3C and 3.3D. Table 3.2 contains the spectral component analysis results of characteristic Raman bands. The amide I bandwidth at half maxima (BWHM) was around 47 cm^{-1} , typical to α -helical conformation, both in the presence and absence of KR7CC. The spectral component analyses as per Dong et al^{3f}, and Maiti et al¹⁶, showed a nominal 2% increase in the α -helical content for

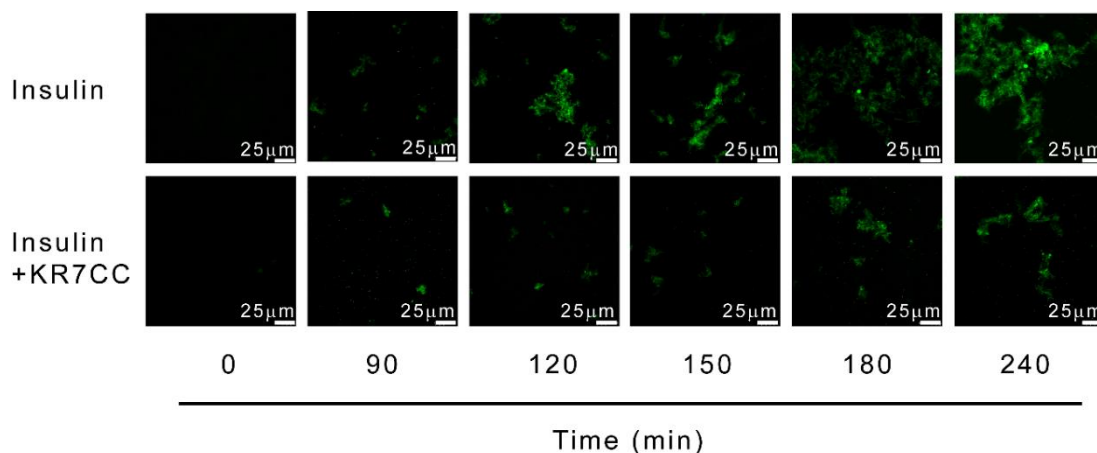


Figure 3.5. Morphological analysis of insulin amyloid aggregates in the presence and absence KR7CC peptide using confocal microscopy. 10 μl aliquots of the reaction mixture were collected at various stages of insulin (2 mg/ml) aggregation pathway with either in the presence or absence of KR7CC peptide. Scale is $25\mu\text{m}$, represented by the white bars.

insulin alone (1657 cm^{-1}) as opposed to the same in the presence of equimolar concentrations of KR7CC (1661 cm^{-1}), suggesting a structural stabilization of insulin in the presence of KR7CC. After 72 h of incubation in 20% acetic acid (pH 1.9), insulin alone showed 62% of β -sheet content (1671 cm^{-1}), while in the presence of KR7CC it was only 27% (1673 cm^{-1}) at the similar time point, justifying the structural stabilization of insulin oligomers in the presence of the inhibitor, KR7CC. In contrast, the unstructured component for insulin alone reduced to 6% from 12% while no such change was obtained in the presence of KR7CC after 72 h of incubation. Collectively, these data depict that KR7CC stabilizes insulin aggregates, retaining the main structural components for reasonably longer time periods, hence, affecting the overall aggregation kinetics. Furthermore, the KR7CC-induced fibrillar species propagate an alternative ‘off-pathway’

aggregation by delaying the aggregation kinetics, relative to the conventional insulin seeds (Figure 3.4).

3.3.3. The inhibitory action of KR7CC induces morphological changes in the resultant intermediates

The aggregating intermediates of insulin in the presence and absence of KR7CC were characterized using ThT-fluorescence based confocal microscopy. The confocal images (Figure 3.5) revealed an increase in size and density of the aggregating species upon increasing the incubation time, both in the presence and absence of KR7CC. However, the aggregates in the

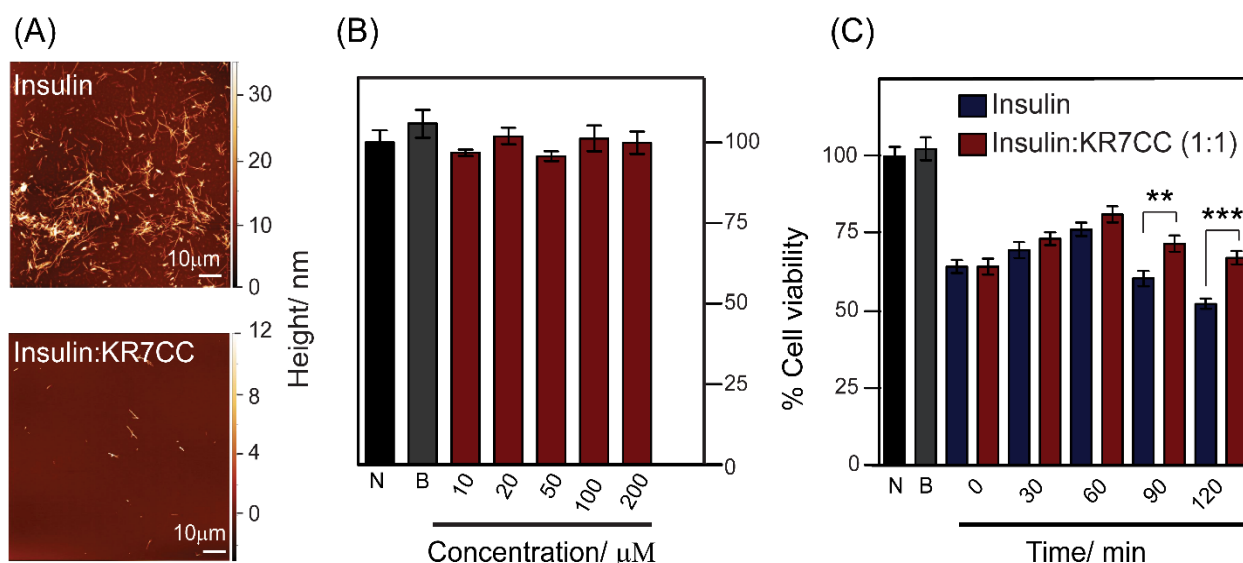


Figure 3.6. KR7CC treatment induces morphologically distinct conformers that have reduced cytotoxicity. (A) AFM images obtained for insulin fibrils alone and in the presence of equimolar concentrations of KR7CC (lower panel). (B) Percentage of viable Rin5F cells (pancreatic islet cell) upon treatment with different concentrations of KR7CC (10, 20, 50, 100, and 200 μM) studied by MTT reduction assay (here, 'N' represents the non-treated control cells, and 'B' for buffer- used as the negative control). (C) The cytotoxic effect of insulin samples in the presence or absence of equimolar KR7CC at the different incubation times (0, 30, 60, 90 and 120 mins). The bar represents Standard Deviations of three independent experiments. Significance was calculated by Mann-Whitney test One-tailed. $p=0.0053$ (**) for 90 min and $p<0.0001$ (***) for 120 min.

presence of KR7CC were apparently smaller in size. Atomic force microscopy (AFM) is a useful technique in characterizing the surface properties of materials and has a wide range of application in protein aggregation studies²³. High resolution AFM was, thus, employed to gain a clearer picture of the fibril morphologies. While aggregation of insulin in the absence of KR7CC displayed

the formation of dense, branched fibrils, treatment with equimolar concentration of KR7CC resulted in unbranched and short fibrillar mass (Figure 3.6A). Taken together, the microscopic studies further confirmed that KR7CC successfully inhibited insulin aggregation process through the effective prevention of the formation of long and dense fibrils.

3.3.4. The KR7CC-induced intermediates reduce the cytotoxicity of amyloid intermediates

Amyloid aggregates have an inherent cytotoxic property. Since KR7CC effectively inhibits the insulin fibrillation by arresting the oligomeric intermediates, it was expected to affect its functional attribute. To prove our hypothesis, we tried to detect the influence of the peptide on insulin-mediated cytotoxicity^{5b, 24}. The MTT (3-(4,5-dimethylthiazol-2-yl)-2,5-diphenyltetrazolium bromide) assay was performed to determine the viability of pancreatic islet cells, Rin5F, upon treatment with insulin in the absence and presence of KR7CC at different incubation time period. As a control, KR7CC was also treated at different concentration to Rin5F cell line. The cyclic

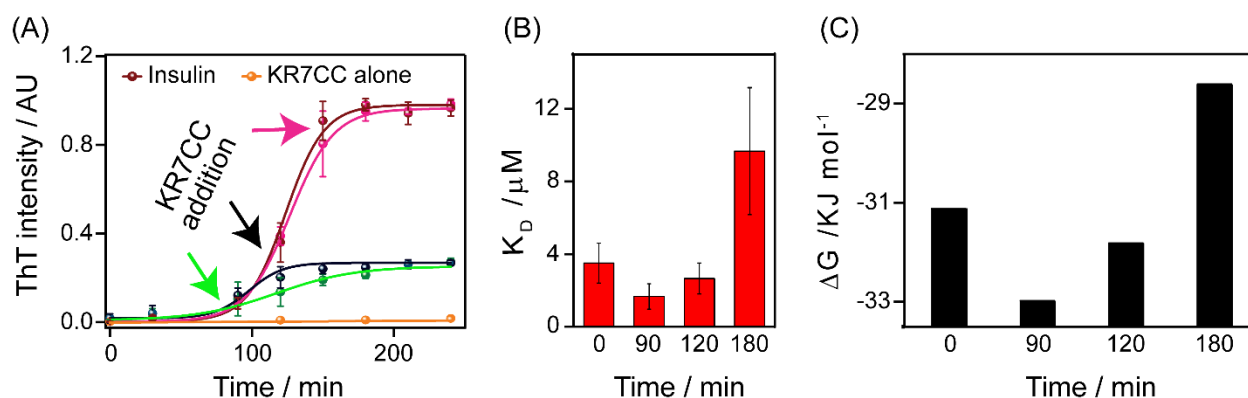


Figure 3.7. Probing the target stage for effective inhibitory action. (A) Effect of equimolar KR7CC addition at different time points of insulin fibrillation pathway (90, 120 and 150 min). KR7CC arrests fiber formation immediately after the addition at 90 and 120 min. (B) Comparison of the dissociation constant values (K_D) of 8 μM KR7CC with the addition of incubated insulin samples at indicated time periods (0, 90, 120 and 180 min). (C) Energy diagram corresponding to the calculated Gibbs free energy demonstrated the inhibition of the fiber growth phase in the presence of KR7CC.

peptide was found to be non-toxic against the Rin5F cells (Figure 3.6B). Close inspection suggested that for the insulin monomer (0 min) and intermediates collected at 30 and 60 min of incubation, toxicity was reduced marginally, in the presence of KR7CC. However, insulin protofibrils and fibrils at 90 min of incubation time period exhibited an amount of 40-45% cytotoxicity to Rin5F cells. In sharp contrast, the presence of equimolar KR7CC dramatically

reduced the cytotoxicity of the cells. Of note, 70% cells are viable even after 120 min of KR7CC incubation (Figure 3.6C). This result clearly demonstrated that the cyclic peptide KR7CC affected the protofibrillar intermediates, reducing its resultant cytotoxicity. Furthermore, the rescue of cytotoxicity exhibited by KR7CC peptide was found similar to that of KR7 (Appendix 3, Figure S3.2). Thus, these studies clearly demonstrated that the inhibitory mechanism of KR7CC is effective in recovering the functional cytotoxicity of the amyloidogenic species, hence serving as a potential inhibitor molecule.

3.3.5. Probing the binding affinity and effective target stage for therapeutic intervention.

Elucidating the binding kinetics of KR7CC with insulin is crucial to understand the aggregation pathway for effective inhibition of fibrillation. To determine the stage where KR7CC mainly acquired threshold energy to inhibit insulin fibrillation, ThT assay was performed for insulin aggregation in the presence of an equimolar concentration of KR7CC at different stages of fibrillation, e.g., 90 min, 120 min, and 150 min and (Figure 3.7A). Aggregation propensity of insulin was totally arrested after adding KR7CC either at the midpoint (120 min) or at the end of lag phase (90 min); whereas there was a partial decrease in ThT fluorescence intensity when KR7CC was introduced at the starting of saturation point (150 min) (Figure 3.7A). The extensive interaction between the KR7CC and insulin at the early stage of fiber elongation phase ascertains the insulin-KR7CC complex formation that motivated us to work out the binding constant (K_D) for insulin aggregates in the context of KR7CC. The K_D values for insulin aggregates at different lengths of KR7CC incubation were determined using fluorescence anisotropy experiments (Appendix 3, Figure S3.3). The K_D values for interaction at 0, 90, 120 and 180 min were 3.5 ± 1.1 , 1.6 ± 0.7 , 2.6 ± 0.8 and $9.7 \pm 3.5 \mu\text{M}$, respectively, suggesting an initial increase in binding affinity from the early monomers to the oligomeric intermediates followed by a drop in affinity for the higher aggregates (Figure 3.7B). This data further confirms that the affinity of the KR7CC to early oligomers is more than either monomeric insulin or insulin fibril. Later, NMR experiments (Figure 3.8) support that the opening of “L^{11B}VEALY^{16B}” is pre-requisite for binding to KR7CC, which is shown in next paragraph. Consequently, higher negative ΔG (Gibbs free energy) values were obtained at 90 min and 120 min, indicating possible interaction period of the peptide with insulin (Figure 3.7C).

3.3.6. Mapping the epitope of KR7CC and insulin interaction

The molecular interaction of insulin with KR7CC leads to structural and functional changes of the aggregating intermediates affecting the entire fibrillation propensity of the protein. Thus, to effectively probe the target species and gain mechanistic insight into the interface of inhibitory action, two-dimensional NMR spectroscopic techniques were employed. A high-resolution Nuclear Overhauser Effect Spectroscopy (NOESY) of the complex (insulin: KR7CC=1:1 molar ratio) confirms the atomic level interaction between KR7CC and insulin in 20% acetic acid- d_4 (pH 1.9), observed as line-broadening in both the A- and B-chains of insulin (Figure 3.8). In strongly acidic conditions, insulin is completely monomeric in nature and prevents the formation of insulin hexamers, probably because of electrostatic repulsion between protonated histidine residues and Zn^{2+} ²⁵. In native insulin monomer conformation, the N-terminal segments of the A- and B-chains are mostly disordered in nature²⁶, resulting in the exposure of the hydrophobic core. Upon aggregation, the C-terminal segment of B-chain (mainly B23-B26) containing the aromatic side chains of Phe24, Phe25, and Tyr26 is exposed to the solvent completely and available for aberrant protein-protein interactions²⁶. Interestingly, in the presence of KR7CC a line-broadening effect was observed for the N-terminal- His5-Leu6-Cys7 residues and the seven sequential aggregation prone Leu11-Val-Glu-Ala-Leu-Tyr-Leu17 residues in the insulin B chain (Figures 3.8A-B). This could be due to chemical exchange or relaxation during binding process in the NMR time scale. On this basis, we predicted that KR7CC has the potential to interfere with hydrophobic interactions necessary to suppress the aggregation process of insulin. Apart from the line-broadening effect, several NOE cross-peaks e.g., His5, Leu6, Cys7, Gly8, Ser9, Val12, Gly23, Phe24, Phe25 and Tyr26 in the B chain as well as few residues in the A chain, namely Val3, Cys7, Ala8, Cys20 and Arg21 exhibited remarkable chemical shift change, indicating a change in the immediate chemical environment upon KR7CC interaction (Figure 3.8C; Table S3.2).

Parallely, the line-broadening effect was obtained for KR7CC in the presence of insulin. Significant broadening was also observed for the indole ring protons of the tryptophan residues of KR7CC upon interaction with insulin (Appendix 3, Figure S3.4). This could be due to rapid chemical-exchange between bound and free states of KR7CC in the NMR time scales. Peak broadening and chemical shift change in NOESY experiment as well as broadening in the indole protons of KR7CC were in good agreement to confirm the binding phenomenon of insulin to

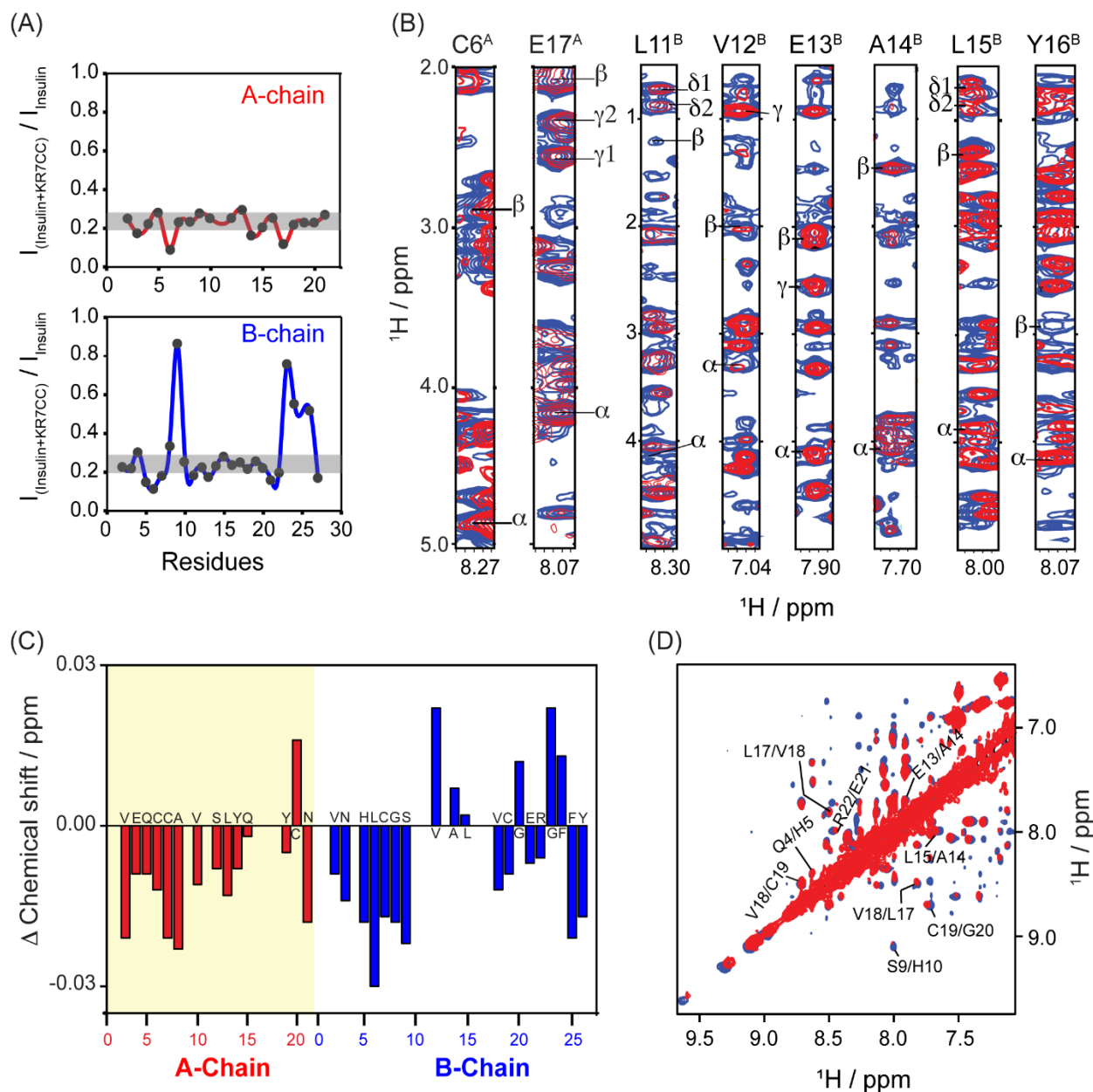


Figure 3.8. Atomistic insight into the interface of inhibitory interaction. Interaction site of KR7CC in insulin by NOESY NMR in 20% acetic acid show (A) specific region broadening of insulin A- and B-chain upon KR7CC interaction. Excessive broadening in central region (L11 to G20) and some N-terminal portion reveal residue specific sequential binding of the B-chain part with KR7CC. The data were collected at 25 °C using Bruker Avance III 700 MHz, equipped with cryo-probe. The Strip plots show the peak broadening of (B) insulin A-chain and the B-chain residues. (C) The observed change in chemical shifts in the insulin A-chain (red) and B-chain (blue) upon interaction with KR7CC. (D) Amide region of the spectra showing the chemical shift change and associated broadening in the presence of an equimolar amount of KR7CC (Red).

KR7CC. Further, to determine the insulin bound KR7CC conformation, we used two-dimensional transferred NOESY (trNOESY) NMR experiments. However, due to insufficient NOEs, we could not determine the full structure of the KR7CC-insulin complex (data not shown).

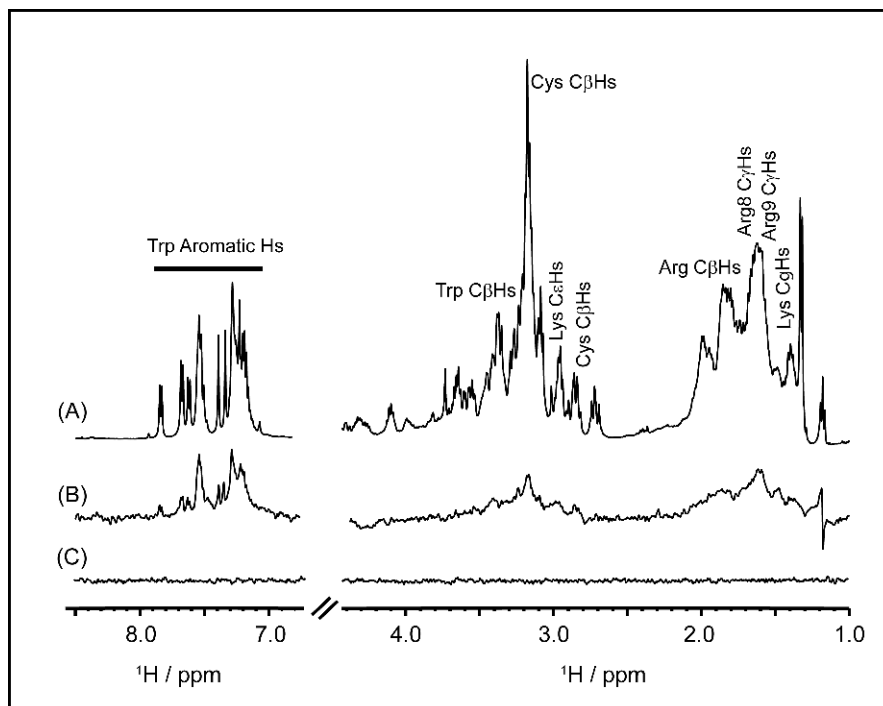


Figure 3.9. Probing the functional inhibitory epitope of KR7CC. Group epitope mapping of KR7CC was performed using one-dimensional ^1H STD (on- and off-resonance: $-1, 50$ ppm, respectively, $t_{\text{sat}} = 2$ s) in the presence (B) and absence (C) of insulin fibril. KR7CC did not show STD effect in the absence of insulin. All the experiments were performed using the Bruker Avance III 500 MHz NMR spectrometer at 25°C .

To further identify the KR7CC residues in close contact with the insulin aggregates, we employed Saturation Transfer Difference (STD) NMR experiment. STD NMR is effectively used to identify the epitope of the ligand binding by probing the magnetization transfer between the receptor (here, insulin) and the aromatic and aliphatic residues of the ligand (here, KR7CC) that come into close interacting proximities (Figure 3.9)²⁷. Interestingly, the tryptophan aromatic region of KR7CC reflected strong STD signals upon addition of insulin fibrils, presumably because of effective magnetization transfer from the high molecular weight fibrils to KR7CC peptide (Figure 3.9B). Additionally, aliphatic protons of Arg and Cys also showed moderate STD effect. No STD signals were detected in absence of the insulin fibrils (Figure 3.9C).

3.3.7. KR7CC stabilizes membrane-bound insulin and inhibits its aggregation

As mentioned earlier, the chronic administration of subcutaneous injection could lead to the formation of an “insulin ball,” compromising the bioavailability of the protein. Previous studies with model membranes had demonstrated the crucial role played by the associated biomembranes in affecting the aggregation propensity of the molecule, thus, promoting the rapid amyloidogenesis at the point of administration^{5g, 5h, 13a}. Thus, protein-lipid interface plays a pivotal role in modulating insulin amyloidogenesis *in vivo*, similar to other well-studied amyloid proteins. Hence, it was essential to check if KR7CC could serve as an effective inhibitor molecule even at the lipid-protein interface. For this purpose, the aggregation kinetics was studied in the presence of eukaryotic model membranes, composed of 6:4 DOPC and Cholesterol^{13a}. The kinetics of insulin aggregation is altered in the presence of 6:4 DOPC/Cholesterol LUVs due to possible surface-level interactions that speed up local aggregation and formation of amyloid fibrils. As a control, the stability of the LUVs was initially tested in three different buffer systems viz. (i) 50 mM citrate phosphate buffer (pH 2.6) with 100 mM NaCl; (ii) HCl buffer (pH 2.0); and (iii) 20% acetic acid buffer (pH 1.9). While the citrate phosphate and acetic acid buffer systems resulted in membrane disruption, HCl served to be the most appropriate choice for further studies. Next, the inhibitory effect of KR7 and KR7CC was studied in the presence of LUVs. Consequently, equimolar peptide concentrations were used to monitor the insulin-membrane mediated aggregation kinetics. Control insulin in HCl buffer showed a lag phase of about 5.6 h, followed by an elongation phase and lastly the saturation phase with a $t_{1/2}$ of about 6 h (Figures 3.10A-C, Table 3.3). The aggregation kinetics was significantly modulated upon addition of 6:4 DOPC/Cholesterol LUVs. Our experimental observations showed a reduction in the lag time of insulin fibrillation in presence of LUVs. The total amount of fibril formation was also reduced by 36% (Figures 3.10A and D). KR7 had a little effect on the lag time as well as $t_{1/2}$ but did not alter the saturation point (Table 3.3; Figures 3.10A-D). Surprisingly, KR7CC showed significant inhibitory effect on the membrane-mediated aggregation kinetics of insulin. Equimolar concentrations of KR7CC increased the $t_{1/2}$ to 5.5 h accompanied by a 46% reduction of the fibrillar forms (Figures 3.10A-D). Of note, kinetic analyses of membrane-mediated insulin fibrillation revealed a maximum increase in the lag phase to 4.5 ± 0.2 h in the presence of KR7CC, while it was 3.2 ± 0.2 h in case of KR7 (Table 3.3; Figure 3.10B).

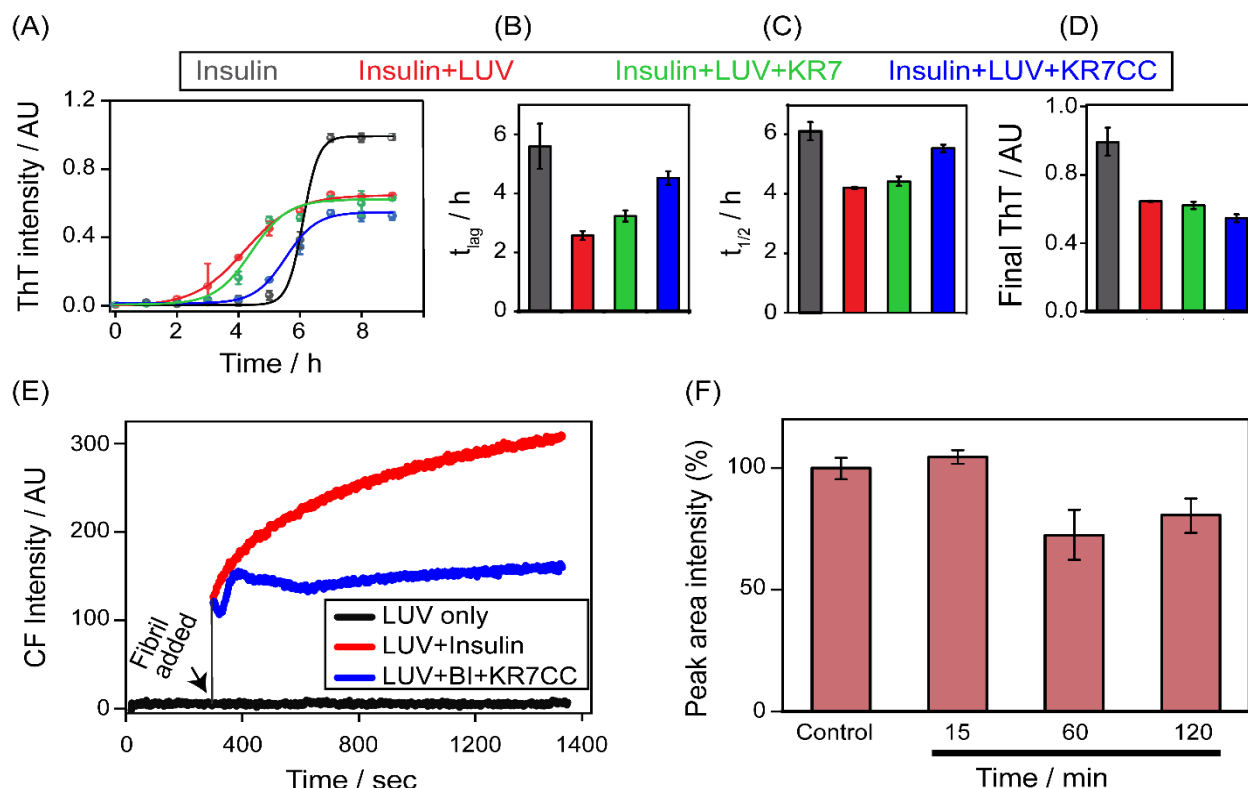


Figure 3.10. Mechanistic insight into the inhibitory attribute of KR7CC. (A) ThT emission profile for 2 mg/ml insulin (black) in HCl buffer (pH 2, at 335K) incubated with 6: 4 DOPC/Cholesterol LUVs (red) and upon addition of KR7 (green) or KR7CC (blue). Fitting the ThT data with Boltzmann equation manifested in the (B) lag time in hours, (C) half time in hours and (D) final ThT intensity indicating the fibrillary content. (E) Vesicle disruption using 6-carboxyfluorescein dye leakage assay. 5 μ l insulin fibrils either alone or in the presence of KR7CC were added to the dye-entrapped 6:4 DOPC/Cholesterol LUVs and monitored for disruption manifesting in a change in the fluorescence intensity over time. (F) Stability of KR7CC peptide in fetal bovine serum was checked by RP-HPLC at different time intervals.

Thus, KR7CC served as the more potent inhibitor when compared to KR7 with its efficacy acting through delaying the lag phase, elongation phase and suppressing the membrane-mediated insulin fibrillation process.

Table 3.3. Calculated parameters obtained from the ThT-based fluorescence kinetic assay in presence of 6:4 DOPC/Cholesterol lipid membrane.

Sample	Lag time (t_{lag}) / h	Half time ($t_{1/2}$) / h
Insulin	5.59 ± 0.77	6.10 ± 0.31
LUV+ Insulin	2.57 ± 0.15	4.20 ± 0.03
LUV+ Insulin: KR7 (1:1)	3.23 ± 0.19	4.42 ± 0.16
LUV+ Insulin: KR7CC (1:1)	4.53 ± 0.22	5.53 ± 0.12

Additionally, the imparted stability of insulin at the lipid peptide interface prevents the insulin-mediated membrane damage. 6-Carboxyfluorescein based dye leakage experiments carried out in the presence and absence of KR7CC tested the effects of insulin aggregates in eukaryotic model membranes. Interestingly, KR7CC inhibited the direct membrane disruption of the vesicles observed in case of insulin alone (Figure 3.10E). The electrostatic interactions between positively charged lipid head groups on the surface of the membrane and the residues of KR7CC could be responsible for the stabilization of membrane integrity²⁸.

3.3.8. KR7CC- a serum-stable therapeutic alternative

In peptide drug development, the peptide must be enzymatically stable in serum, containing various kinds of proteases which can cleave peptide bonds. To check the potential stability of KR7CC, we calculated the presumed effects of KR7CC peptide degradation in fetal bovine serum (FBS). Interestingly, 80% of peptide remained intact even after 2h of incubation in serum (Figure 3.10F). This could be owing to the disulfide bond which helps to improve the thermodynamic stability of KR7CC via the introduction of conformational restrictions to the peptide backbone^{10c}. Collectively, KR7CC was found to be significantly stable and hence an effective, pharmacokinetically active peptide-based inhibitor.

3.4. Conclusion

Among a series of second-generation small peptides designed from the previously reported KR7 peptide comprising of a PWWP motif, our in vitro studies conclude that KR7CC is an effective inhibitor against amyloidogenesis of Insulin. KR7CC effectively arrests all the early oligomeric intermediates, inducing the off-pathway aggregates. Furthermore, KR7CC is a non-toxic, serum

stable peptide and is a good candidate for targeted therapeutic intervention against insulin amyloidogenesis in solution as well in the presence of biological membranes. It serves as a potential candidate to be included as an excipient to prevent insulin amyloidogenesis at the site of administration. Modulation of insulin aggregation by KR7CC proceeds by redirecting the growth of insulin to its less toxic intermediates, making it a potent excipient in formulations of insulin that dramatically improve its shelf life. Additionally, the delineated mechanism of action can be generalized to identify far-fetched and widespread applications in analogous amyloidogenic proteins and peptides such as A β 40, α -synuclein or hIAPP etc.

3.5. Appendix 3

Table S3.1. KR7CC peptide preparation and characterization

Peptide	HPLC gradient (% solvent B; Time)	HPLC t_R (min) and % Purity	Molecular Formula	Calculated MW (Da) for $[M + H]^+$	Observed m/z
KR7CC	10-100; 35min	11.1;99%	$C_{56}H_{81}N_{19}O_9S_2$	1228.59	614.8 [M+2H] ²⁺

Table S3.2. The change in chemical shift values for the A- and B-chain regions of insulin upon incubation with equimolar concentrations of KR7CC as obtained from the two-dimensional NOESY NMR experiment.

A-Chain		B-chain	
Residues	$\Delta\delta$ (ppm)	Residues	$\Delta\delta$ (ppm)
Val3	-0.021	Arg3	-0.014
Cys6	-0.012	His5	-0.018
Cys7	-0.021	Leu6	-0.030
Ala8	-0.023	Cys7	-0.017
Val10	-0.011	Gly8	-0.018
Leu13	-0.013	Ser9	-0.022
Cys20	0.016	Val12	0.022

Arg21	-0.018	Val18	-0.012
		Gly20	0.012
		Gly23	0.023
		Phe24	0.013
		Phe25	-0.021
		Tyr26	-0.017

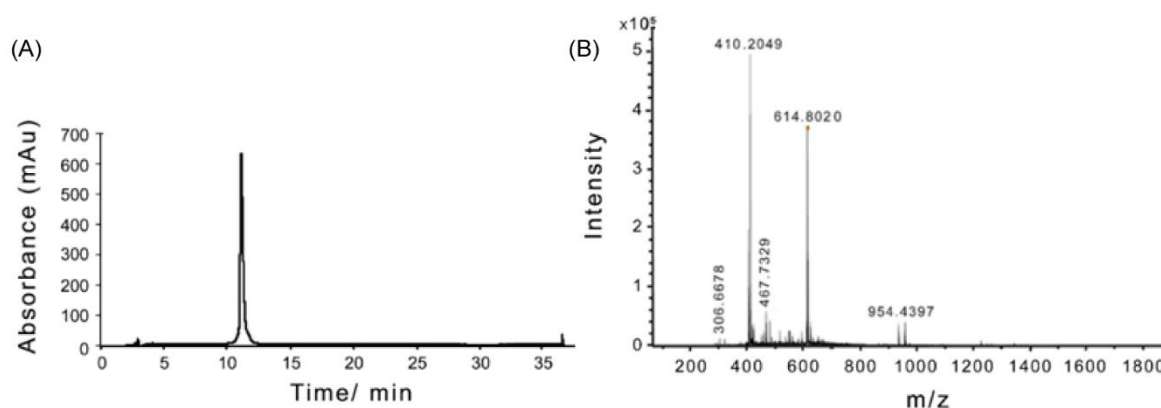


Figure S3.1. KR7CC peptide characterization. (A) Analytical HPLC traces and (B) ESI-MS spectra of the KR7CC peptide.

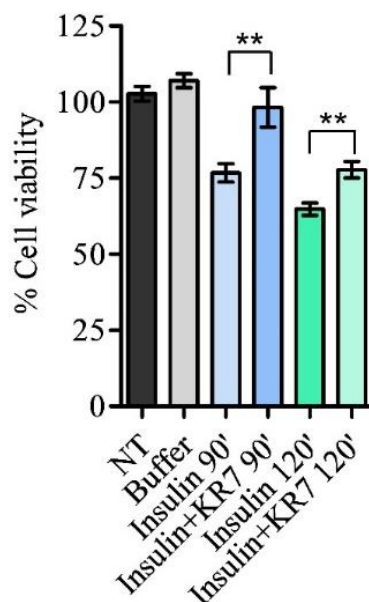


Figure S3.2. Cytotoxicity of insulin protofibril and/or fibrils at 90 min and 120 min incubation period in presence and absence of KR7 peptide. KR7 rescued the cytotoxicity of insulin by almost 20%. The bar represents Standard Deviations of three independent experiments. Significance was calculated by Mann-Whitney test One-tailed. $p=0.0035$ (**).

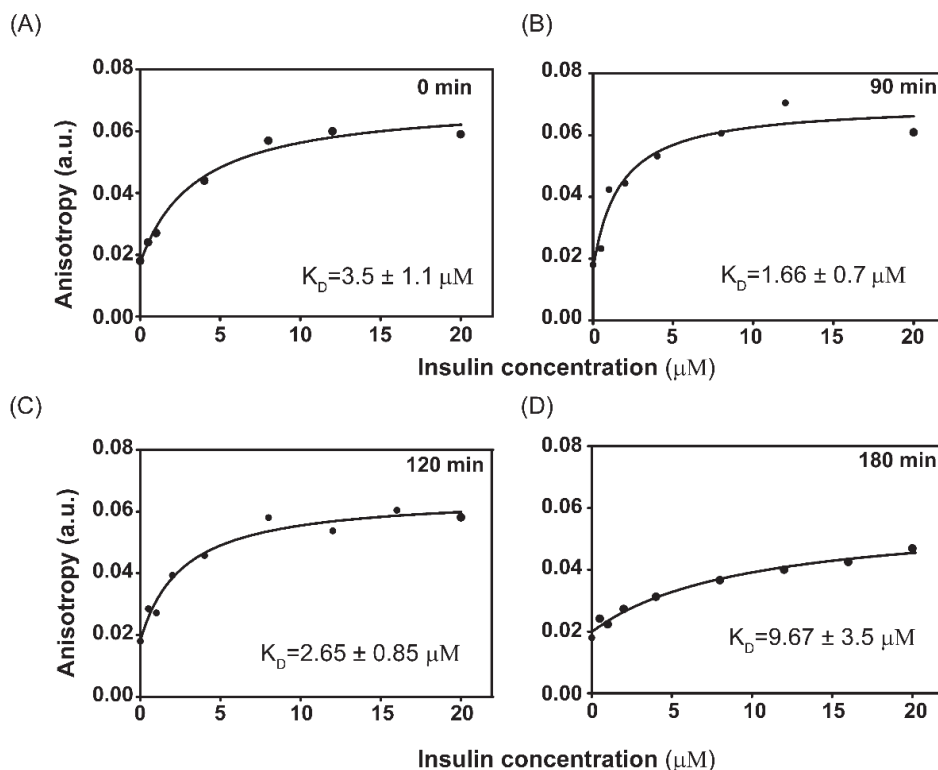


Figure S3.3. The binding of KR7CC to insulin at different time points studied using tryptophan-fluorescence based anisotropic experiments. (A) Anisotropy of the tryptophan fluorescence of $8\mu\text{M}$ KR7CC peptide in 50 mM citrate phosphate buffer, 100 mM NaCl (pH 2.6) upon gradual addition of insulin from $1\mu\text{M}$ to $20\mu\text{M}$ concentration from a 2 mg/ml stock solution at different time intervals, i.e., (A) 0 min, (B) 90 min, (C) 120 min, (D) 180 min.

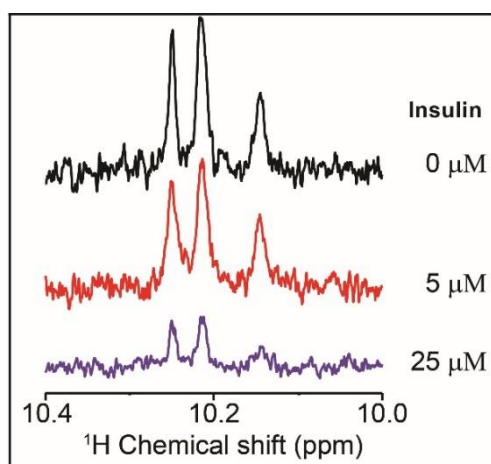


Figure S3.4. The ^1H NMR spectra corresponding to the indole ring protons of tryptophan residues of $50\mu\text{M}$ KR7CC showing the line width broadening in the region upon addition of insulin. The experiments were all recorded at 298 K using the Bruker Avance III 700 MHz spectrometer.

3.6. References

1. (a) Dobson, C. M., Protein misfolding, evolution and disease. *Trends Biochem Sci* **1999**, *24* (9), 329-32; (b) Dobson, C. M., The structural basis of protein folding and its links with human disease. *Philos Trans R Soc Lond B Biol Sci* **2001**, *356* (1406), 133-45; (c) Dobson, C. M., Protein folding and misfolding. *Nature* **2003**, *426* (6968), 884-90.
2. (a) Konarkowska, B.; Aitken, J. F.; Kistler, J.; Zhang, S.; Cooper, G. J., The aggregation potential of human amylin determines its cytotoxicity towards islet beta-cells. *FEBS J* **2006**, *273* (15), 3614-24; (b) Clark, A.; Cooper, G. J.; Lewis, C. E.; Morris, J. F.; Willis, A. C.; Reid, K. B.; Turner, R. C., Islet amyloid formed from diabetes-associated peptide may be pathogenic in type-2 diabetes. *Lancet* **1987**, *2* (8553), 231-4; (c) de Koning, E. J.; Morris, E. R.; Hofhuis, F. M.; Posthuma, G.; Hoppener, J. W.; Morris, J. F.; Capel, P. J.; Clark, A.; Verbeek, J. S., Intra- and extracellular amyloid fibrils are formed in cultured pancreatic islets of transgenic mice expressing human islet amyloid polypeptide. *Proc Natl Acad Sci U S A* **1994**, *91* (18), 8467-71; (d) Mirzabekov, T. A.; Lin, M. C.; Kagan, B. L., Pore formation by the cytotoxic islet amyloid peptide amylin. *J Biol Chem* **1996**, *271* (4), 1988-92.
3. (a) Ahmad, A.; Millett, I. S.; Doniach, S.; Uversky, V. N.; Fink, A. L., Partially folded intermediates in insulin fibrillation. *Biochemistry* **2003**, *42* (39), 11404-16; (b) Banerjee, V.; Das, K. P., Modulation of pathway of insulin fibrillation by a small molecule helix inducer 2,2,2-trifluoroethanol. *Colloids Surf B Biointerfaces* **2012**, *92*, 142-50; (c) Brange, J.; Havelund, S.; Hommel, E.; Sorensen, E.; Kuhl, C., Neutral insulin solutions physically stabilized by addition of Zn²⁺. *Diabet Med* **1986**, *3* (6), 532-6; (d) Chiang, H. L.; Ngo, S. T.; Chen, C. J.; Hu, C. K.; Li, M. S., Oligomerization of Peptides LVEALYL and RGFFYT and Their Binding Affinity to Insulin. *PLoS One* **2013**, *8* (6), e65358; (e) Choudhary, S.; Kishore, N.; Hosur, R. V., Inhibition of insulin fibrillation by osmolytes: Mechanistic insights. *Sci Rep* **2015**, *5*, 17599; (f) Dong, J.; Wan, Z.; Popov, M.; Carey, P. R.; Weiss, M. A., Insulin assembly damps conformational fluctuations: Raman analysis of amide I linewidths in native states and fibrils. *J Mol Biol* **2003**, *330* (2), 431-42.
4. D'Souza, A.; Theis, J. D.; Vrana, J. A.; Dogan, A., Pharmaceutical amyloidosis associated with subcutaneous insulin and enfuvirtide administration. *Amyloid* **2014**, *21* (2), 71-5.
5. (a) Nagase, T.; Katsura, Y.; Iwaki, Y.; Nemoto, K.; Sekine, H.; Miwa, K.; Oh, I. T.; Kou, K.; Iwaya, K.; Noritake, M.; Matsuoka, T., The insulin ball. *Lancet* **2009**, *373* (9658), 184; (b) Iwaya, K.; Zako, T.; Fukunaga, J.; Sorgjerd, K. M.; Ogata, K.; Kogure, K.; Kosano, H.; Noritake, M.; Maeda, M.; Ando, Y.; Katsura, Y.; Nagase, T., Toxicity of insulin-derived amyloidosis: a case report. *BMC Endocr Disord* **2019**, *19* (1), 61; (c) D'Souza, A.; Theis, J. D.; Vrana, J. A.; Buadi, F.; Dispenzieri, A.; Dogan, A., Localized insulin-derived amyloidosis: a potential pitfall in the diagnosis of systemic amyloidosis by fat aspirate. *Am J Hematol* **2012**, *87* (11), E131-2; (d) Gupta, Y.; Singla, G.; Singla, R., Insulin-derived amyloidosis. *Indian J Endocrinol Metab* **2015**, *19* (1), 174-7; (e) Lonsdale-Eccles, A. A.; Gonda, P.; Gilbertson, J. A.; Haworth, A. E., Localized cutaneous amyloid at an insulin injection site. *Clin Exp Dermatol* **2009**, *34* (8), e1027-8; (f) Mangla, A.; Kim, G. J.; Agarwal, N.; Khurana, S.; Catchatourian, R.; Jiang, J. J., Localized insulin amyloidosis with use of concentrated insulin: a potential complication. *Diabet Med* **2016**, *33* (12), e32-e35; (g) Shikama, Y.; Kitazawa, J.; Yagihashi, N.; Uehara, O.; Murata, Y.; Yajima, N.; Wada, R.; Yagihashi, S., Localized amyloidosis at the site of repeated insulin injection in a diabetic patient. *Intern Med* **2010**, *49*

- (5), 397-401; (h) Sie, M. P.; van der Wiel, H. E.; Smedts, F. M.; de Boer, A. C., Human recombinant insulin and amyloidosis: an unexpected association. *Neth J Med* **2010**, *68* (3), 138-40.
6. (a) Brender, J. R.; Heyl, D. L.; Samisetti, S.; Kotler, S. A.; Osborne, J. M.; Pesaru, R. R.; Ramamoorthy, A., Membrane disordering is not sufficient for membrane permeabilization by islet amyloid polypeptide: studies of IAPP(20-29) fragments. *Phys Chem Chem Phys* **2013**, *15* (23), 8908-15; (b) Gibson Wood, W.; Eckert, G. P.; Igbavboa, U.; Muller, W. E., Amyloid beta-protein interactions with membranes and cholesterol: causes or casualties of Alzheimer's disease. *Biochim Biophys Acta* **2003**, *1610* (2), 281-90; (c) Brender, J. R.; Hartman, K.; Reid, K. R.; Kennedy, R. T.; Ramamoorthy, A., A single mutation in the nonamyloidogenic region of islet amyloid polypeptide greatly reduces toxicity. *Biochemistry* **2008**, *47* (48), 12680-8; (d) Brender, J. R.; Lee, E. L.; Hartman, K.; Wong, P. T.; Ramamoorthy, A.; Steel, D. G.; Gafni, A., Biphasic effects of insulin on islet amyloid polypeptide membrane disruption. *Biophys J* **2011**, *100* (3), 685-692; (e) Engel, M. F.; Khemtemourian, L.; Kleijer, C. C.; Meeldijk, H. J.; Jacobs, J.; Verkleij, A. J.; de Kruijff, B.; Killian, J. A.; Hoppener, J. W., Membrane damage by human islet amyloid polypeptide through fibril growth at the membrane. *Proc Natl Acad Sci U S A* **2008**, *105* (16), 6033-8; (f) Janson, J.; Ashley, R. H.; Harrison, D.; McIntyre, S.; Butler, P. C., The mechanism of islet amyloid polypeptide toxicity is membrane disruption by intermediate-sized toxic amyloid particles. *Diabetes* **1999**, *48* (3), 491-8; (g) Zhang, X.; St Clair, J. R.; London, E.; Raleigh, D. P., Islet Amyloid Polypeptide Membrane Interactions: Effects of Membrane Composition. *Biochemistry* **2017**, *56* (2), 376-390; (h) van Maarschalkerweerd, A.; Vetri, V.; Vestergaard, B., Cholesterol facilitates interactions between alpha-synuclein oligomers and charge-neutral membranes. *FEBS Lett* **2015**, *589* (19 Pt B), 2661-7.
 7. (a) Spangler, R. S., Insulin administration via liposomes. *Diabetes Care* **1990**, *13* (9), 911-22; (b) Ramesan, R. M.; Sharma, C. P., Recent advances in the oral delivery of insulin. *Recent Pat Drug Deliv Formul* **2014**, *8* (2), 155-9; (c) Luo, Y. Y.; Xiong, X. Y.; Tian, Y.; Li, Z. L.; Gong, Y. C.; Li, Y. P., A review of biodegradable polymeric systems for oral insulin delivery. *Drug Deliv* **2016**, *23* (6), 1882-91; (d) Sharma, G.; Sharma, A. R.; Nam, J. S.; Doss, G. P.; Lee, S. S.; Chakraborty, C., Nanoparticle based insulin delivery system: the next generation efficient therapy for Type 1 diabetes. *J Nanobiotechnology* **2015**, *13*, 74; (e) Bariya, S. H.; Gohel, M. C.; Mehta, T. A.; Sharma, O. P., Microneedles: an emerging transdermal drug delivery system. *J Pharm Pharmacol* **2012**, *64* (1), 11-29; (f) Grudzielanek, S.; Smirnovas, V.; Winter, R., The effects of various membrane physical-chemical properties on the aggregation kinetics of insulin. *Chem Phys Lipids* **2007**, *149* (1-2), 28-39; (g) Wang, S. S.; Liu, K. N.; Han, T. C., Amyloid fibrillation and cytotoxicity of insulin are inhibited by the amphiphilic surfactants. *Biochim Biophys Acta* **2010**, *1802* (6), 519-30.
 8. (a) Ghosh, A.; Pradhan, N.; Bera, S.; Datta, A.; Krishnamoorthy, J.; Jana, N. R.; Bhunia, A., Inhibition and Degradation of Amyloid Beta (Abeta40) Fibrillation by Designed Small Peptide: A Combined Spectroscopy, Microscopy, and Cell Toxicity Study. *ACS Chem Neurosci* **2017**, *8* (4), 718-722; (b) Paul, A.; Nadimpally, K. C.; Mondal, T.; Thalluri, K.; Mandal, B., Inhibition of Alzheimer's amyloid-beta peptide aggregation and its disruption by a conformationally restricted alpha/beta hybrid peptide. *Chem Commun (Camb)* **2015**, *51* (12), 2245-8.

9. Ratha, B. N.; Ghosh, A.; Brender, J. R.; Gayen, N.; Ilyas, H.; Neeraja, C.; Das, K. P.; Mandal, A. K.; Bhunia, A., Inhibition of Insulin Amyloid Fibrillation by a Novel Amphipathic Heptapeptide: MECHANISTIC DETAILS STUDIED BY SPECTROSCOPY IN COMBINATION WITH MICROSCOPY. *J Biol Chem* **2016**, 291 (45), 23545-23556.
10. (a) Belostozky, A.; Richman, M.; Lisniansky, E.; Tovchigrechko, A.; Chill, J. H.; Rahimipour, S., Inhibition of tau-derived hexapeptide aggregation and toxicity by a self-assembled cyclic d,l-alpha-peptide conformational inhibitor. *Chem Commun (Camb)* **2018**, 54 (47), 5980-5983; (b) Joo, S. H., Cyclic peptides as therapeutic agents and biochemical tools. *Biomol Ther (Seoul)* **2012**, 20 (1), 19-26; (c) Qian, Z.; Rhodes, C. A.; McCroskey, L. C.; Wen, J.; Appiah-Kubi, G.; Wang, D. J.; Guttridge, D. C.; Pei, D., Enhancing the Cell Permeability and Metabolic Stability of Peptidyl Drugs by Reversible Bicyclization. *Angew Chem Int Ed Engl* **2017**, 56 (6), 1525-1529.
11. Coin, I.; Beyermann, M.; Bienert, M., Solid-phase peptide synthesis: from standard procedures to the synthesis of difficult sequences. *Nat Protoc* **2007**, 2 (12), 3247-56.
12. B. Kamber, A. H., K. Eisler, B. Riniker, H. Rink, P. Sieber, W. Rittel, The Synthesis of Cystine Peptides by Iodine Oxidation of S-Trityl-cysteine and S-Acetamidomethyl-cysteine Peptides. *Helvetica Chimica Acta* **1980**, 63(1980), 899-915.
13. (a) Ratha, B. N.; Kim, M.; Sahoo, B.; Garai, K.; Lee, D.; Bhunia, A., Insulin-eukaryotic model membrane interaction: Mechanistic insight of insulin fibrillation and membrane disruption. *Biochim Biophys Acta Biomembr* **2018**, 1860 (9), 1917-1926; (b) Kinoshita, M.; Kakimoto, E.; Terakawa, M. S.; Lin, Y.; Ikenoue, T.; So, M.; Sugiki, T.; Ramamoorthy, A.; Goto, Y.; Lee, Y. H., Model membrane size-dependent amyloidogenesis of Alzheimer's amyloid-beta peptides. *Phys Chem Chem Phys* **2017**, 19 (24), 16257-16266.
14. Biancalana, M.; Koide, S., Molecular mechanism of Thioflavin-T binding to amyloid fibrils. *Biochim Biophys Acta* **2010**, 1804 (7), 1405-12.
15. Banerjee, V.; Kar, R. K.; Datta, A.; Parthasarathi, K.; Chatterjee, S.; Das, K. P.; Bhunia, A., Use of a small peptide fragment as an inhibitor of insulin fibrillation process: a study by high and low resolution spectroscopy. *PLoS One* **2013**, 8 (8), e72318.
16. Dolui, S.; Roy, A.; Pal, U.; Saha, A.; Maiti, N. C., Structural Insight of Amyloidogenic Intermediates of Human Insulin. *ACS Omega* **2018**, 3 (2), 2452-2462.
17. Ratha, B. N.; Kar, R. K.; Kalita, S.; Kalita, S.; Raha, S.; Singha, A.; Garai, K.; Mandal, B.; Bhunia, A., Sequence specificity of amylin-insulin interaction: a fragment-based insulin fibrillation inhibition study. *Biochim Biophys Acta Proteins Proteom* **2019**, 1867 (4), 405-415.
18. (a) Mayer, M.; Meyer, B., Group epitope mapping by saturation transfer difference NMR to identify segments of a ligand in direct contact with a protein receptor. *J Am Chem Soc* **2001**, 123 (25), 6108-17; (b) Mayer, M.; Meyer, B., Characterization of Ligand Binding by Saturation Transfer Difference NMR Spectroscopy. *Angew Chem Int Ed Engl* **1999**, 38 (12), 1784-1788.
19. Jenssen, H.; Aspmo, S. I., Serum stability of peptides. *Methods Mol Biol* **2008**, 494, 177-86.
20. Karamanos, T. K.; Kalverda, A. P.; Thompson, G. S.; Radford, S. E., Mechanisms of amyloid formation revealed by solution NMR. *Prog Nucl Magn Reson Spectrosc* **2015**, 88-89, 86-104.

21. (a) Hua, Q. X.; Weiss, M. A., Mechanism of insulin fibrillation: the structure of insulin under amyloidogenic conditions resembles a protein-folding intermediate. *J Biol Chem* **2004**, *279* (20), 21449-60; (b) Hua, Q. X.; Jia, W.; Weiss, M. A., Conformational dynamics of insulin. *Front Endocrinol (Lausanne)* **2011**, *2*, 48.
22. Ma, Y.; Huang, R.; Qi, W.; Su, R.; He, Z., Fluorescent silicon nanoparticles inhibit the amyloid fibrillation of insulin. *J Mater Chem B* **2019**, *7* (9), 1397-1403.
23. Pleshakova, T. O.; Bukharina, N. S.; Archakov, A. I.; Ivanov, Y. D., Atomic Force Microscopy for Protein Detection and Their Physicochemical Characterization. *Int J Mol Sci* **2018**, *19* (4).
24. Zako, T.; Sakono, M.; Hashimoto, N.; Ihara, M.; Maeda, M., Bovine insulin filaments induced by reducing disulfide bonds show a different morphology, secondary structure, and cell toxicity from intact insulin amyloid fibrils. *Biophys J* **2009**, *96* (8), 3331-40.
25. (a) Hua, Q. X.; Weiss, M. A., Toward the solution structure of human insulin: sequential 2D 1H NMR assignment of a des-pentapeptide analogue and comparison with crystal structure. *Biochemistry* **1990**, *29* (46), 10545-55; (b) Hua, Q. X.; Weiss, M. A., Comparative 2D NMR studies of human insulin and des-pentapeptide insulin: sequential resonance assignment and implications for protein dynamics and receptor recognition. *Biochemistry* **1991**, *30* (22), 5505-15; (c) Jorgensen, A. M.; Kristensen, S. M.; Led, J. J.; Balschmidt, P., Three-dimensional solution structure of an insulin dimer. A study of the B9(Asp) mutant of human insulin using nuclear magnetic resonance, distance geometry and restrained molecular dynamics. *J Mol Biol* **1992**, *227* (4), 1146-63.
26. Zheng, Q.; Lazo, N. D., Mechanistic Studies of the Inhibition of Insulin Fibril Formation by Rosmarinic Acid. *J Phys Chem B* **2018**, *122* (8), 2323-2331.
27. Bhunia, A.; Bhattacharjya, S.; Chatterjee, S., Applications of saturation transfer difference NMR in biological systems. *Drug Discov Today* **2012**, *17* (9-10), 505-13.
28. Walrant, A.; Vogel, A.; Correia, I.; Lequin, O.; Olausson, B. E.; Desbat, B.; Sagan, S.; Alves, I. D., Membrane interactions of two arginine-rich peptides with different cell internalization capacities. *Biochim Biophys Acta* **2012**, *1818* (7), 1755-63.

Chapter 4

4. Peptide-Based Strategies: Combating Alzheimer's Amyloid Beta Aggregation through Ergonomic Design and Fibril Disruption

This chapter has been adapted from the following publication:

Pariary, R., Shome, G., Kalita, S., Kalita, S., Roy, A., Harikishoree, A., Jana, K., Senapati, D., Mandal, B., Mandal, A.K. and Bhunia, A., 2024. Peptide-Based Strategies: Combating Alzheimer's Amyloid Beta Aggregation through Ergonomic Design and Fibril Disruption. *Biochemistry*, (manuscript submitted).

4.1. Introduction

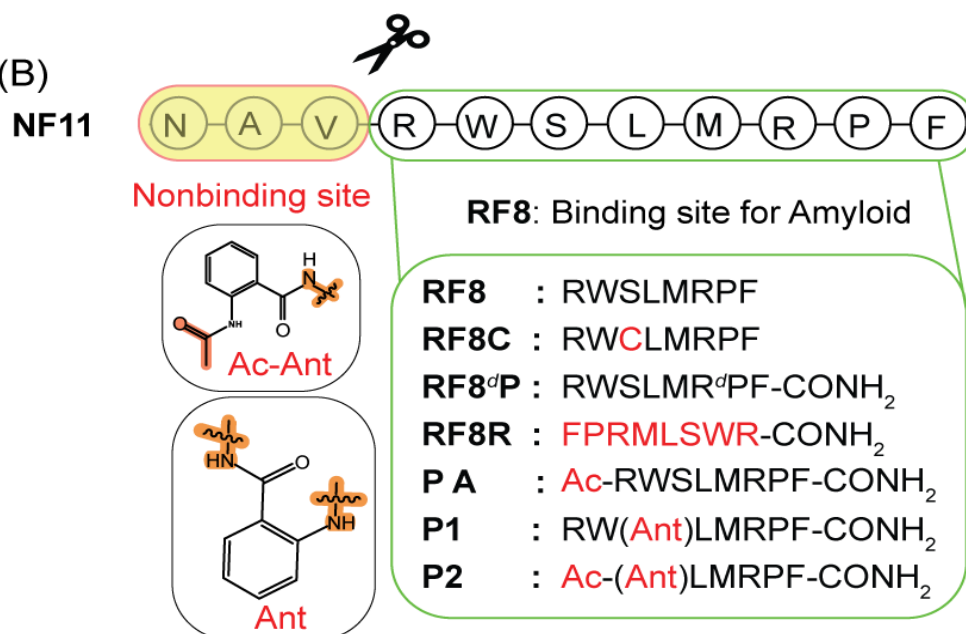
Alzheimer's disease (AD) currently affects more than 40 million individuals globally, and estimates suggest that this figure may climb to around 140 million by 2050 as the world's population ages ¹. In AD, key pathological indicators include the deposition of amyloid plaques of amyloid beta (A β) peptide in extracellular region, and the formation of intracellular neurofibrillary tangles, consisting of tau protein ². The 'amyloid cascade hypothesis' suggests that self-association of A β peptide is a crucial starter in AD, supported by genetic and pathological evidence in both familial and sporadic cases ³. Soluble A β oligomers, formed through the process of amyloid aggregation from soluble native peptides, are more toxic than insoluble amyloids and are responsible for disrupting cell membranes, leading to cell death ⁴. The oligomers can continue to expand and transform into additional fibrils, accelerating the generation of further toxic entities through a remarkably efficient catalytic process ⁵. The primary focus of research was on enhancing the activity of the A β protein through self-recognition segments, particularly L¹⁷VFFA²¹ ⁶. In C-terminal domain, mutation of the consecutive G²⁹xxxG³³xxxG³⁷ motifs with Leu or Ile led to a drastic reduction in A β 40 and A β 42 production, highlighting the unique significance of the GxxxG motif in A β peptides ⁷. Understanding the molecular effects of intrinsic and extrinsic variables on A β aggregation is crucial for designing effective therapeutics to inhibit self-assembly (Scheme 4.1A) ⁸. Approaches encompass chemical chaperones ⁹, small molecules ^{8c, 10}, nanoparticles ¹¹, peptide inhibitors ^{8e, 12}, metal chelators ¹³, and antibodies ¹⁴ designed to selectively target specific

conformations, addressing issues related to the A β peptide. A strategically designed short peptide from self-aggregation segments of A β showed promising outcomes in clinical trials, with improved bioavailability and reduced toxicity¹⁵. A reported peptide, H102 with the sequence HKQLPFFEED, has demonstrated potent abilities in inhibiting and disassembling amyloid fibrils^{12c}. Alternatively, ‘ β -sheet breaker’ peptides, incorporating a recognition motif and a β -breaker element like proline, inhibited the formation as well the disaggregation of preformed A β 40 fibrils¹⁶. A recently designed synthetic paratope incorporating a peptide fragment of A β serves as a potential inhibitor for targeting A β 40^{12b}. Most of these peptides include unstable α -amino acids or their modified forms, making them susceptible to proteolytic degradation¹⁷. In our earlier study, we identified NF11 (NAVRWSLMRPF), derived from modified fragments of the SARS coronavirus E-protein sequence, as particularly effective in targeting A β 40 fibrillation *in vitro*^{8e}. NMR and molecular docking results indicated that essential residues, like R4, W5, L7, R9, and F11 of NF11, played crucial roles in stabilizing the A β 40:NF11 complex. We systemically altered

(A)

A β 40: DAEFRHDSGY¹⁰ EVHHQKLVFF²⁰ AEDVGSNKGA³⁰ IIGLMVGGVV⁴⁰
 A β 42: DAEFRHDSGY EVHHQKLVFF AEDVGSNKGA IIGLMVGGVV IA
 AV20: AEDVGSNKGA IIGLMVGGVV

(B)



Scheme 4.1. (A) Amino acid sequence of A β 40, A β 42 and AV20 peptides. (B) The amino acid sequence of designed RF8 series peptides from NF11 peptide.

the original peptide sequence to improve its therapeutic potential. In this present study, we have used the interacting core sequence of NF11 such as RF8 (RWSLMRPF) fragment and its modified derivatives RF8C, RF8R, RF8dP, Peptide-A (PA), Peptide-1 (P1) and Peptide-2 (P2) (Scheme 4.1B). Here, we incorporate anthranilic acid unit (Ant, 2-amino benzoic acid) in P1 and P2 before LMRPF sequence. Ant, acting as a β -sheet breaker, present in various biologically active compounds, has the potential to induce either a helical or a turn conformation^{18 12a}. Several biophysical experiments, encompassing low-resolution methods such as fluorescence and circular dichroism, along with high-resolution nuclear magnetic resonance (NMR) spectroscopy, in conjunction with atomic force microscopic analysis, were carried out to elucidate the mechanistic interactions at the functional interface involved in inhibiting A β . A β induced neurotoxicity and its mechanism remains complex and obscure, but many evidence suggests that accumulation of intracellular ROS is associated with neuronal damage leading to AD¹⁹. A β fragments induced lipid peroxidation can potentially generate overwhelming free radicals that may affect cellular apoptosis²⁰. In the following study we have investigated the neuroprotective effects of serum stable β -sheet breaker peptide P1 and its underlying mechanism with A β 42 induced neurotoxicity. These findings enhance our comprehension of how the RF8 series of peptide inhibitors modulate the aggregation and cytotoxicity of A β 42, potentially leading to new approaches in peptide-based therapeutics for combating AD.

4.2. Experimental Methods

4.2.1. Chemicals

Unlabeled A β 40 and A β 42 peptides were obtained from Genscript Inc. (Piscataway, NJ, USA), while isotopically labeled (¹⁵N) peptides were purchased from rPeptide Inc. (Bogart, GA, USA). The C-terminal fragment of A β 40 peptide, AV20 and ¹⁵N labeled of AV20 Glycine residues were also purchased from Genscript Inc. (Piscataway, NJ, USA). All RF8 series peptide were purchased from SynPeptide Co Ltd (Shanghai, China). All peptides had a purity exceeding 95% as confirmed by HPLC and mass spectral analysis. Thioflavin T (ThT), 1,1,1,3,3,3-hexafluoro-2-propanol (HFIP) and D₂O were acquired from Sigma-Aldrich (St. Louis, MO, USA). For cell culture, 3-(4,5-dimethylthiazol-2-yl)-2,5-diphenyltetrazolium bromide (MTT) (Himedia, Bangalore, India), Fetal bovine serum (FBS), antibiotic (Himedia, India), DMEM/F12 media (Gibco, USA), and trypsin-EDTA (Himedia, India) were used.

4.2.2. Synthesis and characterization of P1 and P2 peptide

Peptides P1 and P2 were synthesized following the standard protocol of Fmoc/tBu solid phase peptide synthesis (SPPS) using Rink amide MBHA resin (loading 0.7 mmol/g) as the solid support. For each coupling of amino acid, 2 equivalents of Fmoc-amino acids, 2.5 equivalents of coupling reagent (BOP), and 5 equivalents of base (DIPEA) were used. Fmoc deprotection was performed using 20% piperidine in DMF for 21 mins (7 min \times 3). Each coupling was monitored by Kaiser's test. In case of an incomplete reaction, the coupling cycle was repeated, followed by capping (acetylation) with acetic anhydride (Ac_2O , 1 equivalent) and N-methyl-imidazole (NMI, 2 equivalent) in DCM for 1.5 h. After successful synthesis, the final peptides were cleaved from the resin using a cleavage cocktail comprised of 90% TFA, 5% DCM, and 5% H_2O for 3h. The peptides were precipitated in cold diethyl ether, followed by centrifugation to get the crude solid peptides.

The crude peptides were purified by reverse-phase high-performance liquid chromatography (RP-HPLC, Thermo Scientific) using a semi-preparative C_{18} - μ Bondapak column (dimensions 250 \times 10 mm, particle size 12 μm , pore size 175 \AA) maintaining a flow rate of 4 ml/min. The peptides were dissolved in a binary solvent system, using 0.1% TFA in H_2O as solvent A and 0.1% TFA in CH_3CN as solvent B. A UV detector was used with a dual-wavelength set at 214 nm and 254 nm for the individual run. A total run time of 20 mins was used for the purification of both the peptides. A linear gradient of 5 to 100% acetonitrile (CH_3CN) was set for the first 18 mins, followed by 100% CH_3CN till 20 mins. The purity of the peptides was further confirmed with Waters 600E Analytical RP-HPLC System using C_{18} analytical column for a total run time of 20 mins at a flow rate of 1 ml/min. A linear gradient of 5 to 100% CH_3CN was used for 18 mins, followed by 100% CH_3CN for 20 mins, with the UV detection set at 214 nm and 254 nm. After removing acetonitrile by rotary evaporation, the HPLC fragments containing the purified peptides were lyophilised to obtain the purified white solid peptide. The purified peptides were characterised by high resolution mass spectrometry (HRMS) using Agilent-Q-TOF 6500 instrument in the ESI positive mode with the Mass Hunter Work Station software. The purified peptides were also characterized by MALDI-TOF mass spectrometry. The matrix used in the MALDI-TOF experiment was CHCA (α -cyano-hydroxy-cinnamic acid) mixed in a 1:1 ratio with the peptide sample and analyzed using Bruker Daltonics flex analysis software.

4.2.3. Sample preparation

The sample was prepared using a previously described method ²¹. 1 mg of commercially obtained A β peptide was dissolved in HFIP (500 μ l) and then portioned into aliquots of 0.1 mg/ml, followed by overnight lyophilization. The stock aliquots were preserved at -80°C. The aliquots at a concentration of 0.1 mg/ml were resuspended in a 300 μ l solution containing 20 mM sodium phosphate buffer and 50 mM NaCl at pH 7.4 followed by 30 s sonication, resulting in a final concentration of approximately 80 μ M.

4.2.4. Thioflavin T (ThT) Fluorescence Assay

ThT fluorescence assays were conducted to observe the aggregation kinetics of 5 μ M A β 40 at 37 °C and 300 rpm, with equimolar RF8 series inhibitors and 5 μ M ThT. After the screening of potent peptide P1 and P2, ThT assay was performed on 10 μ M A β 42 in absence and/or presence of 1- and 2-fold molar excess of P1 or P2 at 37 °C and 100 rpm in 20 mM sodium phosphate buffer and 50 mM NaCl solution pH 7.4 using 10 μ M ThT. To understand the secondary nucleation of A β 42 aggregation kinetics, 25% preformed fibril seed was added in A β 42 monomer in absence and presence of P1 at 1:1 and 1:2 molar ratio of A β 42 / P1. For defibrillation experiments, A β 42 matured fibrils (5 μ M) were disintegrated using P1 and P2 peptides at 1:1 and 1:2 molar ratios of A β 42 / P1 or P2 with 5 μ M ThT at 37 °C. ThT assay was performed in 96-well black plates, with each well containing a sample volume of 150 μ L. ThT kinetics was monitored in triplicate for 12 h with excitation and emission wavelengths of 440 and 485 nm ²², respectively using BMG LABTECH POLARstar Omega spectrometer (Ortenberg, Germany). Fluorescence intensity data collected at 485 nm for various time intervals were graphed against time. Subsequently, the curve was fitted by the following Boltzmann equation ²³, which is a nonlinear sigmoidal function:

$$Y = F_2 + \left[\frac{F_2 - F_1}{1 + e^{\frac{T - T_{half}}{\tau}}} \right]$$

Here, F_1 represents the fluorescence intensity at 0 h, F_2 represents the maximum fluorescence intensity at saturation phase, $1/\tau$ represents the apparent rate constant of fibril elongation, and T_{half} represents the time at which intensity reaches half of the maximum value. Additionally, the lag time (T_{lag}) can be calculated as $T_{half} - 2\tau$.

4.2.5. Circular dichroism (CD) spectroscopy

CD spectra were obtained to study conformational changes of A β 42 with and without P1 peptide at a 1:1 and 1:2 molar ratio using a JASCO J-815 spectropolarimeter. A β peptide (25 μ M) was dissolved in pH 7.4 buffer containing 20 mM sodium phosphate and 50 mM NaF. Spectra were collected from 200 nm to 260 nm using a quartz cuvette with a path length of 0.2 cm at 25 °C. CD spectra were obtained by averaging three consecutive scans at 100 nm/min with subtracting the buffer or P1 spectra.

4.2.6. Nuclear magnetic resonance (NMR) spectroscopy

2D ^1H - ^{15}N Heteronuclear single quantum coherence spectroscopy (HSQC) NMR spectra were recorded at 286 K using the Bruker AVANCE III 700 MHz (equipped with a QCI Cryoprobe) spectrometer. The obtained NMR data were processed using Topspin v4.0.6 software from Bruker and analyzed using Sparky. 80 μ M ^{15}N -labeled A β 42 peptides were dissolved in a 20 mM sodium phosphate and 50 mM NaCl buffer at pH 7.4, containing 90% H_2O and 10% D_2O for NMR measurements. NMR titration experiments were performed on A β 40/42 (80 μ M) with P1 or P2 at increasing concentration, involving 16 scans and 12 ppm and 40 ppm spectral width along ^1H and ^{15}N directions, respectively. The 2D NMR employed the echo and anti-echo method, collecting 1024 data points for t_2 and 64 for t_1 . CSP was determined using the following equation:

$$\Delta\delta = \sqrt{\Delta\delta_H^2 + (\Delta\delta_N/5)^2}$$

Here, δ_H and δ_N are the differences in chemical shifts between A β and A β :Peptide (P1 or P2) along t_2 and t_1 directions, respectively.

Normalized peak intensity (I/I_0) was calculated using the NMR signal intensity ratios of [A β :P] (I) and A β control (I_0). The running average of (I/I_0) was measured by considering the values of three consecutive residues.

The ^1H NMR spectra for Saturation transfer difference (STD) NMR were acquired using the Bruker AVANCE III 500 MHz instrument, which was equipped with a SMART probe at 298 K. For the 1D STD NMR experiment, a molar ratio of 100:1 was maintained in 100% D_2O with 500

μM P1 or P2 and 5 μM A β 42 fibril. The STD control spectrum for P1 or P2 was recorded in absence of A β 42 fibril. Selective saturation of protein resonance was achieved over a 2.5 s duration using a sequence of 50 Gaussian-shaped pulses, each lasting 49 ms with 1 ms intervals between them. The on-resonance and off-resonance frequencies were adjusted to -1 ppm and 40 ppm, respectively for peptide irradiation. The reference and STD spectra were obtained with 1024 and 2048 scans, respectively, with a spectral width of 12 ppm. The STD NMR spectrum was derived by subtracting the off-resonance spectrum from the on-resonance spectrum, employing the phase cycling^{23a, 24}.

4.2.7. Fluorescence anisotropy

Intrinsic Tryptophan Fluorescence intensity of P1 was measured in 20 mM sodium phosphate and 50 mM NaCl buffer (pH 7.4) with Hitachi F-7000 FL spectrometer at 25 °C after and before addition of A β 42 fibril. 280 nm wavelength was used to excite the tryptophan and emission spectra was recorded with a range of 300–400 nm with 5 nm slit width.

Similarly, steady state fluorescence anisotropy was performed on a QM-400 L-format fluorimeter (HORIBA CANADA PTI) keeping all the parameter same and calculated using the following equation²⁵:

$$\text{Anisotropy (R)} = \frac{(FI_{VV} - G \times FI_{VH})}{(FI_{VV} + 2 \times G \times FI_{VH})}$$

Here, FI_{VV} and FI_{VH} are the intensity at a polarizer orientation towards vertically and horizontally plane, respectively. G is the sensitivity factor for the instrument. To determine the apparent dissociation constant (K_D), the anisotropy (R) values were plotted against different concentration of A β 42 fibril addition and fitted using the single site ligand binding model equation:

$$Y = Y_0 + R_{Max} \left(\frac{X}{X + K_D} \right)$$

Here, Y is anisotropy value of P1 in presence of X μ M concentration of A β 42 fibril, Y_0 is the anisotropy values of P1 alone, R_{Max} is maximum anisotropy values and K_D is the dissociation constant during binding process.

4.2.8. Atomic Force Microscopy (AFM)

The AFM studies were carried out using a Bruker BioScope Catalyst AFM instrument, and the included Nanoscope Analysis software was used to analyse them. A β 42 was incubated at 37 °C in absence and/or presence of P1 or P2 for 12 h. Afterward, droplets of samples were deposited onto a clean mica plate (Muscovite Mica, V-1, 20 mm diameter, EMS, Cat. # 71856-04) and left undisturbed for 20 mins to ensure complete binding with the mica surface. Each mica plate was subjected to a single wash with Milli-Q water to remove any excess unbound sample solution. In the final step, the plates were delicately dried using a controlled ultrapure argon stream to protect against contamination or disturbance of the solution layer. The RTESPA-525 probe was used for each experiment.

4.2.9. Serum stability assay

Peptide (P1 or P2) was added at a final concentration of 1 mg/ml in 1 ml of DMEM/F12 media supplemented with 25% (v/v) fetal bovine serum and incubated it at 37 °C. At each respective time point to precipitate serum proteases, 50 ml of the sample was collected and combined with 200 ml of 96% ethyl alcohol at 4 °C. After 15 mins, the cooled precipitated solution was centrifuged at $17,500 \times g$ for 3 mins. A Shimadzu (Japan) reverse-phase HPLC system equipped with a 250 x 4.6-mm C18 column was employed to analyze the reaction supernatant. The elution gradient ranged from 0.1% TFA in 100% acetonitrile to 0.1% TFA in water, performed at a flow rate of 1 ml/min for 30 min. The non-degradable peptide peak intensity was measured at 220 nm, using SPINCHROME CFR software.

4.2.10. Cell viability assay

SH-SY5Y (Human neuroblastoma) cells were cultured in complete DMEM/F12 media (Gibco, USA). Cells were obtained from National Centre for Cell Science (NCCS, India). Media was supplemented at 37 °C with 12% fetal bovine serum, gentamycin (50 μ g/ml), amphotericin B (2.5 μ g/ml), and penicillin-streptomycin (1 unit/ml, (50 μ g/ml) in a 5% humidified CO₂ incubator. All experiments were performed when the cell confluency ranged between 70% and 80%. Living or

viable cells were quantified with MTT assay; which depicts respiration activity of healthy cells through mitochondrial enzymes. These enzymes convert the MTT compound into formazan crystals and the amount of formazan formed represents viable cells. 96-well plate was seeded with 1×10^4 cells/well and incubated for 24 h. Next day, to check the self-toxicity of the peptides, P1 and P2 at various concentrations (1, 5, 10, 20, 50, and 100 μ M) were added, followed by incubation for 24 h. Similarly, cells were treated for 24 h with A β 42 (10 μ M) fibril in the absence and/or presence of peptides P1 and P2 at a ratio of 1:1 and 1:2. In another set, cells were treated with matured A β 42 (10 μ M) alone. Overnight treatment of matured A β 42 (10 μ M) with peptides P1 and P2 at a ratio of 1:1 and 1:2 was also added onto cells for 24 h incubation. Following day MTT was treated with a final concentration of 0.5 mg/ml and incubated at 37 °C for 3.5 h with 5% CO₂ humidity. In a microplate reader, precipitated formazan was dissolved in dimethyl-sulfoxide (DMSO) of 100 μ l and measurement was taken at 570 nm. Results were compared with control samples and expressed as a percentage of control or non-treated cell. The results were compared to control samples and presented as a percentage relative to nontreated cells (control).

4.2.11. Methods for animal experiments

(a) Animal studies and peptide administration:

In order to investigate the toxicity of our peptides P1 and P2 we requisitioned, 30 male C57BL/6J mice weighing around 25-30 g (6-8 weeks old, healthy) from the Bose Institute, Centre for Translational Animal Research (CTAR), Kolkata, India. Mice were kept according to the guidelines and principle of Institutional Animal Ethics Committee (IAEC), using the CPCSEA approved protocol wide IAEC approval No # IAEC/BI/010/2021 dt. 28/09/2021. They were acclimatized in the animal house for two-three weeks with 12 h light/dark cycle. Food and water were provided ad libitum. Every experiment complied and adhered to National Research Council's Guide for the Care and Use of laboratory Animals (NIH Publication No. 8023, revised 1978, U.S.A). All experiments were performed in accordance with ARRIVE guidelines (Animal Research: Reporting of *In Vivo* Experiments; <https://arriveguidelines.org/arrive-guidelines>). Animals were randomly assigned to five groups where peptides P1 and P2 were administered at 5 mg/kg and 10 mg/kg body weight along with control set receiving PBS only. The dosage was decided keeping in mind our biophysical and cell biology experiments previously done to their efficacious dosage. Peptides were dissolved in PBS and administered intraperitoneally once a week

for four consecutive weeks. The respective dosage of control, P1 and P2 (5 mg/kg and 10 mg/kg) was injected inside the peritoneal cavity very slowly with 26-gauge 1 ml DISPOVAN needle according to their pre-calculated body weights.

(b) Histological and biochemical Assays with demographic parameters:

At the end of four weeks of treatment, the body weights of the animals were measured and the animals were sacrificed by decapitation. Biochemical parameters from the mice serum including urea, creatinine, glutamic oxaloacetic transaminase, and glutamic pyruvic transaminase were analyzed for their sub-chronic toxicity of P1 and P2 administration by using commercially available diagnostic test kits (ARKRAY Healthcare Pvt. Ltd., India). Cell counter and automatic analysis machine was used for blood parameters estimation.

The heart, lung, kidney, liver, and spleen were isolated and fixed onto 10 % neutral buffered formalin for nearly 24-48 h followed by immersion in paraffin wax. Tissue slices were meticulously cut with a microtome to a thickness of 5 μ m. For histological examinations, slides were stained with hematoxylin and eosin (H&E staining), Masson trichrome and periodic acid Schiff. The light microscope (NIKON T₂, India) was used to visualize the stained slides for histopathological alteration, and images were captured at 10x and 40x magnification.

4.2.12. Study of cellular apoptosis by Annexin-V and PI staining

SH-SY5Y cells were seeded with a density of 1×10^6 cells per well onto a 6-well plate. The cells were treated after 24 h with 10 μ M A β 42 alone and with P1, P2 at a ratio of 1:1 and 1:2 (A β 42: Peptide) and cells were further incubated for 24 h. Untreated cells and cells treated with buffer were kept as unstained and controls respectively. Post-treatment, cells were trypsinised and resuspended with annexin binding buffer (Cat no. 51-66121E, BD Biosciences). 3 μ l Annexin V-APC (BioLegends, Japan) and 5 μ l PI (Sigma-Aldrich) were added to the cells, carefully vortexed and incubated at room temperature in the dark for 15 mins. After incubation cells were quantified with flow cytometer (FACS Verse, BD Biosciences). Data was analysed using the BD FACS Suite software with 10,000 cells for each sample. Three independent experiments were performed for each set.

4.2.13. Molecular Docking study

Peptide and protein preparation: P1 peptides coordinates were built in 3D sketcher and prepared by using protein preparation tools with Schrödinger suite of programs ²⁶. The solution structure of A β with PDB: 2LFM ²⁷ prepared for docking using protein preparation tools. Any violations in bond orders, missing atoms were corrected, and structure was energy minimized using OPLSe force field with Schrödinger suite of programs ²⁶.

Peptide docking: Using the results of P1 induced chemical shift perturbed of A β 42 residues were used defined the site point for molecular docking the peptide P1 in GOLD molecular docking program ²⁸ using default settings. GOLD Chem PLP ²⁹ and gold scoring functions ²⁸ were used to the score the peptide binding affinity.

4.3. Results and Discussion

4.3.1. Peptide design

Our previous study, employing NMR and docking techniques, elucidated that the interaction between NF11 and A β 40 inhibits amyloid fibril formation, stabilizing the complex (A β 40:NF11), primarily through the involvement of NF11 residues R4, W5, R9, and F11. In this present study, we have used R⁴WSLMRPF¹¹ (RF8) fragments of NF11 and its synthetic modified derivatives to enhance therapeutic potential (Scheme 4.1B). In order to enhance the thermal stability of the RF8-series peptide, we replaced serine residues with cysteine in RF8, yielding the RF8C peptide ³⁰. A further peptide analogue of RF8 substituting L-proline to D-proline, was also synthesized. It is important to note that the inclusion of proline induces bending in the peptide, prompting folding and hydrogen bond formation, resulting in a β -hairpin structure ³¹. RF8R peptide was designed to reverse the sequence of RF8. We introduced acetyl group (Ac) in N-terminal of RF8 to construct PA peptide. Previously, it was reported that 2-aminobenzoic acid (Ant) functions as a β -breaker by conformational restriction, and offers a notable advantage in resisting proteolytic degradation ^{12a, 17}. For this purpose, we synthesized and characterized P1 and P2 peptides by replacing serine residues with Ant moiety, anticipating an enhancement in their inhibitory effectiveness (Appendix 4, Figures S4.1 and S4.2).

4.3.2. The RF8-series peptides effectively modulate A β 40 aggregation kinetics

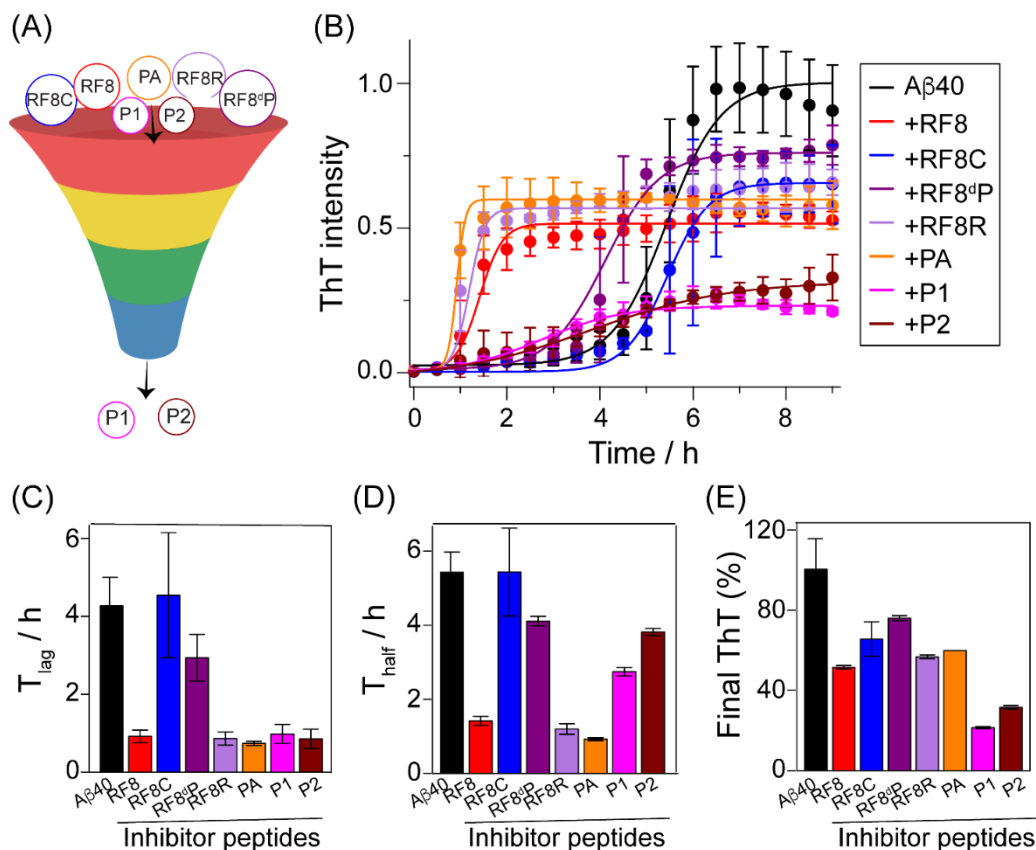


Figure 4.1: Effect of RF8-series peptides on aggregation kinetics of A β 40. (A) The schematic depicts screening of more potent inhibitors against amyloid fibril formation. (B) Normalized ThT kinetics of A β 40 (5 μ M) in presence and/or absence of equimolar RF8-series peptides at 37 $^{\circ}$ C. The corresponding bar plot of (C) T_{lag} , (D) T_{half} and (E) % final ThT intensity were obtained from Boltzmann fitting. The error bars represent the standard deviation for three individual experiments.

A deep understanding of amyloidogenic pathways and the identification of toxic intermediate stages enable targeted screening of inhibitors, enhancing the efficacy of therapeutic strategies against amyloid-related diseases (Figure 4.1A). The effect of RF8 series peptide on A β 40 aggregation kinetics was evaluated by Thioflavin T (ThT) assay which measures fluorescence upon binding to cross β -sheet structures³². The time dependent aggregation kinetics of A β 40 followed a conventional nucleated-growth mechanism without inhibitors, showing immediate fibril elongation and reaching a plateau at 6 h (Figure 4.1B). The time dependent ThT intensity data were fitted using a sigmoidal equation (solid lines) to derive kinetic parameters. A β 40

displayed a distinct lag phase lasting 256 ± 44 min, followed by an elongation or growth phase, and ultimately reached saturation with a half-life (T_{half}) of approximately 326 ± 32 min (Figures 4.1C-E). The introduction of the RF8 peptide and its derivatives at 1:1 molar ratio of $[A\beta 40]/[\text{peptide}]$ resulted in a modification of the fibrillation rate of $A\beta 40$, as observed through changes in the lag time and a reduction in the final fibril mass (Figures 4.1B-E). In the presence of RF8, RF8R, and PA peptides, there was an observed reduction in lag time and half-life time of aggregation kinetics, with nearly comparable patterns, along with approximately 50% decrease in the total amount of fibril formation (Figures 4.1B-E). In the presence of RF8dP peptide, both T_{lag} and T_{half} increased compared to previous peptides, but only achieved a 20% inhibition of fibril

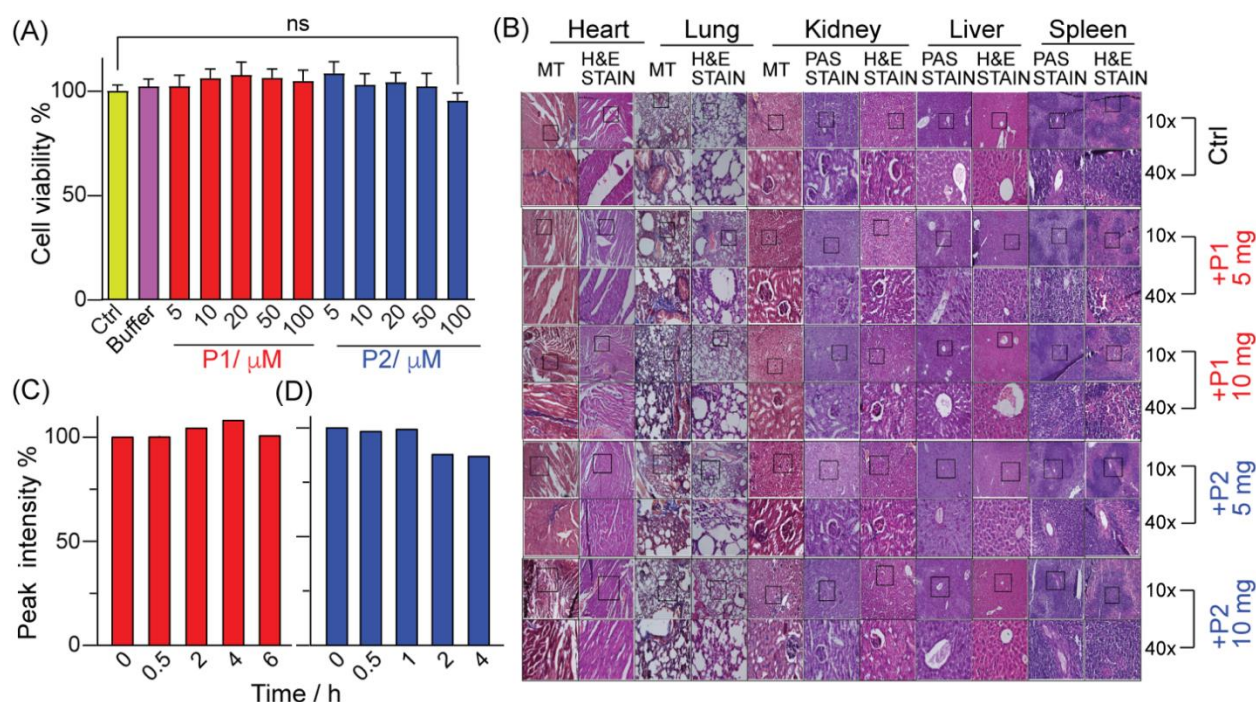


Figure 4.2: The characterization of P1 and P2 peptides *in vivo*. (A) Viability of SH-SY5Y cells upon treatment with a graded concentrations of Peptide P1 and P2 up to 100 μM . Only media served as a control. Values are represented as mean \pm SEM ($n = 6$). Statistical analysis was done by one-way ANOVA. (ns and ctrl denote non-significant and control cells, respectively). (B) Histopathological studies corresponding to sub-chronic toxicity in mice ($n=6$ each group) by treatment with Peptide P1 and P2 at a concentration of 5 mg/kg and 10mg/kg body weight. Ctrl-control mice treatment with PBS as vehicle. 10x and 40x magnified images of heart, lungs, kidney, liver, and spleen are shown. PAS-periodic acid-Schiff; H&E-hematoxylin-eosin; MT - Massen Trichome. The stability of (C) P1 and (D) P2 peptides in serum at different time intervals.

formation (Figures 4.1B-E). RF8C showed minimal effect on both lag time and T_{half} , yet it led to a 30% reduction in A β 40 fibrillar forms (Figures 4.1B-E). Interestingly, in the presence of equimolar P1 and P2, there was a dramatic decrease in ThT intensity by nearly 80% and a shorter lag time observed compared to A β 40 alone, indicating alterations in their structural transformations during fibrillation (Figures 4.1B-E). Therefore, P1 and P2 demonstrated superior inhibitory activity against A β 40 fibril formation compared to the other peptide in the series. Thus, the subsequent segment of this study predominantly concentrated on the inhibitory effects of P1 and P2.

4.3.3. Evaluation of acute and Sub-chronic Toxicity of P1 and P2 in-vivo

After observing promising outcomes of P1 and P2 peptides in inhibiting the aggregation of A β 40, we performed reduction of the tetrazolium compound 3-(4,5-dimethylthiazol-2-yl)-2,5-diphenyltetrazolium bromide in living cells by mitochondrial NAD(P)H-dependent dehydrogenase enzymes based MTT assay ³³. At preliminary stages the cytotoxicity of the peptides itself in a graded concentration manner were tested in SH-SY5Y cells, which is considered a model cell line for amyloid related experiments (Figure 4.2A) ³⁴. As shown in Figure 4.2A there was no discernible cytotoxicity against P1 and P2 upto a maximum concentration of 100 μ M. Hence these peptides were deemed to be non-toxic in cellular models.

Further on toxic nature of peptides was tested *in-vivo* C57BL6/J mice models. C57BL6/J mice is considered as a model organism for AD or Parkinson's disease related studies ³⁵. A total of 30 mice were recruited for the study and divided into 5 groups having 6 mice per group. Peptides P1 and P2 at a concentration of either 5 or 10 mg/kg body weight were administered intraperitoneally once a week for a period of four weeks. During treatment, no mortality, or changes in the behavioral pattern of the mice were observed for each group (Figure S4.3). The demographic parameters of the mice such as body weight and isolated organs weight remain unchanged throughout the course of treatment (Appendix 4, Figures S4.3A and S4.3B). These organs were carefully sectioned and stained with Haematoxylin-eosin (H&E), Masson's Trichrome (MT) and Periodic acid Schiff (PAS) to understand the overall tissue microanatomy and underlying cytoarchitectural changes in response to treatment. Overall microanatomy and tissue architecture remained unchanged in case of P1 at 5 mg and 10 mg per kg body weight (Figure 4.2B). In case of P2 noticeable changes were observed in the higher dosage of 10 mg/kg body weight where the tissue structure of the heart and lungs were slightly dilapidated in compared to control (Figure

4.2B). The glomerulus appeared to be small and defragmented at places and the spleen had changes in overall cellular mass and glycolipid composition appeared to be different than control group (Figure 4.2B and Appendix 4, Figure S4.3B). Slight changes were also observed in P2 in 5 mg/kg dosage in comparison to control group (Figure 4.2B). Besides this tissue histopathological changes, we also tested the haematological parameters in the blood obtained from mice after complete treatment regimen. P2 with 5 mg/kg treatment showed anomalous parameters in respect to control group along with elevated levels of W.B.C and platelet. Rest of the groups including P1 showed parameters within normal range when compared to control group (Table S4.1). Biochemical analysis of blood serum was also done to obtain the metabolite-based toxicity parameters. Slightly elevated levels of serum creatinine and serum glutamic pyruvic transaminase was observed in P2 10 mg/kg treatment group suggesting changes in biochemical profile in kidney and liver respectively (Table S4.1 and Appendix 4, Figure S4.4). Although none of the other groups showed any kind of discernible changes when compared to control group (Table S4.1 and Appendix 4, Figure S4.4). Overall reports obtained from *in-vivo* toxicity studies suggested that P2 might have some inflammatory and toxic effects *in-vivo* but P1 is completely safe and further use in other preclinical studies can be undertaken.

In the process of developing peptide-based drug molecules, it is essential for the peptide to remain stable against enzymatic degradation in serum, which contains a variety of proteases capable of breaking peptide bonds. To evaluate the potential stability of P1 and P2 peptides, we measured the expected degradation of P1 and P2 peptides in fetal bovine serum. Surprisingly, the P1 peptide remained fully intact even following a 6 h incubation period in serum (Figure 4.2C). This may be attributed to the Ant moiety, which contributes to enhancing resistance for proteolytic degradation of P1 by introducing conformational restrictions to the peptide backbone. In contrast, ~20% degradation of P2 peptide was occurred after being exposed to serum for 2 h (Figure 4.2D). This indicates the presence of Ant moiety in between W and L residues in P1 gives more stability than the presence of terminal Ant moiety in P2.

4.3.4. P1 and P2 inhibits A β 42 fibrillation

Next, we examined A β 42 fibril formation *in vitro*, with and without P1 and P2 peptide, using a highly reproducible ThT-based protocol. A β 42 aggregation kinetics, as detected in ThT assay, typically follows a sigmoidal pattern, characteristic of amyloid fibrillation (Figure 4.3A). As depicted in Figure 4.3A, P1 reduced fluorescence intensity in a dose-dependent manner and

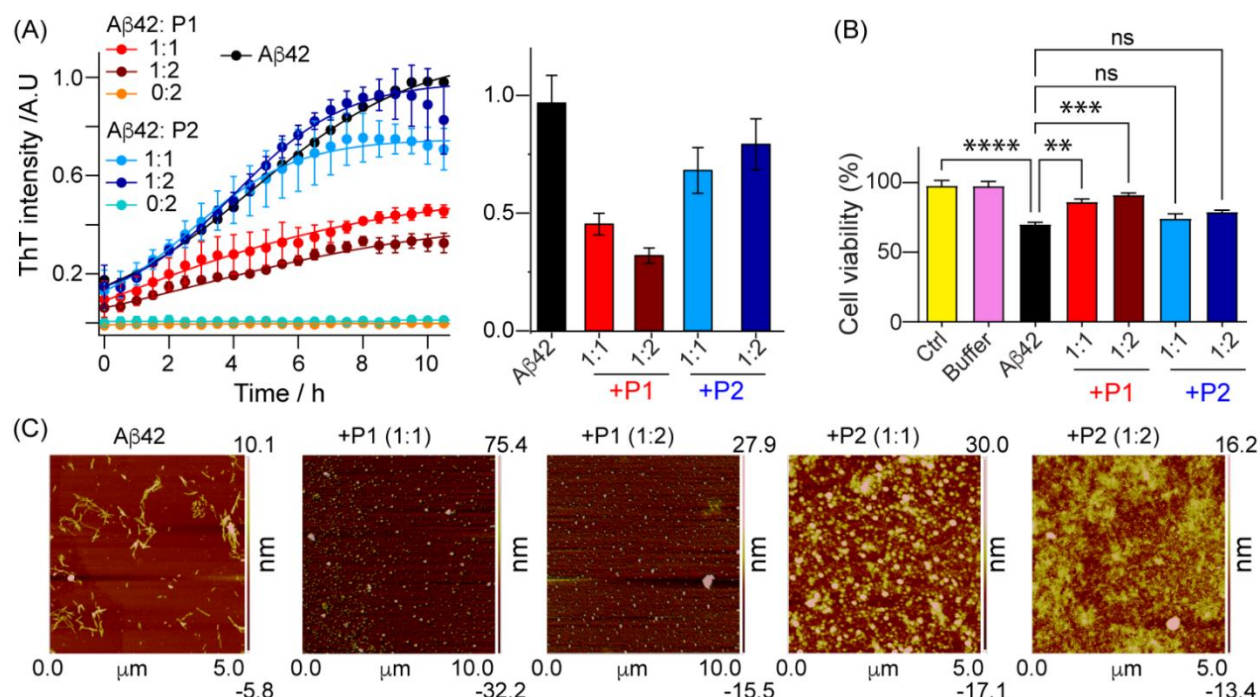


Figure 4.3. The inhibitory effect of P1 and P2 peptides on the aggregation kinetics of Aβ42 fibril. (A) ThT kinetic profiles of Aβ42 (10 μM) at 37 °C in absence or presence of P1 and P2 at 1:1 and 1:2 molar ratio of (Aβ42: Peptide) in 20 mM sodium phosphate and 50 mM NaCl buffer at pH 7.4. The bar plot of final normalized ThT intensity of corresponding aggregation kinetics. (B) SH-SY5Y cells were treated with Aβ42 alone and with Peptides P1 and P2 at a ratio of 1:2 of Aβ42: P1 and P2. Values are represented as mean ± SEM, n=9. Significance was calculated between control and Aβ42 alone by one way ANOVA and Dunnett's multiple comparisons test. Unpaired two tailed T-test were performed between Aβ42 alone and Aβ42+P1 and P2. ns, **, ***, **** denotes non-significant, p<0.01, p<0.001 and p<0.0001, respectively. (C) AFM images of Aβ42 fibril in absence and presence of P1 and P2 with the ratio of Aβ42 to peptide 1:1 and 1:2.

specifically, a 2-fold molar excess of P1 led to ~75% inhibition of Aβ42 fibril formation, suggested P1 prevents primary nucleation event. Contrastingly, the addition of equimolar excess of P2 resulted in a ~25% inhibition of Aβ42 amyloid formation, whereas a two-fold molar excess of P2 did not enhance efficacy, implying a lack of dose-dependency (Figure 4.3A). These results indicate P1 prevents Aβ42 aggregation more efficiently than P2. The fluorescence intensity of P1 and P2 alone remained unchanged with time (Figure 4.3A). It was important to mention that exploring the C-terminal portion of the Aβ peptide could elucidate the dynamic interplay between toxicity and the aggregation of peptide molecules. Previously, our group investigated the aggregation kinetics of 20-residue peptide fragment (AV20) derived from the C-terminal segment of Aβ40³⁶.

Interestingly, P1 inhibited AV20 aggregation whereas P2 exhibited accelerated aggregation kinetics of AV20 (Appendix 4, Figure S4.5). Overall, our results suggest that P1 serves as a potent inhibitor against the amyloid fibril formation of A β 40, A β 42, and AV20.

Various toxic effects of A β species on neuronal cells were well documented³⁷. Therefore, we investigated the role of ergonomically designed peptides P1 and P2 against the amyloidogenic regions of A β 42. The potential role of these peptides against A β 42 species mediated cellular damage or death were investigated using MTT reduction assays. SH-SY5Y cells were incubated with A β 42 (10 μ M) alone and in the presence of P1/P2 at a ratio of 1:1 and 1:2 for A β 42: Peptide. Cell viability was reduced to ~70% in the presence of A β 42 alone, which was significantly recovered at around ~ 85-90% in the presence of P1, at a ratio of 1:1 and 1:2 of A β 42: P1 (Figure 4.3B). The recovery of cell viability was also observed for P2 but limited to around ~70-80% (Figure 4.3B). These data show the potential effect of designed peptides against A β 42 cytotoxicity, where P1 is more potent than P2.

AFM images corroborate well with ThT fluorescence findings by analyzing the alterations in the morphology of A β 42 aggregates in the presence of inhibitory peptides (P1 and P2). AFM detected the existence of elongated, denser, branching fibrils in incubated A β 42 samples with an average length of 791 nm (Figure 4.3C). In contrast, no characteristic fibrillar structure was observed when co-incubated with P1. In the presence of P1 at 1:1 and 1:2 molar ratios of A β 42/P1, spherical-shaped amorphous aggregates were identified (Figure 4.3C). On the other hand, A β 42 incubated with 1:1 and 1:2 concentration of P2 exhibited amorphous-like aggregates (Figure 4.3C). The appearance of non-toxic, amorphous aggregates indicates that P1 induces the aggregation of A β 42 away from its typical pathway towards off-pathway aggregation.

4.3.5. Conformational variation of A β 42 in presence of P1 drives the off pathway aggregate formation

In order to determine the effect of inhibitor P1 on the conformational conversion of A β 42 during aggregation, far-UV CD spectroscopy was employed for monitoring the development of secondary structure of A β 42 over time in presence and absence of P1. At the start of incubation, A β 42 alone exhibited a negative band near 198 nm, indicating A β 42 predominantly adopt a random coil conformation (Figure 4.4A). After 12 h of incubation, the 198 nm peak diminished and shifted to

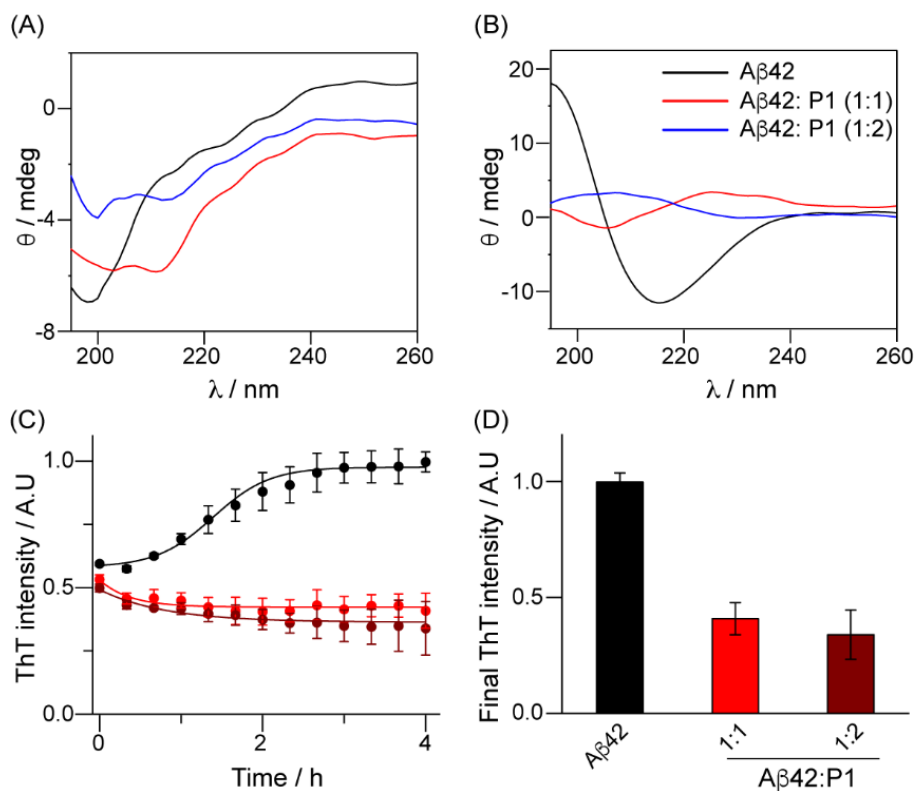


Figure 4.4. P1 induces conformational changes to form off pathway aggregates. Far UV CD spectra for Aβ42 in presence or absence of 1 and 2-fold molar excess of P1 at (A) 0 h and (B) incubated at 37 °C for 12 h. (C) ThT aggregation kinetic of Aβ42 in absence (black) and presence of P1 at ratios of Aβ42-to P1 of 1:1 (red) and 1:2 (brown) in the presence of 25 % seeds. (D) Final ThT intensity value of Aβ42 and Aβ42+P1 in presence of 25% seeds.

about ~218 nm, indicating a transition towards a β -sheet-rich conformation in Aβ42 (Figure 4.4B). The CD spectra of Aβ42 in the presence of P1 at a molar ratio of 1:2 exhibited a shift towards around 200 nm, resembling the spectrum of Aβ42 with P1 at 0 min. Additionally, when combined with P1, the CD amplitudes at 218 nm increased in comparison to Aβ42 alone (Figure 4.4B). Taken together, the results indicate that P1 effectively redirected the formation of toxic amyloid beta fibrils into unstructured off-pathway non-toxic species.

To further investigate the impact of P1 on Aβ42 aggregation, seeding experiments were conducted by introducing sonication-generated fibril fragments into Aβ42 monomer solutions that promoted immediate growth of fibrillar structures. In Figure 4.4C, the immediate addition of 25% seeds to Aβ42 samples initiated a rapid increase in ThT fluorescence, signifying the onset of Aβ42 aggregation. We found that the addition of P1 of 1:1 and 1:2 molar ratio delayed the elongation

process and decreased fibrillar mass compared to A β 42 samples with only 25% seeds (Figures 4.4C-D), confirming P1-induced fibrillar species disrupt A β 42 fibril elongation by promoting an alternative 'off-pathway' aggregation.

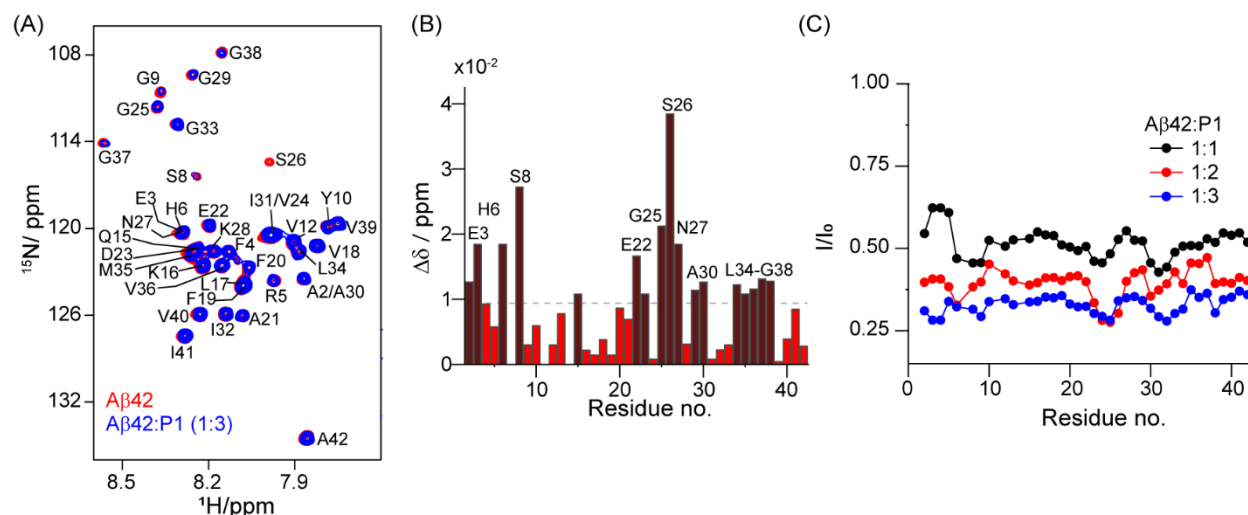


Figure 4.5: Atomistic insight into the interface of inhibitory mechanism. $^1\text{H}/^{15}\text{N}$ -HSQC spectra of ^{15}N labeled A β 42 (80 μM), before (red) and after (blue) addition of (A) P1 at 1:3 molar ratio (A β 42:P1). The NMR was recorded on Bruker AVANCE III 700 MHz, equipped with a QCI Cryoprobe, at 286 K. The chemical shift perturbation (CSP) value of (B) A β 42:P1 present at 1:3 molar ratio. The grey threshold line represents the average of all CSP and brown bar of residues indicates higher CSP values. (C) Running average signal intensity (I/I_0) of for three consecutive residues of A β 42 in the presence of P1 at a molar ratio of 1:1 (black), 1:2 (red) and 1:3 (blue), respectively.

4.3.6. Mechanistic insight of binding interaction using NMR

To investigate the interaction between A β 42 and P1, we studied the binding mechanism of P1 with A β 42 using 2D ^1H - ^{15}N HSQC NMR spectroscopy. The NMR spectra of ^{15}N -labeled A β 42 was obtained for [A β 42]/[P1] molar ratios of 1:0, 1:1, 1:2 and 1:3 in 90% 20 mM sodium phosphate with 50 mM NaCl and 10% D_2O (pH 7.4) at 286 K (Figure 4.5). The conditions were established to keep dissolved A β 42 in its monomeric and stable state. The addition of P1 led to the substantial changes in the amide-NH region of the NMR spectra (Figure 4.5A). The residues including A2, E3, H6 and S8 from N-terminal flexible region and E22, G25, S26, N27, G29, A30, L34, M35, V36, G37, G38 from α -helix region exhibited perturbations above the threshold chemical shift perturbation (CSP) values when P1 was present at a molar ratio of 1:3 [A β 42]/[P1] (Figures 4.5A-B). The detected perturbations imply that the addition of P1 alters the local chemical environment

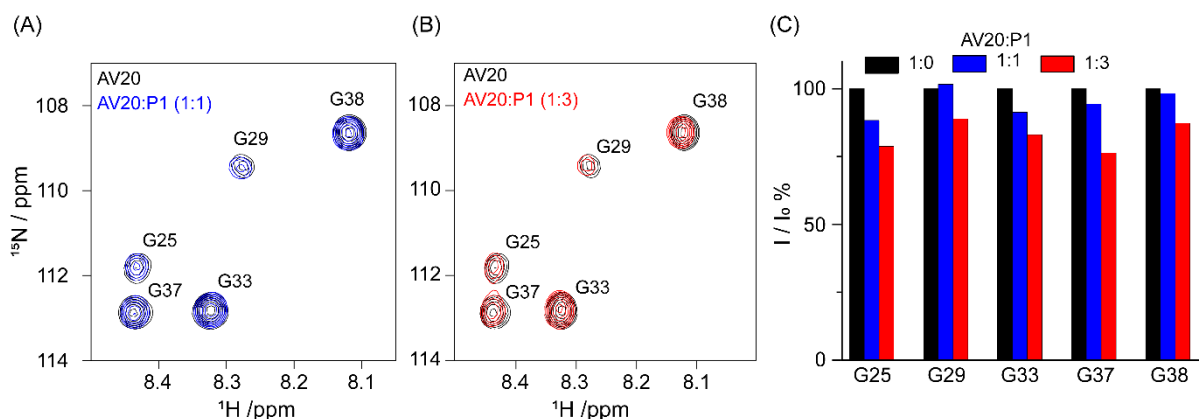


Figure 4.6. 2D ^1H - ^{15}N HSQC NMR spectra for AV20 (80 μM) dissolved in 20 mM sodium phosphate and 50 mM NaCl, pH 7.4, in the absence (black) and / or presence of P1 at (A) 1:1 (blue) and (B) 1:2 (red) molar ratio. NMR spectra were recorded at 290 K on Bruker AVANCE III 700 MHz. (C) % of intensity broadening (I/I_0) of five glycine residues of AV20 with increasing the concentration of P1.

surrounding these residues. Titrating the A β 42 with P1 at equimolar ratio (1:1) resulted in sequential region-specific line broadening for H6-Y10, D23-S26 and G29-I32 segments (Figure 4.5C). Increasing P1 concentration at 1:2 molar ratio ($[\text{A}\beta 42]/[\text{P1}]$) led to higher line broadening effects with a consistent pattern (Figure 4.5C). At a 1:3 molar ratio of P1, there was a notable $\sim 70\%$ drop in signal intensity, indicating direct association between N-terminal and C-terminal residues of A β 42 with P1 (Figure 4.5C). A potential binding site for P1 on A β 42 was suggested

by the CSP as well as significant loss of signal intensity specifically, within the stretches of E³FR⁵ from N-terminal and G²⁵SN²⁷, I³¹IGL³⁴, G³⁸VV⁴⁰ from C-terminal. Recent research have revealed the dock-lock mechanism of A β fibril formation, in which unstructured A β monomers briefly bind to fibril surfaces before integrating into the primary lattice³⁸. P1 may disrupt crucial domain interactions, altering A β 42 fibrillation by interfering with monomer dock-lock interactions. Reportedly, the overall three-fold symmetric structure of the fibril is stabilized by significant interfilamentous connections established by R5, D7, and S8 at the N-terminus³⁹. Interacting with N-terminal residues, P1 made these segments inaccessible, thereby disrupting the interfilamentous connections crucial for A β 42 amyloidogenesis. Further, the repeated GxxxG motif (G²⁹xxxG³³ and G³³xxxG³⁷) found in the C-terminus is a distinctive characteristic shared by A β , crucial for stabilizing helix-helix and sheet-to-sheet interactions⁴⁰. The GxxxG motif extends the lifespan of toxic oligomers and is critical for cellular toxicity due to a greater conformational flexibility⁴¹.

The higher line broadening effect observed in the C-terminal region of A β 42, highlighting a prominent role of this hydrophobic-rich stretch for intermolecular interaction with P1.

Furthermore, in order to comprehend the impact of the C-terminus, we performed 2D ^1H - ^{15}N HSQC NMR of selectively ^{15}N -labeled the glycine residues within the GxxxG motifs of AV20, both in the absence and presence of P1, at molar ratios of 1:1 and 1:3. We observed that the glycine residues of AV20 exhibited CSP and line broadening in a dose-dependent manner when P1 was introduced, indicating binding to the GxxxG motif of AV20 (Figure 4.6). The interaction between P1 and the hydrophobic segments containing the GxxxG motif explains the decreased membrane damage and cytotoxicity observed, as these segments disrupt membrane integrity by internalizing into the lipid membrane's hydrophobic acyl region.

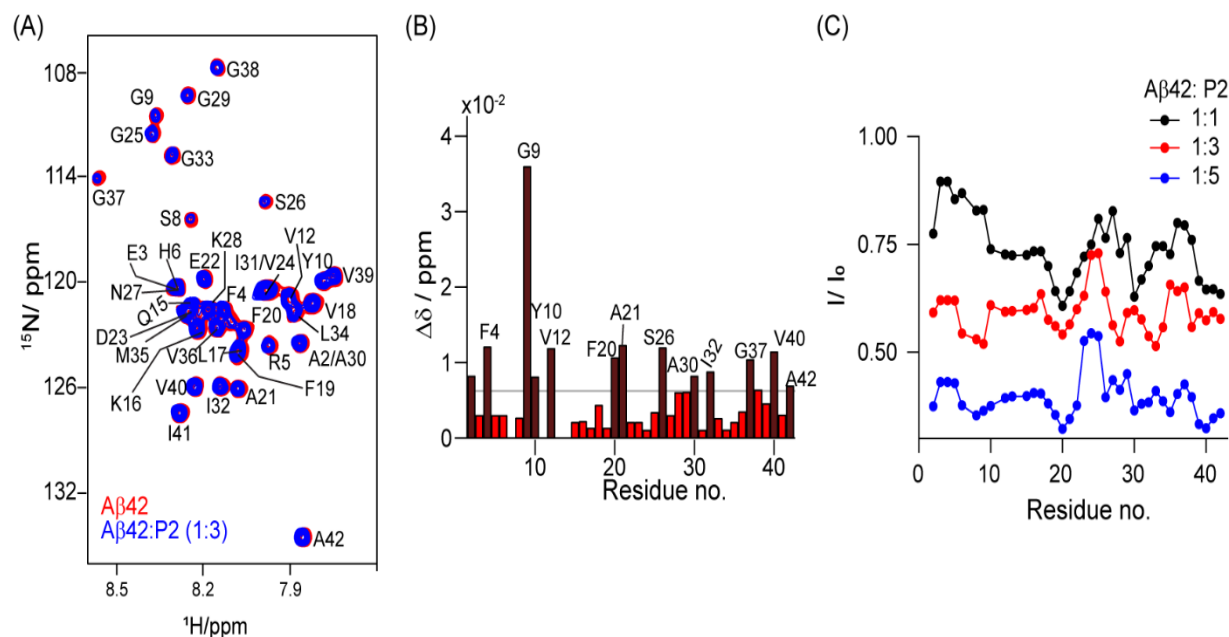


Figure 4.7. (A) $^1\text{H}/^{15}\text{N}$ -HSQC spectra of ^{15}N labeled A β 42 (80 μM), before (red) and after (blue) addition of P2 at 1:3 molar ratio (A β 42:P2). The NMR was recorded on Bruker AVANCE III 700 MHz, equipped with a QCI Cryoprobe, at 286 K. (B) The chemical shift perturbation (CSP) value of A β 42:P2 present at 1:3 molar ratio. The grey threshold line represents the average of all CSP and brown bar of residues indicates higher CSP values. (C) Running average signal intensity (I/I_0) of for three consecutive residues of A β 42 in the presence of P2 at a molar ratio of 1:1 (black), 1:3 (red) and 1:5 (blue), respectively.

Similarly, the atomistic insight into the mechanism of A β 42 in the presence of P2 was monitored using 2D ^1H - ^{15}N HSQC NMR at variable sub stoichiometric concentrations (Figures 4.7). At a 1:3 molar ratio, as depicted in Figure 4.7, A β 42 residues showed lower signal intensity reduction and CSP in the presence of P2. This suggests that P2 did not effectively induce structural rearrangement in A β 42. HMQC profiles at 1:3 molar exhibited moderate CSPs, primarily involving N-terminal residues such as F4, G9, Y10, and V12, the central segment containing F20 and A21, and C-terminal hydrophobic residues, including S26, A30, I32, G37, V40, and A42 (Figure 4.7B). In the presence of a 1:3 molar ratio of [A β 42]/[P2], residue-specific gradual changes in signal intensity were observed for the A β 42 backbone residues, particularly in segments H⁶DSG⁹, V¹⁸FFA²¹, I³²GL³⁴ and G³⁸VVIA⁴² of A β 42 (Figures 4.7C). Further, a substantial loss of signal intensity was observed in A β 42 spanning regions F¹⁹-E²² and A³⁰-I³² upon decreasing the concentration to 1:1 ([A β 42]/[P2]) (Figure 4.7C). As the P2 concentration increased, broad segments were observed for A β 42 spanning from H6 to Y10, F19 to A21, A30 to I32, and V39 to I41, indicating potential interaction sites of P2 with A β 42 at 1:5 molar ratios (A β 42:P2) (Figure 4.7C).

Upon addition of P1 and P2, A β 42 exhibited concentration-dependent broadening of NMR peaks and a reduction in overall signal intensity due to fast intermediate exchange regime between free and P1 or P2 bound A β 42 complex at NMR time scale (Figure 4.8A). The overall signal intensity values were plotted against peptide concentration and fitted with a single-site binding model equation to calculate apparent decay constant (K_D). The P1-A β 42 monomer complex has a K_D of $37.67 \pm 9.5 \mu\text{M}$, while the P2-A β 42 monomer complex has a K_D of $80.15 \pm 27.6 \mu\text{M}$ (Figure 4.8B). Strong binding affinity of P1 to the A β 42 monomer compared to P2 may be attributed to the presence of R and W residues in the N-terminal of P1, responsible for salt bridge and π -alkyl interactions with A β 42 residues.

Further, one-dimensional saturation transfer difference (STD) NMR was performed to identify and characterize the binding epitope of P1 to A β 42 fibrils (Figure 4.8C). In this methodology, effective magnetization is transferred from the A β 42 fibril to the protons of P1 through spin-diffusion, particularly those in close proximity to the fibril. No STD signal was detected from P1 alone, at the specified on-resonance frequency of -1 ppm (Figure 4.8Ciii). Interestingly, strong saturation transfer difference (STD) signals were observed for the indole ring protons of W2, benzene ring of Ant3, and phenyl ring protons of F8 of P1 upon addition of matured fibrils (Figure 4.8Cii). This observation suggests efficient magnetization transfer from the fibrils to P1 aromatic residues that

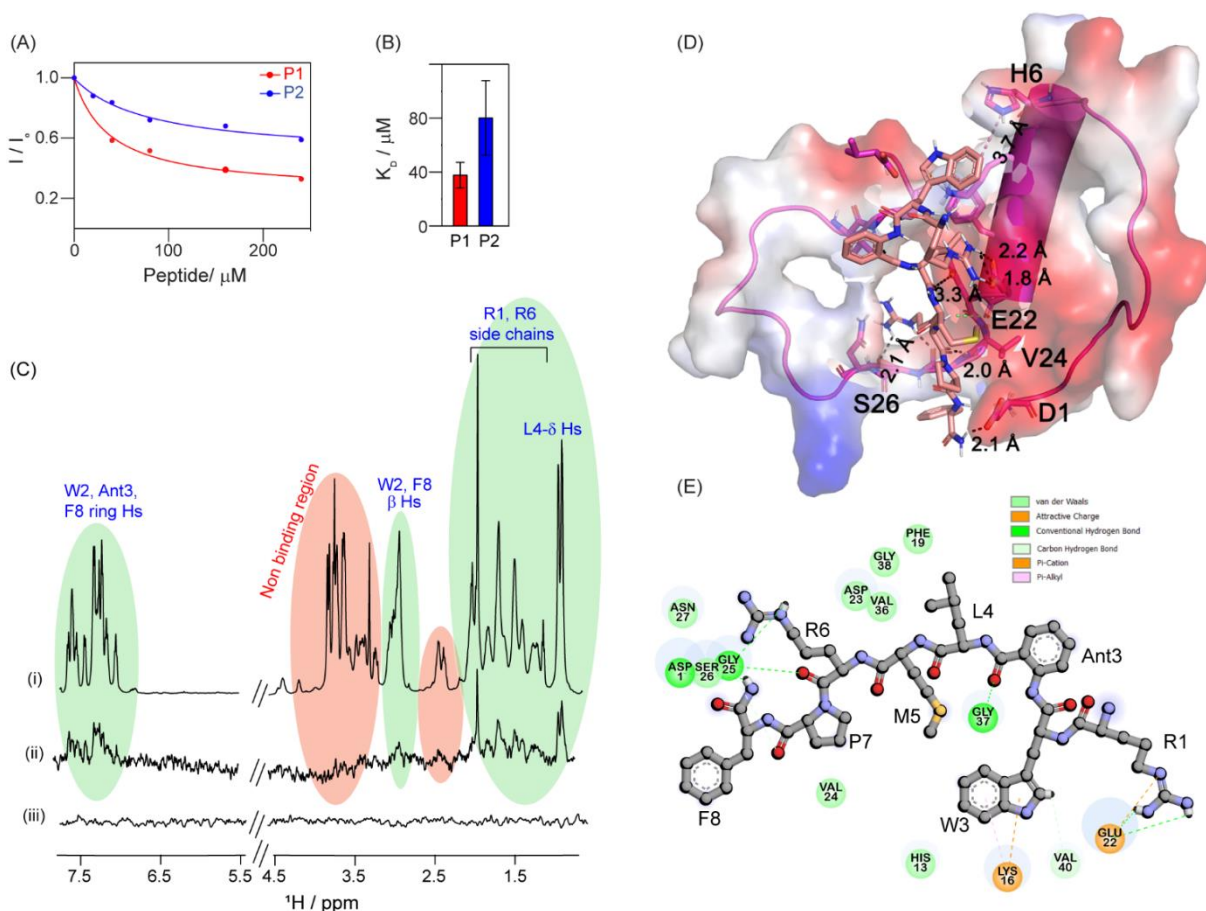


Figure 4.8: Mapping of binding epitope. (A) Relative change of NMR intensity of Aβ42 monomer upon titration with P1 (red) and P2 (blue) peptide. (B) Calculated apparent dissociation constant (K_D) based on a single site binding model fitting. (C) Group epitope mapping of P1 was performed using one-dimensional ^1H STD in 100% D_2O . The reference NMR spectra (i) and STD NMR spectra of P1 in presence (ii) and absence (iii) of Aβ42 fibrils at 1:300 molar ratio ($\text{A}\beta_{42}\text{Fibril}:\text{P1}$). NMR experiments were executed using the Bruker Avance III 500 MHz NMR spectrometer at 298 K. (D) Predicted binding mode of P1. Transparent electrostatic potential surface view of P1 cartoon model of Aβ42. (E) 2D Interaction diagram of P1 Peptide with Aβ42. R1, Ant3, R6 residues of P1 mediated hydrogen bonding interactions with E22, G37, and S26 residues were highlighted in green. π -cation interaction of R1 / W2 with E22 / K16 were highlighted in orange. π -alkyl and van der Waal interaction are highlighted in light green.

are closer proximity to Aβ42 fibril. In addition, notable STD effects were observed for the aliphatic protons C^βHs , C^γHs , and C^δHs of R1 and R6, along with the C^δHs of L4 whereas, minimal STD effects were noted for the C^βHs of W2 and F8 (Figure 4.8Cii).

Furthermore, to get an insight into molecular interaction of the P1 peptide with A β , we have employed chemical shift perturbed residues of A β 42 as interaction site points and evaluated the binding pattern of the peptide P1 poses with the peptide P1 binding epitopes knowledge gained from our STD binding experiments. As the NMR experiments of P1 with A β 42 were performed in aqueous environment, we have used NMR structure (2LFM.pdb) to simulate the structure of such native state. Our molecular docking results show that the peptide P1 bind to A β with a very high ChemPLP fitness score of 79.6. The P1 was docked into deep cavity between the N and C-terminus (Figure 4.8D) and was involved in a multitude of polar interactions / π -alkyl interactions with the main chain and side chain atoms of A β 42, respectively (Figure 4.8E). R1 of peptide P1 mediates salt bridge interactions with carboxyl group of E22 (1.8 Å, 2.2 Å) of A β peptide. W2 of the peptide P1 would get engaged in face to edge π -alkyl interactions (3.7 Å) with H6 residue, π -cation interaction with K16 (2.7 Å), and van-der-Waals contacts (2.3 Å, not shown for clarity) with V40 main chain atoms of A β peptide. Ant₃ of P1 interacts with its main chain carbonyl (C=O) atoms was engaged in hydrogen bonding to the main chain NH₂ atoms G37 (2.0 Å) of A β 42. The L4 main chain carbonyl atoms of P1 were in van der Waal contacts (3.3 Å) with E22 carboxylic side chain atoms. The side chain atoms of R6 residue of P1 pentapeptide was anchored in hydrogen bonding interactions (2.1 Å) with S26 hydroxyl side chain atoms of A β 42. Interestingly, the P7 main chain amide atoms of peptide P1 maintain van der waals contact with V24 main chain NH₂ (2.0 Å, respectively) of A β 42. The terminal NH₂ atoms of F8, residue of P1 was engaged in π -alkyl interactions with D1 (2.1 Å) residues. The molecular docking results are completely on agreement with HSQC NMR data where P1 particularly interacts with N and C-terminal residues to stabilize the complex.

4.3.7. P1 and P2 peptides effectively disintegrate A β 42 matured fibril into nontoxic fragments

Mature fibrotic aggregates of A β in the brains of AD patients persist over time and can catalyze secondary nucleation reactions, accelerating the formation of toxic oligomers from monomers, effectively acting as seeds for oligomerization⁴². Thus, disrupting the A β aggregates may be an effective approach for reducing toxicity in neuronal cells. To evaluate the stability of A β 42 fibrils in the presence of P1 and P2, we incubated preformed A β 42 fibrils with P1 and P2, maintaining the same stoichiometric ratios as those utilized in the inhibition experiments. In Figure 4.9A, a dose-dependent immediate drop in ThT intensity indicated the disaggregation of matured A β 42

fibers upon the introduction of P1 and P2. When treated with P1 at molar ratios of 1:1 and 1:2 ($[A\beta_{42}^{Fibril}]/[P1]$), final ThT fluorescence intensity of mature $A\beta_{42}$ fibrils decreased by approximately 50% and 65%, respectively (Figure 4.9A). Additionally, in Figure 4.9A, the final ThT fluorescence intensity of matured fibers decreased by ~30% when treated with P2 compared to $A\beta_{42}$ fibrils. This suggests that P1 peptide has more ability than P2 to disrupt preformed $A\beta_{42}$ fibrils, which could have implications for their potential therapeutic use in AD or related amyloidosis disorders. Further, to confirm that the defibrillation results were not due to P1

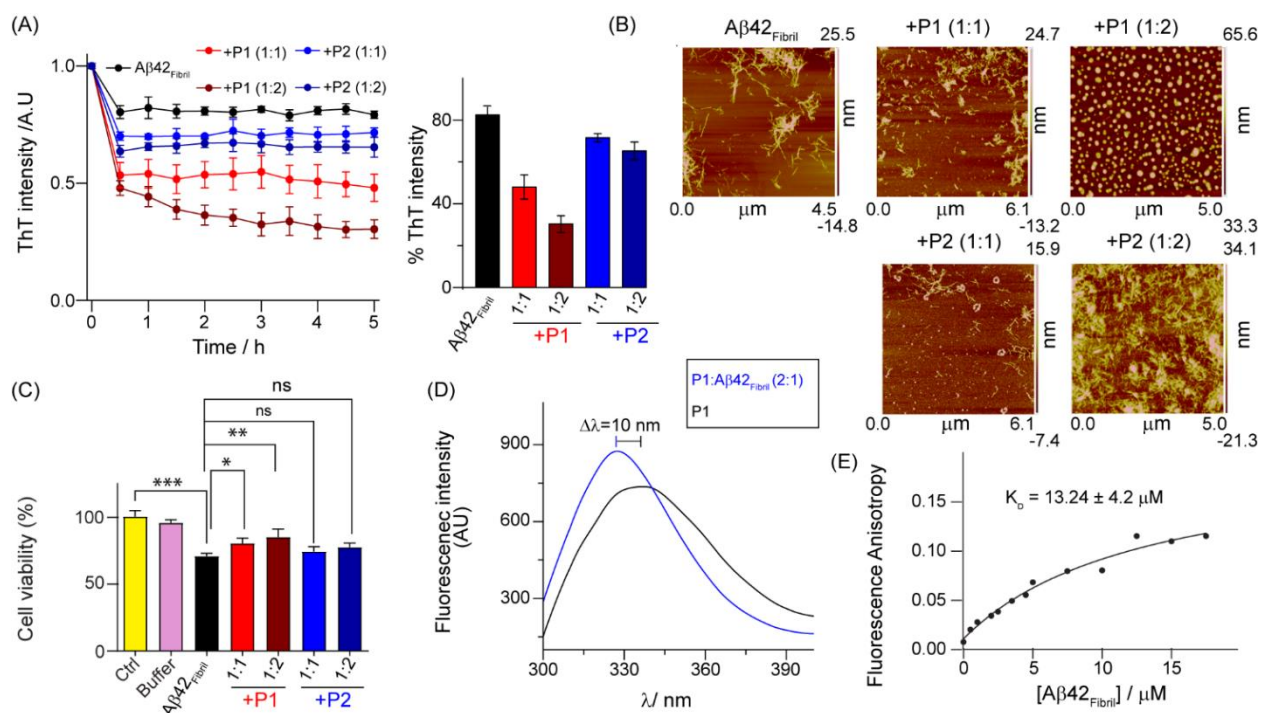


Figure 4.9. Disruption matured $A\beta_{42}$ fibrils by P1 and P2. (A) Normalized ThT fluorescence intensity of $A\beta_{42}$ fibril disaggregation process with varying peptide concentrations. The bar plot indicates the % ThT intensity after disintegration of preformed fibril. (B) Morphologies of matured $A\beta_{42}$ fibrils in absence and presence of P1 and P2 at 1:1 and 1:2 molar ratio during the fibril disaggregation process observed by AFM. (C) SH-SY5Y cells were treated with 10 μ M preformed $A\beta_{42}$ fibril and with Peptides P1 and P2 at a ratio of 1:2 of $A\beta_{42}$: P1 and P2. Values are represented as mean \pm SEM, n=6. Significance was calculated between control and $A\beta_{42}$ alone by one way ANOVA and Dunnett's multiple comparisons test. Unpaired two tailed T-test were performed between $A\beta_{42}$ alone and $A\beta_{42}$ +P1 and P2. ns, *, **, *** denotes non-significant, $p < 0.05$, $p < 0.01$ and $p < 0.001$, respectively. (D) Blue shift in tryptophan fluorescence of P1 in presence of $A\beta_{42}$ fibril. (E) The steady state anisotropy of P1 in presence of different concentration of $A\beta_{42}$ fibril.

displacing ThT from the fibrils, we kept the ratio of A β 42 fibrils to P1 (1:2) constant while altering ThT concentrations (Appendix 4, Figure S4.6). Consistent ThT values across all ThT concentrations indicated the disruption of fibrils by P1 and validated that the decrease in ThT fluorescence was not due to P1 competing with ThT for binding to A β 42 fibrils. We utilized AFM microscopy to investigate P1 and P2 effectiveness in disrupting preformed fibrils of A β 42. The matured fibrillar networks of A β 42 disintegrated into short, thinly branched fibrils upon co-incubation of preformed A β 42 fibrils with equimolar P1 (Figure 4.9B). However, a remarkable difference in the morphology of A β 42 fibrils was observed when exposed to P1 at 1:2 molar ratio, suggest that P1 interacts with A β 42 fibrils and facilitates their disaggregation into spherical particles (Figure 4.9B). Further AFM characterization of A β 42 fibrils in the presence of P2 showed relatively shorter fibrils compared to matured A β 42 fibrils (Figure 4.9B). Taken together, these findings strongly indicate that P1 exhibits greater efficacy than P2 in disassembling A β 42 fibrils.

According to plaque hypothesis, amyloid plaques and matured fibrils play a considerable role as nucleation sites of various forms of A β ⁴³. These plaques need to be removed to reduce the overall amyloid load and deter the progression of neuronal degeneration⁴⁴. The resultant ThT and AFM data showed promising role of our designed peptides in disintegration of matured A β 42 fibril. However, to verify our *in vitro* data we performed cellular experiments to verify whether these effects of disintegration is pronounced upon neuronal cells. Hence, we incubated SH-SY5Y cells with matured A β 42 fibril along with a mixture of overnight incubated A β 42 fibril and P1/P2 at a ratio of 1:1 and 1:2 of A β 42: Peptide. Matured A β 42 fibril was able to reduce the cell viability around ~70%. Addition of P1 to matured A β 42 fibril followed by overnight disintegration significantly recovered the cell viability to around ~80-90 % (Figure 4.9C). Likewise, P2 was also able to recover cell viability at around ~ 70-80% (Figure 4.9C). The above results suggest that P1 being more potent than P2 can disintegrate matured A β 42 fibril and the disintegrated species are non-toxic to cells, which can be seen through recovery of cellular viability when compared to mature A β 42 fibril alone and control cells.

To determine the binding affinity of P1 for A β 42 fibrils, fluorescence anisotropy was conducted. Upon addition of half fold molar excess of A β 42 fibrils, the tryptophan fluorescence emission peak of P1 shifted about ~10 nm towards the shorter wavelengths (blue shift) and became more intense (Figure 4.9D). The interaction between P1 and A β 42 fibrils showed a moderate binding affinity in

trigger early stages apoptosis in SH-SY5Y cells, which includes changes in membrane lipid composition not amounting to DNA damage which occurs during late phases of apoptosis. A β 42 triggered apoptosis in around ~30% of the cells, when compared to control cells having buffer only. Incubation of P1 and P2 with A β 42 in a ratio of 1:1 and 1:2 of A β 42:Peptide, drastically reduced the number of apoptotic cells to less than ~2-3%; culminating a reduction of over 90% effect on overall apoptosis (Figure 4.10). These data suggest the protective role of P1 and P2 in inhibiting neuronal apoptosis, which in turn may reduce overall neuroinflammation. The mean fluorescence intensity of annexin V binding to cells and their count was further plotted as a histogram (Figure 4.10). The Bar diagram represents the statistical significance of the experiment in respect to binding of Annexin V and its fluorescence intensity (Figure 4.10). Reduction in apoptosis helps to reduce neuroinflammation, which has a range of downstream effects and the most beneficial being delay in neurodegeneration.

4.4. Conclusion

In this study, we have described the development and application of a peptide-based approach for identifying effective inhibitors against AD. In summary, among the peptides investigated in the RF8 series, our study highlighted that P1 as a highly effective inhibitor of the A β 40 aggregation process. P1 was synthesized with a recognition motif designed for the target A β , incorporating anthranilic acid (Ant) as β breaker element. The modulation of A β 42 and AV20 aggregation kinetics through P1 restricts the primary nucleation events and elongation pathways by promoting the formation of off-pathway aggregates. Additionally, non-toxic, serum-stable P1 peptide disrupted and dispersed preformed amyloid fibrils into non-toxic aggregates. NMR spectroscopy revealed that the crucial binding site of A β 42 with the P1 peptide involved the N and C-terminal region, especially containing the GxxxG motif. Molecular docking and NMR examinations have shown that P1 binds to A β at hydrophobic regions through hydrogen bonding, van der Waals and electrostatic interaction, effectively preventing the amyloid aggregation process. The non-toxicity of P1 in mouse models and its ability to decrease A β -induced neurotoxicity and neuronal apoptosis in human neuroblastoma cells highlighted its therapeutic potential. Our findings propose that the peptide-based therapeutic, with its structural adaptability and moderate affinity for the targeted amyloid protein or peptide epitope, may uncover promising treatments for AD and other amyloidosis.

4.5 Appendix 4

Table S4.1: Biochemical Chart. Effect of P1 and P2 on haematological in mice (n= 6 per group). PCV-Packed Cell Volume; WBC-white blood cells; MCV-Mean Corpuscular Volume; MCH-Mean Corpuscular Haemoglobin; MCHC- Mean Corpuscular Haemoglobin concentration; ESR-Erythrocyte Sedimentation Rate.

HAEMATOLOGICAL PARAMETERS	Control Mice	P1-5mg Mice	P1-10mg Mice	P2-5mg Mice	P2-10mg Mice	Normal Range
Haemoglobin %	7.3±1.5	11.7±2.4	10.5±2.2	11.2±3	9.8±1.8	6.1-19.73
Red Blood Cell Count/Lac (10 ⁶)	4.9±0.4	6.8±0.5	6.9±0.2	6.8±0.6	5.9±0.3	3.57-11.7
PCV % (Haematocrit)	21.4±3	32.7±2	30.5±5	32±4	28.4±3.5	
MCV (fL)	43.6±2.6	48±6	44.2±8	47±4	48.1±3.7	39-95.18
MCH (pg)	14.8±5.8	17.2±6	15.2±4	16.4±7	16.6±3	27-58.22
MCHC g/L	34.1±6	35.7±8	34.4±8	34.6±4.6	34.5±2.5	
Platelets count/Lac (10 ⁶)	3.6±0.8	6.5±0.5	7.6±1.1	12.1±1.3	5.7±0.5	0.59-6.75
W.B.C Total Count/ Cu mm	4100±600	3500±800	6200±1200	9300±1500	6500±900	5500-12500
Neutrophils %	29±3	27±2	24±5	53±4	21±2	3-27
Lymphocytes%	66±15	70±3	71±10	42±5	76±4	12-41
Monocytes %	03±2	02±1	03±1	03±2	02±1	00-04
Eosinophils %	02±1	01±2	02±1	02±2	01±1	00-01
Basophil %	00±0	00±0	00±0	00±0	00±0	00-01
ESR mm/1 st hr	50±6	18±4	32±5	20±3	30±8	

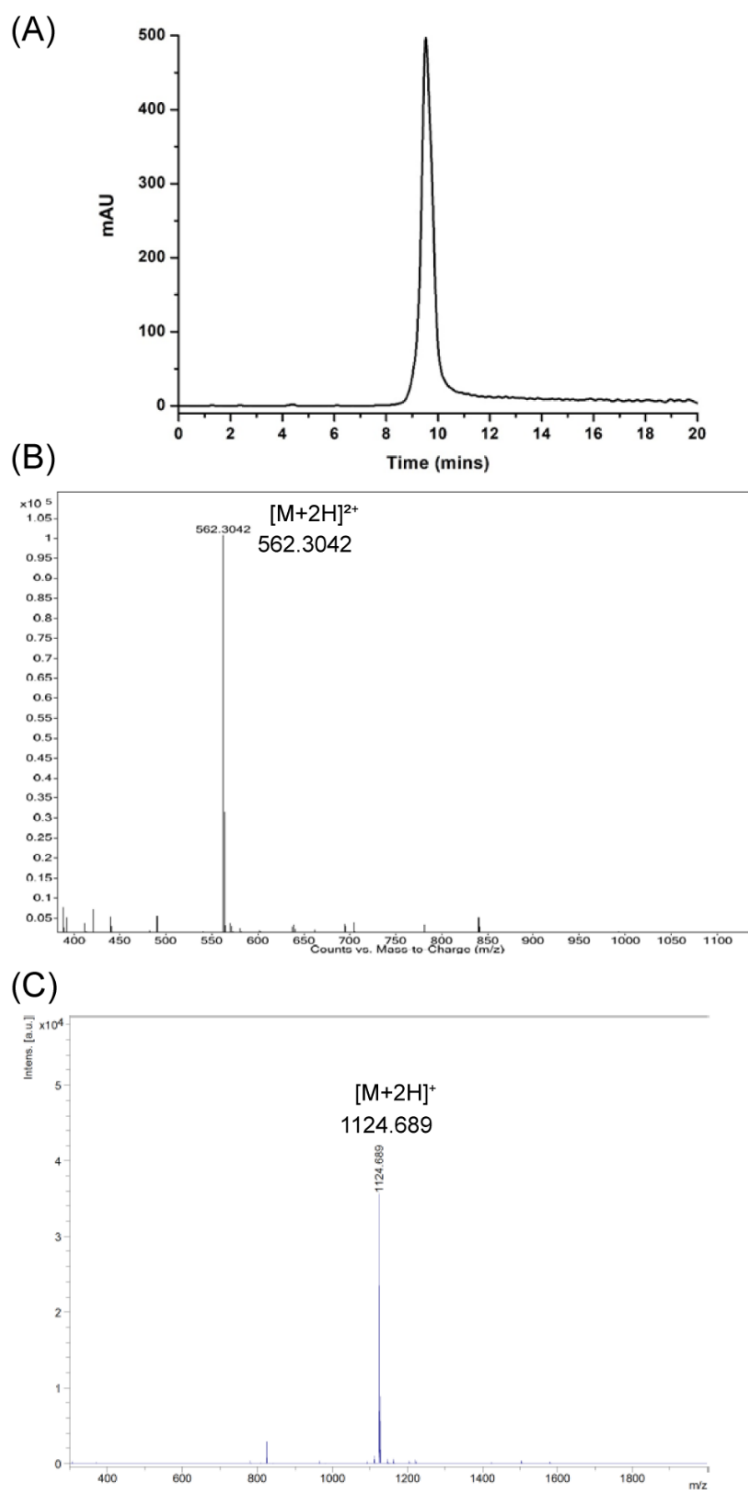


Figure S4.1. Peptide P1 characterization. (A) HPLC profile of P1, (B) ESI mass profile of P1. Calculated mass for $C_{55}H_{78}N_{16}O_8S$ is 1122.5909, observed mass 562.3042, $[M+2H]^{2+}$, (C) MALDI mass spectrum of P1, observed mass 1124.689, $[M+2H]^+$.

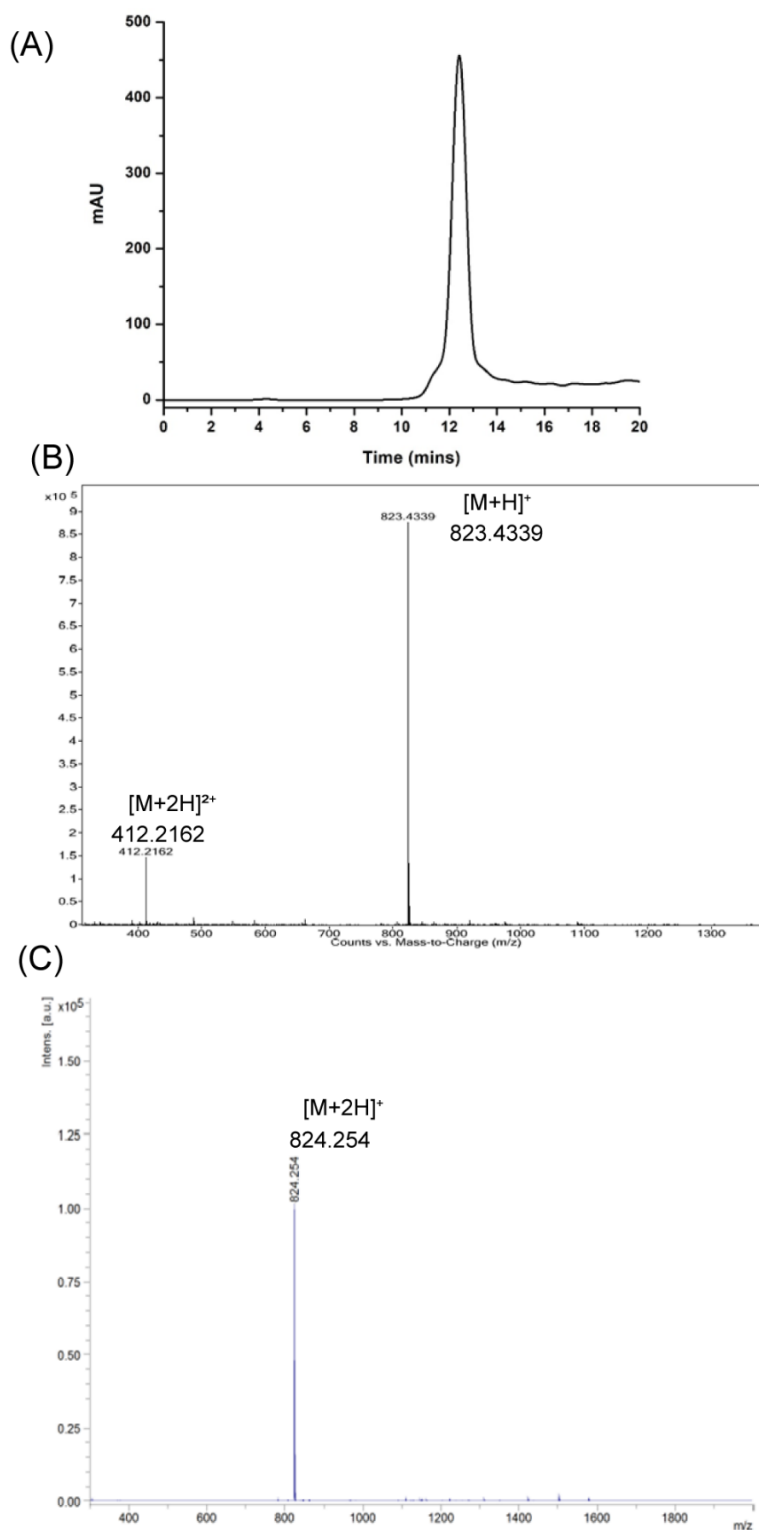


Figure S4.2. Peptide P2 characterization. (A) HPLC profile of P2 and (B) ESI mass spectrum of P2. Calculated mass for $C_{40}H_{58}N_{10}O_7S$ is 822.4211, observed mass, 823.4339, $[M+H]^+$ and 412.2162, $[M+2H]^{2+}$, (C) MALDI mass spectrum of P2, observed mass 824.254 $[M+2H]^+$.

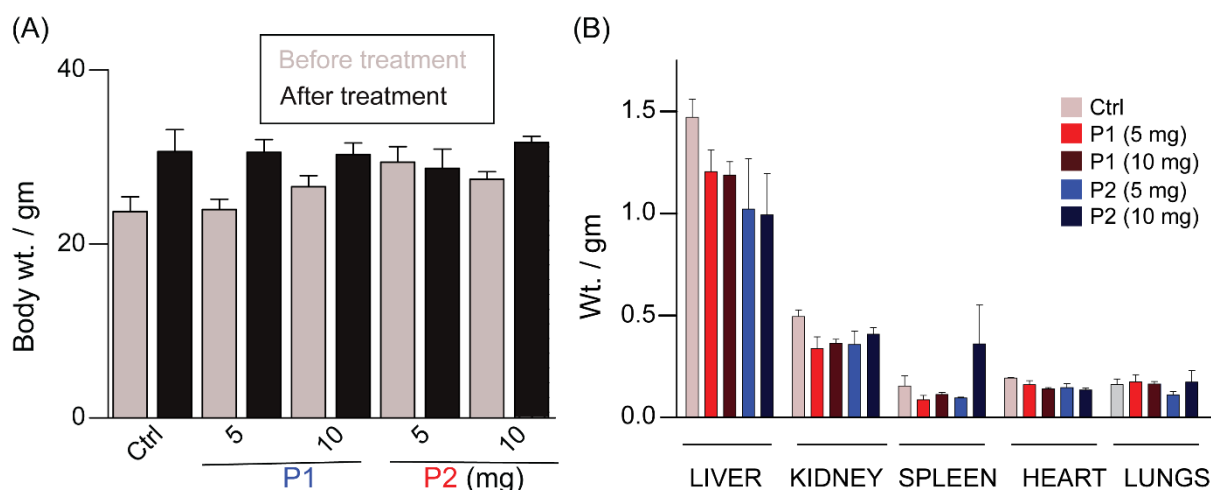


Figure S4.3. Mouse (C57BL6/J) were treated intraperitoneally with indicated concentration of Peptides P1 and P2. (A) Body weight was measured before and after Peptides P1 and P2 treatment. (B) Organ weight of liver, kidney, spleen, heart and lungs for control and peptides P1 and P2 treated mice after sacrifice.

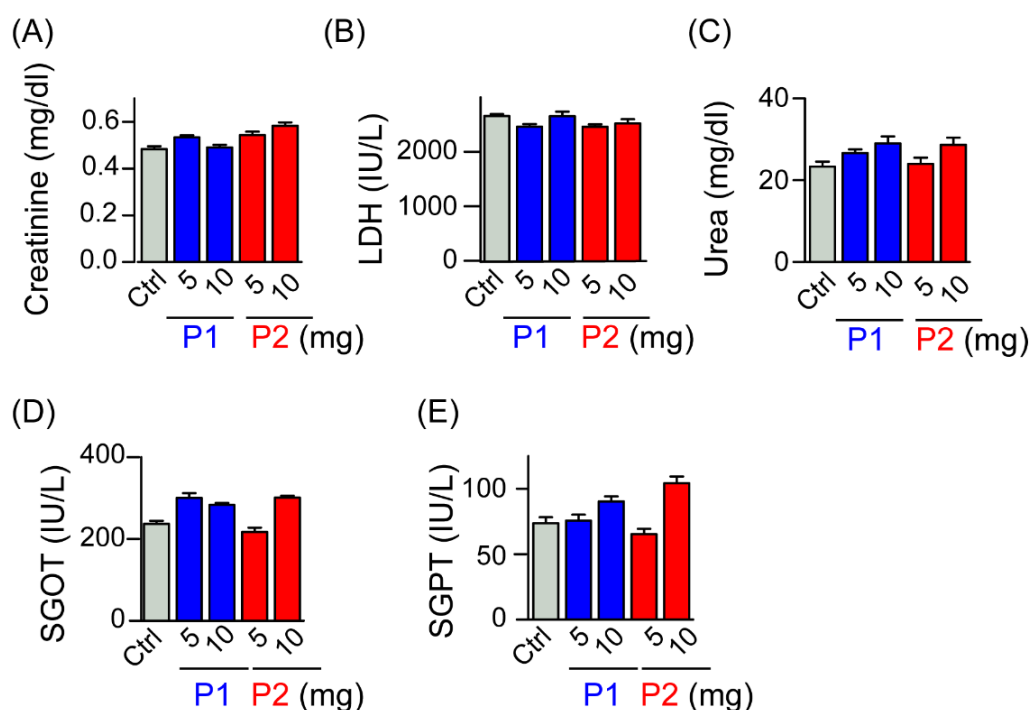


Figure S4.4. Effect of peptides P1 and P2 on various biochemical parameters such as (A) Creatinine, (B) LDH, (C) Urea, (D) serum glutamic oxaloacetic transaminase (SGOT), (E) serum glutamic pyruvic transaminase (SGPT).

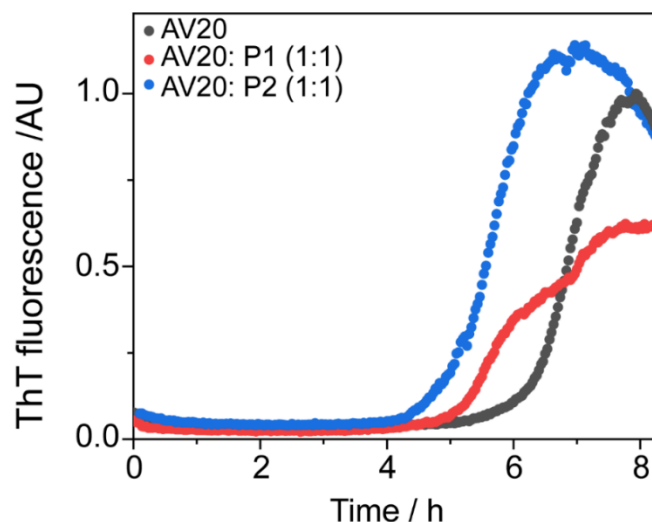


Figure S4.5. AV20 peptide (100 μ M) aggregation in absence and presence of equimolar P1 and P2 (AV20: Peptide= 1:1) monitored using ThT fluorescence at 37 $^{\circ}$ C.

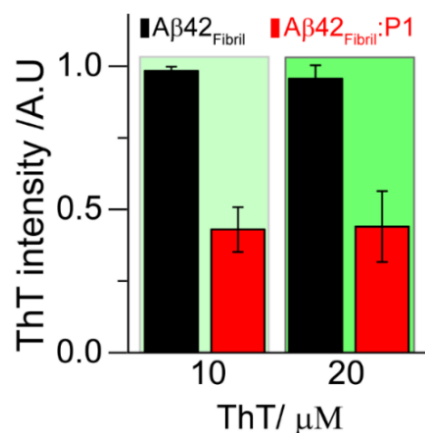


Figure S4.6. The bar plot indicates no competition for amyloid A β 42 fibril binding between ThT and P1. Preformed A β 42 fibril was dissolved in 20 mM sodium phosphate with 50 mM NaCl in absence (black) and presence (red) of P1 at 1:2 molar ratio of A β 42/P1 and varying the concentration of ThT (10 and 20 μ M) at 37 $^{\circ}$ C.

4.6. References

1. (a) Alzheimer's, A., 2012 Alzheimer's disease facts and figures. *Alzheimers Dement* **2012**, 8 (2), 131-68; (b) Habchi, J.; Chia, S.; Galvagnion, C.; Michaels, T. C. T.; Bellaiche, M. M. J.; Ruggeri, F. S.; Sanguanini, M.; Idini, I.; Kumita, J. R.; Sparr, E.; Linse, S.; Dobson, C. M.; Knowles, T. P. J.; Vendruscolo, M., Cholesterol catalyses Abeta42 aggregation through a heterogeneous nucleation pathway in the presence of lipid membranes. *Nat Chem* **2018**, 10 (6), 673-683.

2. Citron, M., Alzheimer's disease: strategies for disease modification. *Nat Rev Drug Discov* **2010**, 9 (5), 387-98.
3. (a) Hardy, J.; Selkoe, D. J., The amyloid hypothesis of Alzheimer's disease: progress and problems on the road to therapeutics. *Science* **2002**, 297 (5580), 353-6; (b) Walsh, D. M.; Selkoe, D. J., A beta oligomers - a decade of discovery. *J Neurochem* **2007**, 101 (5), 1172-84.
4. (a) Gazit, E., The "Correctly Folded" state of proteins: is it a metastable state? *Angew Chem Int Ed Engl* **2002**, 41 (2), 257-9; (b) Larson, M. E.; Lesne, S. E., Soluble Abeta oligomer production and toxicity. *J Neurochem* **2012**, 120 Suppl 1 (Suppl 1), 125-139; (c) Arosio, P.; Cukalevski, R.; Frohm, B.; Knowles, T. P.; Linse, S., Quantification of the concentration of Abeta42 propagons during the lag phase by an amyloid chain reaction assay. *J Am Chem Soc* **2014**, 136 (1), 219-25; (d) Shankar, G. M.; Li, S.; Mehta, T. H.; Garcia-Munoz, A.; Shepardson, N. E.; Smith, I.; Brett, F. M.; Farrell, M. A.; Rowan, M. J.; Lemere, C. A.; Regan, C. M.; Walsh, D. M.; Sabatini, B. L.; Selkoe, D. J., Amyloid-beta protein dimers isolated directly from Alzheimer's brains impair synaptic plasticity and memory. *Nat Med* **2008**, 14 (8), 837-42.
5. Cohen, S. I.; Linse, S.; Luheshi, L. M.; Hellstrand, E.; White, D. A.; Rajah, L.; Otzen, D. E.; Vendruscolo, M.; Dobson, C. M.; Knowles, T. P., Proliferation of amyloid-beta42 aggregates occurs through a secondary nucleation mechanism. *Proc Natl Acad Sci U S A* **2013**, 110 (24), 9758-63.
6. (a) Bett, C. K.; Serem, W. K.; Fontenot, K. R.; Hammer, R. P.; Garino, J. C., Effects of peptides derived from terminal modifications of the abeta central hydrophobic core on abeta fibrillization. *ACS Chem Neurosci* **2010**, 1 (10), 661-78; (b) Matharu, B.; El-Agnaf, O.; Razvi, A.; Austen, B. M., Development of retro-inverso peptides as anti-aggregation drugs for beta-amyloid in Alzheimer's disease. *Peptides* **2010**, 31 (10), 1866-72.
7. Kienlen-Campard, P.; Tasiaux, B.; Van Hees, J.; Li, M.; Huysseune, S.; Sato, T.; Fei, J. Z.; Aimoto, S.; Courtoy, P. J.; Smith, S. O.; Constantinescu, S. N.; Octave, J. N., Amyloidogenic processing but not amyloid precursor protein (APP) intracellular C-terminal domain production requires a precisely oriented APP dimer assembled by transmembrane GXXXG motifs. *J Biol Chem* **2008**, 283 (12), 7733-44.
8. (a) Chen, J.; Armstrong, A. H.; Koehler, A. N.; Hecht, M. H., Small molecule microarrays enable the discovery of compounds that bind the Alzheimer's Abeta peptide and reduce its cytotoxicity. *J Am Chem Soc* **2010**, 132 (47), 17015-22; (b) Sinha, S.; Lopes, D. H.; Du, Z.; Pang, E. S.; Shanmugam, A.; Lomakin, A.; Talbiersky, P.; Tennstaedt, A.; McDaniel, K.; Bakshi, R.; Kuo, P. Y.; Ehrmann, M.; Benedek, G. B.; Loo, J. A.; Klarner, F. G.; Schrader, T.; Wang, C.; Bitan, G., Lysine-specific molecular tweezers are broad-spectrum inhibitors of assembly and toxicity of amyloid proteins. *J Am Chem Soc* **2011**, 133 (42), 16958-69; (c) Habchi, J.; Arosio, P.; Perni, M.; Costa, A. R.; Yagi-Utsumi, M.; Joshi, P.; Chia, S.; Cohen, S. I.; Muller, M. B.; Linse, S.; Nollen, E. A.; Dobson, C. M.; Knowles, T. P.; Vendruscolo, M., An anticancer drug suppresses the primary nucleation reaction that initiates the production of the toxic Abeta42 aggregates linked with Alzheimer's disease. *Sci Adv* **2016**, 2 (2), e1501244; (d) Rezaei-Ghaleh, N.; Andreetto, E.; Yan, L. M.; Kapurniotu, A.; Zweckstetter, M., Interaction between amyloid beta peptide and an aggregation blocker peptide mimicking islet amyloid polypeptide. *PLoS One* **2011**, 6 (5), e20289; (e) Ghosh, A.; Pradhan, N.; Bera, S.; Datta, A.; Krishnamoorthy, J.; Jana, N. R.; Bhunia, A., Inhibition and Degradation of Amyloid

- Beta (A β 40) Fibrillation by Designed Small Peptide: A Combined Spectroscopy, Microscopy, and Cell Toxicity Study. *ACS Chem Neurosci* **2017**, 8 (4), 718-722.
9. Chaudhuri, T. K.; Paul, S., Protein-misfolding diseases and chaperone-based therapeutic approaches. *FEBS J* **2006**, 273 (7), 1331-49.
 10. (a) Nie, Q.; Du, X. G.; Geng, M. Y., Small molecule inhibitors of amyloid beta peptide aggregation as a potential therapeutic strategy for Alzheimer's disease. *Acta Pharmacol Sin* **2011**, 32 (5), 545-51; (b) Habchi, J.; Chia, S.; Limbocker, R.; Mannini, B.; Ahn, M.; Perni, M.; Hansson, O.; Arosio, P.; Kumita, J. R.; Challa, P. K.; Cohen, S. I.; Linse, S.; Dobson, C. M.; Knowles, T. P.; Vendruscolo, M., Systematic development of small molecules to inhibit specific microscopic steps of A β 42 aggregation in Alzheimer's disease. *Proc Natl Acad Sci U S A* **2017**, 114 (2), E200-E208.
 - 11 Huang, Y.; Chang, Y.; Liu, L.; Wang, J., Nanomaterials for Modulating the Aggregation of beta-Amyloid Peptides. *Molecules* **2021**, 26 (14).
 12. (a) Paul, A.; Nadimpally, K. C.; Mondal, T.; Thalluri, K.; Mandal, B., Inhibition of Alzheimer's amyloid-beta peptide aggregation and its disruption by a conformationally restricted alpha/beta hybrid peptide. *Chem Commun (Camb)* **2015**, 51 (12), 2245-8; (b) Paul, A.; Kumar, S.; Kalita, S.; Kalita, S.; Sarkar, D.; Bhunia, A.; Bandyopadhyay, A.; Mondal, A. C.; Mandal, B., An explicitly designed paratope of amyloid-beta prevents neuronal apoptosis in vitro and hippocampal damage in rat brain. *Chem Sci* **2020**, 12 (8), 2853-2862; (c) Lin, L. X.; Bo, X. Y.; Tan, Y. Z.; Sun, F. X.; Song, M.; Zhao, J.; Ma, Z. H.; Li, M.; Zheng, K. J.; Xu, S. M., Feasibility of beta-sheet breaker peptide-H102 treatment for Alzheimer's disease based on beta-amyloid hypothesis. *PLoS One* **2014**, 9 (11), e112052.
 13. (a) Wang, J.; Wang, K.; Zhu, Z.; He, Y.; Zhang, C.; Guo, Z.; Wang, X., Inhibition of metal-induced amyloid beta-peptide aggregation by a blood-brain barrier permeable silica-cyclen nanochelator. *RSC Adv* **2019**, 9 (25), 14126-14131; (b) Pradhan, K.; Das, G.; Kar, C.; Mukherjee, N.; Khan, J.; Mahata, T.; Barman, S.; Ghosh, S., Rhodamine-Based Metal Chelator: A Potent Inhibitor of Metal-Catalyzed Amyloid Toxicity. *ACS Omega* **2020**, 5 (30), 18958-18967.
 14. (a) Ladiwala, A. R.; Bhattacharya, M.; Perchiacca, J. M.; Cao, P.; Raleigh, D. P.; Abedini, A.; Schmidt, A. M.; Varkey, J.; Langen, R.; Tessier, P. M., Rational design of potent domain antibody inhibitors of amyloid fibril assembly. *Proc Natl Acad Sci U S A* **2012**, 109 (49), 19965-70; (b) Kaye, R.; Head, E.; Sarsoza, F.; Saing, T.; Cotman, C. W.; Necula, M.; Margol, L.; Wu, J.; Breydo, L.; Thompson, J. L.; Rasool, S.; Gurlo, T.; Butler, P.; Glabe, C. G., Fibril specific, conformation dependent antibodies recognize a generic epitope common to amyloid fibrils and fibrillar oligomers that is absent in prefibrillar oligomers. *Mol Neurodegener* **2007**, 2, 18.
 15. Jökar, S.; Khazaei, S.; Behnammanesh, H.; Shamloo, A.; Erfani, M.; Beiki, D.; Bavi, O., Recent advances in the design and applications of amyloid-beta peptide aggregation inhibitors for Alzheimer's disease therapy. *Biophys Rev* **2019**.
 16. Soto, C.; Kindy, M. S.; Baumann, M.; Frangione, B., Inhibition of Alzheimer's amyloidosis by peptides that prevent beta-sheet conformation. *Biochem Biophys Res Commun* **1996**, 226 (3), 672-80.

17. Cheng, R. P.; Gellman, S. H.; DeGrado, W. F., beta-Peptides: from structure to function. *Chem Rev* **2001**, *101* (10), 3219-32.
18. (a) Haynes, S. W.; Gao, X.; Tang, Y.; Walsh, C. T., Assembly of asperlicin peptidyl alkaloids from anthranilate and tryptophan: a two-enzyme pathway generates heptacyclic scaffold complexity in asperlicin E. *J Am Chem Soc* **2012**, *134* (42), 17444-7; (b) Dalsgaard, P. W.; Larsen, T. O.; Christophersen, C., Bioactive cyclic peptides from the psychrotolerant fungus *Penicillium algidum*. *J Antibiot (Tokyo)* **2005**, *58* (2), 141-4; (c) Ramesh, V. V.; Priya, G.; Kotmale, A. S.; Gonnade, R. G.; Rajamohanam, P. R.; Sanjayan, G. J., Multifaceted folding in a foldamer featuring highly cooperative folds. *Chem Commun (Camb)* **2012**, *48* (91), 11205-7.
19. Boldogh, I.; Kruzel, M. L., Colostrinin: an oxidative stress modulator for prevention and treatment of age-related disorders. *J Alzheimers Dis* **2008**, *13* (3), 303-21.
20. Zaretsky, D. V.; Zaretskaia, M. V.; Molkov, Y. I., Membrane channel hypothesis of lysosomal permeabilization by beta-amyloid. *Neurosci Lett* **2022**, *770*, 136338.
21. Bera, S.; Gayen, N.; Mohid, S. A.; Bhattacharyya, D.; Krishnamoorthy, J.; Sarkar, D.; Choi, J.; Sahoo, N.; Mandal, A. K.; Lee, D.; Bhunia, A., Comparison of Synthetic Neuronal Model Membrane Mimics in Amyloid Aggregation at Atomic Resolution. *ACS Chem Neurosci* **2020**, *11* (13), 1965-1977.
22. Sahoo, B. R.; Genjo, T.; Nakayama, T. W.; Stoddard, A. K.; Ando, T.; Yasuhara, K.; Fierke, C. A.; Ramamoorthy, A., A cationic polymethacrylate-copolymer acts as an agonist for beta-amyloid and an antagonist for amylin fibrillation. *Chem Sci* **2019**, *10* (14), 3976-3986.
23. (a) Pariary, R.; Ghosh, B.; Bednarikova, Z.; Varnava, K. G.; Ratha, B. N.; Raha, S.; Bhattacharyya, D.; Gazova, Z.; Sarojini, V.; Mandal, A. K.; Bhunia, A., Targeted inhibition of amyloidogenesis using a non-toxic, serum stable strategically designed cyclic peptide with therapeutic implications. *Biochim Biophys Acta Proteins Proteom* **2020**, *1868* (5), 140378; (b) Korshavn, K. J.; Satriano, C.; Lin, Y.; Zhang, R.; Dulchavsky, M.; Bhunia, A.; Ivanova, M. I.; Lee, Y. H.; La Rosa, C.; Lim, M. H.; Ramamoorthy, A., Reduced Lipid Bilayer Thickness Regulates the Aggregation and Cytotoxicity of Amyloid-beta. *J Biol Chem* **2017**, *292* (11), 4638-4650.
24. Das, A.; Gangarde, Y. M.; Pariary, R.; Bhunia, A.; Saraogi, I., An amphiphilic small molecule drives insulin aggregation inhibition and amyloid disintegration. *Int J Biol Macromol* **2022**, *218*, 981-991.
25. Bera, S.; Kar, R. K.; Mondal, S.; Pahan, K.; Bhunia, A., Structural Elucidation of the Cell-Penetrating Penetratin Peptide in Model Membranes at the Atomic Level: Probing Hydrophobic Interactions in the Blood-Brain Barrier. *Biochemistry* **2016**, *55* (35), 4982-96.
26. Schrödinger.
27. Vivekanandan, S.; Brender, J. R.; Lee, S. Y.; Ramamoorthy, A., A partially folded structure of amyloid-beta(1-40) in an aqueous environment. *Biochem Biophys Res Commun* **2011**, *411* (2), 312-6.
28. Jones, G.; Willett, P.; Glen, R. C.; Leach, A. R.; Taylor, R., Development and validation of a genetic algorithm for flexible docking. *J Mol Biol* **1997**, *267* (3), 727-48.

29. (a) Baxter, C. A.; Murray, C. W.; Clark, D. E.; Westhead, D. R.; Eldridge, M. D., Flexible docking using Tabu search and an empirical estimate of binding affinity. *Proteins* **1998**, *33* (3), 367-82; (b) Eldridge, M. D.; Murray, C. W.; Auton, T. R.; Paolini, G. V.; Mee, R. P., Empirical scoring functions: I. The development of a fast empirical scoring function to estimate the binding affinity of ligands in receptor complexes. *J Comput Aided Mol Des* **1997**, *11* (5), 425-45.
30. Drobecq, H.; Boll, E.; Senechal, M.; Desmet, R.; Saliou, J. M.; Lacapere, J. J.; Mougél, A.; Vicogne, J.; Melnyk, O., A Central Cysteine Residue Is Essential for the Thermal Stability and Function of SUMO-1 Protein and SUMO-1 Peptide-Protein Conjugates. *Bioconjug Chem* **2016**, *27* (6), 1540-6.
31. (a) Nowick, J. S.; Brower, J. O., A new turn structure for the formation of beta-hairpins in peptides. *J Am Chem Soc* **2003**, *125* (4), 876-7; (b) Zhao, B.; Yang, D.; Wong, J. H.; Wang, J.; Yin, C.; Zhu, Y.; Fan, S.; Ng, T. B.; Xia, J.; Li, Z., A Thioether-Stabilized d-Proline-l-Proline-Induced beta-Hairpin Peptide of Defensin Segment Increases Its Anti-Candida albicans Ability. *Chembiochem* **2016**, *17* (15), 1416-20.
32. Biancalana, M.; Koide, S., Molecular mechanism of Thioflavin-T binding to amyloid fibrils. *Biochim Biophys Acta* **2010**, *1804* (7), 1405-12.
33. Horsley, J. R.; Jovceviski, B.; Wegener, K. L.; Yu, J.; Pukala, T. L.; Abell, A. D., Rationally designed peptide-based inhibitor of Abeta42 fibril formation and toxicity: a potential therapeutic strategy for Alzheimer's disease. *Biochem J* **2020**, *477* (11), 2039-2054.
34. Lopez-Suarez, L.; Awabdh, S. A.; Coumoul, X.; Chauvet, C., The SH-SY5Y human neuroblastoma cell line, a relevant in vitro cell model for investigating neurotoxicology in human: Focus on organic pollutants. *Neurotoxicology* **2022**, *92*, 131-155.
35. Yang, D.; Qiao, J.; Wang, J. X.; Wei, W. Y.; Zhao, Z. X.; Cai, H. Y., [Effects of B-GOS on cognitive behavior and depression of transgenic mice with Alzheimer's disease]. *Zhongguo Ying Yong Sheng Li Xue Za Zhi* **2021**, *37* (3), 240-246.
36. Sarkar, D.; Chakraborty, I.; Condorelli, M.; Ghosh, B.; Mass, T.; Weingarh, M.; Mandal, A. K.; La Rosa, C.; Subramanian, V.; Bhunia, A., Self-Assembly and Neurotoxicity of beta-Amyloid (21-40) Peptide Fragment: The Regulatory Role of GxxxG Motifs. *ChemMedChem* **2020**, *15* (3), 293-301.
37. (a) Carrillo-Mora, P.; Luna, R.; Colin-Barenque, L., Amyloid beta: multiple mechanisms of toxicity and only some protective effects? *Oxid Med Cell Longev* **2014**, *2014*, 795375; (b) Oguchi, T.; Ono, R.; Tsuji, M.; Shozawa, H.; Somei, M.; Inagaki, M.; Mori, Y.; Yasumoto, T.; Ono, K.; Kiuchi, Y., Cilostazol Suppresses Abeta-induced Neurotoxicity in SH-SY5Y Cells through Inhibition of Oxidative Stress and MAPK Signaling Pathway. *Front Aging Neurosci* **2017**, *9*, 337.
38. Brender, J. R.; Ghosh, A.; Kotler, S. A.; Krishnamoorthy, J.; Bera, S.; Morris, V.; Sil, T. B.; Garai, K.; Reif, B.; Bhunia, A.; Ramamoorthy, A., Probing transient non-native states in amyloid beta fiber elongation by NMR. *Chem Commun (Camb)* **2019**, *55* (31), 4483-4486.
39. Soldner, C. A.; Sticht, H.; Horn, A. H. C., Role of the N-terminus for the stability of an amyloid-beta fibril with three-fold symmetry. *PLoS One* **2017**, *12* (10), e0186347.

40. D.Sarkar, A. B., Delineating the Role of GxxxG Motif in Amyloidogenesis: A New Perspective in Targeting Amyloid-Beta Mediated AD Pathogenesis. . *ACS Bio & Med Chem Au* **2023**.
41. Hung, L. W.; Ciccotosto, G. D.; Giannakis, E.; Tew, D. J.; Perez, K.; Masters, C. L.; Cappai, R.; Wade, J. D.; Barnham, K. J., Amyloid-beta peptide (Abeta) neurotoxicity is modulated by the rate of peptide aggregation: Abeta dimers and trimers correlate with neurotoxicity. *J Neurosci* **2008**, *28* (46), 11950-8.
42. (a) Yang, H.; Li, J.; Li, X.; Ma, L.; Hou, M.; Zhou, H.; Zhou, R., Based on molecular structures: Amyloid-beta generation, clearance, toxicity and therapeutic strategies. *Front Mol Neurosci* **2022**, *15*, 927530; (b) Karran, E.; De Strooper, B., The amyloid hypothesis in Alzheimer disease: new insights from new therapeutics. *Nat Rev Drug Discov* **2022**, *21* (4), 306-318.
43. (a) Hasecke, F.; Niyangoda, C.; Borjas, G.; Pan, J.; Matthews, G.; Muschol, M.; Hoyer, W., Protofibril-Fibril Interactions Inhibit Amyloid Fibril Assembly by Obstructing Secondary Nucleation. *Angew Chem Int Ed Engl* **2021**, *60* (6), 3016-3021; (b) McLaurin, J.; Yang, D.; Yip, C. M.; Fraser, P. E., Review: modulating factors in amyloid-beta fibril formation. *J Struct Biol* **2000**, *130* (2-3), 259-70.
44. (a) Ghosh, S.; Ali, R.; Verma, S., Abeta-oligomers: A potential therapeutic target for Alzheimer's disease. *Int J Biol Macromol* **2023**, *239*, 124231; (b) Zhang, Y.; Chen, H.; Li, R.; Sterling, K.; Song, W., Amyloid beta-based therapy for Alzheimer's disease: challenges, successes and future. *Signal Transduct Target Ther* **2023**, *8* (1), 248.
45. (a) Takada, E.; Okubo, K.; Yano, Y.; Iida, K.; Someda, M.; Hirasawa, A.; Yonehara, S.; Matsuzaki, K., Molecular Mechanism of Apoptosis by Amyloid beta-Protein Fibrils Formed on Neuronal Cells. *ACS Chem Neurosci* **2020**, *11* (5), 796-805; (b) Kumar, S.; Paul, A.; Kalita, S.; Ghosh, A. K.; Mandal, B.; Mondal, A. C., Protective effects of beta-sheet breaker alpha/beta-hybrid peptide against amyloid beta-induced neuronal apoptosis in vitro. *Chem Biol Drug Des* **2017**, *89* (6), 888-900.
46. Wallberg, F.; Tenev, T.; Meier, P., Analysis of Apoptosis and Necroptosis by Fluorescence-Activated Cell Sorting. *Cold Spring Harb Protoc* **2016**, *2016* (4), pdb prot087387.

Chapter 5

5. Enhancing Amyloid Beta Inhibition and Disintegration by Natural Compounds: A Study utilizing Spectroscopy, Microscopy and Cell Biology

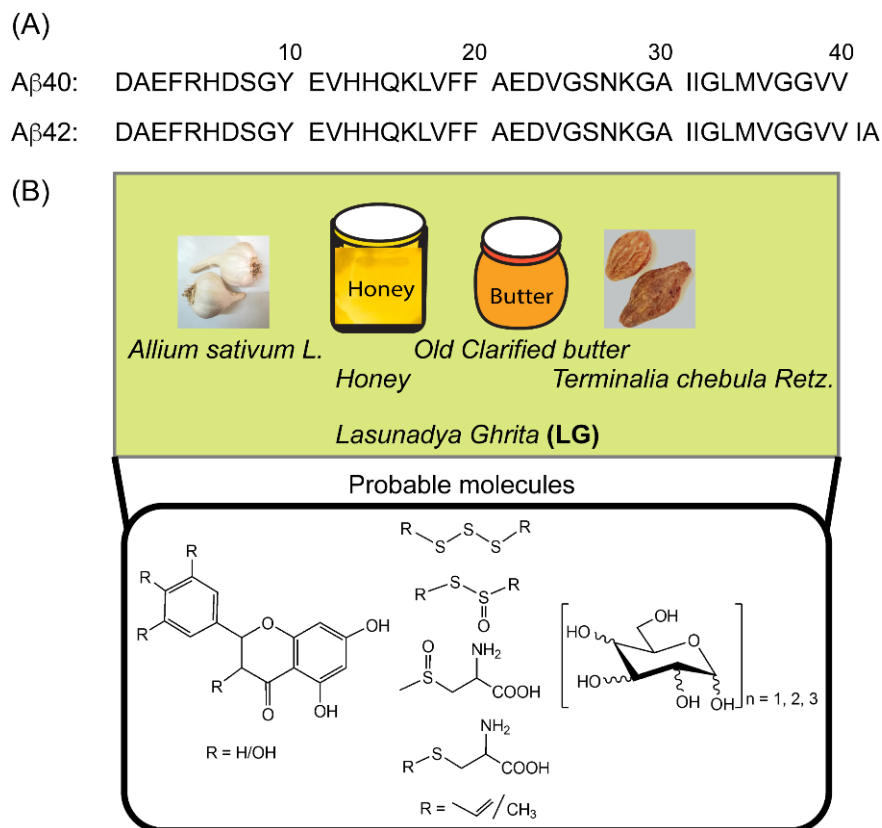
This chapter has been adapted from the following reference:

Pariary, R., Shome, G., Dutta, T., Roy, A., Misra, A.K., Jana, K., Rastogi, S., Senapati, D., Mandal, A.K. and Bhunia, A., 2024. Enhancing Amyloid Beta Inhibition and Disintegration by Natural Compounds: A Study utilizing Spectroscopy, Microscopy and Cell Biology. *Biophysical Chemistry*, (manuscript under review).

5.1. Introduction

The hallmark of neurodegenerative diseases like Alzheimer's disease (AD) is associated with deposits of protein aggregates during senescence or aging ¹. AD accounts for more than 60-70% cases of overall dementia worldwide ². Major etiopathologies of AD disease include the aggregation of amyloid and extracellular deposition of the intrinsically disordered β -amyloid (A β) peptide (Scheme 5.1A), leading to metal-ion dysregulation ³. Various factors including decrease in acetylcholine levels (Ach), formation of neurofibrillary tangles (NFTs) contribute to oxidative stress, neuronal inflammation, and cellular cytotoxicity in a cascading pathological sequence ⁴. Protein-folding stages of amyloid provide significant insight into understanding the amyloidogenic tendency ^{4a, 5}. The intermediate oligomeric or proto-fibrillar stages produce a dynamic heterogeneous pool of transitory conformers that initiate early nucleation events and impart their toxic effects ⁶. Moreover, AD being a multifactorial disease requires several drugs in a multi-targeted manner ⁷. Decades of amyloid research have been dedicated towards developing prospective therapeutic strategies to combat AD. Among the preventive interventions, diet-based nutraceuticals containing natural compounds show potency in delaying disease onset ⁸. Furthermore, the attention on natural extracts has increased due to their therapeutic efficacy in treating disorders like dementia, cancer, and cardiovascular diseases ⁹. Separately, in light of the exigency posed by the COVID pandemic, repurposing of drugs emerges as a compelling strategy to treat refractory diseases. As speculated under the traditional health care system, herbal or

Ayurvedic (traditional Indian medicine) and traditional Chinese medicine (TCM) each follow unique perspectives on aging, age-related degenerative disorders, and methods to prevent premature aging¹⁰. In recent years, there has been an increase in research on various Ayurvedic herbal formulations, with emerging scientific validation of their pharmaceutical characteristics¹¹.



Scheme 5.1. Schematic representation of (A) A β peptides amino acid sequence and (B) major components of *Lasunadya Ghrita* (LG).

In traditional medicine, treatments are often aimed to a particular target in the body. But using Ayurveda or Indian traditional medicine, molecules that modulate multiple targets at once might work better for treating diseases like AD because of its complexity and multifactorial effect¹². *Lasunadya Ghrita* (LG) (Scheme 5.1B), an Ayurveda formulation, has lasun (garlic) and ghrita (clarified butter) as its primary components and is used in psychiatric disorders in Ayurvedic therapeutic practices¹³. Therefore, LG, which is used to treat gut dysregulation and mental illnesses was considered for treating AD¹³. Furthermore, garlic (*Allium sativum*) extract, with its potent antioxidant activity, exhibits significant potential in protecting neurons, preventing cognitive decline, enhancing learning and memory, along with reduction of ischemia or reperfusion-related neuronal death¹⁴. Honey, containing carbohydrates and polyphenols acts as a

natural antioxidant by quenching biological reactive oxygen species (ROS), thereby protecting neurons from oxidative damage, promoting regeneration, and modulating signaling pathways ¹⁵. Additionally, the aqueous extract of Haritaki (*Terminalia chebula* Retz), enriched with hydrolyzable tannins and phenolic compounds, exhibits acetylcholinesterase inhibitory (AChEI) activities, antioxidant, and anti-inflammatory effects ¹⁶. Pre-emptive screening of LG extracts in various forms indicated its inhibitory activity towards different aggregate-prone proteins. Thus, we aimed to characterize its active compounds and mechanism of action in vitro and in vivo against progressive amyloidogenesis in AD.

5.2. Experimental Methods

5.2.1. Chemicals.

The unlabeled and labeled (¹⁵N and ¹⁵N, ¹³C) Aβ40 / Aβ42 peptides were purchased from Genscript Inc. (Piscataway, NJ, USA) and rPeptide Inc. (Bogart, GA, USA), respectively with >95 % purity. ThT: Thioflavin T and HFIP: 1, 1, 1, 3, 3, 3-hexafluoro-2-propanol were obtained from Sigma-Aldrich (St. Louis, MO, USA). Protease inhibitor cocktail (Roche #04693132001), MTT: 3-(4,5-dimethylthiazol-2-yl)-2,5-diphenyltetrazolium bromide (Himedia, Bangalore India) and H₂DCF-DA: 2',7'- dichlorodihydrofluoresceindiacetate (Sigma-Aldrich, USA) were purchased. Fetal bovine serum (Gibco,USA), DMEM/F12 media (Gibco, USA), trypsin-EDTA (Himedia, India) and antibiotics (Himedia, India) were used for cell culture.

5.2.2. Preparation of Lasundya Ghritha extract

The extraction process is crucial for isolating natural products from raw materials. The most often used approach for phytochemical analysis is solvent extraction. At room temperature, the LG was extracted in five different solvents (100 ml each). Firstly, LG (30 g) was treated with n-hexane then followed on the undissolved solid or precipitate with ethyl acetate, chloroform, methanol, and water for 2 h in each solvent under stirring at room temperature. The suspension was filtered on a paper filter and permeate was concentrated under pressure then lyophilized, stored at -20 °C and finally used for all biophysical experiments.

5.2.3. Chemical characterization of LG water extract using LC-MS

The lyophilized LG_{WE} was dissolved in autoclaved water and filtered. The extracts were fractionated in a 1.7 µl BEH C18 analytical column equipped with an ACCQUITY UPLC M-

Class before being passed on to XEVO G2-X'S QToF mass spectrometry (Water Corporation, Milford MA, Massachusetts, USA) in an Electrospray Ionization Mass Spectrometry (ESI) positive mode system. A gradient combination of water and acetonitrile made up the liquid phase. Progenesis QiP software (Waters Corporation, Milford, MA, USA) was used to process and analyze raw MS spectra against the Uniprot database using the standard search parameter. The mass data were well-matched with previously reported data ¹⁷.

5.2.4. A β 40 / A β 42 sample preparation.

A previously known procedure was used to prepare the sample ¹⁸. Briefly, 1 mg powder peptide A β 40 / A β 42 was dissolved in HFIP and subsequently placed on ice for 40 min. The peptide solution was aliquoted into 0.1 mg/ml and lyophilized for overnight. The stock aliquots were stored at -80 °C. The 0.1 mg/ml aliquots were dissolved in 20 mM sodium phosphate buffer and 50 mM NaCl (pH 7.4) to obtain ~0.3 mg/ml final concentration and sonicated for 30 s.

5.2.5. Amyloid Fibrillation study by Thioflavin T assay

50 mg/ml freeze-dried/ lyophilized extract of LG was prepared in autoclaved water. 0.25 mg/ml concentration of all the extract was used. 0.02 mg/ml experimental solution of A β 40 / A β 42 was prepared with varying concentration (mg/ml) ratios of [A β]/[LG_{WE}] (1:0.25, 1:0.5, 1:2.5, 1:12.5, and 1:25) in 20 mM sodium phosphate buffer and 50 mM NaCl solution pH 7.4 using 5 μ M ThT. Each sample were incubated at 37 °C in 96-well black plate with shaking 300 rpm for A β 40 and 100 rpm for A β 42, respectively. The ThT fluorescence was monitored for 12 h at an excitation / emission of 440 / 485 nm ¹⁹. The water fraction was selected among other fractions because it shows the maximum amyloid inhibition.

Defibrillation of A β 40 / A β 42 matured fibrils (5 μ M) was carried out using 0.25 mg/ml LG_{WE} in presence of 5 μ M ThT maintain the above conditions. For the ThT competition experiment ²⁰, A β fibrils were incubated at various ThT concentrations (5 μ M, 10 μ M, 15 μ M) in presence of 0.25 mg/ml LG_{WE}. BMG LABTECH POLARstar Omega spectrometer (Ortenberg, Germany) was used to measure the ThT intensity in a 96-well black plate with top optics mode.

5.2.6. Circular dichroism (CD) spectroscopy

The transition in the global conformation of A β 40 / A β 42, with or without LG_{WE}, was examined using Jasco J-815 CD spectrometer (Japan). A β 40/ A β 42 (25 μ M) was dissolved in 20 mM sodium

phosphate buffer and 50 mM NaF solution at pH 7.4 and titrated with LG_{WE} at 1:2.5 and 1:12.5 concentration ratio of [A β]: [LG_{WE}]. The samples are incubated at 37 °C for 12 h. The CD spectra of 0 h and 12 h samples were recorded at 25 °C with a wavelength range of 190-260 nm. The CD spectra are taken by averaging three consecutive scans at 100 nm/min speed and subtracting buffer or LG_{WE} signal.

5.2.7. Nuclear magnetic resonance (NMR) spectroscopy

All NMR studies were recorded using TOPSPIN 3.5 software (Bruker Biospin, Switzerland) on a 500 MHz Bruker Avance III NMR spectrometer with a SMART probe. The temperature of NMR probe was kept at 283 K to ensure that no fibrillation occurred during the experimental time frame. 2D NMR data was processed using Topshim software (Bruker) and analyzed by Sparky software.

¹⁵N labelled A β 40 / A β 42 (0.3 mg/ml) was dissolved in 90% buffer (20 mM sodium phosphate and 50 mM NaCl) and 10% D₂O at pH 7.4. 12 ppm spectral width along ¹H direction and 40 ppm along ¹⁵N direction were used for the measurement of two-dimensional (2D) ¹H-¹⁵N SOFAST HMQC spectra. The 2D NMR was recorded using States-TPPI method with 32 scans and 2048 (t₂) and 64 (t₁) complex data points. 2D NMR titration experiment was performed in presence of LG_{WE} at 283 K. The NMR signal intensity ratios of [A β :LG_{WE}] (I) and A β control (I₀) were used to calculate normalized peak intensity (I/I₀). The running average of intensity was measured by taking I/I₀ of the three consecutive residues. The CSP of residues was determined by using equation:

$$\Delta\delta = \sqrt{(\Delta\delta_H)^2 + (0.2 \Delta\delta_N)^2}$$

Where $\Delta\delta_H$ and $\Delta\delta_N$ represented the chemical shift difference of H and N direction, respectively between A β 40 / A β 42 alone and A β +LG_{WE}.

¹³C and ¹⁵N labelled A β 40 (0.3 mg/ml) was dissolved in 100 % D₂O. 4096 and 512 complex data points were collected along t₂ and t₁ dimension, respectively with 8 scans for ¹³C- HSQC NMR experiment ²¹. The 2D ¹H-¹³C A β 40 HSQC NMR spectra were recorded either in the presence and/or in the absence of LG_{WE} within a spectral width 10 ppm (¹H) and 236 ppm (¹³C) on Bruker AVANCE III 700 MHz, equipped with Cryoprobe at 286 K. The chemical shift assignments were completed by using previous report ²¹⁻²².

5.2.8. Atomic Force Microscopy (AFM)

A β 40 / A β 42 was dissolved to 40 μ M in 20 mM sodium phosphate and 50 mM NaCl at pH 7.4, with or without a LG_{WE} at 1:2.5 and 1:12.5 ratio of A β :LG_{WE}. The mixture was then incubated in at 37 °C and 250 rpm for 12 h. The AFM experiments were conducted using a Bruker BioScope Catalyst AFM instrument, and the analysis was carried out using the integrated Nanoscope Analysis software. Initially, samples of varying concentrations are partially diluted in the sol-vent. Subsequently, drops of freshly prepared A β 40/A β 42 solutions are cast onto a blank mica plate (Muscovite Mica, V-1, 20 mm diameter, EMS, Cat. # 71856-04) and allowed to remain undisturbed for 20 min to facilitate full binding with the mica surface. After the thorough binding, each mica plate underwent a single wash with Milli-Q water to eliminate any excess unbound sample solution. Finally, the plates were carefully dried in a controlled ultrapure argon stream to prevent contamination or disturbance of the solution layer. For each experiment RTESPA-525 probe has been used. The experiment was performed in Saha Institute of Nuclear Physics, Kolkata.

5.2.9. LUVs preparation for Fura 2 assay

Total brain lipid extract (TBLE) at a concentration of 2 mg/ml was dissolved in chloroform, dried under N₂ gas flow, and subsequently lyophilized to make a lipid films. To prepare the samples, the solution of Fura-2 dye-filled vesicles was initially diluted with a buffer solution containing 10 mM HEPES, 100 mM Fura-2 pentapotassium salt, 100 mM NaCl, and adjusted to pH 7.4²³. The lipids underwent five freeze-thaw cycles and vigorous vortexing, followed by extrusion through a 100 nm polycarbonate nucleopore membrane filter (Whatman) using a mini extruder setup (Avanti Polar Lipids) for a minimum of 21 times. 0.1 mg/ml LUVs were taken. 10 μ M A β 40 in absence or presence of LG_{WE} at 1:2.5 and 1:12.5 ratio (A β 40:LG_{WE}) was added into LUVs. After 30 min of incubation, 1 mM CaCl₂ was added and measured the fluorescence by taking the ratio of 340:380 nm. Triton X was used as a positive control.

5.2.10. Cell viability assay

Human neuroblastoma cells (SH-SY5Y) obtained from National Centre for Cell Science (NCCS, India) and cultured in complete DMEM/F12 media (Gibco, USA) supplemented with 12% fetal bovine serum, gentamycin (50 μ g/ml), penicillin-streptomycin (1 unit/ml, (50 μ g/ml), and amphotericin B (2.5 μ g/ml) in a 5% humidified CO₂ incubator at 37 °C. All experiments were conducted at 70-80% confluency. MTT was used to measure viability of cells, which depicts

activity of healthy cells by mitochondrial enzymes²⁴. These mitochondrial enzymes in live cells convert the MTT compound into purple formazan crystals, correspondingly the amount of formazan formed represents cell viability. A 96-well plate was seeded with 1×10^4 cells/well and incubated for 24 h. Next day, various concentrations of LG_{WE} (0.05, 0.10, 0.25, 0.50, and up to a concentration of 1.0 mg/ml) were added and incubated for 24 h to check the toxicity of the compounds. Similarly, cells were treated with A β 40 / A β 42 (10 μ M) oligomer or fibril in the absence and/or presence of LG_{WE} (0.05 and 0.25 mg/ml) at a ratio (A β : LG_{WE}) of either 1:2.5 or 1:12.5 for 24 h. At a final concentration of 0.5 mg/ml MTT solution was given to each well, and incubated at 37 °C for 3.5 h with 5% CO₂ humidity. Precipitated formazan was dissolved in 100 μ l of dimethyl-sulfoxide (DMSO) and measurement was taken at 570 nm in a microplate reader. Results were compared with control samples and expressed as a percentage of control or non-treated cell.

5.2.11. Dot blot assay

A β 40 preformed fibrils in the absence and presence of LG_{WE} (0.05 and 0.25 mg/ml) at a ratio (A β : LG_{WE}) of 1:2.5 and 1:12.5 respectively was spot-ted onto a nitrocellulose membrane. The membrane was further incubated with blocking buffer for about 1 h at room temperature and probed with anti-amyloid OC (#AB2286, Merck, USA) antibody overnight. The following day membrane was washed three times with TBST solution (Tris-buffered saline pH 7.4 with 0.01% Tween-20), and probed with HRP goat anti-rabbit secondary antibody (#111-035-003, Jackson laboratory, Baltimore, USA) for 2 h at room temperature. The blot was again washed for three times with TBST buffer and developed with ECL (Coumaric acid and luminol with H₂O₂) solution. Image was captured in Chemidoc imaging system (BioRad).

5.2.12. Lactate dehydrogenase (LDH) assay

Cytosolic LDH enzyme is released into the culture medium during disruption or loss of cellular membrane integrity. Therefore, cell damage was assessed by measuring LDH release in the culture medium. LDH released was measured in SH-SY5Y cells colorimetrically according to the manufacturer's protocol (Himedia EZcount LDH cell assay kit). Cells were seeded into FBS-free medium for 12 h and subsequently co-incubated with 10 μ M A β 40 at 37 °C for 24 h with or without of LG_{WE} (0.05 and 0.25 mg/ml). 50 μ l of LDH reagent was then added to each well, incubated for at least 10 min in dark condition at 37 °C and the ongoing reaction was stopped by adding 50 μ l of stop solution. The absorbance was assessed at 580 nm using a reference filter of >600 nm.

Total LDH release was measured by adding 1% (W/V) Triton X-100 into the control cell for 1 h. The formula expressing total LDH activity in Percentage (%) (LDH in the supernatant + LDH in the cell lysate):

$$\% \text{ LDH released} = (\text{LDH activity in the medium} / \text{total LDH activity}) \times 100$$

5.2.13. Intracellular ROS measuring assay

Peroxide sensitive fluorescent probe 2',7'-Dichlorofluorescein diacetate (DCFH-DA) was used to measure intracellular reactive oxygen species spectrofluorimetrically in SH-SY5Y cells. Cells were seeded in 96 well plate, incubated with 10 μM A β 40 alone and with LG_{WE} at a concentration of 0.05 and 0.25 mg/ml for 24 h. Following day DCFH-DA at a concentration of 5 μM was added in the phenol red free media and incubated for 40 min in the dark at 37 °C. Non-fluorescent chemical probe DCFH-DA was converted into DCFH, which was subsequently oxidized to highly fluorescent DCF by intracellular ROS. Cells were immediately washed twice with PBS. Fluorescent intensity was measured by a microplate reader (BMG LABTECH POLARstar Omega, Ortenberg, Germany) with excitation and emission at 490 nm and 520 nm, respectively.

5.2.14. Measurement of intracellular calcium (Ca^{2+}).

Cell penetrative Ca^{2+} sensitive dye Fura2-AM (Invitrogen, USA) was used to measure free intracellular Ca^{2+} level in SH-SY5Y cell. 1×10^6 cells were treated with A β 40 (10 μM) alone and with LG_{WE} (at a concentration of 0.05 and 0.25 mg/ml) for 2 h. Next day, 5 μM Fura-2 AM in Krebs-Ringer-HEPES (KRH) buffer (5 mM KCl, 135 mM NaCl, 1 mM MgSO_4 , 0.4 mM KH_2PO_4 , 5.5 mM glucose, 1 mM CaCl_2 , 20 mM HEPES, pH 7.4) was added and incubated for 45 min at 37 °C. In a microplate reader, the fluorescence intensity was recorded with excitation at 340 nm and 380 nm and emission spectra at 525 nm, respectively. Results are expressed as a ratio of 340 / 380 values. Mean \pm SEM of multiple measurements were taken from three different experiments and expressed in the increase of ratio of 340/ 380 fluorescent unit (RFU) relative to the baseline reading.

5.2.15. Study of cellular apoptosis by Annexin-V PI staining

SH-SY5Y cells were seeded with a density of 1×10^6 cells per well onto a 6-well plate. After 24 h, cells were then treated with 10 μM A β 40 alone and with LG_{WE} at a concentration of 0.05 and 0.25 mg/ml for 24 h. Non-treated and cells treated with buffer were kept as controls and unstained. Post-treatment, cells were trypsinised and resuspended with annexin binding buffer (Cat. #

556454, BD pharmingen). 5 µl Annexin V-APC (BioLegends, Japan) and 10 µl PI (Sigma-Aldrich) were added to the cells, gently vortexed and incubated for 15 min at RT in the dark. After incubation cells were washed with annexin binding buffer and quantified with flow cytometer (FACS Verse, BD Biosciences). Utilizing the BD FACS Suite software, the analysis involved 10,000 cells for each sample. Three in-dependent experiments were performed for each set.

5.2.16. Methods for *in vivo* animal experiments.

a. *All animal experiments were done according to our previous published method*²⁰.

b. *Animals.*

C57BL/6J male mice (6-8 weeks old, healthy) weighing around 20-30 g were obtained from the Bose Institute, Centre for Translational Animal Research (CTAR), Kolkata, India. Every animal was maintained pertaining to the guidelines and principle of the Institutional Animal Ethics Committee (IAEC), using the CPCSEA approved protocol wide IAEC approval No # IAEC/BI/029/2022 dt. 02/08/2022. Before conducting any experiment, all animals were acclimatized in the animal house for at least two-three weeks along with constant 12 h light/dark cycle with water and food ad libitum. All experiments complied and adhered to the National Research Council's Guide for the Care and Use of laboratory Animals (NIH Publication No. 8023, revised 1978, U.S.A). All experiments also performed with ARRIVE guide-lines (Animal Research: Reporting of *In Vivo* Experiments; <https://arriveguidelines.org/arrive-guidelines>).

c. *Design of experiments.*

24 C57BL/6J male Mice were randomly divided into four (4) groups: Control, water extract of LG (1 mg), LG (5 mg), LG (10 mg). Each group contained Six (6) animals and administration was performed intraperitoneally with the following Schedule:

Control – Only phosphate buffered saline (PBS) as vehicle.

T1 (1 mg): 1 mg /kg body wt. of LG_{WE} dissolved in PBS

T2 (5 mg): 5 mg /kg body wt. of LG_{WE} dissolved in PBS

T3 (10 mg): 10 mg /kg body wt. of LG_{WE} dissolved in PBS

Mice were given injection once per week for four weeks consecutively i.e., a month and were later sacrificed one week after completion of the final treatment. Blood was collected on the day of

sacrifice in previously earmarked vials for biochemical and hematological examinations. The liver, spleen and kidney were isolated very carefully for histopathological examination and investigated for cytoarchitectural alterations after additional procedure.

d. Preparation of LG_{WE} and administration of LG_{WE} intraperitoneally.

Body weights of each animal and calculated doses of LG_{WE} to be injected were recorded before their treatment. 70% ethanol was applied into the abdominal cavity of the mice. 26-gauge DISPOVAN needle with a capacity of 1 ml was inserted into the peritoneal cavity. The needle and the syringe were kept at a suitable angle with respect to the body of the animal. The respective dosage of LG_{WE} (1 mg/kg, 5 mg/kg and 10 mg/kg) and PBS for control group was injected inside the peritoneal cavity very slowly. The needle was carefully removed with utmost care and subtle compression was applied all over the region. Afterwards, the animals were returned to their respective cages. After completion of treatment for four weeks body weights of animals were recorded.

e. Examination of blood for biochemical and hematological parameters

Biochemical parameters including serum glutamic oxaloacetic transaminase, serum urea, serum glutamic pyruvic trans-aminase and creatinine were analyzed for their sub-chronic toxicity of LG_{WE} by taking help of commercially available diagnostic test kits (ARKRAY Healthcare Pvt. Ltd., India). Standard kits by following the manufacturer's manual and cell counter were used for blood parameters (hemoglobin, red blood cells, white blood cells, eosinophil, neutrophil, basophil, monocyte, and lymphocyte) estimation.

f. Histopathological examinations for subchronic toxicity of LG_{WE}.

Liver, Kidney, Spleen were carefully isolated after sacrificing the animals and individual weights were recorded for each specific organ. The preserved tissues of liver, kidney, and spleen tissues were histopathologically evaluated. LG_{WE} treated mice and control mice were sacrificed by decapitation following a month of treatment regimen. The liver, kidney and spleen were isolated and fixed onto 10% neutral buffered formalin for approximately 24-48 h. The organs were then further processed and immersed in paraffin wax. Each tissue sections were carefully cut with a microtome with a thickness of 5 μ m. Prepared slides were stained with hematoxylin and eosin (H&E staining), gomori trichrome and periodic acid-s chiff for histological examinations. Stained

Slides were observed using the light microscope (NIKON T₂, India) for histopathological alternation, and pictures were taken at 10x and 20x magnification.

5.3. Results and Discussion

5.3.1. Solvent extraction and isolation of LG

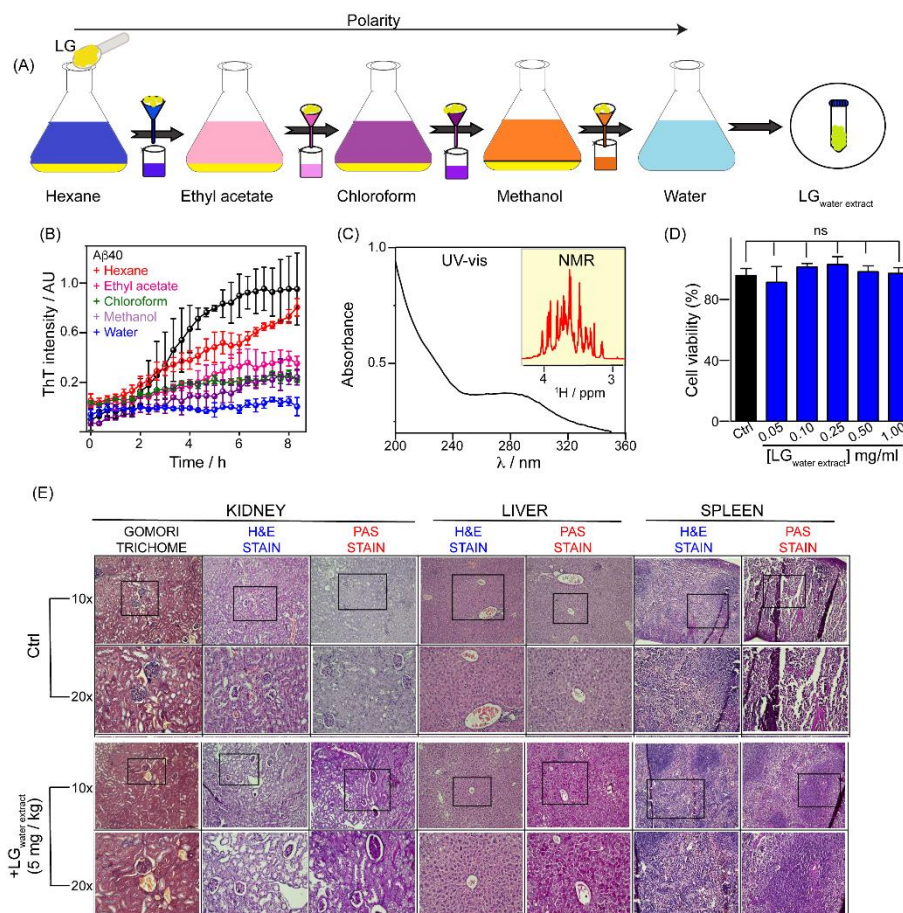


Figure 5.1. The solvent extraction and characterization of LG. (A) Schematic showing the solvent extraction process. (B) Time dependent ThT kinetics for A β 40 in the absence and/or presence of LG solvent extracts. Error bars represent the average of triplicate experiments. (C) Absorption spectra recorded on LG_{WE} solution. NMR spectra of LG_{WE} compounds in inset. (D) Viability of SH-SY5Y cells upon treating with a graded concentration of LG_{WE}. Media served as a control. Values are represented as mean \pm SEM (n = 6). Statistical analysis was done by one-way ANOVA. (ns and ctrl denote non-significant and control cells, respectively). (E) Histopathological studies of the effect of LG_{WE} at sub-chronic toxicity on mice (n=6 each group) at a concentration of 5 mg/kg. Ctrl-control mice. 10x and 20x magnified images of kidney, liver, and spleen are shown. PAS-periodic acid-Schiff; H&E-hematoxylin-eosin.

LG exhibits insolubility in a singular solvent because of the various compounds and their diverse chemical compositions ¹³. Hence, a solvent extraction method with a gradual increase in the polarity of the solvents has been established (Figure 5.1A) ²⁵. Hexane, a nonpolar solvent, dissolved natural lipids and fat compounds ²⁶. On the other hand, methanol and water being polar solvents dissolved all ionic and polar molecules present in LG. All the solvent extracts thus collected, and then lyophilized for subsequent experiments.

Table 5.1. Probable Compounds identified from LG Water Extract Using LC-MS Analysis.

	Compound Name	Molecular mass (g/mol)	m/z	Ion Mode
1	Chrysin	254	294.93	Positive
2	Quercetin	302	303.99	Positive
3	Myricetin	318	318.90	Positive
4	Luteolin	286	324.93	Positive
5	Kaempferol	286	324.93	Positive
6	Apigenin	270	270.98	Positive
7	Galangin	270	270.98	Positive
8	Pinochembrin	256	294.93	Positive
9	Chebolic acid	356	394.87	Positive
10	Ellagic acid	198	198.94	Positive
11	Methyl syringate	212	252.85	Positive
12	Ethyl gallate	198	198.94	Positive
13	Coumarin	146.14	184.97	Positive
14	Hydroxymethylfurfural	126	126.97	Positive
15	Ascorbic acid	176	176.93	Positive
16	Gallic acid	170	135.90	Positive
17	Niacin	123	123.97	Positive
18	Vitamin B6	169	169.85	Positive
19	Riboflavin	376	376.88	Positive
20	Folic acid	441	406.81	Positive
21	Dially trisulfide	178	178.93	Positive
22	Alliin	177	178.92	Positive
23	Allicin	162	162.88	Positive

24	E/Z- ajoene	234	234.94	Positive
25	Methyl allyl disulfide	120	120.92	Positive
26	S-methyl-I-cysteine (SMC)	135	135.95	Positive
27	S-allyl-cysteine	161	161.95	Positive
28	S-methyl-L-cysteine sulfoxide (SMCS)	151	151.92	Positive
29	Diallyl sulfide	114	114.95	Positive
30	Monosaccharide (Glucose, fructose)	180	180.95	Positive
31	Disaccharide (Sucrose, Maltose, Isomaltose, Turanose)	342	380.91, 364.73	Positive
32	Gluconolactone	178	178.92	Positive
33	Gluconic acid	196	196.96	Positive
34	Trisaccharide (Erllose, Panose)	504	528.79	Positive

5.3.2. Screening and characterization of LG extract

First, we investigated the anti-amyloid efficacy of LG extracts using a ThT-based time kinetics assay on A β 40, revealing their specific impact on amyloid aggregation. ThT experiments of solvent extracts alone did not increase ThT fluorescence (Appendix 5, Figure S5.1A). In contrast, aggregation kinetics of A β 40 exhibited the typical sigmoidal pattern, with an early lag phase, followed by a fast growth phase, and ultimately a plateau phase suggesting the formation of matured fibrils (Figure 5.1B). Interestingly, all the solvent extracts upon their addition reduced the intensity of the saturation phase of the A β 40 aggregation kinetics, demonstrating an inhibitory effect in a polarity dependent manner (Figure 5.1B and Appendix 5, Figure S5.1B); water extracts of LG (LG_{WE}) showing maximum inhibitory effect (~ 82% inhibition) (Figure 5.1B). Hence, we concentrated our study on LG_{WE}. To characterize the molecules, present in LG_{WE}, ultraviolet (UV) absorption spectra and nuclear magnetic resonance (NMR) were conducted (Figure 5.1C). LG_{WE} revealed a strong band at 280 nm in UV-visible range, suggesting the presence of aromatic/polyphenolic compounds (Figure 5.1C). A characteristic NMR signal of carbohydrates was also found in the range of 4.5 to 5.5 ppm (Figure 5.1C inset). Interestingly, LC-MS identified 34 compounds in LG_{WE}, belonging to polyphenols, acid derivatives and vitamins, sulfur compounds, and carbohydrates (Table 5.1). Next, we tested the cytotoxic effects of LG_{WE} in SH-

SY5Y human neuroblastoma cells²⁷. An MTT assay performed with increasing concentrations of LG_{WE} indicated no discernible toxicity even at 1 mg/ml concentration up to 24 h (Figure 5.1D)^{1b}.

Furthermore, the cytotoxicity of LG_{WE} was also tested in C57BL6/J mouse model, suitable for studying neuronal diseases²⁸. LG_{WE} at different doses with PBS control was administered intraperitoneally once a week for four weeks. There was no observable mortality or behavioural changes among any group; rather, their demographic parameters, such as overall body weight and organ weight post-sacrifice remained unchanged (Appendix 5, Figure S5.2). We did not observe any kind of discernible cytoarchitectural changes in T₁, T₂, and T₃ when compared to the control group (Figure 5.1E and Appendix 5, Figure S5.3). These organs (liver, kidney, and spleen tissues)

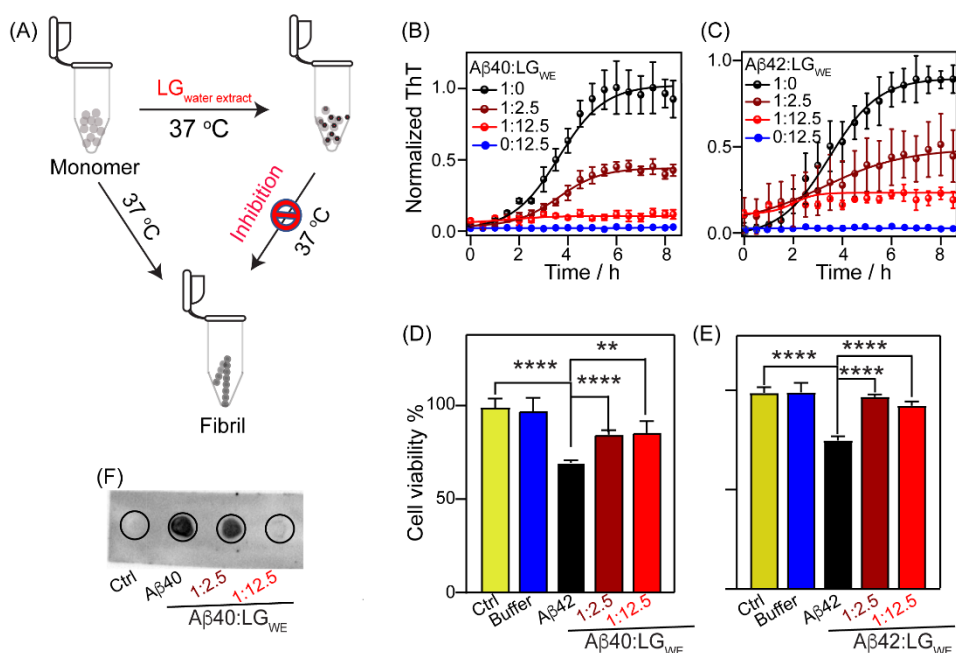


Figure 5.2. Inhibitory effect of LG_{WE} on Aβ40/Aβ42 aggregation kinetics. (A) Schematic representation of fibril inhibition by LG_{WE}. ThT aggregation kinetics profile of Aβ40 (B) and Aβ42 (C) in absence (black) and presence of LG_{WE} at an Aβ:LG_{WE} ratio of 1:2.5 (brown) and 1:12.5 (red), respectively at 37 °C. The blue ThT curve represents 0.25 mg/ml LG_{WE} alone. SH-SY5Y cells were treated with Aβ40 (D) and Aβ42 (E) alone and with LG_{WE} at Aβ:LG_{WE} ratio of 1:2.5 and 1:12.5. Values are represented as mean ± SEM, n=10. Significance was calculated between control and Aβ alone by one way ANOVA and Dunnett's multiple comparisons test. Unpaired two tailed T-test were performed between Aβ40/Aβ42 and Aβ+LG_{WE}. ** and **** denote p<0.01 and p<0.0001, respectively. (F) Dot blot analysis (n=3/experiments) of Aβ40 fibril alone and in presence of Aβ40:LG_{WE} at a ratio of 1:2.5 and 1:12.5.

were stained with (a) Haematoxylin-eosin for overall tissue architecture; (b) PAS to detect changes in polysaccharides or mucosal substances; and (c) Gomori Trichrome for renal tissues. Although minute differences were observed in PAS stains of the kidney and liver for T₂ and T₃ in comparison to the control, probably due to changes in metabolism and other unknown factors. Besides, none of the studied groups showed any severe changes in haematological and biochemical parameters compared to control (Table S5.1, Appendix 5). A slight increase in liver enzymes SGOT and SGPT was observed in T₂; all other parameters of biochemical nature were well within the range when compared to control (Appendix 5, Figure S5.4). These overall parameters corroborate the safety and standard of the compound for further *in vivo* studies.

5.3.3. LG_{WE} inhibits A β 40/A β 42 aggregation and toxicity

Having known that LG_{WE} is non-toxic, a detailed analysis of its inhibitory effects against amyloid beta aggregation was performed (Figure 5.2A). The ThT kinetics of A β 40/A β 42 showed a sigmoidal aggregation pattern measured as a function of time (Figures 5.2B-C). As shown in Figures 5.2B and C, ThT fluorescence systematically dropped with an increasing concentration of LG_{WE} demonstrating its inhibitory effect on A β 40/A β 42 aggregation in a dose-dependent manner. The addition of 0.25 mg/ml of LG_{WE} (A β 40:LG_{WE} = 1:12.5), resulted in the highest amount of amyloid fibril inhibition (nearly 90% inhibition) (Figure 5.2B). Under identical experimental conditions, LG_{WE} by itself had no effect on ThT intensity (Figures 5.2B-C). It was observed that at an A β 42:LG_{WE} ratio of 1:2.5 and 1:12.5, LG_{WE} exhibited a substantial inhibitory effect reducing A β 42 fibrillization by almost 52% and 80%, respectively (Figure 5.2C). The inhibition was caused by delaying the lag phase, indicating that LG_{WE} most likely hindered the nucleation event of A β 40/A β 42. It is well noted that oligomers and protofibrils of A β species induce various kinds of cytotoxicity in neuronal cells ²⁹. Further, to implicate our ThT based *in vitro* data in cellular models, we investigated the potential role of LG_{WE} in recovering cellular viability against A β 40/A β 42 species mediated cellular damage and neurotoxicity in SH-SY5Y cells (Figures 5.2D-E). MTT assay showed a significant reduction in cell viability (~60%) compared to control cells and buffer when was able to considerably recover cell viability by ~80-90%, respectively (Figures 5.2D-E). Consistent with our ThT data (Figures 5.2B-C), the cell viability assay shows the treated with A β 40/A β 42 in the presence of different concentrations of LG_{WE} (Figures 5.2D-E). However,

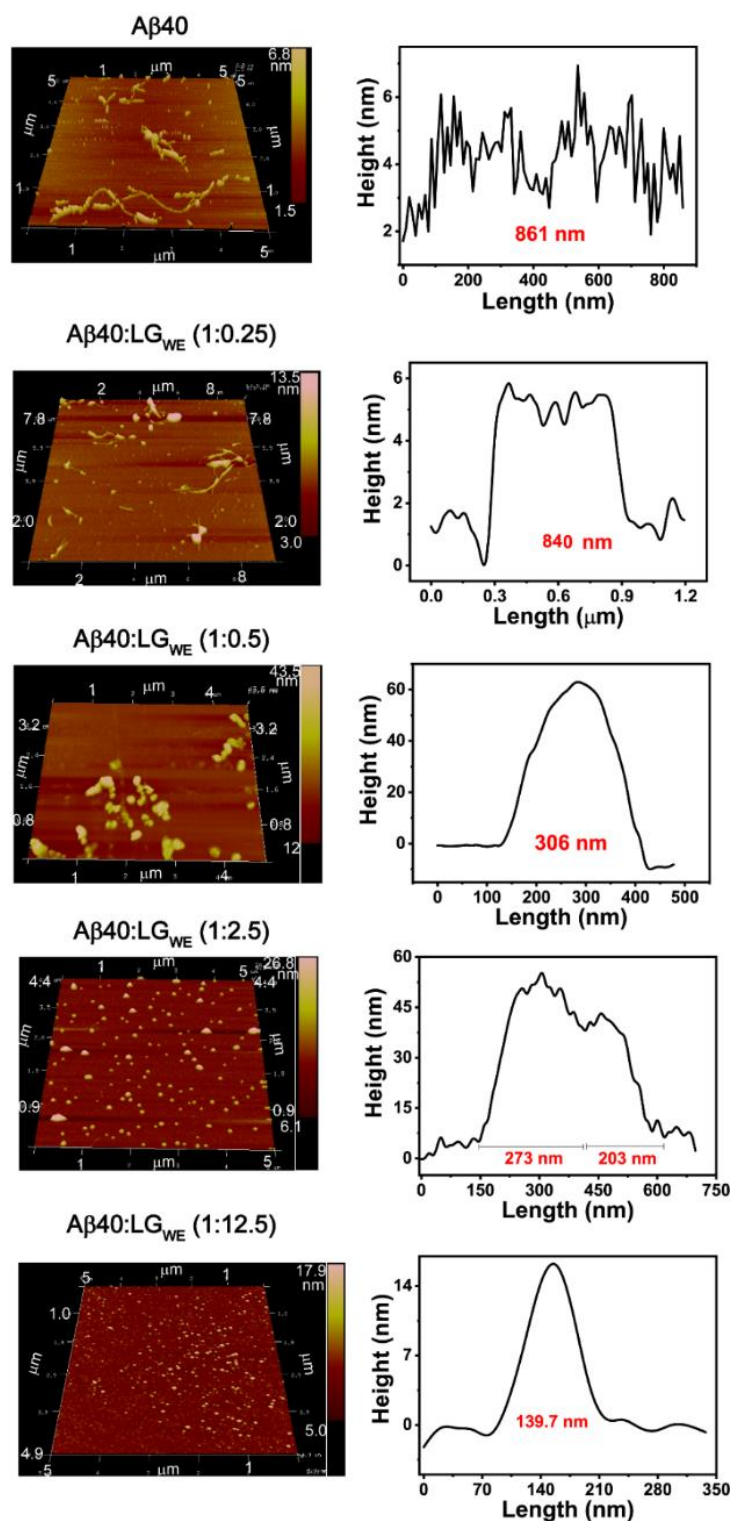


Figure 5.3. Aggregates morphology visualized by AFM (left panel). Length profile of the Aβ40 fibril and Aβ40:LG_{WE} aggregates at 1:0.25, 1:0.5, 1:2.5, 1:12.5 ratio (right panel).

addition of LG_{WE} at a ratio of 1:2.5 and 1:12.5 (A β :LG_{WE}) to A β 40/A β 42 recovering potential of LG_{WE} over A β mediated neurotoxicity. Moreover, to confirm the inhibition of A β 40 amyloidosis by LG_{WE}, a dot blot assay was performed (Figure 5.2F). The chemiluminescence signal intensity from OC antibody binding to A β 40 was diminished in the presence of LG_{WE} at 1:2.5 ratio of A β 40/LG_{WE} and almost disappeared oligomers or fibrils of A β 40 (Figure 5.2F). Notably, no cross reactivity between the OC antibody (specific for A β 40) and LG_{WE} was found when spotted alone on the membrane in case of A β 40 and LG_{WE} at a 1:12.5 mg/ml ratio, indicating complete inhibition of (Appendix 5, Figure S5.5). The differences in cytotoxicity indicated that LG_{WE} induced A β species to divert from the formation of amyloid fibrils, inhibited aggregation-prone intermediates, and generated morphologically distinct structures.

5.3.4. LG_{WE} modulates morphology and secondary conformation of A β 40 and A β 42

Next, to gain insights into the morphological changes in amyloid aggregation, we conducted a statistical analysis of fibril morphology of A β in the absence and/or in the presence of LG_{WE} using atomic force microscopy (AFM). A β 40 alone produced a long fibril with an average length of 861 nm, while a round shaped amorphous morphology with an average length 273 or 203 nm and 139.7 nm appeared in the presence of LG_{WE} at ratio of 1:2.5 and 1:12.5, respectively (Figure 5.3). Further, a precise morphological comparison of aggregates across samples at lower doses of LG_{WE} resulted in short and fragmented

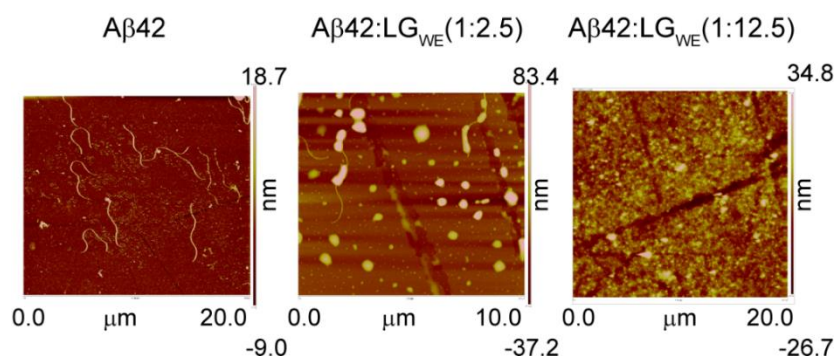


Figure 5.4. AFM images of A β 42 fibrils and A β 42:LG_{WE} aggregates at 1:2.5 and 1:12.5 ratio.

fibrils (Figure 5.3). The LG_{WE} mediated A β 40 fibrils in the presence of 1:0.25 and 1:0.5 ratio of A β 40:LG_{WE} showed a length of 840 nm and 306 nm, respectively; the fibrils were much shorter than the matured A β 40 fibrils (Figure 5.3). Interestingly, a similar effect was observed for A β 42 in the absence and/or in the presence of LG_{WE} (Figure 5.4). Next, we used far-UV CD to investigate

how A β 40 changed its structural conformation with and without LG_{WE}. A β 40 retained its random coil conformation, irrespective of the presence or absence of LG_{WE} at the beginning of incubation (0 h) (Figure 5.5A). However, after 12 h of incubation at 37 °C, A β 40 exhibited a CD spectrum with a maximum at 200 nm and a minimum at 220-223 nm, signifying its transient state marked by a progressive accumulation of β sheets (Figure 5.5B)³⁰. When incubated with either 1:2.5 or 1:12.5 A β 40:LG_{WE}, the CD spectra revealed a gradual structural transition in A β 40 that was characterized by a reduction in CD molar ellipticity (Figure 5.5B). Nearly, a 75 % decrease in CD intensity at 222 nm was observed in presence of LG_{WE} as compared to A β 40 alone, indicating a reduction in β sheet aggregates in A β 40 (Figure 5.5B). Separately, a minor change of secondary structure was observed for A β 42 when incubated with a 2.5 excess concentration LG_{WE} (Figure 5.5C). A further increase in LG_{WE} concentration to a 1:12.5 (A β 42:LG_{WE}) ratio, reduced the molar ellipticity value by 40% and shifted the CD minima after incubation at 37 °C (Figure 5.5C). This indicated significant disruption of the structural transition of A β 42 toward a β -sheet-rich configuration. The CD results in conjunction with ThT fluorescence and AFM images, indicating efficient inhibition of A β 40/A β 42 aggregation by LG_{WE}.

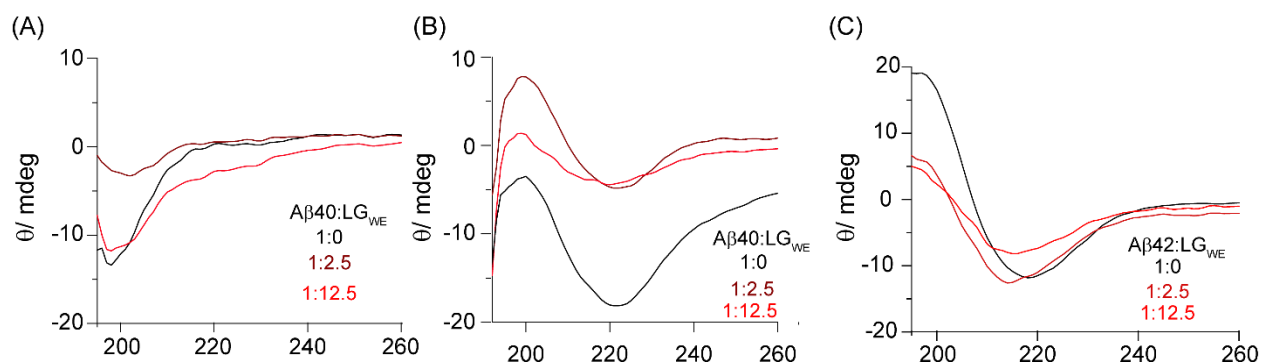


Figure 5.5. (A) CD spectra of A β 40 in absence (black) and presence of LG_{WE} at 1:2.5 (brown) and 1:12.5 (red) ratio of A β 40/LG_{WE} before (A) and after (B) incubation at 37 °C in 20 mM sodium phosphate buffer along with 50 mM sodium fluoride at pH 7.4. (C) CD spectra of A β 42 with or without LG_{WE} at 1:2.5 and 1:12.5 ratio of A β 42/LG_{WE} after incubation at 37 °C.

5.3.5. LG_{WE} disintegrates mature A β 40 and A β 42 fibrils into non-toxic species

Considering the hypothesized role of plaques as nucleating sites for toxic oligomers, the disassembly of amyloid could emerge as a promising approach to diminish toxicity and reduce

amyloid plaque loads³¹. To assess the stability of A β 40 fibrils in the presence of LG_{WE}, we incubated the preformed A β 40/A β 42 fibrils with A β :LG_{WE} 1:12.5 ratio. Upon the addition of LG_{WE} to preformed A β 40 fibril, a spontaneous reduction in ThT fluorescence was observed, suggesting that LG_{WE} may have the potential to destabilize matured fibrils (Figure 5.6A). Hence, to verify that the observed outcome was not a result of ThT displacement by LG_{WE} from the fibrils,

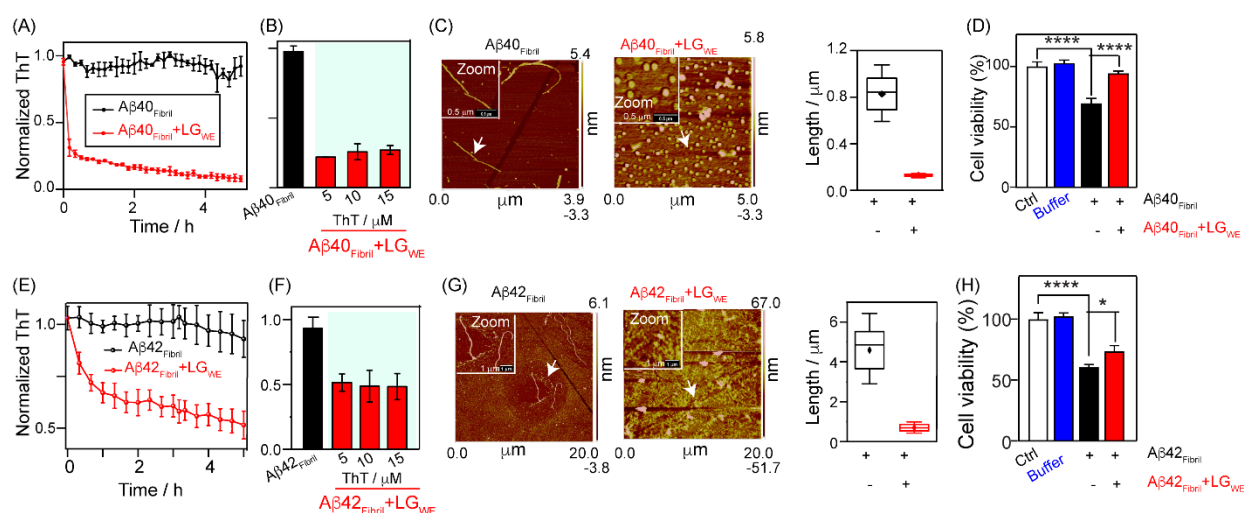


Figure 5.6. Disaggregation of amyloid fibrils by LG_{WE}. Disintegration of matured A β 40 fibril (A) and A β 42 fibril (E) upon addition of 0.25 mg/ml LG_{WE} (A β :LG_{WE} = 1:12.5). The bar plot represents no competition for amyloid A β 40 fibril (B) and A β 42 fibril (F) binding between ThT and LG_{WE}. AFM images of mature A β 40 fibril (C) and A β 42 fibril (G) after and before addition of 0.25 mg/ml LG_{WE} and AFM fibril length distribution. The diamond square, rectangular box and centre line represent mean, mean \pm SD, and median, respectively. SH-SY5Y cells were treated with 10 μ M preformed A β 40 fibril (D) and/or A β 42 fibril (H) alone and with LG_{WE} at the ratio of 1:12.5 (A β :LG_{WE}). Values are represented as mean \pm SEM, n=9. One way ANOVA with Dunnett's comparisons test was performed between control and A β 40/A β 42 alone. Unpaired two tailed T-test between A β 40/A β 42 and A β 40/A β 42+LG_{WE} were done. **** and * denotes p<0.0001 and p<0.05, respectively.

we maintained the ratio of A β :LG_{WE} (1:12.5) constant, while varying the ThT concentrations (5, 10, 15 μ M). The almost uniform ThT-intensity values across all concentrations of ThT confirmed that the reduction in ThT fluorescence was due to LG_{WE} disintegrating the fibrils (Figure 5.6B). Next, we performed AFM of the disintegrated species, obtained from ThT experiments. The incubation of preformed A β 40 fibril in the presence of LG_{WE} at 1:12.5 ratio resulted in a disappearance of fibrillar morphology in AFM (Figure 5.6C). When LG_{WE} was present, the AFM-measured length distributions revealed much shorter aggregates, in contrast to matured fibrils

formed in its absence (Figure 5.6C). Furthermore, MTT assay was also performed upon incubation of matured amyloid fibrils in absence and/or presence of LG_{WE} at a concentration ratio of 1:12.5 (A β 40:LG_{WE}). A reduced cell viability (~60%) was observed for A β 40 fibrils, which was recovered by around >90 % after incubation of the fibrils with LG_{WE} (Figure 5.6D). These results suggest that LG_{WE} is able to disintegrate matured amyloid fibrils into smaller fragments, which renders them non-toxic in nature towards neuronal cells. Similarly, after incubation of matured A β 42 fibrils with LG_{WE}, we found a rapid decrease in ThT intensity over time indicating the disruption of preexisting fibrils (Figure 5.6E). Increasing ThT excess in repeated experiments excludes competitive binding with LG_{WE} on matured A β 42 fibrils, yielding consistent intensity trends (Figure 5.6F). The AFM analysis provided additional support to the observation, revealing

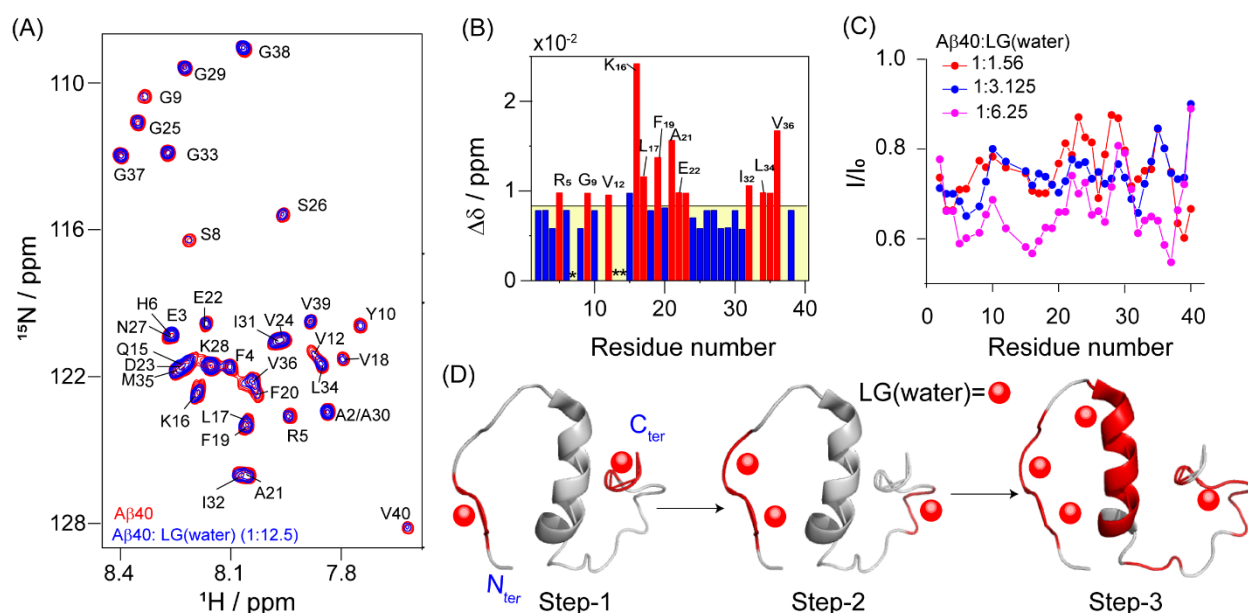


Figure 5.7. Structural insights into LG_{WE} interaction with A β 40. 2D $^1\text{H}/^{15}\text{N}$ SOFAST-HMQC NMR spectra of (A) A β 40 and before (red) and after (blue) addition of LG_{WE} at 1:12.5 ratio of A β 40:LG_{WE}. (B) The CSP bar plot of A β 40 in the presence of LG_{WE} (A β 40:LG_{WE} =1:12.5). Red bar represents the CSP value above the black threshold line. (C) Relative average of intensity broadening of A β 40 upon titration with LG_{WE} at 1:1.56 (red), 1:3.125 (blue) and 1:6.25 (pink) mg/ml ratio of A β 40:LG_{WE}. Cartoon of stepwise interaction mechanism of (D) A β 40 (PDB: 2LFM) with LG_{WE}. Step 1, 2 and 3 indicate for 1:1.56, 1:3.125 and 1:6.25 A β :LG_{WE} interaction highlighted by red color. NMR spectra was recorded at 283 K using Bruker Avance III 500 MHz NMR spectrometer, equipped with a SMART probe.

that LG_{WE} treated fibrils exhibited smaller, non-fibrillar aggregates in comparison to untreated matured fibrils (Figure 5.6G). The cytotoxicity assay further confirms formation of an alternative

non-cytotoxic structures of A β 42 matured fibril on addition of LG_{WE} which recover the cell viability beyond ~70-80%, suggesting a robust effect of LG_{WE} on amyloid fibril disintegration (Figure 5.6H).

5.3.6. Insights into the interaction mechanism of LG_{WE} with A β 40 and A β 42 using NMR

To gain molecular insights into the binding interaction of LG_{WE} with amyloid species at an atomic resolution, we utilized the high-resolution 2D ¹H-¹⁵N Heteronuclear Multiple Quantum Coherence (HMQC) NMR experiments. The A β 40 amide resonances in the absence of LG_{WE} showed dispersed NMR peaks of lower molecular species (Figure 5.7A).

However, upon addition of LG_{WE} (A β 40:LG_{WE}=1:12.5), not only substantial loss of signal intensity was observed but we also found residue specific chemical shift perturbation (CSP) (Figure 5.7A). Interestingly, the CSP was observed for the central hydrophobic region, particularly K16, L17, F19, A21, E22 and D23 residues and C-terminal hydrophobic residues, including I32, L34, M35, and V36, indicating LG_{WE} induced structural rearrangement for A β 40 (Figure 5.7B). The residue specific signal intensity pattern showed remarkable changes for the stretches S8-V12 and K16-A21. This revealed the direct involvement of these hydrophobic rich stretches in the molecular interaction of A β 40 with LG_{WE} (Appendix 5, Figures S5.6A-B). Further, to gain stepwise atomistic insights into the interface of this inhibitory interaction, HMQC NMR of A β 40 was performed with different concentrations of LG_{WE}. At 1:1.56 ratio (A β 40:LG_{WE}), the flexible N and C-terminal of A β 40 first interact with LG_{WE} (Figures 5.7C-D). Upon increasing the ratio of A β 40:LG_{WE} to 1:3.125, interactions were additionally observed along C-terminal hydrophobic segments (Figures 5.7C-D). At even higher concentrations of 1:6.25 (A β 40:LG_{WE}), the interaction was observed at the central hydrophobic core as well (Figures 5.7C-D). According to recent studies, the A β 40 oligomerization and fibril propagation processes are mainly driven by specific segments, like the N and C terminus, H¹³HQK¹⁶ segments, hinge or turn regions, and central hydrophobic K¹⁶LVFFA²¹ segments³². Additionally, the GxxxG motif, particularly G33 to G37 residues, plays a vital role in cellular toxicity by enhancing structural flexibility, prolonging the existence of toxic oligomers, and is necessary for inducing cellular damage³³. Thus, the observation of a direct molecular association between LG_{WE} compounds and these segments underscored the inherent inaccessibility necessary for amyloid fibril formation. To further confirm the binding sites more accurately, we assigned the carbon backbone and side chain methyl group

of A β 40 from ^1H - ^{13}C HSQC NMR in the presence or absence of LG_{WE} at a 1:12.5 concentration ratio of A β 40²¹⁻²². Interestingly, the α -carbon of D1, R5, Y10, V12, H13/H14, A21, and M35 were found to have intensity broadening upon titration with LG_{WE} (Figure 5.8A). We also noticed the signal intensity to have broadened for the pair of γ -methyl groups of V12, V18, and V24 (Figure 5.8B). In addition, treatment of LG_{WE} perturbed the γ and δ -methyl groups of I31, I32 and L17/L34 (Figure 5.8B). Interestingly, LG_{WE} was able to interact with A β 42, similar to its binding to A β 40 (Figure 5.9A). The degree of perturbation was largest for the N-terminal residues (R5, S8 and G9) followed by the central hydrophobic residues (Q15, V18, F20) followed by the C terminal residues (M35, V36, I31, L34, M35, G37, V39) of A β 42 in the presence of 1:12.5 mg/ml ratio of A β 42:LG_{WE} (Figure 5.9B). A significant loss of signal intensity for the stretches R5 to H13, Q15

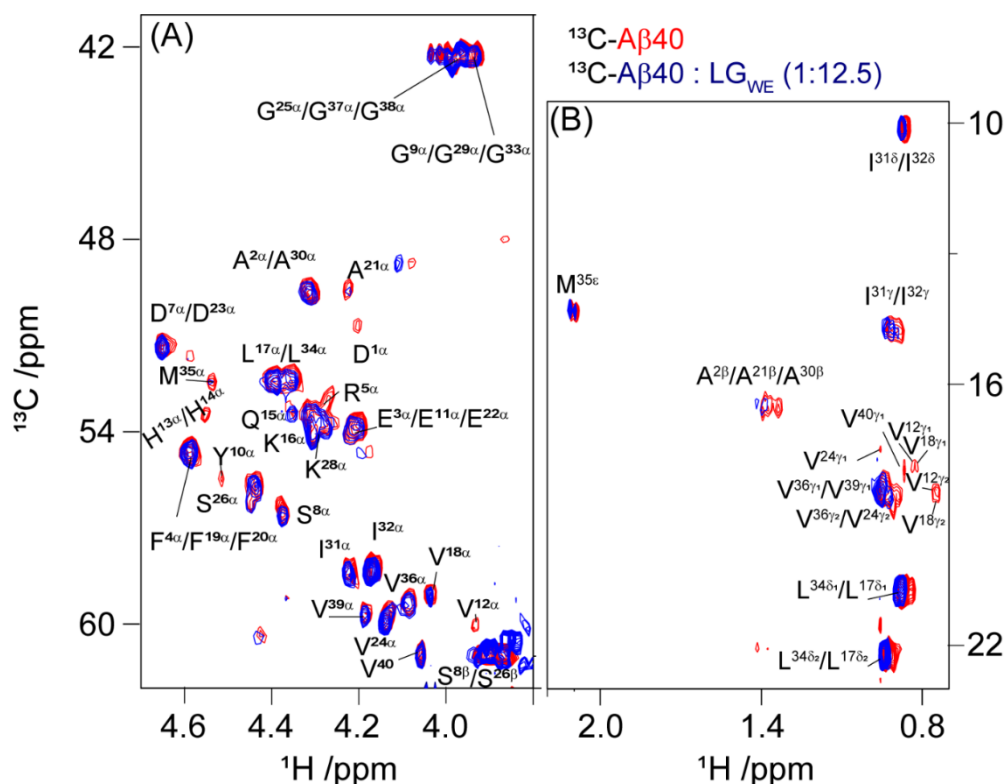


Figure 5.8. 2D NMR $^{13}\text{C}/^1\text{H}$ HSQC spectra of A β 40 in absence (red) and presence of water extract of LG (blue) at 1:12.5 ratio (A β 40:LG_{WE}): (A) backbone chain (B) side chain carbons . Spectra was recorded on a Bruker Avance III 700 MHz NMR, equipped with a Cryoprobe at 286 K.

to E22, and G37 to A42 suggested a potential binding site for LG_{WE} on A β 42 (Appendix 5, Figures S5.6C-D). Upon decreasing the concentration of LG_{WE} to a 1:1.56 ratio of A β 42:LG_{WE}, six residues I31, I32, G33, V36, G37, and G38 from the C-terminal and three residues F19, F20, and A21 from the central hydrophobic region showed an intense residue specific broadening indicating

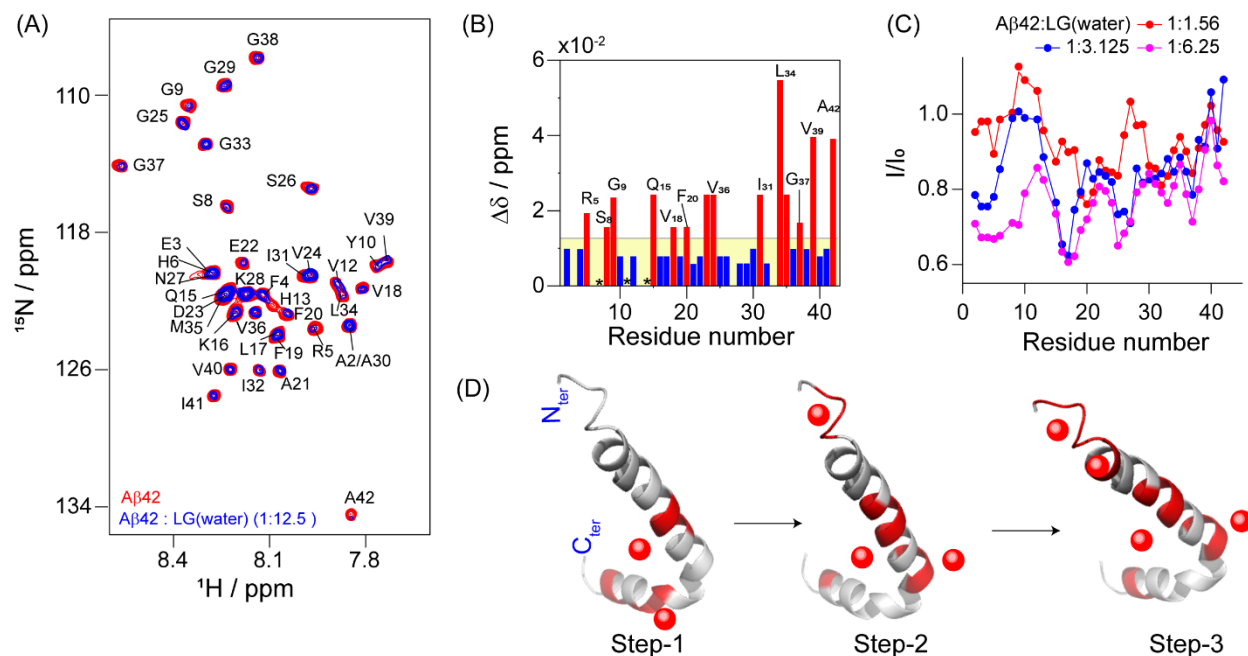


Figure 5.9. Atomic insights into LG_{WE} interaction with A β 42. (A) 2D $^1\text{H}/^{15}\text{N}$ SOFAST-HMQC NMR spectra of A β 42 and before (red) and after (blue) addition of LG_{WE} at 1:12.5 ratio of A β 40:LG_{WE}. (B) The CSP bar plot of A β 42 in the presence of LG_{WE} (A β 42:LG_{WE} = 1:12.5). Red bar represents the CSP value above the black threshold line. (C) Relative average of intensity broadening of A β 42 upon titration with LG_{WE} at 1:1.56 (red), 1:3.125 (blue) and 1:6.25 (pink) mg/ml ratio of A β 42:LG_{WE}. Cartoon of stepwise interaction mechanism of (D) A β 40 (PDB: 1IYT) with LG_{WE}. Step 1, 2 and 3 indicate for 1:1.56, 1:3.125 and 1:6.25 A β 42:LG_{WE} interaction highlighted by red color. NMR spectra was recorded at

that they were very close to LG_{WE} (Figures 5.9C-D). A loss of signal intensity was also observed for the three residue stretches E3-R5, K16-V18, and G25-N27 that indicated the potential LG_{WE} interaction site on A β 42 when present in a A β 42:LG_{WE} ratio of 1:3.125 (Figures 5.9C-D). A further increase in concentration ratio of A β 42:LG_{WE} to 1:6.25 increased line broadening effects in the segment specific interaction sites involving A2-H6, K16-F19, G25-N27 and V36-G38 residues (Figures 5.9C-D). Taken together, the interaction of LG_{WE} extracts with the hydrophobic central,

and C-terminal regions of A β 40/A β 42 may have translated in observed reduction in membrane damage and toxicity to neuronal cells.

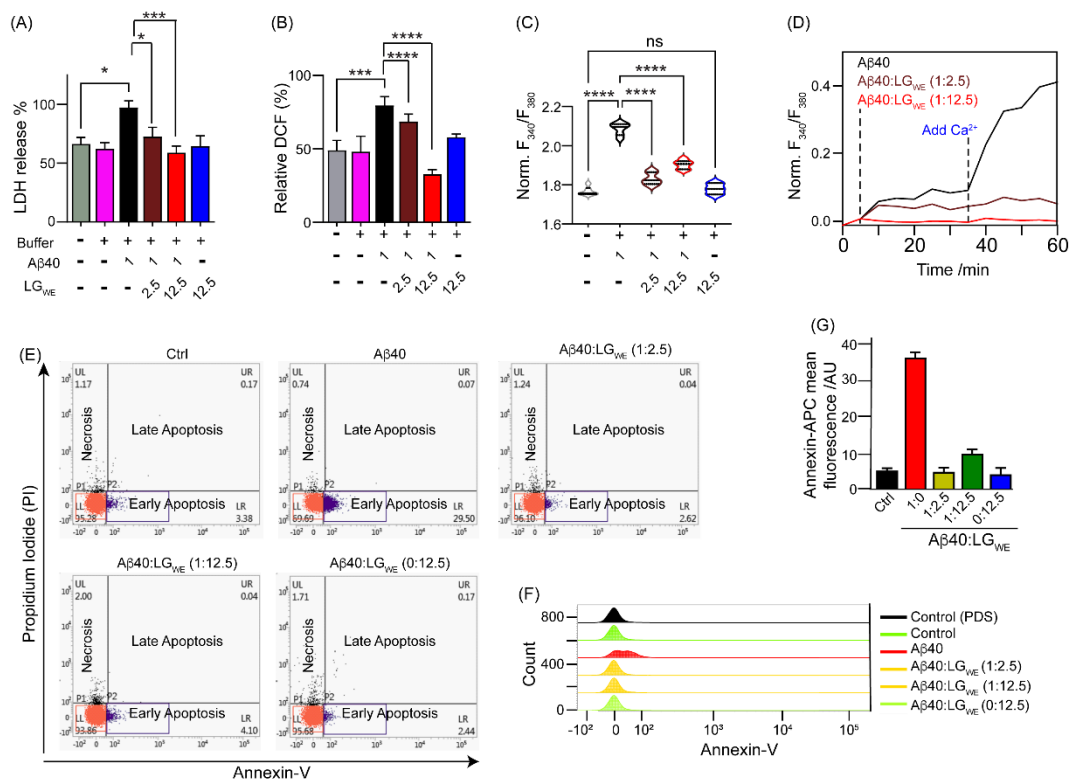


Figure 5.10. Amelioration of neurotoxic effects of A β 40 by LG_{WE}. (A) LDH release after treatment with A β 40 (10 μ M) for 24 h in the absence and presence of LG_{WE} at a ratio of 1:2.5 and 1:12.5 (A β 40:LG_{WE}). Values are represented as mean \pm SEM, n=6. (B) Effect of LG_{WE} on A β 40 (10 μ M) induced ROS generation in SH-SY5Y cells using relative DCF measurement. Values are indicated as mean \pm SEM, n=6. (C) The change of intracellular calcium (Ca²⁺) in SH-SY5Y cells upon addition of LG_{WE} on A β 40 was shown in violin plot with the fluorescence ratio 340/380 plotted in Y-axis. Values are represented as mean \pm SEM, n=6. One way ANOVA with Dunnett's comparisons test between control and A β 40 alone and unpaired two tailed T-test between A β 40 and A β 40+LG_{WE} was performed. ns = non-significant, * p<0.05, *** p<0.001 and **** p<0.0001. (D) The influx of Ca²⁺ ions into TLBE LUVs after addition of A β 40 aggregates and A β 40:LG_{WE} at 1:2.5 and 1:12.5 ratio. (E) Flow cytometry analysis of cell death in Annexin V and PI-stained cells showing the percentage of necrotic, late apoptotic, early apoptotic, and viable cell populations in SH-SY5Y cells upon treatment with A β 40 (10 μ M), A β 40: LG_{WE} in concentration ratios of 1:2.5 and 1:12.5 along with control and LG_{WE} alone for 24 h. (F) Overlaid histogram plot of Annexin V-APC fluorescence treatment groups. The movement of histogram towards right indicated higher apoptosis and annexin V binding. (G) The bar diagram represented the mean fluorescence intensity of Annexin V-APC.

5.3.7. *Effect of LG_{WE} on A β 40 induced cell membrane damage*

Next, we explore the cellular mechanisms underlying LG_{WE}'s protective role against A β amyloidosis by looking the cellular pathways responsible for amyloid-related damages. Amyloid proteins damage the neurons either by enhancing apoptosis or ROS production, and/or membrane leakage³⁴. Moreover, oligomeric species of A β 40 is known to induce membrane damage among neuronal cells³⁵. So, we investigated the role of LG_{WE} in preventing the membrane damage potential of A β 40 using lactate dehydrogenase (LDH) assay. SH-SY5Y cells treated with A β 40 released a significant amount of cytosolic LDH into the culture medium compared to buffer and control cells (Figure 5.10A). However, co-incubation of A β 40:LG_{WE} at a ratio of 1:2.5 and 1:12.5, substantially reduced LDH leakage in SH-SY5Y cells (Figure 5.10A). In contrast, LG_{WE} alone did not exhibit LDH release. These findings indicate that LG_{WE} at a concentration of 0.25 mg/ml was sufficient to inhibit A β 40 mediated cellular damage and membrane leakage. It can also be speculated that LG_{WE} components may provide a protection to the extracellular membrane damage during neuro-inflammation.

5.3.8. *LG_{WE} ameliorates oxidative stress injury and calcium homeostasis*

As evidenced earlier, A β 40/A β 42 amyloidosis promotes neuronal cell death by generating intracellular ROS leading to mitochondria mediated apoptosis³⁶. Therefore, we have checked whether LG_{WE} can prevent A β mediated ROS generation. Intracellular ROS generation was measured by using fluorescent probe 2',7'-dichlorodihydrofluorescein diacetate (DCFH-DA) in SH-SY5Y cells (Figure 5.10B). An increase in the fluorescent intensity compared to control cells was observed on treatment with A β 40 (Figure 5.10B). However, co-incubation with a 1:2.5 ratio of A β 40:LG_{WE} significantly reduced fluorescent intensity, and completely quenched it at a ratio of 1:12.5 (A β 40:LG_{WE}) (Figure 5.10B). LG_{WE} (0.25 mg/ml) alone did not show significant enhancement of fluorescent intensity (Figure 5.10B). Thus, it can be concluded that LG_{WE} can effectively inhibit ROS production mediated by A β 40 and prevent its downstream effectors. Calcium dyshomeostasis results in synaptic dysfunction followed by memory impairment and neuronal degeneration³⁷. Therefore, we measured intracellular free calcium treating with A β 40 in the presence or absence of LG_{WE}. A β 40 significantly increased intracellular calcium levels in SH-SY5Y cells as compared to untreated control cells. While, co-incubation with LG_{WE} in a ratio of 1:2.5 and 1:12.5, significantly reduced intracellular calcium in comparison to A β 40 treated cells

(Figure 5.10C). This is attributed to A β 40 forming pores in the cell membrane, which allows extracellular calcium to move inside the cell. The recovery of calcium oscillation by addition of LG_{WE} suggests prevention of A β 40 mediated membrane pore formation ^{1b}. This data is well corroborated with A β mediated influx of calcium ions into large unilamellar vesicles (LUVs) by incorporating the calcium-sensitive Fura-2 dye within the vesicles ²³. Here, the LUVs used for neuronal model membrane constituted of total brain lipid extract (TBLE), containing 55% unknown lipids, sphingolipids, brain ceramides, gangliosides, cerebroside etc ^{18b}. After adding A β 40 on TBLE LUVs, a noticeable influx of Ca²⁺ occurred inside the LUV, while less influx was observed in presence of A β 40:LG_{WE} at 1:2.5 and 1:12.5 concentration ratios (Figure 5.10D). After A β 40-induced membrane disruption, Ca²⁺ was expected to penetrate inside the pores of the LUVs. However, the physical integrity of the membrane was retained in presence of A β 40:LG_{WE}.

5.3.9. LG_{WE} protects against A β 40 mediated neuronal apoptosis

Studies have shown that accumulation of A β triggers generation of intracellular free radicals which lead to the activation of caspases via release of cytochrome-c from mitochondria ³⁸. As a result cellular apoptosis is triggered and can be tracked with annexin V/ propidium Iodide (PI) staining using a fluorescent associated cell sorter (FACS) machine. Treatment of SH-SY5Y cells with A β 40 enhances number of apoptotic cells approximately by 30% in comparison to control cells (Figure 5.10E). But, co-incubation with LG_{WE} at a ratio of 1:2.5 and 1:12.5 completely inhibited enhancement of apoptotic cells (Figure 5.10E). Importantly, LG_{WE} has no effect in triggering apoptosis even at higher concentration tested. The mean fluorescence intensity of annexin V binding to cells was further plotted as a histogram (Figure 5.10F) and a bar diagram (Figure 5.10G). The data showed a significant reduction in annexin V binding upon incubation of LG_{WE} with A β 40 suggesting reduction of cellular apoptosis. Therefore, our overall data provides a mechanistic insight into LG_{WE} interaction with A β proteins; binding of LG_{WE} not only inhibits A β amyloidosis but also promotes defibrillation of A β amyloids, rendering them non-toxic in neuronal environment. As a result, reduction in neuronal ROS, apoptosis, LDH release and calcium dyshomeostasis was evidential. Therefore, detrimental effects of neuroinflammation which can affect downstream cellular process related to ageing or neurodegeneration may be reduced with LG_{WE}.

5.4. Conclusion

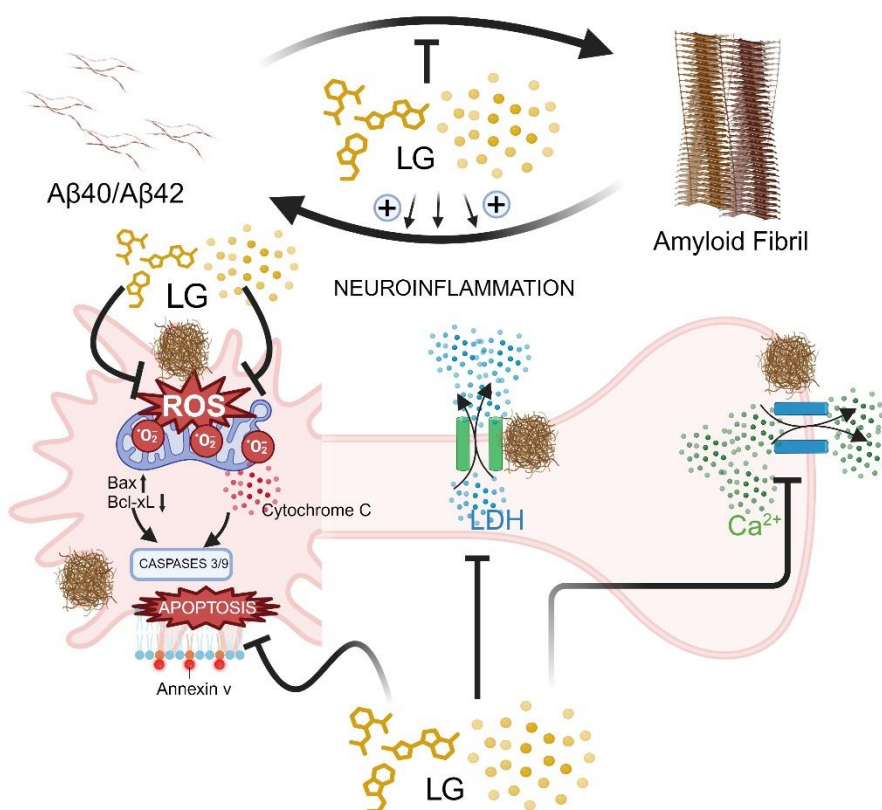


Figure 5.11. Schematic representation of the overall functions of LG_{WE} on Aβ₄₀/Aβ₄₂ peptides. LG_{WE} inhibits Aβ₄₀/Aβ₄₂ aggregation as well disaggregates preformed fibrils. In addition, LG_{WE} prevents Aβ mediated neuronal damage by inhibiting LDH leakage, ROS

In the present study, we have taken a comprehensive approach to characterize the compound LG through several processes of extraction and purification to explore its anti-amyloid properties. Of all the extracts obtained, we demonstrated that LG_{WE} had maximum efficiency in inhibiting the aggregation kinetics of Aβ peptides. Biophysical experiments including ThT, CD, NMR in combination with AFM showed that LG_{WE} was not only highly efficient in inhibiting the amyloid cascade reaction but also displayed disaggregating property towards preformed fibrillar species (Figure 5.11). NMR studies led us to conclude that LG_{WE} prevents further self-assembly by binding not only to the central hydrophobic amyloid-prone region but also C-terminal residues of Aβ₄₀/Aβ₄₂. Moreover, LG_{WE} protects Aβ₄₀ induced neurotoxicity, ROS generation, and apoptosis and maintains calcium homeostasis (Figure 5.11). The non-toxic nature of LG_{WE} *in vivo* and its natural

product composition may encourage and promote human trials. This makes LG a potential agent for further investigation into its active compounds. Identification of the bioactive compounds in LG_{WE} responsible for the anti-amyloidosis effects may provide promising leads for the development of effective anti-amyloidosis agents. Thus, it presents itself as a potential disease modifying therapeutic candidate against treatment of AD.

5.5. Appendix 5

Table S5.1. Biochemical Chart. Effect of LG_{WE} on haematological in mice (n= 6 in each group). WBC-white blood cells; RBC-red blood cells; Hb-haemoglobin; PCV-Packed cell volume; MCH-Mean corpuscular haemoglobin; ESR- Erythrocyte sedimentation rate; MCV-Mean corpuscular volume; MCHC- Mean corpuscular haemoglobin concentration.

PARAMETERS	Control	T1 1 mg/kg	T2 5 mg/kg	T3 10 mg/kg	Normal Range
Haemoglobin %	6.5±2	8.4±1.5	5.8±2.5	6.2±3	6.1-19.73
Red blood cell Count/Lac (10 ⁶)	4.6±0.5	4.9±0.6	3.8±0.3	3.9±0.5	3.57-11.7
PCV % (Haematocrit)	19.2±4	24.1±5	16.6±2	18.9±3.5	
MCV (fL)	41.5±7	49.1±10	43.1±12	48.4±5	39-95.18
MCH (pg)	15.0±10	17.1±8	14.9±10	15.8±12	27-58.22
MCHC g/L	33.8±8	34.8±5	34.9±8	32.8±8	
Platelets count/Lac (10 ⁶)	4.66±1	2.95±0.7	3.32±1.2	5.3±1.5	0.59-6.75
W.B.C total count/ Cu mm	4000±1000	4500 ±700	3500 ±1500	4700 ±1000	5500-12500
Neutrophils %	22±5	18±3	15±2	42±3	3-27
Lymphocytes%	75±10	79±5	80±3	52±15	12-41
Monocytes %	02±1	02±2	03±1	02±1	00-04
Eosinophils %	01±2	01±1	02±1	04±1	00-01
Basophil %	00±0	00±0	00±0	00±0	00-01
ESR mm/1 st hr	42±3	32±2	52±3	48±5	

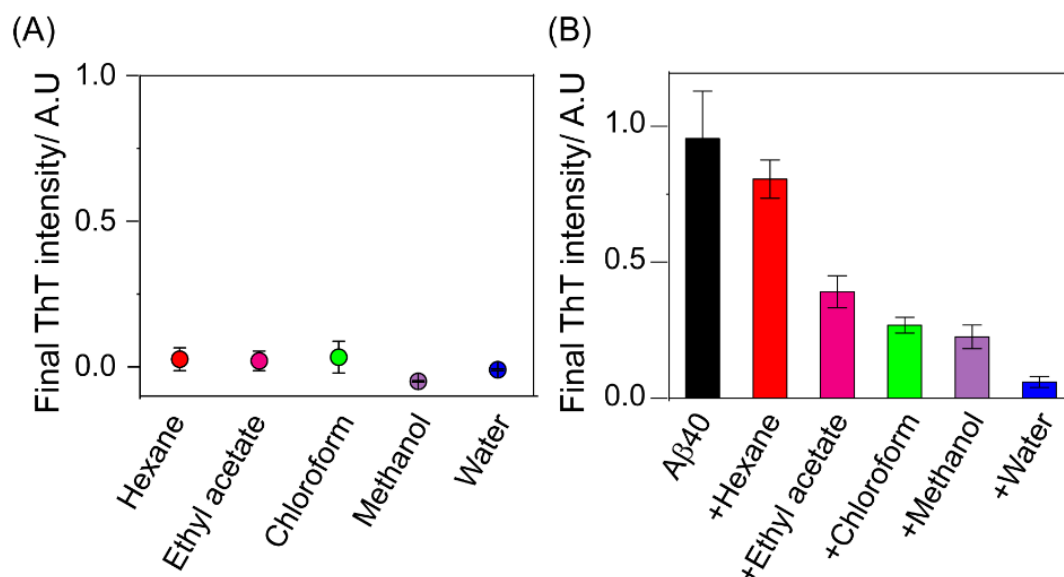


Figure S5.1. (A) ThT intensity of hexane (red), ethyl acetate (violet), chloroform (green), methanol (purple) and water (blue) extract compounds in the absence of Aβ40. (B) The bar plot of final ThT intensity value of all LG extracts in presence of Aβ40 (5 μM).

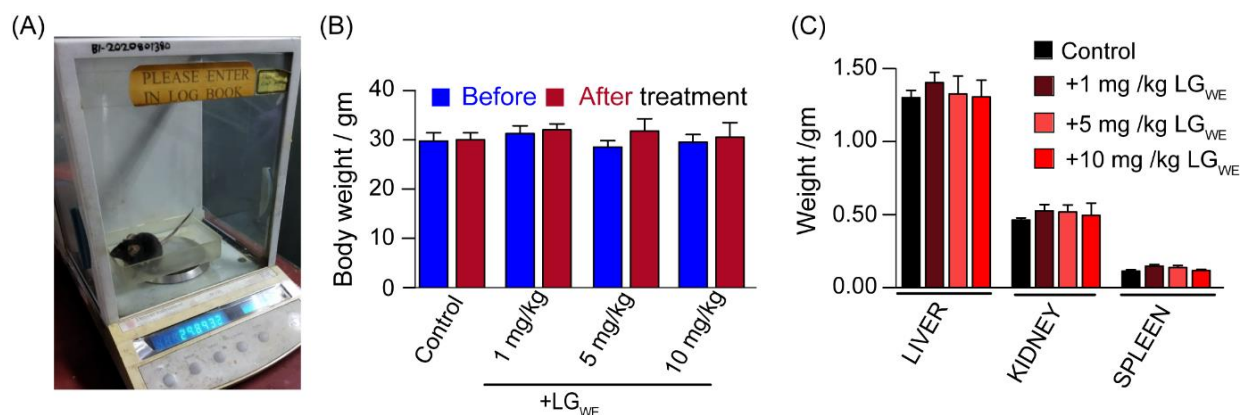


Figure S5.2. (A) Mouse (C57BL/6J) were treated intraperitoneally with indicated concentration of LG_{WE}. (B) Body weight was measured before and after LG_{WE} treatment. (C) Organ weight of liver, kidney, and spleen for control and LG_{WE} treated mice after sacrifice.

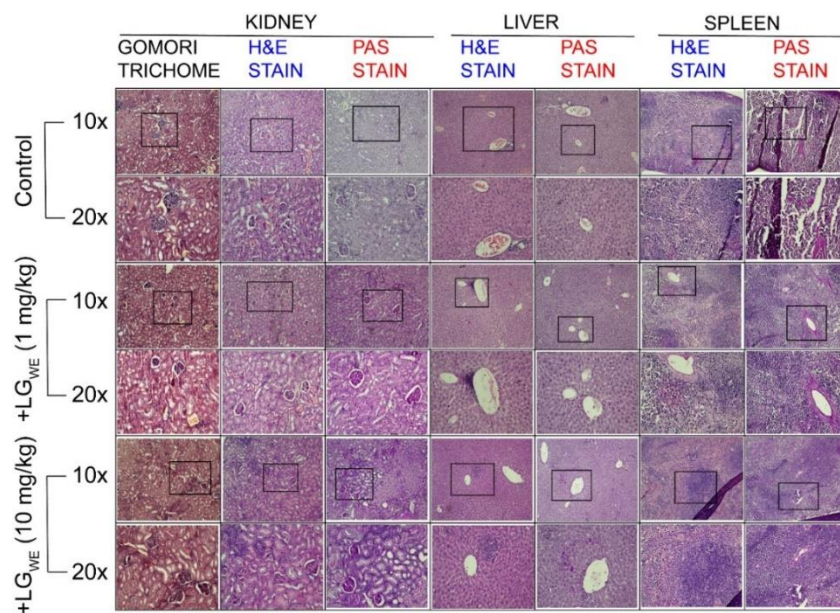


Figure S5.3. (A) Histopathological examination of kidney, liver and spleen of the mice treated with 1 mg and 10 mg water extract of LG per kg body weight of mice. The organ sections were stained with Hematoxylin and eosin (H and E staining), Gomori Trichrome and Periodic Acid-Schiff (PAS) and viewed under 10x and 20x magnification. The control images are the same images as depicted in Figure 5.1E.

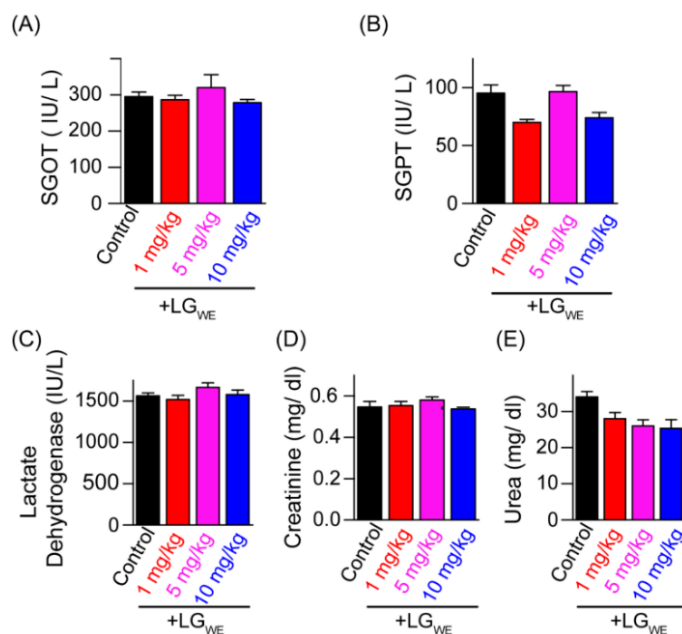


Figure S5.4. Effect of water exact of LG on various biochemical parameters such as (A) SGOT: serum glutamic oxaloacetic transaminase, (B) SGPT: serum glutamic pyruvic transaminase, (C) LDH: Lactate dehydrogenase, (D) Creatinine, (E) Urea.

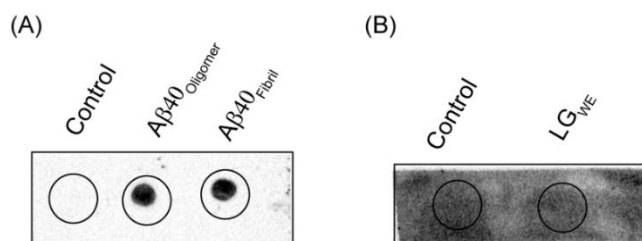


Figure S5.5. (A) A β 40 and (B) Water extract of LG (LG_{WE}) 0.25 mg/ml alone were spotted onto nitrocellulose membrane and probed with anti-amyloid OC antibody to check for any kind of cross reactivity.

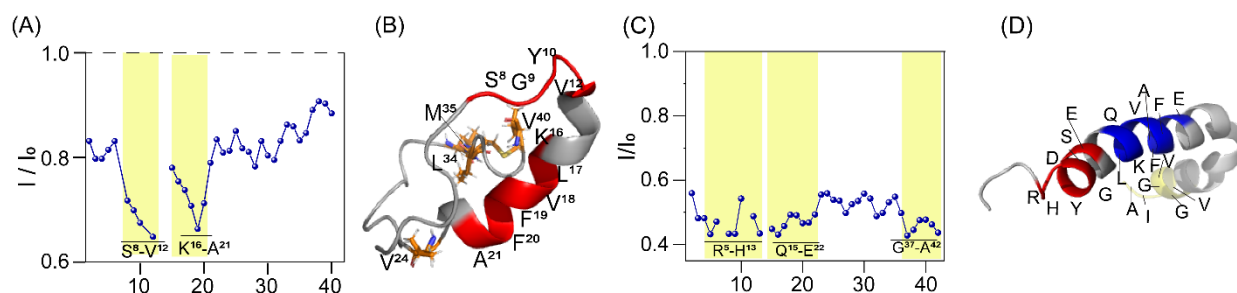


Figure S5.6. Running average peak intensity of (A) A β 40 and (C) A β 42 in presence of LG_{WE} at 1:12.5 of A β / LG_{WE} ratio for three consecutive amino acid residues. SFHMQC NMR spectra were recorded on 500 MHz Bruker Avance III NMR spectrometer with a SMART probe at 283 K. (B) The carton figures of LG_{WE} interaction site of A β 40 (PDB: 2LFM), highlighted by red color. (D) The carton figures of LG_{WE} interaction site of A β 42 (PDB: 1IYT), highlighted by red (N-terminal residues), blue (central hydrophobic residues) and yellow (C-terminal residues) colours.

5.6. References

- (a) Martinez-Cue, C.; Rueda, N., Cellular Senescence in Neurodegenerative Diseases. *Front Cell Neurosci* **2020**, *14*, 16; (b) Paul, A.; Kumar, S.; Kalita, S.; Kalita, S.; Sarkar, D.; Bhunia, A.; Bandyopadhyay, A.; Mondal, A. C.; Mandal, B., An explicitly designed paratope of amyloid-beta prevents neuronal apoptosis in vitro and hippocampal damage in rat brain. *Chem Sci* **2020**, *12* (8), 2853-2862; (c) Scheltens, P.; De Strooper, B.; Kivipelto, M.; Holstege, H.; Chetelat, G.; Teunissen, C. E.; Cummings, J.; van der Flier, W. M., Alzheimer's disease. *Lancet* **2021**, 397 (10284), 1577-1590.
- Holtzman, D. M.; Morris, J. C.; Goate, A. M., Alzheimer's disease: the challenge of the second century. *Sci Transl Med* **2011**, *3* (77), 77sr1.
- (a) Cristovao, J. S.; Santos, R.; Gomes, C. M., Metals and Neuronal Metal Binding Proteins Implicated in Alzheimer's Disease. *Oxid Med Cell Longev* **2016**, *2016*, 9812178; (b) Murphy, M. P.; LeVine, H., 3rd, Alzheimer's disease and the amyloid-beta peptide. *J Alzheimers Dis* **2010**, *19* (1), 311-23.

4. (a) Knowles, T. P.; Vendruscolo, M.; Dobson, C. M., The amyloid state and its association with protein misfolding diseases. *Nat Rev Mol Cell Biol* **2014**, *15* (6), 384-96; (b) Limbocker, R.; Chia, S.; Ruggeri, F. S.; Perni, M.; Cascella, R.; Heller, G. T.; Meisl, G.; Mannini, B.; Habchi, J.; Michaels, T. C. T.; Challa, P. K.; Ahn, M.; Casford, S. T.; Fernando, N.; Xu, C. K.; Kloss, N. D.; Cohen, S. I. A.; Kumita, J. R.; Cecchi, C.; Zasloff, M.; Linse, S.; Knowles, T. P. J.; Chiti, F.; Vendruscolo, M.; Dobson, C. M., Trodusquemine enhances Abeta(42) aggregation but suppresses its toxicity by displacing oligomers from cell membranes. *Nat Commun* **2019**, *10* (1), 225.
5. (a) De Strooper, B.; Karran, E., The Cellular Phase of Alzheimer's Disease. *Cell* **2016**, *164* (4), 603-15; (b) Ballard, C.; Gauthier, S.; Corbett, A.; Brayne, C.; Aarsland, D.; Jones, E., Alzheimer's disease. *Lancet* **2011**, *377* (9770), 1019-31; (c) Heller, G. T.; Shukla, V. K.; Figueiredo, A. M.; Hansen, D. F., Picosecond Dynamics of a Small Molecule in Its Bound State with an Intrinsically Disordered Protein. *J Am Chem Soc* **2024**, *146* (4), 2319-2324.
6. (a) Wells, C.; Brennan, S.; Keon, M.; Ooi, L., The role of amyloid oligomers in neurodegenerative pathologies. *Int J Biol Macromol* **2021**, *181*, 582-604; (b) Hubin, E.; van Nuland, N. A.; Broersen, K.; Pauwels, K., Transient dynamics of Abeta contribute to toxicity in Alzheimer's disease. *Cell Mol Life Sci* **2014**, *71* (18), 3507-21; (c) Cohen, S. I.; Linse, S.; Luheshi, L. M.; Hellstrand, E.; White, D. A.; Rajah, L.; Otzen, D. E.; Vendruscolo, M.; Dobson, C. M.; Knowles, T. P., Proliferation of amyloid-beta42 aggregates occurs through a secondary nucleation mechanism. *Proc Natl Acad Sci U S A* **2013**, *110* (24), 9758-63; (d) Abelein, A.; Kaspersen, J. D.; Nielsen, S. B.; Jensen, G. V.; Christiansen, G.; Pedersen, J. S.; Danielsson, J.; Otzen, D. E.; Graslund, A., Formation of dynamic soluble surfactant-induced amyloid beta peptide aggregation intermediates. *J Biol Chem* **2013**, *288* (32), 23518-28.
7. Carreiras, M. C.; Mendes, E.; Perry, M. J.; Francisco, A. P.; Marco-Contelles, J., The multifactorial nature of Alzheimer's disease for developing potential therapeutics. *Curr Top Med Chem* **2013**, *13* (15), 1745-70.
8. (a) Nasri, H.; Baradaran, A.; Shirzad, H.; Rafieian-Kopaei, M., New concepts in nutraceuticals as alternative for pharmaceuticals. *Int J Prev Med* **2014**, *5* (12), 1487-99; (b) Dadhania, V. P.; Trivedi, P. P.; Vikram, A.; Tripathi, D. N., Nutraceuticals against Neurodegeneration: A Mechanistic Insight. *Curr Neuropharmacol* **2016**, *14* (6), 627-40; (c) Ahmed, R.; Melacini, G., A solution NMR toolset to probe the molecular mechanisms of amyloid inhibitors. *Chem Commun (Camb)* **2018**, *54* (37), 4644-4652.
9. (a) Ono, K.; Yoshiike, Y.; Takashima, A.; Hasegawa, K.; Naiki, H.; Yamada, M., Potent anti-amyloidogenic and fibril-destabilizing effects of polyphenols in vitro: implications for the prevention and therapeutics of Alzheimer's disease. *J Neurochem* **2003**, *87* (1), 172-81; (b) Demain, A. L.; Vaishnav, P., Natural products for cancer chemotherapy. *Microb Biotechnol* **2011**, *4* (6), 687-99; (c) Lin, S. R.; Chang, C. H.; Hsu, C. F.; Tsai, M. J.; Cheng, H.; Leong, M. K.; Sung, P. J.; Chen, J. C.; Weng, C. F., Natural compounds as potential adjuvants to cancer therapy: Preclinical evidence. *Br J Pharmacol* **2020**, *177* (6), 1409-1423; (d) Chang, X.; Zhang, T.; Zhang, W.; Zhao, Z.; Sun, J., Natural Drugs as a Treatment Strategy for Cardiovascular Disease through the Regulation of Oxidative Stress. *Oxid Med Cell Longev* **2020**, *2020*, 5430407; (e) Palmioli, A.; Mazzoni, V.; De Luigi, A.; Bruzzone, C.; Sala, G.; Colombo, L.; Bazzini, C.; Zoia, C. P.; Inserra, M.; Salmona, M.; De Noni, I.; Ferrarese, C.; Diomedea, L.; Airolidi, C., Alzheimer's Disease Prevention through Natural Compounds: Cell-

- Free, In Vitro, and In Vivo Dissection of Hop (*Humulus lupulus* L.) Multitarget Activity. *ACS Chem Neurosci* **2022**, *13* (22), 3152-3167; (f) Baptista, F. I.; Henriques, A. G.; Silva, A. M.; Wiltfang, J.; da Cruz e Silva, O. A., Flavonoids as therapeutic compounds targeting key proteins involved in Alzheimer's disease. *ACS Chem Neurosci* **2014**, *5* (2), 83-92.
10. (a) Pandey, M. M.; Rastogi, S.; Rawat, A. K., Indian traditional ayurvedic system of medicine and nutritional supplementation. *Evid Based Complement Alternat Med* **2013**, *2013*, 376327; (b) Yuan, H.; Ma, Q.; Ye, L.; Piao, G., The Traditional Medicine and Modern Medicine from Natural Products. *Molecules* **2016**, *21* (5); (c) Cai, C.; Fang, J.; Ke, H., Editorial: Traditional medicine and phytochemicals for neurodegenerative diseases treatment: application of interdisciplinary technologies in novel therapeutic target and drug discovery. *Front Neurosci* **2023**, *17*, 1268710.
 11. (a) Lu, K.; Chakroborty, D.; Sarkar, C.; Lu, T.; Xie, Z.; Liu, Z.; Basu, S., Triphala and its active constituent chebulinic acid are natural inhibitors of vascular endothelial growth factor-a mediated angiogenesis. *PLoS One* **2012**, *7* (8), e43934; (b) Sivasankar, S.; Lavanya, R.; Brindha, P.; Angayarkanni, N., Aqueous and alcoholic extracts of Triphala and their active compounds chebulagic acid and chebulinic acid prevented epithelial to mesenchymal transition in retinal pigment epithelial cells, by inhibiting SMAD-3 phosphorylation. *PLoS One* **2015**, *10* (3), e0120512; (c) Kuboyama, T.; Tohda, C.; Komatsu, K., Effects of Ashwagandha (roots of *Withania somnifera*) on neurodegenerative diseases. *Biol Pharm Bull* **2014**, *37* (6), 892-7; (d) Uabundit, N.; Wattanathorn, J.; Mucimapura, S.; Ingkaninan, K., Cognitive enhancement and neuroprotective effects of *Bacopa monnieri* in Alzheimer's disease model. *J Ethnopharmacol* **2010**, *127* (1), 26-31; (e) Bopardikar, M.; Bhattacharya, A.; Rao Kakita, V. M.; Rachineni, K.; Borde, L. C.; Choudhary, S.; Koti Ainaravapu, S. R.; Hosur, R. V., Triphala inhibits alpha-synuclein fibrillization and their interaction study by NMR provides insights into the self-association of the protein. *RSC Adv* **2019**, *9* (49), 28470-28477.
 12. Ramsay, R. R.; Popovic-Nikolic, M. R.; Nikolic, K.; Uliassi, E.; Bolognesi, M. L., A perspective on multi-target drug discovery and design for complex diseases. *Clin Transl Med* **2018**, *7* (1), 3.
 13. V. Tiwari, S. R., A. Katiyar, A. Nischal, Effects of a multi route (oral and nasal) application of Lasunadya Ghrita (An ayurvedic formulation) in cases of primary depression: Inferences from a non randomized open label clinical trial *Indian Journal of Traditional Knowledge* **2021**, *20* (3), 618-628.
 14. Sripanidkulchai, B., Benefits of aged garlic extract on Alzheimer's disease: Possible mechanisms of action. *Exp Ther Med* **2020**, *19* (2), 1560-1564.
 15. (a) Mijanur Rahman, M.; Gan, S. H.; Khalil, M. I., Neurological effects of honey: current and future prospects. *Evid Based Complement Alternat Med* **2014**, *2014*, 958721; (b) Iftikhar, A.; Nausheen, R.; Muzaffar, H.; Naeem, M. A.; Farooq, M.; Khurshid, M.; Almatroudi, A.; Alrumaihi, F.; Allemailem, K. S.; Anwar, H., Potential Therapeutic Benefits of Honey in Neurological Disorders: The Role of Polyphenols. *Molecules* **2022**, *27* (10).
 16. Afshari, A. R.; Sadeghnia, H. R.; Mollazadeh, H., A Review on Potential Mechanisms of *Terminalia chebula* in Alzheimer's Disease. *Adv Pharmacol Sci* **2016**, *2016*, 8964849.
 17. (a) Shang, A.; Cao, S. Y.; Xu, X. Y.; Gan, R. Y.; Tang, G. Y.; Corke, H.; Mavumengwana, V.; Li, H. B., Bioactive Compounds and Biological Functions of Garlic (*Allium sativum* L.).

- Foods* **2019**, *8* (7); (b) Bradley, J. M.; Organ, C. L.; Lefer, D. J., Garlic-Derived Organic Polysulfides and Myocardial Protection. *J Nutr* **2016**, *146* (2), 403S-409S; (c) Fadzil, M. A. M.; Mustar, S.; Rashed, A. A., The Potential Use of Honey as a Neuroprotective Agent for the Management of Neurodegenerative Diseases. *Nutrients* **2023**, *15* (7); (d) Bag, A.; Bhattacharyya, S. K.; Chattopadhyay, R. R., The development of Terminalia chebula Retz. (Combretaceae) in clinical research. *Asian Pac J Trop Biomed* **2013**, *3* (3), 244-52; (e) Yao, G.; Miao, X.; Wu, M.; Lv, Z.; Bai, Y.; Chang, Y.; Ouyang, H.; He, J., Pharmacokinetics of active compounds of a Terminalia chebula Retz. Ethanolic extract after oral administration rats using UPLC-MS/MS. *Front Pharmacol* **2023**, *14*, 1067089.
18. (a) Korshavn, K. J.; Satriano, C.; Lin, Y.; Zhang, R.; Dulchavsky, M.; Bhunia, A.; Ivanova, M. I.; Lee, Y. H.; La Rosa, C.; Lim, M. H.; Ramamoorthy, A., Reduced Lipid Bilayer Thickness Regulates the Aggregation and Cytotoxicity of Amyloid-beta. *J Biol Chem* **2017**, *292* (11), 4638-4650; (b) Bera, S.; Gayen, N.; Mohid, S. A.; Bhattacharyya, D.; Krishnamoorthy, J.; Sarkar, D.; Choi, J.; Sahoo, N.; Mandal, A. K.; Lee, D.; Bhunia, A., Comparison of Synthetic Neuronal Model Membrane Mimics in Amyloid Aggregation at Atomic Resolution. *ACS Chem Neurosci* **2020**, *11* (13), 1965-1977.
 19. Sahoo, B. R.; Genjo, T.; Nakayama, T. W.; Stoddard, A. K.; Ando, T.; Yasuhara, K.; Fierke, C. A.; Ramamoorthy, A., A cationic polymethacrylate-copolymer acts as an agonist for beta-amyloid and an antagonist for amylin fibrillation. *Chem Sci* **2019**, *10* (14), 3976-3986.
 20. Pariary, R.; Dolui, S.; Shome, G.; Mohid, S. A.; Saha, A.; Ratha, B. N.; Harikishore, A.; Jana, K.; Mandal, A. K.; Bhunia, A.; Maiti, N. C., Coomassie brilliant blue G-250 acts as a potential chemical chaperone to stabilize therapeutic insulin. *Chem Commun (Camb)* **2023**, *59* (52), 8095-8098.
 21. (a) Yan, Y.; Liu, J.; McCallum, S. A.; Yang, D.; Wang, C., Methyl dynamics of the amyloid-beta peptides Abeta40 and Abeta42. *Biochem Biophys Res Commun* **2007**, *362* (2), 410-4; (b) Fawzi, N. L.; Libich, D. S.; Ying, J.; Tugarinov, V.; Clore, G. M., Characterizing methyl-bearing side chain contacts and dynamics mediating amyloid beta protofibril interactions using (1)(3)C(methyl)-DEST and lifetime line broadening. *Angew Chem Int Ed Engl* **2014**, *53* (39), 10345-9.
 22. Yamaguchi, T.; Matsuzaki, K.; Hoshino, M., Transient formation of intermediate conformational states of amyloid-beta peptide revealed by heteronuclear magnetic resonance spectroscopy. *FEBS Lett* **2011**, *585* (7), 1097-102.
 23. Sciacca, M. F.; Kotler, S. A.; Brender, J. R.; Chen, J.; Lee, D. K.; Ramamoorthy, A., Two-step mechanism of membrane disruption by Abeta through membrane fragmentation and pore formation. *Biophys J* **2012**, *103* (4), 702-10.
 24. Sarkar, D.; Maity, N. C.; Shome, G.; Varnava, K. G.; Sarojini, V.; Vivekanandan, S.; Sahoo, N.; Kumar, S.; Mandal, A. K.; Biswas, R.; Bhunia, A., Mechanistic insight into functionally different human islet polypeptide (hIAPP) amyloid: the intrinsic role of the C-terminal structural motifs. *Phys Chem Chem Phys* **2022**, *24* (36), 22250-22262.
 25. Sasidharan, S.; Chen, Y.; Saravanan, D.; Sundram, K. M.; Yoga Latha, L., Extraction, isolation and characterization of bioactive compounds from plants' extracts. *Afr J Tradit Complement Altern Med* **2011**, *8* (1), 1-10.

26. Saini, R. K.; Prasad, P.; Shang, X.; Keum, Y. S., Advances in Lipid Extraction Methods-A Review. *Int J Mol Sci* **2021**, *22* (24).
27. (a) Agholme, L.; Lindstrom, T.; Kagedal, K.; Marcusson, J.; Hallbeck, M., An in vitro model for neuroscience: differentiation of SH-SY5Y cells into cells with morphological and biochemical characteristics of mature neurons. *J Alzheimers Dis* **2010**, *20* (4), 1069-82; (b) Kumar, S.; Paul, A.; Kalita, S.; Kumar, A.; Srivastav, S.; Hazra, S.; Ghosh, A. K.; Mandal, B.; Mondal, A. C., A Peptide Based Pro-Drug Ameliorates Amyloid-beta Induced Neuronal Apoptosis in In Vitro SH-SY5Y Cells. *Curr Alzheimer Res* **2017**, *14* (12), 1293-1304.
28. Yang, D.; Qiao, J.; Wang, J. X.; Wei, W. Y.; Zhao, Z. X.; Cai, H. Y., [Effects of B-GOS on cognitive behavior and depression of transgenic mice with Alzheimer's disease]. *Zhongguo Ying Yong Sheng Li Xue Za Zhi* **2021**, *37* (3), 240-246.
29. (a) Tanokashira, D.; Mamada, N.; Yamamoto, F.; Taniguchi, K.; Tamaoka, A.; Lakshmana, M. K.; Araki, W., The neurotoxicity of amyloid beta-protein oligomers is reversible in a primary neuron model. *Mol Brain* **2017**, *10* (1), 4; (b) Choi, Y. J.; Chae, S.; Kim, J. H.; Barald, K. F.; Park, J. Y.; Lee, S. H., Neurotoxic amyloid beta oligomeric assemblies recreated in microfluidic platform with interstitial level of slow flow. *Sci Rep* **2013**, *3*, 1921; (c) Sun, H.; Liu, J.; Li, S.; Zhou, L.; Wang, J.; Liu, L.; Lv, F.; Gu, Q.; Hu, B.; Ma, Y.; Wang, S., Reactive Amphiphilic Conjugated Polymers for Inhibiting Amyloid beta Assembly. *Angew Chem Int Ed Engl* **2019**, *58* (18), 5988-5993; (d) Barz, B.; Liao, Q.; Strodel, B., Pathways of Amyloid-beta Aggregation Depend on Oligomer Shape. *J Am Chem Soc* **2018**, *140* (1), 319-327.
30. (a) Fatafta, H.; Khaled, M.; Owen, M. C.; Sayyed-Ahmad, A.; Strodel, B., Amyloid-beta peptide dimers undergo a random coil to beta-sheet transition in the aqueous phase but not at the neuronal membrane. *Proc Natl Acad Sci U S A* **2021**, *118* (39); (b) Gursky, O.; Aleshkov, S., Temperature-dependent beta-sheet formation in beta-amyloid Abeta(1-40) peptide in water: uncoupling beta-structure folding from aggregation. *Biochim Biophys Acta* **2000**, *1476* (1), 93-102.
31. (a) Hasecke, F.; Niyangoda, C.; Borjas, G.; Pan, J.; Matthews, G.; Muschol, M.; Hoyer, W., Protofibril-Fibril Interactions Inhibit Amyloid Fibril Assembly by Obstructing Secondary Nucleation. *Angew Chem Int Ed Engl* **2021**, *60* (6), 3016-3021; (b) McLaurin, J.; Yang, D.; Yip, C. M.; Fraser, P. E., Review: modulating factors in amyloid-beta fibril formation. *J Struct Biol* **2000**, *130* (2-3), 259-70; (c) Zhang, Y.; Chen, H.; Li, R.; Sterling, K.; Song, W., Amyloid beta-based therapy for Alzheimer's disease: challenges, successes and future. *Signal Transduct Target Ther* **2023**, *8* (1), 248; (d) Ghosh, S.; Ali, R.; Verma, S., Abeta-oligomers: A potential therapeutic target for Alzheimer's disease. *Int J Biol Macromol* **2023**, *239*, 124231.
32. Zhao, J.; Li, K.; Wan, K.; Sun, T.; Zheng, N.; Zhu, F.; Ma, J.; Jiao, J.; Li, T.; Ni, J.; Shi, X.; Wang, H.; Peng, Q.; Ai, J.; Xu, W.; Liu, S., Organoplatinum-Substituted Polyoxometalate Inhibits beta-amyloid Aggregation for Alzheimer's Therapy. *Angew Chem Int Ed Engl* **2019**, *58* (50), 18032-18039.
33. (a) D.Sarkar, A. B., Delineating the Role of GxxxG Motif in Amyloidogenesis: A New Perspective in Targeting Amyloid-Beta Mediated AD Pathogenesis. . *ACS Bio & Med Chem Au* **2023**; (b) Sarkar, D.; Chakraborty, I.; Condorelli, M.; Ghosh, B.; Mass, T.; Weingarth, M.; Mandal, A. K.; La Rosa, C.; Subramanian, V.; Bhunia, A., Self-Assembly and Neurotoxicity

- of beta-Amyloid (21-40) Peptide Fragment: The Regulatory Role of GxxxG Motifs. *ChemMedChem* **2020**, *15* (3), 293-301.
34. Hensley, K.; Carney, J. M.; Mattson, M. P.; Aksenova, M.; Harris, M.; Wu, J. F.; Floyd, R. A.; Butterfield, D. A., A model for beta-amyloid aggregation and neurotoxicity based on free radical generation by the peptide: relevance to Alzheimer disease. *Proc Natl Acad Sci U S A* **1994**, *91* (8), 3270-4.
35. Narayan, P.; Ganzinger, K. A.; McColl, J.; Weimann, L.; Meehan, S.; Qamar, S.; Carver, J. A.; Wilson, M. R.; St George-Hyslop, P.; Dobson, C. M.; Klenerman, D., Single molecule characterization of the interactions between amyloid-beta peptides and the membranes of hippocampal cells. *J Am Chem Soc* **2013**, *135* (4), 1491-8.
36. Yang, Y.; Chen, T.; Zhu, S.; Gu, X.; Jia, X.; Lu, Y.; Zhu, L., Two macrocyclic polyamines as modulators of metal-mediated Abeta40 aggregation. *Integr Biol (Camb)* **2015**, *7* (6), 655-62.
37. (a) Higgins, D.; Graupner, M.; Brunel, N., Memory maintenance in synapses with calcium-based plasticity in the presence of background activity. *PLoS Comput Biol* **2014**, *10* (10), e1003834; (b) Hagenston, A. M.; Bading, H., Calcium signaling in synapse-to-nucleus communication. *Cold Spring Harb Perspect Biol* **2011**, *3* (11), a004564.
38. (a) Kumari, S.; Dhapola, R.; Reddy, D. H., Apoptosis in Alzheimer's disease: insight into the signaling pathways and therapeutic avenues. *Apoptosis* **2023**, *28* (7-8), 943-957; (b) Hwang, S.; Lim, J. W.; Kim, H., Inhibitory Effect of Lycopene on Amyloid-beta-Induced Apoptosis in Neuronal Cells. *Nutrients* **2017**, *9* (8).

Summary and future outlook

Amyloid disorders are growing in global importance, leading to increased research on effective targeted therapeutics. Despite the advances, the exact mechanism of aggregation *in vivo*, remains far from being elusive, majorly owing to the complexities and heterogenous properties of the different protein systems. Decades of amyloid research have been dedicated to delineating the intermediate oligomeric or proto-fibrillar stages that form the pathogenic conformers underlying the disease etiology. However, these intermediates form a dynamic heterogeneous pool of several transient conformers, significantly different from the well-defined fibrillar forms, and are difficult to characterize. Without the atomic-level information on the growth of amyloid fibers, it has been challenging to design inhibitors or excipients to block fiber growth. The protein-folding intermediates have been implicated in harbouring the essential chemical cues that provide useful insight into understanding the amyloidogenic propensity. These intermediates are often structurally similar to the low molecular weight early conformers of the protein but form a chemically distinct pool that nucleates the early aggregation events. Our research on amyloid peptides or protein primarily focused to understand their atomic-level structure and dynamics to identify novel epitopes for targeted therapeutic intervention. This thesis aimed to discover novel small molecules and peptides that can inhibit the aggregation of insulin and A β amyloid, while being structurally distinct from existing inhibitors. In chapter 2, our findings demonstrate that small molecule inhibitors, like CBBG and PADs, act as a chemical chaperone, effectively preventing insulin aggregation and the disintegration of fibrils to non-toxic smaller fragments. Our results present CBBG and PADs as promising avenues for treating type 2 diabetes, as these small molecules enhance the efficiency and availability of therapeutic insulin in its active form. Additionally, CBBG also plays a vital role in stimulating insulin secretion from pancreatic β -cells.

Conducting similar experiments with peptide-based inhibitor in the presence of biological membranes may help us understand the effectiveness of inhibitor at the protein's functional interface. Designing peptide-based inhibitors for targeting inhibition of amyloid aggregation may be a constructive approach, as these peptides selectively interact with amyloid peptides or protein, offering advantages such as high selectivity, low toxicity, and potential for precise molecular design. There are several limitations including size, proteolytic cleavage of peptides, low membrane permeability, and the lack of effective methods for delivery. A number of modification strategies have been widely implemented to address the primary technical challenges to using

peptides as drug. Cyclization of linear peptides enhance proteolytic stability due to its structural rigidity and increase better-penetrating capability into the cell membranes. In chapter 3, we have shown that a cyclic peptide, KR7CC effectively inhibits the progression of early oligomeric intermediates and triggers the formation of off-pathway aggregates, making it a promising, non-toxic peptide with serum stability for targeted therapeutic intervention against insulin amyloidogenesis, both in solution and in the presence of biological membranes. Synthetic modification by introduction of β - breaker element in a peptide sequence is another approach to enhance stability and superior activity of the peptide. Our studies in chapter 4, is one such example wherein incorporating anthranilic acid into the RF8 peptide sequence yields Peptide1 (P1), a novel, nontoxic, serum-stable peptide. P1 inhibits A β 42 aggregation, disrupts matured β -sheet fibrils into non-toxic forms and effectively reduce neuronal apoptosis. Our investigations propose a potent peptide based therapeutic approach that diminishes the cytotoxicity of aggregating species by redirecting the kinetics of amyloid fibrillation towards off-pathway. These methods could inspire novel drug design investigations and address the pressing demand for discovering new disease-modifying therapeutics for prevalent amyloid diseases that currently lack effective remedies. Additionally, increasing bioavailability and effectiveness requires the utilization of suitable delivery methods, with clinical trials potentially exploring combinations for enhanced efficacy of designed inhibitors.

Searching for novel natural compounds with demonstrated efficacy against neurodegenerative disorders, while maintaining a high safety profile, is crucial for advancing the search for therapeutics that can modify the progression of these diseases. Although natural compound-based drugs offer numerous benefits, their production faces several challenges such as low solubility, limited bio-availability and lack of quality. The difficulty in identifying a single active component due to the synergistic effects between multiple components limits the effectiveness of natural extracts. Consequently, taking a comprehensive approach, a characterization of the traditional Indian medicine Lasunadya Ghrita (LG) has been discussed in chapter 5 through various processes of extraction and purification to explore its anti-amyloid properties. The water extract of LG protects A β 40 induced neurotoxicity, reduces ROS generation, and prevents apoptosis and maintains calcium homeostasis, potentially serving as an additional mechanism for neuroprotection. The *in vivo* non-toxicity of LG, along with its composition as a natural product, may provide encouragement and pave the way for future human trials.

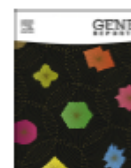
Peer-reviewed publications

Gene Reports 16 (2019) 100423



Contents lists available at ScienceDirect

Gene Reports

journal homepage: www.elsevier.com/locate/genrep

Mitochondrial-membrane association of α -synuclein: Pros and cons in consequence of Parkinson's disease pathophysiology

Ranit Pariary¹, Dipita Bhattacharyya¹, Anirban Bhunia^{*}

Department of Biophysics, Bose Institute, P-1/12 CIT Scheme VII (M), Kolkata 700054, India

ARTICLE INFO

Keywords:

Mitochondria
 α -synuclein
 Membrane
 Cardiolipin
 Membrane-protein interaction
 Neurodegenerative disease
 Parkinson's disease
 Fusion
 Fission

ABSTRACT

The mitochondrial association of α -synuclein has been known to play a crucial homeostatic role in the neuronal cells. The slightest of a tweak in this association cause for activating the neurodegenerative mechanism, ultimately leading to neuronal loss, the pathological feature of Parkinson's disease. Studies so far have highlighted several intrinsic and extrinsic factors that alter this association, promoting protein misfolding and mitochondrial dysfunction, both of which bring about cooperative cellular degeneracy. Despite the years of effort, the exact molecular association remains unspecified, forbidding the characterization of disease etiology. In this review, we summarize the accumulating evidence for this mitochondrial membrane association, sewing the scattered links to a clear understanding of this interaction.

1. Introduction

Parkinson's disease (PD) is the most well-spread movement disorder and the second most common neurodegenerative disorder (Meissner et al., 2011) after Alzheimer's disease (AD). The disease is identified by motor disturbances such as resting tremor, rigidity, bradykinesia, and postural instability, prompted by the slow and progressive death of dopaminergic (DA) neurons from the substantia nigra (Wood-Kaczmar et al., 2006; Gazewood et al., 2013; Rao et al., 2006; Rezak, 2007). The SNCA locus from the fourth chromosome, encoding the α -synuclein protein is among the first loci recognized and identified to be associated with the autosomal dominant inherited form of PD (Polymeropoulos et al., 1997; Klein and Westenberger, 2012; Bras and Singleton, 2009). Several point mutations in the SNCA gene have been known to underlie the early onset of PD (Corti et al., 2011; Gasser, 2009). The disease pathophysiology is almost always marked by the presence of dense cellular inclusions mainly composed of the amyloidogenic protein aggregates in the form of Lewy bodies in the DA neurons (commonly referred to as Lewy neurites). Ever since its discovery, (Nussbaum, 2017) and association with the Lewy neurites, the protein, and its familial mutants have surfaced as a much sought-after subject of interest for many scientific groups (Stefanis, 2012; Dehay et al., 2015) studying protein dynamics associated with PD. However, despite the decades of research, the exact disease etiology remains inexplicit. Especially, not

much knowledge has been gathered over the natural physiological role of the wild-type (WT) protein even though more about the disease association of the protein is known.

α -Synuclein is localized particularly in the nerve terminals and has also been known to be distributed in the cytosol, associated with the nucleus, endoplasmic reticulum (ER) and mitochondria; more specifically the mitochondria-associated membranes (MAMs) with ambiguous functionality (George et al., 1995; Iwai et al., 1995; Li et al., 2007; Guardia-Laguarta et al., 2014). Several convergent studies have highlighted the membrane-associated folding of the protein that underlies the dynamics, affecting protein homeostasis *in vivo*. However, to understand the disease etiology, it is particularly important to understand the triggering factors that initiate the protein misfolding associated with the disease pathophysiology. Studies have shown that the α -synuclein aggregation kinetics depends on the dynamic equilibrium between the native structures, i.e., the monomers and tetramers (Bartels et al., 2011; Dettmer et al., 2015a). The protein is natively unfolded and can adopt several conformations upon interactions with the cellular factors. Alteration of a single factor can promote the transformation into the neurotoxic species of the protein (Rajagopalan and Andersen, 2001). Several internal and external factors control the aggregation process of α -synuclein. High protein concentration (due to gene mutations and constitutive expressions), low pH (acidosis in PD patients), high interaction with cellular metabolites, and altered native

^{*} Corresponding author.

E-mail address: bhunias@jcbiose.ac.in (A. Bhunia).

¹ Both authors contributed equally.

<https://doi.org/10.1016/j.genrep.2019.100423>

Received 5 January 2019; Received in revised form 4 May 2019; Accepted 22 May 2019

Available online 04 June 2019

2452-0144/ © 2019 Elsevier Inc. All rights reserved.



Cite this: DOI: 10.1039/d3cc01791e

Received 13th April 2023,
Accepted 27th May 2023

DOI: 10.1039/d3cc01791e

rsc.li/chemcomm

Coomassie brilliant blue G-250 acts as a potential chemical chaperone to stabilize therapeutic insulin†

Ranit Pariary,^{‡a} Sandip Dolui,^{‡b} Gourav Shome,^{‡c} Sk Abdul Mohid,^a
 Achintya Saha,^{‡d} Bhisma N Rath,^{‡e} Amaravathi Harikishore,^c Kuladip Jana,^c
 Atin K Mandal,^{*c} Anirban Bhunia^{‡*a} and Nakul C Maiti^{‡*b}

Our studies show Coomassie Brilliant Blue G-250 as a promising chemical chaperone that stabilises the α -helical native human insulin conformers, disrupting their aggregation. Furthermore, it also increases the insulin secretion. This multipolar effect coupled with its non-toxic nature could be useful for developing highly bioactive, targeted and biostable therapeutic insulin.

Insulin amyloidoma marked by extracellular fibrils at the injection site is a medical condition complicating insulin therapy.¹ The instability of monomeric insulin and its fibrillation also interfere with its manufacture, long-term storage, and pharmaceutical use.² Overcoming this problem through inclusion of a chemical chaperone such as small molecule, peptide or macrocycle may abrogate fibrilization in insulin formulations.³ Recent reports have established promising effect of Coomassie Brilliant Blue G-250 (CBBG) and its analogues in preventing amyloid fibrilization.⁴ In the current investigation, we have examined the interaction of the CBBG dye with human insulin (HI) and its stabilizing effect on the helical folds of HI protein.

CBBG, a nontoxic dye consisting of a triphenylmethane moiety (Fig. S1, ESI†), is an FDA-approved drug for ophthalmic use.⁵ Our studies with mice treated with CBBG revealed that a maximum dose of 10 mg kg⁻¹ does not cause mortality or

abnormal behavioural patterns (Fig. S2, ESI†). Over the treatment period, all groups gained body weight and maintained kidney and spleen weight, although marginal weight loss was detected for the liver at CBBG doses \geq 5 mg kg⁻¹ (Fig. S2, ESI†). Haematological as well as biochemical parameters did not alter much with CBBG doses (Table S1, ESI†). We found no significant cytoarchitectural changes in the kidneys, liver, and spleen after administering 1 mg kg⁻¹ or 5 mg kg⁻¹ of CBBG (Fig. 1A); however, a CBBG dosage of 10 mg kg⁻¹ showed minor changes

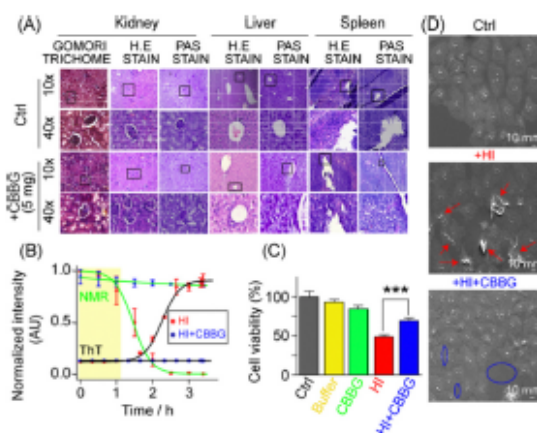


Fig. 1 Inhibition of HI fibrils by equimolar CBBG. (A) Histopathological studies of the effect of sub-chronic toxicity on mice ($n = 6$ each group) for 5 mg kg⁻¹ CBBG treatment. The image is shown at 10 \times and 40 \times magnification (haematoxylin and eosin stain and periodic acid-Schiff stain). (B) Overlay of ThT fluorescence (black line) and ¹H NMR kinetic traces (green line) of HI alone (red ball) and HI:CBBG (blue ball) at 60 °C in 25 mM HCl, 0.1 M NaCl, pH ~ 1.6. (C) MTT assay showing cell viability of RIN5f cells with treatment of CBBG, HI fibrils and the co-incubated HI:CBBG sample (50 μ M). Values are represented as mean \pm SEM, $n = 6$. ***Indicates $p < 0.001$, significance was analysed using the Mann-Whitney two tailed t -test. (D) SEM image of RIN5f cell with addition of HI fibrils and co-incubated HI:CBBG (1:1).

^aDepartment of Biophysics, Bose Institute, Salt Lake, Kolkata 700 091, India.
 E-mail: bhunia@jbbose.ac.in

^bStructural Biology and Bioinformatics Division, CSIR-IICT, 4 Raja S C Mullick Road, Kolkata 700 032, India. E-mail: nmaiti@iict.res.in

^cDivision of Molecular Medicine, Bose Institute, Salt Lake, Kolkata 700 091, India.
 E-mail: mandalak@jbbose.ac.in

^dDepartment of Chemical Technology, University of Calcutta, 92 APC Road, Kolkata 700 009, India

^eSchool of Biological Sciences, Nanyang Technological University, 60 Nanyang Drive, 637551, Singapore

^fCenturion University of Technology and Management, Odisha 761211, India

† Electronic supplementary information (ESI) available. See DOI: <https://doi.org/10.1039/d3cc01791e>

‡ These authors contributed equally.



Contents lists available at ScienceDirect

International Journal of Biological Macromolecules

journal homepage: www.elsevier.com/locate/ijbiomac

An amphiphilic small molecule drives insulin aggregation inhibition and amyloid disintegration

Anirban Das^{a,1}, Yogesh M. Gangarde^{a,1}, Ranit Pariary^c, Anirban Bhunia^c, Ishu Saraogi^{a,b,*}

^a Department of Chemistry, Indian Institute of Science Education and Research Bhopal, Bhopal Bypass Road, Bhauri, Bhopal 462066, MP, India

^b Department of Biological Sciences, Indian Institute of Science Education and Research Bhopal, Bhopal Bypass Road, Bhauri, Bhopal 462066, MP, India

^c Department of Biophysics, Bose Institute, Sector V, EN 80, Bidhan Nagar, Kolkata 700 091, India

ARTICLE INFO

Keywords:
Chemical chaperone
Excipient
Sulfonate
Inhibitors
Disaggregation

ABSTRACT

The aggregation of proteins into ordered fibrillar structures called amyloids, and their disintegration represent major unsolved problems that limit the therapeutic applications of several proteins. For example, insulin, commonly used for the treatment of diabetes, is susceptible to amyloid formation upon exposure to non-physiological conditions, resulting in a loss of its biological activity. Here, we report a novel amphiphilic molecule called PAD-S, which acts as a chemical chaperone and completely inhibits fibrillation of insulin and its biosimilars. Mechanistic investigations and molecular docking lead to the conclusion that PAD-S binds to key hydrophobic regions of native insulin, thereby preventing its self-assembly. PAD-S treated insulin was biologically active as indicated by its ability to phosphorylate Akt, a protein in the insulin signalling pathway. PAD-S is non-toxic and protects cells from insulin amyloid induced cytotoxicity. The high aqueous solubility and easy synthetic accessibility of PAD-S facilitates its potential use in commercial insulin formulations. Notably, PAD-S successfully disintegrated preformed insulin fibrils to non-toxic smaller fragments. Since the structural and mechanistic features of amyloids are common to several human pathologies, the understanding of the amyloid disaggregation activity of PAD-S will inform the development of small molecule disaggregators for other amyloids.

1. Introduction

Efficient approaches to deal with protein aggregation represent a major unmet need in human health. In particular, aggregation of proteins into ordered β -sheets called amyloids has been shown to occur in several human pathologies [1,2]. Amyloids are extraordinarily stable, and disrupt normal cellular processes either due to lack of the natively folded protein, or toxicity resulting from aggregated protein [3]. Although various quality control mechanisms exist in vivo to deal with these aggregates often at the expense of large amounts of ATP [4], disaggregating amyloids using small molecules is a challenge and has hindered the use of therapeutic proteins like insulin.

Insulin, a 51-amino acid peptide hormone (Fig. 1A), has an important role in glucose metabolism [5]. Underproduction or insensitivity to this vital hormone can result in an increase in blood glucose level of an individual resulting in diabetes [6], often requiring administration of

insulin from external sources. This has resulted in a large worldwide demand for insulin necessitating its production on an industrial scale. However, insulin forms amyloid aggregates upon exposure to conditions like acidic pH (2–4), elevated temperature, mechanical agitation: conditions frequently encountered during its commercial production. The relative ease of insulin aggregation poses a problem during its manufacture and pharmaceutical use [7,8]. The resulting loss of biological activity reduces the effective dose of insulin, preventing precise control of glucose levels in patients. Additionally, subcutaneous amyloid plaques and cutaneous allergic reactions have been observed in many diabetic patients at the site of repeated insulin injections [9–11]. Hence, efforts to develop small molecules that inhibit insulin aggregation and disaggregate amyloids are of prime importance.

Although several natural and synthetic small molecules and peptides [12–19] have been studied for insulin aggregation inhibition, they suffer from practical limitations, including lack of specificity, incomplete

* Corresponding author at: Department of Chemistry, Indian Institute of Science Education and Research Bhopal, Bhopal Bypass Road, Bhauri, Bhopal 462066, MP, India.

E-mail address: ishu@iiserb.ac.in (I. Saraogi).

¹ These authors contributed equally.

<https://doi.org/10.1016/j.ijbiomac.2022.07.155>

Received 16 May 2022; Received in revised form 8 July 2022; Accepted 19 July 2022

Available online 27 July 2022

0141-8130/© 2022 Elsevier B.V. All rights reserved.



Contents lists available at ScienceDirect

BBA - Proteins and Proteomics

journal homepage: www.elsevier.com/locate/bbapap

Targeted inhibition of amyloidogenesis using a non-toxic, serum stable strategically designed cyclic peptide with therapeutic implications

Ranit Pariary^a, Baijayanti Ghosh^b, Zuzana Bednarikova^c, Kyriakos Gabriel Varnava^d,
Bhisma N. Ratha^a, Sreyan Raha^e, Dipita Bhattacharyya^a, Zuzana Gazova^c,
Vijayalekshmi Sarojini^d, Atin K. Mandal^b, Anirban Bhunia^{a,*}

^a Department of Biophysics, Bose Institute, P-1/12 CIT Scheme VII (M), Kolkata, 700054, India

^b Department of Molecular Medicine, Bose Institute, P-1/12 CIT Scheme VII (M), Kolkata, 700054, India

^c Department of Biophysics, Institute of Experimental Physics, Slovak Academy of Sciences, Kosice, Slovakia

^d School of Chemical Sciences, The University of Auckland, Private Bag, 92019, Auckland, New Zealand

^e Department of Physics, Bose Institute, 93/1 APC Road, Kolkata 700009, India



ARTICLE INFO

Keywords:
Amyloid
Inhibition
NMR
Microscopy
Raman spectroscopy

ABSTRACT

Amyloidogenic disorders are currently rising as a global health issue, prompting more and more studies dedicated to the development of effective targeted therapeutics. The innate affinity of these amyloidogenic proteins towards the biomembranes adds further complexities to the systems. Our previous studies have shown that biologically active peptides can effectively target amyloidogenesis serving as an efficient therapeutic alternative in several amyloidogenic disorders. The structural uniqueness of the PWWP motif in the de novo designed heptapeptide, KR7 (KPWWPRR-NH₂) was demonstrated to target insulin fiber elongation specifically. By working on insulin, an important model system in amyloidogenic studies, we gained several mechanistic insights into the inhibitory actions at the protein-peptide interface. Here, we report a second-generation non-toxic and serum stable cyclic peptide, based primarily on the PWWP motif that resulted in complete inhibition of insulin fibrillation both in the presence and absence of the model membranes. Using both low- and high-resolution spectroscopic techniques, we could delineate the specific mechanism of inhibition, at atomistic resolution. Our studies put forward an effective therapeutic intervention that redirects the default aggregation kinetics towards off-pathway fibrillation. Based on the promising results, this novel cyclic peptide can be considered an excellent lead to design pharmaceutical molecules against amyloidogenesis.

Introduction

Protein amyloidogenesis plays a crucial role in the pathophysiology of several human diseases, including neurodegenerative disorders such as Alzheimer's and Parkinson's as well as metabolic disorders like Diabetes [1–3]. The association of amyloidogenesis with the devastating pathological implications has led to an increase in developing inhibitors against this aggregation. Scientific advancements using *in vitro*, *in vivo*, and *in silico* strategies have added to our gradual understanding of the system [4–7]. However, success in implementing such approaches has been limited, in part, due to the complexity of the aggregation process and also in part because of the fact that the mechanisms and targets of the inhibitors are often poorly defined.

Over the years, several amyloidogenic model proteins have been identified, including insulin, amyloid β , α -synuclein, etc. that underly

some of the most devastating disorders (such as Type-II Diabetes, Alzheimer's and Parkinson's Disease). The ease of availability of insulin over other amyloidogenic proteins has attracted several research groups to use it as a model protein for understanding amyloidogenesis [8–13]. Insulin, apart from being an excellent amyloid model, is widely known for its significant pharmaceutical importance. However, owing to its innate aggregation propensity, insulin forms amyloid intermediates during its commercial production, formulation, transportation, and storage [14]. Furthermore, insulin has been shown to form amyloid deposits at the site of administration [15–22], mostly due to a membrane-induced amyloidogenic attribute. Such deposits have often been referred to as the “insulin ball,” [15,19] which not only complicates the diagnosis of systemic amyloidosis in diabetes but also reduces insulin bioavailability and hence raises treatment costs [15,17]. In fact, biomembranes have been found to play crucial roles in modulating the

* Corresponding author at: Department of Biophysics, Bose Institute, P-1/12 CIT Scheme VII (M), Kolkata, 700054, India
E-mail address: bhunla@jbose.ac.in (A. Bhunia).

<https://doi.org/10.1016/j.bbapap.2020.140378>

Received 1 October 2019; Received in revised form 24 January 2020; Accepted 31 January 2020

Available online 04 February 2020

1570-9639/ © 2020 Elsevier B.V. All rights reserved.



Zinc oxide nanoparticle interface moderation with tyrosine and tryptophan reverses the pro-amyloidogenic property of the particle

Kanti Kusum Yadav ^{a, b}, Monalisha Ojha ^c, Ranit Pariary ^d, Manoranjan Arakha ^e, Anirban Bhunia ^d, Suman Jha ^{c, *}

^a Department of Biotechnology and Medical Engineering, National Institute of Technology, Rourkela, Odisha, 769008, India

^b Department of Biotechnology, School of Agriculture and Biosciences, Karunya Institute of Technology and Sciences, Coimbatore, Tamil Nadu, 641114, India

^c Department of Life Science, National Institute of Technology, Rourkela, Odisha, 769008, India

^d Department of Biophysics, Bose Institute, Kolkata, West Bengal, 700054, India

^e Centre for Biotechnology, Siksha 'D' Anusandhan, Bhubaneswar, Odisha, 751003, India

ARTICLE INFO

Article history:

Received 9 June 2021

Received in revised form

23 September 2021

Accepted 19 October 2021

Available online xxx

Keywords:

Insulin

Fibrillation

Nanoparticle surface functionalization

ZnONP

Cytotoxicity

ABSTRACT

Zinc oxide nanoparticle with negative surface potential (ZnONP) enhances bovine insulin fibrillation. Here, we are exploring ZnONP with positive surface potential (ZnONP_{unc}) and surface functionalized with tyrosine and tryptophan amino acids to observe the effects of surface potential and surface functional groups on the fibrillation. ZnONP_{unc}, despite of inversed surface potential, enhances the insulin fibrillation with increase in the interface concentration at physiological pH. Whereas, the interface moderation with the amino acids mitigates the surface-mediated insulin fibrillation propensity. Additionally, the study indicates that the change in interfacial functional groups at ZnONP_{unc} significantly reverses the interface-mediated destabilization of insulin conformation. The functional groups from the amino acids, like C=O, N-H and aromatic functional groups, are anticipated to further stabilize the insulin conformation by forming hydrogen bond and van der Waals interactions with the key amyloidogenic sequences of insulin, A13-A20 from A-chain and B9-B20 from B-chain. Hence, the altered interaction profile, with change in interfacial functional groups, mitigates the interface-mediated insulin fibrillation and the ZnONP_{unc}-fibril-mediated cytotoxicity.

© 2021 Elsevier B.V. and Société Française de Biochimie et Biologie Moléculaire (SFBBM). All rights reserved.

1. Introduction

Protein aggregation has been the centre of attention for researchers in the field of biology, biophysics and medicine [1]. Amyloid fibril is a highly ordered aggregate with core made of cross β -sheet structure, following the nucleation kinetics. In nucleation kinetics, formation of nuclei (also called as seed) is a rate-limiting step in amyloid fibrillation [2,3]. Furthermore, it has been proved that proteins, not linked with any pathological conditions, can also form similar fibril-like structures under appropriate *in vitro* conditions, suggesting that amyloid formation is a generic property of all polypeptides [4]. Till date, approximately 35 proteins are linked to different disorders such as Parkinson's, Huntington's, Alzheimer's, type II diabetes etc [5]. Insulin is one of the most

extensively studied amyloidogenic protein with pharmaceutical importance [6]. It is a small (51 a. a.), predominantly α -helical, protein with two polypeptide chains (chain A and chain B) covalently attached by one interchain and two intrachain disulphide bonds to each other [7]. It is secreted by pancreatic β -cells as zinc ion co-ordinated hexameric quaternary structure, but monomeric structure is the physiologically active structure. However, in absence of zinc ions, insulin exists in different association states depending on pH of the medium; native quaternary conformations (hexamer/tetramer/dimer) are much stable than the monomeric state of the protein [8]. It is suggested that insulin fibrillation is exhibited by partially unfolded monomer, preceding dissociation of the native quaternary conformations [9]. *In vitro* fibrillation of insulin has been studied under different pH conditions, temperatures, ionic strength and different solid/liquid/air interfaces [8–12]. Insulin, for exhibiting different degree of structure, has been adopted as one of the model protein to underline the protein aggregation and misfolding disorders [9,13,14]. Moreover,

* Corresponding author.

E-mail address: jhas@nitrrkl.ac.in (S. Jha).

<https://doi.org/10.1016/j.biochi.2021.10.011>

0300-9084/© 2021 Elsevier B.V. and Société Française de Biochimie et Biologie Moléculaire (SFBBM). All rights reserved.

Received: 14 November 2019 | Revised: 11 June 2020 | Accepted: 12 July 2020

DOI: 10.1002/prot.25983



RESEARCH ARTICLE

PROTEINS
WILEY

High-resolution structure of a partially folded insulin aggregation intermediate

Bhisma N. Rath¹ | Rajiv K. Kar¹ | Jeffrey R. Brender² | Ranit Pariary¹ |
Bankanidhi Sahoo³ | Sujan Kalita⁴ | Anirban Bhunia¹¹Department of Biophysics, Bose Institute, Kolkata, India²Radiation Biology Branch, National Institutes of Health, Bethesda, Maryland³TIFR Centre for Interdisciplinary Sciences, Hyderabad, India⁴Department of Chemistry, Indian Institute of Technology Guwahati, Guwahati, India

Correspondence

Anirban Bhunia, Department of Biophysics, Bose Institute, P-1/12 CIT Scheme VII (M), Kolkata 700054, India.

Email: anirbanbhunia@gmail.com, bhunia@jcb.bose.ac.in

Present address

Bhisma N. Rath, Department of Phytopharmaceuticals, Centurion University of Technology and Management, Paralakhemundi, India

Funding information

Council of Scientific and Industrial Research, 02(0292)/17/EMR-II; Department of Biotechnology, Ministry of Science and Technology, Grant/Award Number: BT/PR29978/MED/30/2037/2018; Department of Biotechnology, Government of India

Peer Review

The peer review history for this article is available at <https://publons.com/publon/10.1002/prot.25983>.

Abstract

Insulin has long been served as a model for protein aggregation, both due to the importance of aggregation in the manufacture of insulin and because the structural biology of insulin has been extensively characterized. Despite intensive study, details about the initial triggers for aggregation have remained elusive at the molecular level. We show here that at acidic pH, the aggregation of insulin is likely initiated by a partially folded monomeric intermediate. High-resolution structures of the partially folded intermediate show that it is coarsely similar to the initial monomeric structure but differs in subtle details—the A chain helices on the receptor interface are more disordered and the B chain helix is displaced from the C-terminal A chain helix when compared to the stable monomer. The result of these movements is the creation of a hydrophobic cavity in the center of the protein that may serve as nucleation site for oligomer formation. Knowledge of this transition may aid in the engineering of insulin variants that retain the favorable pharmacokinetic properties of monomeric insulin but are more resistant to aggregation.

KEYWORDS

aggregation, amyloid, FCS, insulin, molecular dynamics, NMR

1 | INTRODUCTION

The accumulation of misfolded proteins is a common pathological feature of a number of devastating neurodegenerative disorders, such as Alzheimer's and Parkinson's disease, and several metabolic diseases, such as type II diabetes. Formation of amyloid usually requires a protein

to pass through several intermediate forms prior to achieving a β -sheet rich fibrillar structure.^{1–3} According to the amyloid hypothesis, the formation of amyloid involves both an initial nucleation phase followed by an explosive growth phase.^{4–6} The oligomers formed during the nucleation phase have long been implicated in disease progression and cytotoxicity, under both in vitro and in vivo conditions.^{7–12} Hence, obtaining structural understanding of amyloid intermediates may help to devise inhibitors for either treatment or prevention.

Besides the pathogenic amyloid proteins, insulin, a peptide hormone having therapeutic importance, also displays high propensity to form amyloid fibril. Because it is readily available and fibrillizes easily

Abbreviations: ThT, Thioflavin T; CD, circular dichroism; t_{lag} , lag time; $t_{1/2}$, half-time; τ_D , diffusion time; FCS, fluorescence correlation spectroscopy; TMR, tetramethylrhodamine; TEM, transmission electron microscopy; AFM, atomic force microscopy; NMR, nuclear magnetic resonance; TOCSY, total correlation spectroscopy; NOESY, nuclear overhauser effect spectroscopy; MD simulation, molecular dynamics simulation; d_4 , deuterio acetic acid.

Raman Spectroscopic Insights of Phase-Separated Insulin Aggregates

Published as part of ACS Physical Chemistry Au virtual special issue "Ultrafast Spectroscopy of Chemical Transformations".

Sandip Dolui, Anupam Roy, Uttam Pal, Shubham Kundu, Esha Pandit, Bhisma N Ratha, Ranit Pariary, Achintya Saha, Anirban Bhunia, and Nakul C. Maiti*

Cite This: ACS Phys. Chem. Au 2024, 4, 268–280

Read Online

ACCESS |

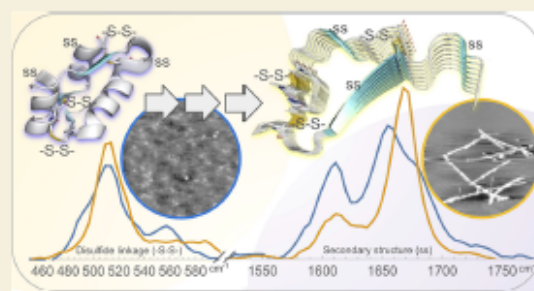
Metrics & More

Article Recommendations

Supporting Information

ABSTRACT: Phase-separated protein accumulation through the formation of several aggregate species is linked to the pathology of several human disorders and diseases. Our current investigation envisaged detailed Raman signature and structural intricacy of bovine insulin in its various forms of aggregates produced in situ at an elevated temperature (60 °C). The amide I band in the Raman spectrum of the protein in its native-like conformation appeared at 1655 cm^{-1} and indicated the presence of a high content of α -helical structure as prepared freshly in acidic pH. The disorder content (turn and coils) also was predominately present in both the monomeric and oligomeric states and was confirmed by the presence shoulder amide I maker band at $\sim 1680 \text{ cm}^{-1}$. However, the band shifted to $\sim 1671 \text{ cm}^{-1}$ upon the transformation of the protein solution into fibrillar aggregates as produced for a longer time of incubation. The protein, however, maintained most of its helical conformation in the oligomeric phase; the low-frequency backbone α -helical conformation signal at $\sim 935 \text{ cm}^{-1}$ was similar to that of freshly prepared aqueous protein solution enriched in helical conformation. The peak intensity was significantly weak in the fibrillar aggregates, and it appeared as a good Raman signature to follow the phase separation and the aggregation behavior of insulin and similar other proteins. Tyrosine phenoxo moieties in the protein may maintained its H-bond donor–acceptor integrity throughout the course of fibril formation; however, it entered in more hydrophobic environment in its journey of fibril formation. In addition, it was noticed that oligomeric bovine insulin maintained the orientation/conformation of the disulfide bonds. However, in the fibrillar state, the disulfide linkages became more strained and preferred to maintain a single conformation state.

KEYWORDS: amyloid, tyrosine, fermi doublet, fluorescence, aggregation, phase separation



INTRODUCTION

Protein misfolding and fibrillization of well-defined globular proteins and intrinsically disordered proteins (IDPs) have emerged as an important pathological signature and a key molecular marker of various amyloid-related human diseases and disorders.^{1–13} While IDPs remained energetically at higher energy state, a high rate of thermal fluctuation rendered its stability entropically favorable. However, hydrophobic interactions and subsequent zipping among amyloidogenic regions of disordered proteins lead to the formation of water-insoluble and thermodynamically more stable β -sheet-rich protein fibrils.^{14,15} Thus, protein kinematics plays a significant role in the stability of disordered proteins in the solution phase. However, highly folded globular proteins in their native states are quite stable mainly due to their folded structure stabilized by different noncovalent molecular interactions.^{16,17} Disulfide linkages also, in some cases, added additional stability to their

tertiary folded structure.¹⁸ Thus, the folded proteins are much in a lower energy state compared to IDPs. Therefore, heat or other harsh conditions (low pH, addition of salt, denaturants) are often required for globular protein to unfold fully or partially to initiate the aggregation and fibrilization process.^{19–23}

It has been well established through several in situ investigations that the fibril formation of both types of proteins, IDPs and globular, proceeds via formation of soluble oligomeric state, regardless of the initial incubation conditions

Received: November 30, 2023

Revised: January 30, 2024

Accepted: January 31, 2024

Published: February 15, 2024

